University of Sussex

Local Structure and Global Connectivity in The Cerebral Cortex

NeuroInformatics, Histology and Ultra High Resolution Diffusion MRI in The Rhesus and Marmoset Monkey Brain

Colin Reveley

Submitted for the degree of Doctor of Philosophy

University of Sussex

DATE

Declaration

I hereby declare that this thesis has not been and will not be submitted in whole or in part to another University for the award of any other degree.

Signature:

Colin Reveley

UNIVERSITY OF SUSSEX

Colin Reveley, Doctor of Philosophy

Local Structure and Global Connectivity in The Cerebral Cortex NeuroInformatics, Histology and Ultra High Resolution Diffusion MRI in The Rhesus and Marmoset Monkey Brain

Summary

This thesis concerns the cortical connectivity in Primates. The efficacy of Diffusion weighted MRI (dMRI) is examined. White matter ("WM") systems subjacent to cortex ("superficial WM") are found to be a limiting factor to dMRI tractography. Superficial WM systems are examined with dMRI itself, and with analysis of histological data from the scanned brains. dMRI data was acquired ex-vivo at exceptional spatial and angular resolution (250μm in Rhesus, 150μm in Marmoset). The superficial WM was found to be complex, and with current dMRI methods, an effective barrier to tracking to and from around 50% of cortex in Rhesus. The quality of our data allowed Gray matter seeding, so that penetration both into and out of cortex was examined.

We summarize the history of cortical connectivity and current work in tractography. We present an account of the formation and properties of the superficial WM. We compare tracking behaviors to tracer results, and develop a series of scalar maps on cortical surface models to summarize tracking behaviors. We attempt to explain these maps by examining the underlying tracking behavior and the brain tissue itself, revealing the intricate nature of the superficial WM.

Chapter 4 contains a separate but related project in which a histologically accurate high resolution 3D and surface atlas of the Rhesus cortex is constructed with unprecedented accuracy. A method to rapidly and accurately non-linearly transform the atlas to a scan of another animal is developed, thus labelling its cortex. accuracy is by comparison to histology of the scanned animals.

Collaborations and Publications Arising from this Thesis

Parts of this work were carried out in collaboration Chapter 3 is the basis for a paper in preparation, and was a collaboration with Audrunas Gruslys, parts of it are contained in his thesis and in (Gruslys et al., 2014). Gruslys contributed software expertise and custom algorithms to implement requirements defined closely with me to achieve neuroscientific goals. Chapters 4 and 5 contain part of the research program that led to the *Proceedings of the National Academy of Sciences* publication cited below and parts of chapter 4 and 5 are contained in that paper. All text, figures and research in chapters 4 and 5 are my own.

Colin Reveley, Anil K. Seth, Carlo Pierpaoli, Afonso C. Silva, David Yu, Richard C. Saunders, David A. Leopold, and Frank Q. Ye. 2015. Superficial White Matter Fiber Systems Impede Detection of Long-Range Cortical Connections in Diffusion MR Tractography. Proceedings of the National Academy of Sciences, May, 201418198. doi:10.1073/pnas.1418198112.

Acknowledgements

Thank you to my family

and to Anil, Audrunas, David and Frank

Contents

1 Introduction **1**

1.1 Overview of Cortical Connectivity 1

1.2 Diffusion MRI and Cortical Connectivity 4

1.3 Cortical Fiber Systems 8

1.3.1 Local Fiber Systems 10

1.4 What is in This Thesis 15

2 Methods **17**

2.1 Summary Of Data Used in this Thesis 17

2.2 Diffusion Imaging and Modelling 18

2.2.1 DWI - Diffusion Weighted Imaging 18

2.2.2 The Diffusion Tensor Model 19

2.2.3 Tractography 26

2.2.4 Surface Methods 27

2.3 Structure Tensor Analysis of Histological Data 34

2.4 Data Sets And Analyses as applied In This Study 37

2.4.1 MRI Data Analysis Specific to this Study 40

2.4.2 Tracer Surgeries 42

2.4.3 Preparation and analysis of histological data in this study 43

2.4.4 FSL Results 44

2.5 Anatomical Terms and (selected) Rhesus Landmarks 48

3 Accurate Labelling of Macaque Cortex **50**

3.1 Introduction 51

3.2 Construction Of Atlas 53

3.2.1 Artifact removal from original MRI images and creation of "surrogate" ultra high resolution MRI volume 57

3.2.2 Reconstruction of 2D sections to high resolution 3D atlas 60
3.3 Mapping The Digital Atlas Onto Other Brains 65
3.3.1 Validation of digital labelling against histological sections 66
3.3.2 Consistency in the mapping software 71
3.3.3 Summary 76

4 Tracer and dMRI Tractography Compared 77
4.1 Introduction 78
4.2 Tractography Compared to Tracer Results 79
4.2.1 Corpus Callosum Connectivity 80
4.2.2 Autoradiographic WM Tracer Comparison 84
4.2.3 Cortical Tracer Labelling Comparisons 87
4.2.4 GM Terminations are Similar for Diverse Seeding Strategies 90
4.3 Global DTI Cortico-Cortical Connectivity and Cortical Shape 91
4.3.1 Mapping Methods 91
4.3.2 Grey Matter to Gray Matter Connectivity Maps 92
4.3.3 Gray Matter to White Matter Maps 95
4.4 Global DTI Cortico-Cortical Connectivity in Marmoset 102
4.5 Spatial Resolution 107
4.6 Summary 112

5 Local Fibers and DTI 113
5.1 Introduction 113
5.2 Diffusion Data And Tissue Properties: Initial Comparison 115
5.3 Relationship of Representative Tracking Behaviors To Derived Scalar Maps 119
5.4 Superficial Fiber Structures and Tracking Behaviors 126
5.4.1 Crown Fibers 131
5.5 Superficial Fiber Structures and Tracking in the Marmoset 136
5.6 Anatomy and Diffusion at the IPS 140
5.6.1 Diffusion Tracking and Anatomical Tracing in the IPS 140
5.6.2 Local Fiber Anatomy at the IPS 145
5.7 Summary & Conclusion 152

6 Conclusion 153

Bibliography 157

Chapter 1

Introduction

Abstract

In this introductory chapter, the concepts methods and history of cortical connectivity are briefly described. Subsequently a non-technical description of dMRI and it's relation to the study of cortical connectivity is presented. "Gyral bias" is presented as a significant obstacle for the use of dMRI in estimating cortical connectivity. Three points presented in (Van Essen et al., 2013) as the primary candidate explanations are enumerated, and these are returned to throughout the thesis to assess whether they adequately explain the phenomena. Finally, the nature of different white matter tracts is briefly discussed, with an emphasis on local fibers. A synthesis of literature is used to develop a hypothesis of the developmental formation and thus "function" broadly construed of local fiber systems is presented, which forms a conceptual background for the empirical work of the thesis.

1.1 Overview of Cortical Connectivity

The primate and particularly human forebrain is notable for the large neocortical sheet and "white matter" of myelinated axons subserving connectivity intracortically and between cortex and other brain areas. Despite sharing a roughly similar laminar architecture, the primate cerebral cortex consists of dozens of areas distinguished by their cytoarchitectonic profiles (Brodmann, 1909; Zilles and Amunts, 2010), sensory maps (Tootell et al., 1998), functional specialization (Op de Beeck et al., 2008), and spontaneous activity covariation (Smith et al., 2013).

While cortical regions can be identified by form and function, cortical and other brain region are neither wholly segregated nor wholly integrated Varela et al. (2001) in their operation, and may form complex hierarchies (Felleman and Van Essen, 1991). Understanding these functional mechanisms requires knowledge of their anatomical substrate. Partly due to advances in MRI, recent attention within neuroscience has increasingly focused on understanding how connectivity or "connectomics" underpins brain function (Sporns, 2013).

History of Cortical Connectivity

Historically, knowledge of anatomical connectivity within the brain primarily stems from studies of animal models, or very limited inference from gross dissection (Schmahmann and Pandya, 2006) The macaque monkey has been a fruitful neuroscientific model because the functional organization of its brain is in many ways similar to that of the human (Kaas, 2012; Mantini et al., 2012; Tsao et al., 2008). The study of cortical connectivity has focused to a large extent on the macaque monkey due to its vision dominated brain and similarity to the human brain in many regards including cortical cytoarchitecture at a superficial level (Brodmann, 1909). The major sulci and gyri in the macaque brain mirror those in the human brain to a significant extent. Much of what is known about human cortico-cortical connectivity is derived from anatomical studies of the macaque.

Prior to about 1970 connectivity was assessed by lesioning of gray matter regions and subsequent silver staining of necrotic axons . In the 1970's the introduction of tracing techniques permitted accurate (Cowan et al., 1972) assessment of the afferents of a brain region. Tracers permit the labelling of cell bodies or synapses (retrograde and anterograde) from an injection site via axonal transport.

Tracer injections in the macaque have revealed that virtually all cortical areas give rise to long- range connections, many of which project to other cortical areas to potentially form processing hierarchies (Felleman and Van Essen, 1991). Tracers are a direct method in that axons traced are guaranteed to have connectivity to some part of the the injection site (however complex their white matter trajectory). A vast literature of tracer studies in the macaque exists (Stephan and Kotter, 1999), and this data continues to shape views of functional organization in the human brain. However, despite it's advantage, studying long-range connections through tracer injections is time consuming, and prone to sampling

biases, since a given experiment can measure connectivity to only one or a small number of cortical sites.

Moreover, while the macaque brain is a good approximation of the human brain in many respects, both species have undergone profound evolutionary changes since the time of their most recent common ancestor living more than 20 million years ago (Perelman et al., 2011), particularly in regard to the massive expansion of the cerebral cortex (Van Essen et al., 2012a). Thus it is of great value to assess human anatomical connections directly and comprehensively (Crick and Jones, 1993), a recognition that is central to the Human Connectome Project (Sporns et al., 2005; Van Essen and Ugurbil, 2012).

It is therefore desirable to investigate connectivity in the human brain directly. Studying human neuroanatomical connections poses distinct experimental challenges, since tract tracing must be conducted either noninvasively or post-mortem (Sporns, 2013). Post-mortem tracer studies allow for some tracking of cortico-cortical connections, for example using carbocyanine dyes (Mufson et al., 1990; Tardif and Clarke, 2001) . However, questions about the accuracy of these methods in the adult brain have limited their use (Molnr et al., 2006) (but see (Seehaus et al., 2013)). Magnetic resonance imaging (MRI) is the more common method to evaluate neuroanatomical connections in the human brain, and has the advantage of being noninvasive and applicable to live subjects, including patients (Van Essen et al., 2012b). Resting state functional MRI can be used to estimate functional relationships between cortical regions in a way that does not examine the anatomical connections themselves. fMRI is not examined in this thesis. Foremost among MRI methods for inferring long-range anatomical connections is diffusion-weighted magnetic resonance imaging, often abbreviated as diffusion MRI or simply dMRI. In dMRI, the local anisotropic diffusion profile of water molecules within each voxel is taken as a basis for inferring the local fiber orientation distribution, in the simplest case described as a tensor model with a single principal axis (Basser et al., 1994; Pierpaoli et al., 1996). A range of diffusion models and algorithms have been developed over the past two decades in an attempt to derive anatomical pathways from features of the water diffusion displacement profile in each voxel. These methods, generally termed as dMRI tractography (Behrens et al., 2003a; Mori and van Zijl, 2002; Wedeen et al., 2005, 2012), can be divided into deterministic methods in which the best estimates of various pathways are depicted as streamlines or streamtubes, and probabilistic methods in which a family of possible trajectories is

estimated accounting for noise induced uncertainty. Chapter 2 describes these.

1.2 Diffusion MRI and Cortical Connectivity

Diffusion MRI methods have proven remarkably successful in the modeling of large white matter bundles in vivo in human volunteers (Catani et al., 2003). While there are certain inherent challenges, such as the difficulty in following the course of fiber tracts through regions consisting of crossing or abutting fiber pathways, these problems have been ameliorated by improvements in both local orientation modeling and tractography algorithms (Jbabdi et al., 2010). At present, the most successful fiber tracking employs probabilistic or deterministic approaches on high angular resolution diffusion imaging (HARDI) or diffusion spectrum imaging (DSI) data. Comparison with known fiber pathways has been used to validate computed dMRI track lines at a qualitative level (Schmahmann et al., 2007), and more direct studies have compared diffusion methods with manganese and postmortem tracers in the same brains (Jbabdi et al., 2013; Dauguet et al., 2007; Dyrby et al., 2007). In recent years the clinical value of this method has become apparent, as tractography has become a viable tool both for surgical planning (Kleiser et al., 2009) and the monitoring of neuropathology (Kitamura et al., 2008).

Building upon these successes, many investigators now use diffusion tractography to identify and study long-range projections of the cerebral cortex, including cortico-cortical projections. The neurons that compose these projections send their axons from cell bodies in the gray matter into fasciculi in the deep white matter. After traveling through the deep white matter, the axons then emerge to enter a different cortical region. Thus the use of dMRI to track cortico-cortical connections involves two additional and daunting challenges. The first challenge is that the diffusion anisotropy measured in the cortex and near the white matter / gray matter boundary (WGB) is often too low to model local orientation, which is a prerequisite for inclusion in a track line. The second challenge is that it is extremely difficult to determine precisely where small axonal tracts join and leave larger white matter fasciculi (Jbabdi and Johansen-Berg, 2011). These limitations have prompted neuroscientists to adopt pragmatic heuristics for studying cortical connectivity using dMRI. For example, to facilitate the crossing of the WGB, it has become common practice to construct large-volume cortical seeds that include a portion of the adjacent white matter, just deep to the infragranular layers of cortical neurons. Then, to combat the inherently ambiguous detection of axonal branching in deep white matter fasciculi, in-

vestigators often apply so-called waypoints, which create a priori spatial restrictions that selectively limit the results to fibers along trajectories of interest. While debatable at a theoretical level, these methods allow investigators to visualize certain types of cortico-cortical connections that would otherwise resist characterization using the dMRI method. A common assumption is that in the future, when the spatial and angular resolution of dMRI acquisition improves, fewer such methodological adjustments will be required to obtain accurate results, and this is an assumption examined in this thesis.

A recent study comparing tract-tracer and dMRI tractography concluded that the anatomical accuracy of dMRI tractography is intrinsically limited, but it did not investigate the specific factors leading to this finding (Thomas et al., 2014).

It has been noted that dMRI tractography exhibits a "gyral bias" in that tracks ter-

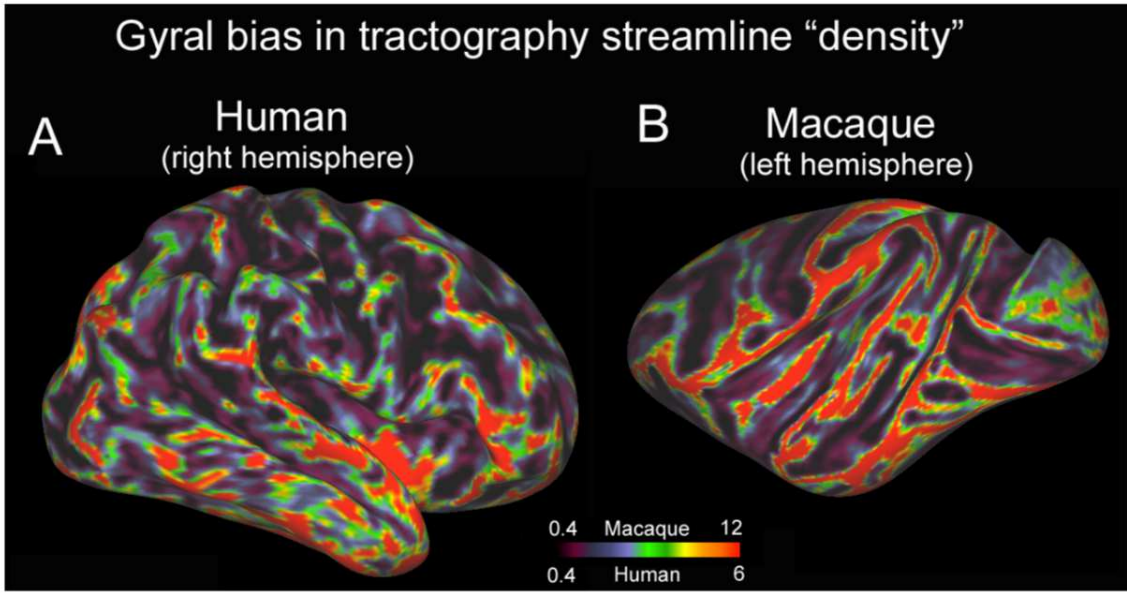

Figure 1.1: From (Van Essen et al., 2013) Tractography seeded from the WM voxels of an entire hemisphere in Human (**A.** 1.25mm isotropic resolution and Macaque **B.** 430μm as mean number of terminations at the WGB

minate heavily on gyri rather than sulci. "gyral bias" is examined in depth in this thesis. Figure 1.1 shows a figure from (Van Essen et al., 2013). A 430μm postmortem Macaque DWI is seeded with tracks from every WM voxel of the hemisphere and the total number of intersections at the WGB (white gray boundary surface , see Chapter 2) is plotted. Similarly for 1.25mm isotropic human data. (using FSL see Chapter 2). While not quantitative, or necessarily qualitatively well motivated (we take the approach of seeding specific

centrally located structures known to connect to all cortex, and roughly equidistant from it like the internal capsule, corpus callosum and thalamus when qualitatively assessing gyral bias from WM to GM in this thesis) a clear bias towards gyral terminations is striking, **to the extent sulcal regions seem unreachable from white matter.**

The reasons for this gyral bias as it appears in figure 1.1 may be enumerated

1. Gyral bias reflects an actual connectivity bias (Chen et al., 2013; Nie et al., 2011)
2. Reconstructed local fiber orientations on walls and fundi are tangent to the cortical column.
3. The assumption that tracking should follow the path involving the least angular deviation (straightest line)
4. The "wedging" effect of cortical folding. in fundi, the radial axis of the cortex from pia to WGB radiates inward, while at crowns outward. For each region of the WGB the cortical volume is much larger at gyri than sulci.
5. An anatomical feature prevents tracks terminating on sulci

None of the items in this list are mutually exclusive needless to say. With respect to point **1.** (Nie et al., 2011) noted an apparent preponderance of anatomical terminations on gyral crowns in primate species including Rhesus, Chimpanzee and Human. This work was extended in (Chen et al., 2013) to suggest that cortical folds themselves form by the outward "pushing" of axons to form gyri. However, it is not without some irony that the sole evidence for either claim comes from diffusion imaging, a method whose properties and limits form the topic of this thesis. No developmental evidence exists to support this notion, and tracer studies in the macaque (Lewis and Van Essen, 2000a; Van Essen et al., 2013; Markov et al., 2014) show no clear bias of connectivity density on sulci and gyri, though a systematic study has yet to be performed.

Point **2.** and point **3.** Are illustrated in figure 1.2 (from (Van Essen et al., 2013)). Figure 1.2 **C.** shows a schematic of a simple configuration of axons entering a gyrus, and making sharp turns to terminate on the walls till only the last few terminate on the crown. **D.** shows the fiber orientations reconstructed by DWI. These fail to resolve the orientations curving towards the wall (point **2.**). Partly this issue may be related to spatial resolution. The issue is examined in the present work in chapters 4 and 5 (e.g. figures

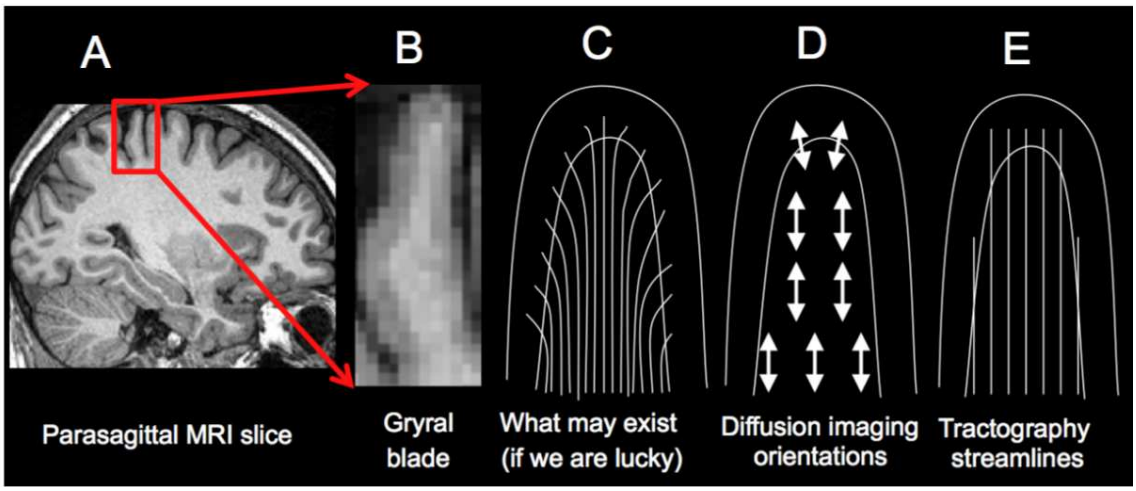

Figure 1.2: From (Van Essen et al., 2013)

5.2, 5.3. (Van Essen et al., 2013)) note similar patterns in the angles of high resolution diffusion orientations (430μm, substantially lower than the 250μm employed here in rhesus or 150μm in marmoset) relative to folding in the rhesus, but note "A critical issue is how this evidence from diffusion imaging relates to the anatomy of axons in the white matter." (Van Essen et al., 2013)) pp17.

Point **3.** refers to the "orientation continuity assumption" of tracking algorithms. While dMRI supports "crossing fibers" via many local models, tracking algorithms proceed by choosing to integrate via the orientation that minimizes the deviation from their current path (this is useful for tracking WM bundles) (Behrens et al., 2007). As a consequence, sharp turns as in figure 1.2 **C** would still not result in tracking terminations because even if the local models spatially resolved the turns they would be avoided unless they minimized angular deviation. In this thesis we approach this issue by seeding the gray matter of the cortex rather than the white. Gray matter seeded tracks should not show a gyral bias due to the "orientation continuity assumption", indeed with respect to point **2.** where modelling and spatial resolution are high enough minimization of angular deviation in tracks travelling down the cortical column should ensure deep WM penetration since that is the "straightest" trajectory to sample and integrate from.

Point **4.** is illustrated in figure 1.3 and is discussed more fully in section 1.3. Because of the physical forces applied to the cortical mantle at different depths in sulci and gyri, the area of GM per mm^2 subjacent WM is much greater at a fundus than a crown. Moreover, the radial axis of cortex points into WM at the crown (C), but away at the

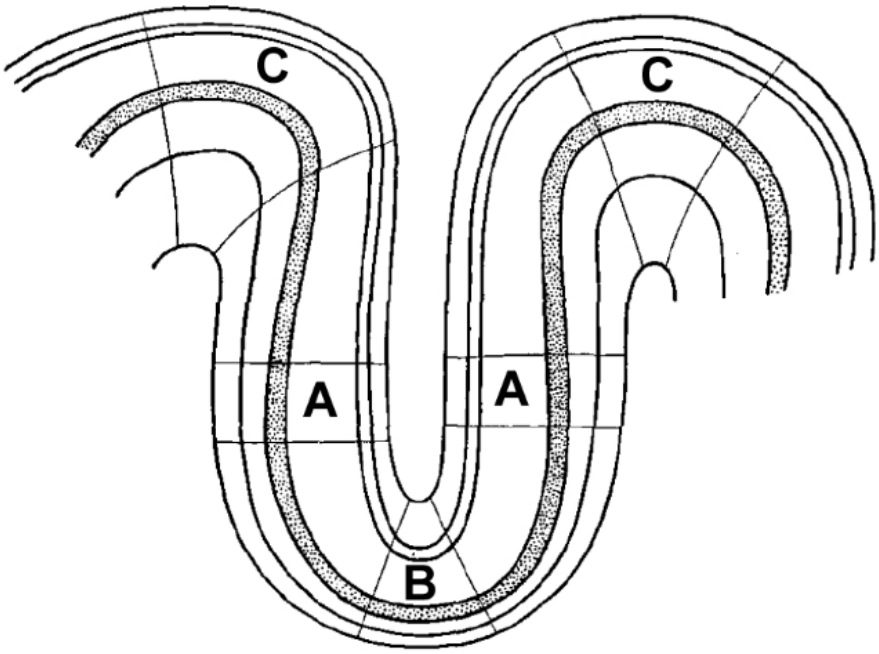

Figure 1.3: From (Van Essen et al., 2013) See text, discussion of point **4.**

fundus (B) (see also e.g. figure 5.2 in our own data) It is possible sulci may have marginally fewer terminations (see section 1.3, figure 1.5), however it is likely that axons are geometrically inclined to disperse relative to the columnar radial axis of cortex, where gyral terminations are inclined to converge. the number of axons entering and leaving the fundus per mm^2 of GM may be lower, though not necessarily per mm^3. Estimating the "wedge" of the cortex and the fiber angles provide information about points **2.** and **3.**

Point **5.**, that there may be as yet unknown anatomical issues involves the full complexity of cortical neuroanatomy. Plainly cortical anatomy is complex and subtle, while MRI data is necessarily a crude model. This thesis concentrates on one important, relatively simple anatomical feature, as it relates to the issues above and wider questions of diffusion imaging and anatomy, outlined conceptually in the following section 1.3.

1.3 Cortical Fiber Systems

While the body of tracer studies in the macaque is large, few studies have focused on the white matter itself architecture, rather than the afferent or efferent labelling of cortical tissue. Since the Gross anatomical studies of the 19th century, (Dejerine, 1895),

the only major systematic monograph of white matter structure has been (Schmahmann and Pandya, 2006) in which the authors autoradiographic examined materials from autoradiographic tracer injections collected from experiments over a long period to build a composite picture of the major white matter paths in the rhesus. In addition, information about smaller, local pathways and termination patterns was presented. (Schmahmann and Pandya, 2006) derive from their anterograde tracer atlas a simple schematic of fiber types We follow the terminology of (Schmahmann and Pandya, 2006) in this thesis in referring

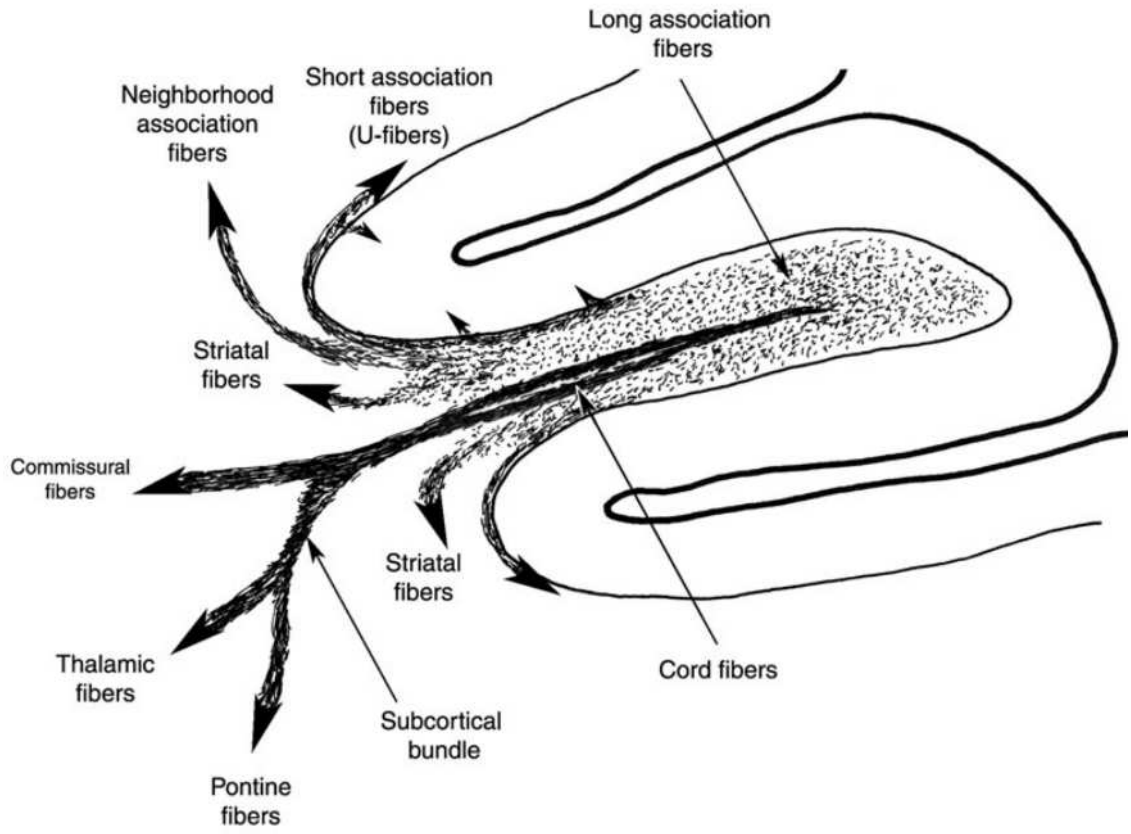

Figure 1.4: From (Schmahmann and Pandya, 2006) a crude, coronal schematic of fiber organization in an idealized gyrus. The termination patterns of the different fiber types is not shown, nor is the schematic intended as more than a sketch.

to WM fiber types

1. **Cord Fibers** connect cortex to the pons, thalamus, commisures and other subcortical structures. These fibers radiate to and from central structures through the WM of e.g. the corona radiata and internal capsule. They are coherent, well defined and dominate anisotropy.

2. **Striatal Fibers** connect cortex to the caudate and putamen and for present purposes may be regarded as part of the Cord

3. **Long Association Fibers** Are **intracortical** bundles. They are large, discrete "fasiculi" often travelling rostrocaudally and always within deep cortical white matter. Each is named, and is thought to subserve specific brain functions by joining cortical regions in different lobes as "highways". dMRI methods have shown great success in delineating these bundles (Schmahmann et al., 2007) as discrete entities, however axons leave and join multiple fasiculi in complex ways as yet not full understood.

4. **Local Association Fibers** or **"u-fibers" or "local fibers"** leave a cortical area and considered as a bundle, travel to an adjacent gyrus, in the WM immediately subjacent to layer 6 (i.e. hugging the cortical sheet).

5. **Neighbourhood Association Fibers** or **"Neighbourhood fibers"** Like local fibers do not enter deep WM as fasiculi, broadly hugging the cortical sheet. However they do impinge more deeply and travel further, for example linking two subdivisions of a lobe. The Superior and Inferior parietal lobules are linked by a neighbourhood fiber discussed in chapter 5, in particular section 5.6

While not exhaustive, these categories serve as a taxonomy in this work.

1.3.1 Local Fiber Systems

The local fiber systems subjacent to layer VI are the key anatomical these of this thesis. Their properties and morphogenesis are not well explored in the literature. Briefly, we take the position hypothesized in (Van Essen et al., 1997) and extrapolate a further hypothesis on the form and function of local fibers. (Van Essen et al., 1997) seeks to explain why cortical folding occurs. If at some abstract point in early development the cortex is a flat sheet or toroid, then the shortest path between any two points is a straight line. Figure 1.5 **A.** shows development as an abstract sphere. neurons migrate to cortex along radial glial lines. upon reaching cortex, those functional regions that preferentially connect develop more axonal connections between them. These cause physical tension. The difference between strongly and weakly connected regions in terms of axon number need not be large for there to be a net tension between preferentially connected regions.

As a result (figure 1.5 **b.**) the cortical sheet is pulled such that preferentially connected regions have shorter axonal lengths. Gyri form, with strongly, compactly connected regions lying on either side of gyral walls (figure 1.5 **c.**). This cortical folding causes shear-

ing effects shown in (figure 1.5 **d.**), and discussed in point **4.** in section and figure 1.3.

Short axons between the walls of a gyral blade in the adult animal reduce the diameter and myelination necessary to achieve a given spike time accuracy and energy expenditure per spike (Wang et al., 2008). Less or even absent myelination in short axons reduces oligodendrocyte energy expenditure. However, the axons linking regions that were not pulled together remain and these now conceptually join two adjacent gyral crowns or "outward folds" (figure 1.5 **c.**). Their paths have not been lengthened however they are longer than axons crossing a gyral blade. These are local association fibers. The longer distance will require wider more myelinated axons in local association fibers, but these are still much shorter and thinner than cord or long association axons. The g-ratio (the ratio of the axon diameter to the the myelinated fiber diameter) that maximizes conduction speed is fairly constant over all axons, however for shorter axons the ratio of myelin relative to axon diameter tends to be larger Paus et al. (2009).

In summary, at the point of figure 1.5 **a.** the shortest distance between any two points on the cortical sheet is a straight line. The mechanism in **b.** shortens some paths, but lengthens none. We expect u-fibers to be thickest (contain the most axons) at the fundus, and for an average axon to be more myelinated and have a wider diameter. The majority of axons and all the longest axons pass under the fundus, which thus contains more, wider and more myelinated axons in the superficial white matter.

To reify the notions above in a more concrete way, figure 1.6 shows a developmental experiment in which a lisencephalic region of cortex (the occipital pole) was subjected to a change in its afferents early in development. Figure 1.6 Top row shows 3 patterns of LGN to V1 connectivity drive by radial glial lines resulting from a 50% reduction in LGN cells and thus connections and activity. Whichever of the 3 patterns, either the number of V1 columns or input to columns is reduced. The bottom of the figure shows a 3 year old macaque brain that has undergone this procedure. V1 has developed folds, very possibly because relatively distal but functionally useful regions have developed intra-V1 connectivity to permit processing that compensates for the paucity of LGN afference. While conjectural, (Van Essen et al., 1997) and figure 1.6 do mutually support each other.

In a rather ad-hoc analysis, Almut Shuz and Valentino Braitenburg (Schz et al., 2002) estimated the number of axons in 3 groups within the human brain according to location and length. figure **??** shows their estimates. The vast majority of axons in the cortex never leave the gray matter and are less than 1mm long (figure 1.7 A). Of those that enter

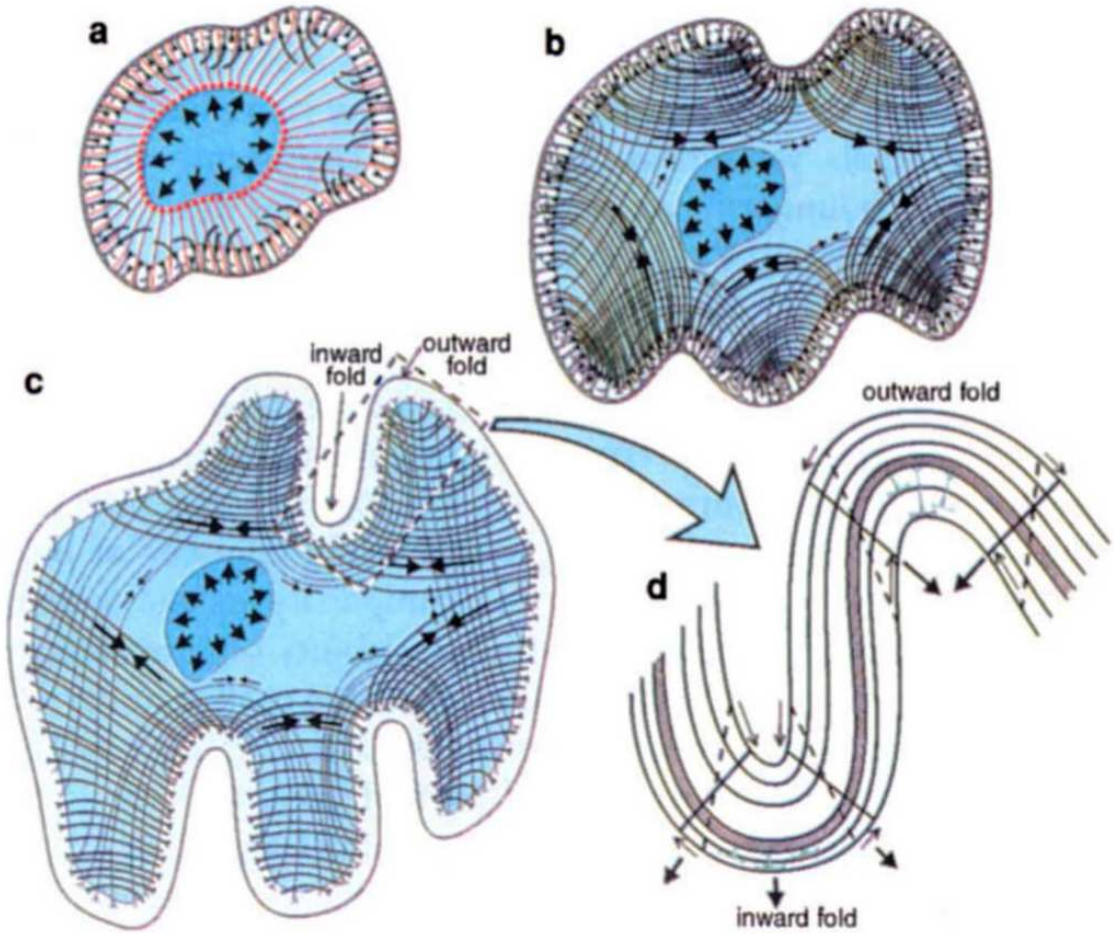

Figure 1.5: From (Van Essen et al., 1997) a. neurons (black) migrate to cortex along radial glia (red). b tension forms as strongly interconnected regions pull towards each other. c this leads to outward folds that separate strongly interconnected regions and inward folds that separate (relatively) weakly connected regions. d cortical folding causes shearing that stretches the radial axis (broken lines) so that sulci have compressed lower layers and gyri have compressed upper layers. We expect that the number of axons leaving and terminating on a fundus per mm2 be sparse compared to crown for geometric reasons see figure 1.3

the WM, the vast majority are, according to (Schz et al., 2002) in local fiber systems, enervating the walls of adjacent gyri with afferent and efferent connections via many axons. Only a small proportion, about 1% is estimated to contribute to the cord and long association fibers.

(Schz et al., 2002) Estimate that the majority of white matter axons are in local fibers.

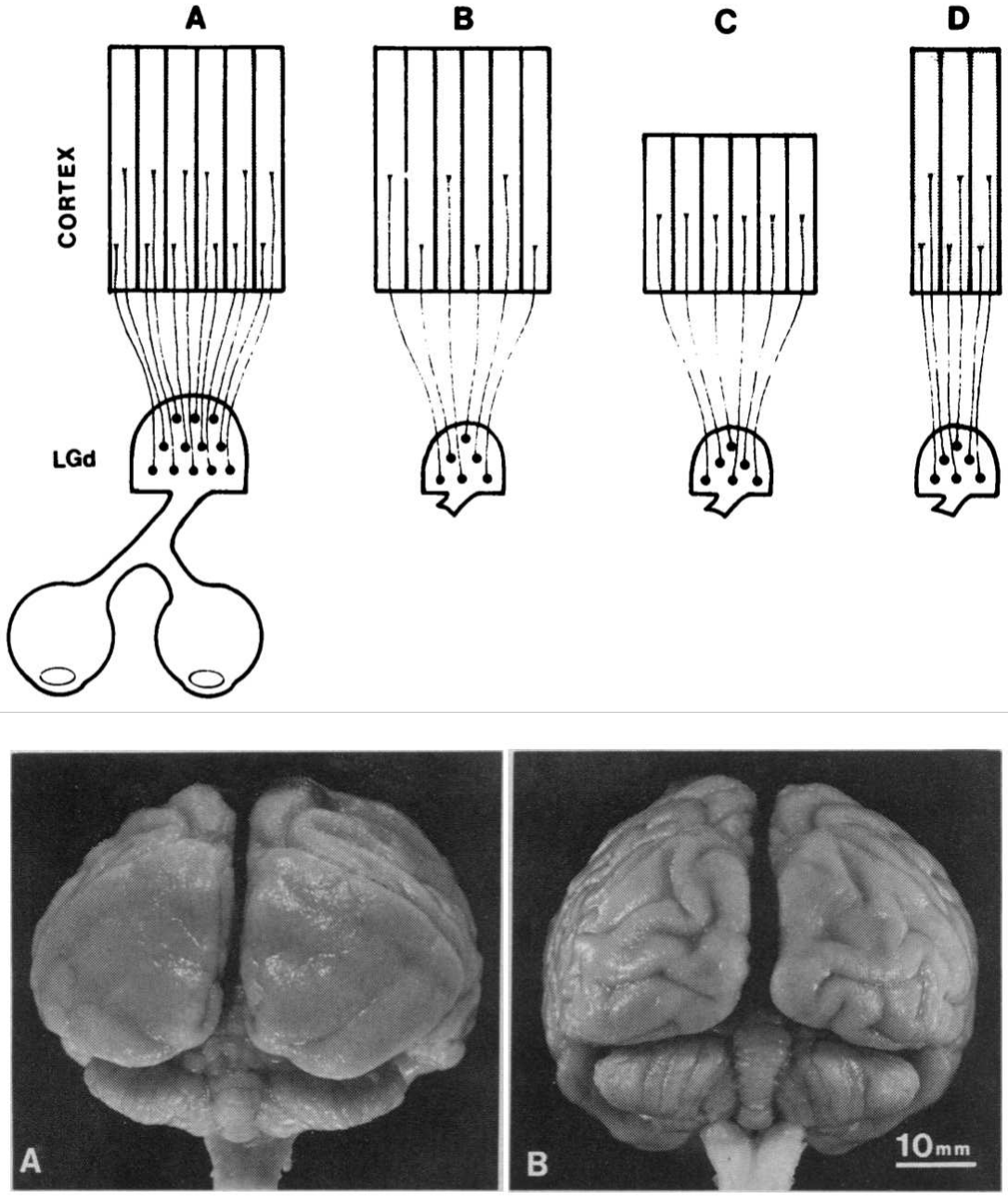

Figure 1.6: From (Rakic, 1988) Around half LGN neurons are suppressed at an early developmental stage. There is thus weak input to V1 that may follow one of the patterns in upper B,C,D. Lower left shows a 3 year old control monkey. Lower right shows 3 year old monkey with impoverished V1 input. V1 has become encephelated, possibly due to a greater need for communication within V1 and thus greater axonal tension and the formation of local fibers

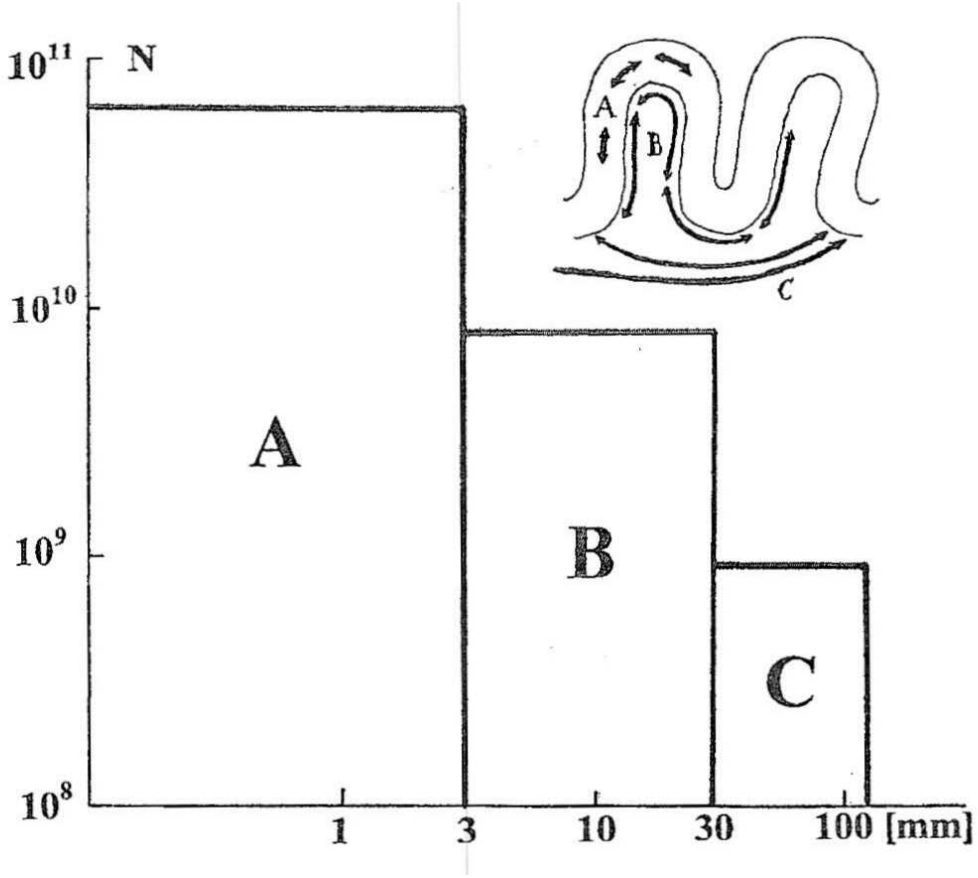

Figure 1.7: From (Schz et al., 2002) Number of fibers (log-log plot) in GM only (A), in local/u-fibers (B) and in long range cord, callosal and deep fasiculi. see (Wang et al., 2008) on WM axon scaling

1.4 What is in This Thesis

The thesis follows a structure in which a naive experimenter seeks to replicate tracer findings using dMRI methods, and proceeds to investigate the method's shortcomings through a progression of computational methods and analysis of white matter features histologically, to reveal the anatomical explanation behind the original "failed" tracer simulation experiments. A brief final section employs a synthesis of all methods and data to put forward a well motivated hypothesis for the function of the local fiber systems in a region of the Rhesus brain. Chapter 3 is a standalone project concerning the construction of a histologically accurate high resolution 3D Rhesus cortical atlas, and it's non-linear mapping to subject scans.

- Chapter 2 **Methods** Diffusion MRI methods are described first in a general way, in addition to software used in this thesis. Surface methods are also described as well as histological image processing used. The specific methods used to acquire and process the data used in this thesis are presented in detail, followed by a brief assessment of the ex-vivo data dMRI modelling properties under FSL.

- Chapter 3 **Accurate Labelling of Macaque Cortex** A system for the construction of high resolution (250μm), 3D atlas of macaque cortex based on (Saleem and Logothetis, 2012) is presented. The atlas consists of a high resolution "surrogate" MRI of the atlas animal, together with labels. the labels reflect the histological properties of the scanned animal very accurately due to the properties of (Saleem and Logothetis, 2012). Highly accurate cortical surface models are also produced. The GPU based system forms the heart of a pipeline that is able to head extract and label MRIs of other animals in a highly accurate way, and produce high resolution "surrogate" scans and automatic surface models. We validate the system with histology and quantitative comparisons between multiple scans of the same animals.

- Chapter 4 **Tracer and dMRI Tractography Compared**The properties of GM and WM seeded tractography in Rhesus and Marmoset are compared to results from tracer studies. The observed behaviors of tracking are observed to have a generalizable pattern. Tracking to and from the entire GM is analyzed in a series of scalar maps. Tracking from GM to WM is analyzed in a further series of maps, and a comparison to the explanation of "gyral bias" outlined in Chapter 1 is described. Finally, the role of dMRI spatial resolution is examined with respect to tracer comparisons

- Chapter 5 **Local Fibers and DTI** Following from Chapter 4 this chapter seeks to determine the mechanism by which maps such as the PVI derive their properties. On the one hand, we explore this using dMRI itself. We also employ histology from the same brains as scanned. We determine the relation between tracking and tissue properties, and note myelin patterns in GM and the composition of local fibers. We discuss local fibers along gyri. We examine tracking, histology and anatomy in the marmoset brain. Finally, we focus on the IPS in the rhesus. By bringing all the methods together, with the addition of a tracer injection, We characterize the relation of dMRI to anatomy at the sulcus, and finally analyze the structure of the local fibers at the IPS region using histology, image processing, tensor maps and tracking to develop a hypothesis about how they may subserve the function of the lateral parietal lobe

- Chapter 6 **Summary and Conclusion**

Chapter 2

Methods

Abstract

Diffusion MRI methods are described first in a general way, in addition to software used in this thesis. Surface methods are also described as well as histological image processing used. The specific methods used to acquire and process the data used in this thesis are presented in detail, followed by a brief assessment of the ex-vivo data dMRI modelling properties under FSL.

2.1 Summary Of Data Used in this Thesis

The MRI data in this thesis consisted of two slightly overlapping groups. For the diffusion MRI work, postmortem macaque and marmoset brains were scanned at high field and for long periods. For the atlas work, macaques were scanned in-vivo and some of the ex-vivo data was re-used.

Table 2.2 shows the data

For the diffusion data sets, all animals were euthanized and perfused by NIH vetinary staff. All MRI procedures including sample preparation were conducted by Frank Ye at the NIMH. Histological procedures were performed by David Yu at the NIMH. Tracer surgeries were carried out by Richard Saunders at the NIMH. Histological data and methods were used in chapters 3,4,5. MRI data was used in chapters 3,4,5. Structure tensor was used in chapter 5. DTI was used in 4 and 5. surface methods were used in 3,4,5.

Case	Species	Scans	Histol	Notes
T	Rhesus	T1w 500μm	Nissl	In vivo, heavily lesioned
A	Rhesus	T1w 5 @ 500μm 1 @ 330μm	-	Naive "POSH"
B	Rhesus	T1w 4 @ 500μm 1 @ 370μm	-	Naive "PUFFIN"
DB58	Rhesus	MTR @ 250μm	Gallyas	Naive ex-vivo, diffusion subject A
CV3X	Rhesus	MTR @ 250μm	-	Naive ex-vivo, diffusion subject B
D99	Rhesus	T1 @ 500μm	-	Naive original atlas subject

Table 2.1: table of atlas MRI data, used in chapter 3

Case	Species	Dir	Res	Histol	MT	Notes
A	Rhesus	121	250μm	Gallyas,Nissl	250μm	Good SNR, Whole brain
B	Rhesus	60	250μm	-	250μm	Lower SNR, Whole brain
R	Marmoset	126	150μm	-	150μm	Good SNR, Whole brain
P	Marmoset	60	150μm	Gallyas	75μm	V High SNR, one hem

Table 2.2: table of diffusion MRI info, used in chapters 4,5,6

2.2 Diffusion Imaging and Modelling

2.2.1 DWI - Diffusion Weighted Imaging

Diffusion in an isotropic medium (a fluid at equilibrium) follows a Gaussian dispersal pattern, shown in figure 2.1 A. The Rate of diffusion is Determined by a scalar diffusion coefficient D (fig 2.1 B)

The brain is not an isotropic medium. Diffusion is hindered by structure, particularly myelinated axons in the white matter (fig 2.1 C). As in figure fig 2.1 C, diffusion in the gray matter is often assumed to be isotropic. However in the ex-vivo data studied here we find that this is not the case; cytoarchitecture and myeloarchitecture both give rise to complex patterns of anisotropy that presumably correlate to tissue properties, though this is not explored beyond some cases to the appearance of isotropy in regions of matted GM myelination.

Diffusion Weighted Imaging Proceeds by acquiring many (30-512) acquisitions over the same sample. each acquisition differs by the application of a gradient vector that causes signal attenuation along that vector when diffusion is rapid.

These volumes may then be used to make a model of the diffusion field in the sample.

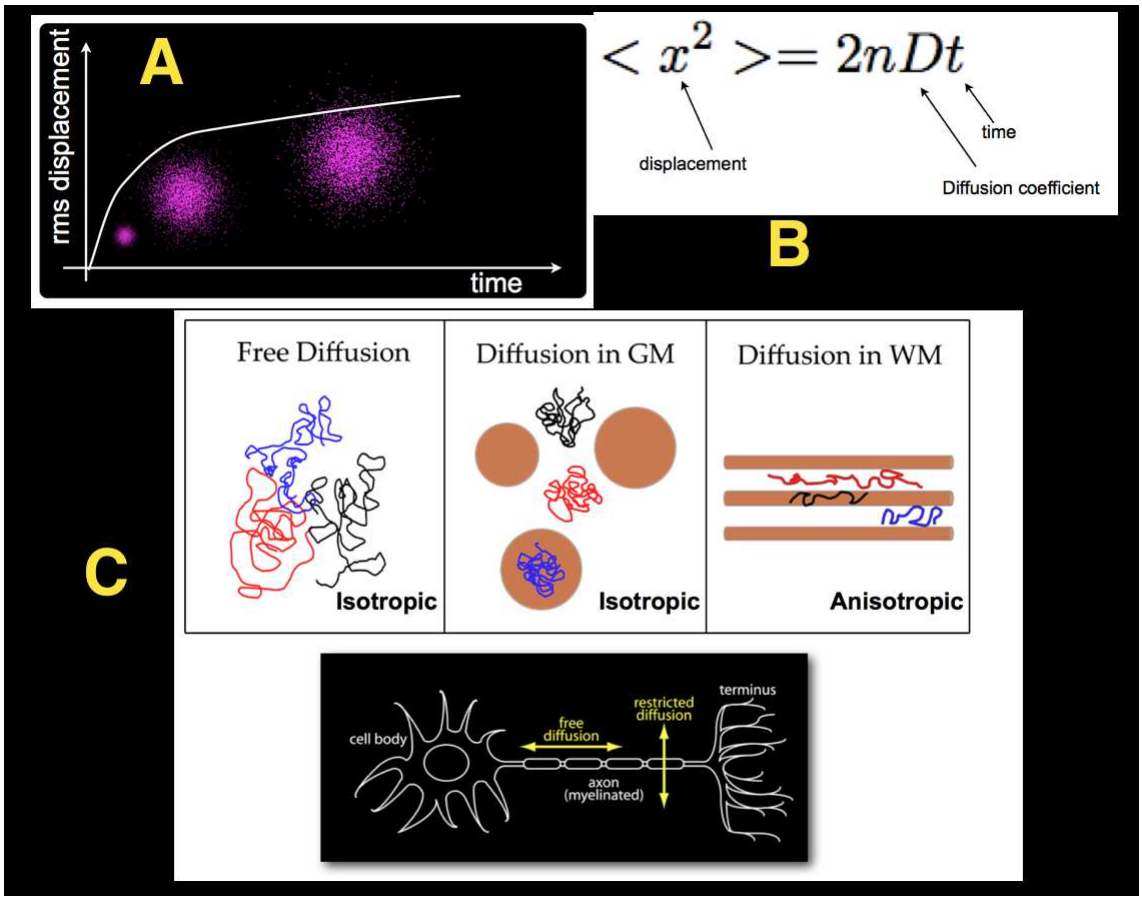

Figure 2.1: A isotropic, free diffusion and B definition of scalar diffusion coefficient. C Diffusion in the brain is anisotropic. Note the assumption that myelin is the only source of anisotropy in the brain, and the assertion that gray matter is isotropic. Our work shows neither are true, that diffusion can characterize gray matter and this not only useful in itself but important for tractography.

We use two primary models in this work: The Diffusion Tensor, and FSL statistical modelling. The former is used mainly to explore static tissue properties, and the latter as a basis for tractography.

2.2.2 The Diffusion Tensor Model

The diffusion tensor model is shown in Equation 2.1. The nine elements describe a Diffusion coefficient (D) in each of three orthogonal axes (x, y, z) with respect to the others. Diagonalization of this matrix produces 3 eigenvectors $v_1 v_2 v_3$ which define a coordinate space (3 orthogonal axes), and 3 eigenvalues $\lambda_1 \lambda_2 \lambda_3$. The orientation of the axes of this coordinate space with respect to the scanner space define the principle direction of diffusion (figure 2.2 A, C). The eigenvalues define (apparent) diffusion coefficients along each

axis (Figure 2.2 B, C)

$$\bar{D} = \begin{bmatrix} D_{xx} & D_{xy} & D_{xz} \\ D_{xy} & D_{yy} & D_{yz} \\ D_{xz} & D_{yz} & D_{zz} \end{bmatrix} \tag{2.1}$$

The eigensystem thus defines an elipsoid that represents the diffusion in a voxel, estimated from the intensities in the DWI acquisitions given information about the gradients applied in the scanner (b-vectors). The Eigenvectors define the orientation in space, while the eigenvalues define the shape of this elipsoid. The tensor model elipsoid therefore assumes that diffusion is Gaussian. The direction of the largest eigenvector is an estimate of the direction in which there is most diffusion (even if it is only the largest by a small amount). This forms the basis for traditional DTI tractography.

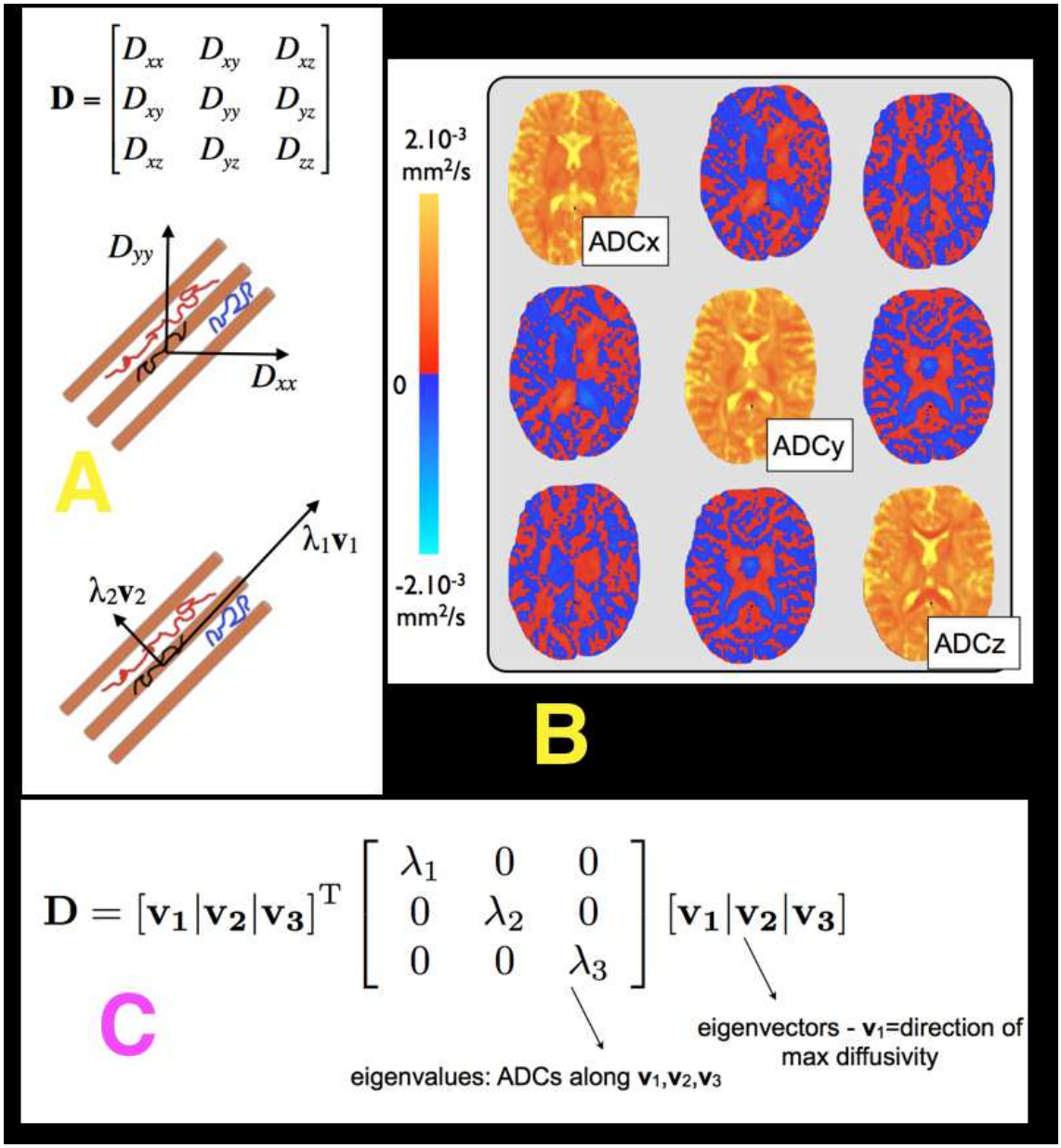

Figure 2.2: The Diffusion Tensor. A, The Tensor and its diffusivity in the x and y axis of the scanner with respect to a schematic of a fibre. The eigensystem creates a coordinate system in the voxel with the first eigenvalue/vector oriented in the direction of most diffusion. B the apparent diffusion coefficients in are the eigenvalues/diagonal elements. C definitions of diffusion coefficients, tensor and eigensystem w.r.t each other

The Diffusion Tensor as a metric of static tissue properties

The eigenvectors of the tensor can be ignored, and diffusion properties based purely on elipsoid shape (eigenvalues) examined. Such measures are termed "rotationally invariant" and metaphorically can be regarded as a "stain" for different tissue properties.

The rate of diffusion in each axis is related to the size of the eigenvalues. The sum of the eigenvalues (trace of the matrix) is linearly related to the total rate of diffusion in a voxel (equation 2.6 where TR indicates trace and λ_n eigenvalue n). We use this measure to examine how restricted diffusion is in a region, irrespective of anisotropy. The trace (or alternatively the "mean diffusivity" equation 2.7 where MD indicates mean diffusivity) is an important comparator to measure of anisotropy and myelin content in identifying anatomical properties. The Radial and axial diffusivities look at diffusion in only some directions. The radial diffusivity (eqn 2.8 where RD indicates radial diffusivity) appears modulated primarily by myelin content, axial (eqn 2.9 where AD indicates axial diffusivity) by axonal composition (Alexander et al., 2007).

we can ignore both the volume and orientation of tensor elipsoid and look only at its shape, that is the manner in which water is diffusing rather than how rapidly. We do this by examining the relationships of the eigenvalues, scaled by a local factor (generally here simply the largest eigenvalue).

Equations 2.2, 2.3, 2.4, 2.5 show the commonly used Fractional Anisotropy measure (the proportion of tensor volume that's anisotropic, roughly) and the less commonly used Linear, Planar and Spherical maps respectively, where FA indicates fractional anisotropy, c_l, c_p, c_s indicate linear, planar and spherical indices respectively and λ_n indicates eigenvalue n.

$$\mathrm{FA} = \frac{1}{\sqrt{2}} \frac{\sqrt{(\lambda_1 - \lambda_2)^2 + (\lambda_2 - \lambda_3)^2 + (\lambda_1 - \lambda_3)^2}}{\sqrt{\lambda_1^2 + \lambda_2^2 + \lambda_3^2}} \tag{2.2}$$

$$c_l = \frac{\lambda_1 - \lambda_2}{\lambda_1} \tag{2.3}$$

$$c_p = \frac{\lambda_2 - \lambda_3}{\lambda_1} \tag{2.4}$$

$$c_s = \frac{\lambda_3}{\lambda_1} \tag{2.5}$$

$$TR = \lambda_1 + \lambda_2 + \lambda_3 \tag{2.6}$$

$$MD = TR/3 \tag{2.7}$$

$$RD = (\lambda_1 + \lambda_2)/2 \tag{2.8}$$

$$AD = \lambda_1 \tag{2.9}$$

Figure 2.3 shows an elipsoid with high c_l, B high c_p and C high c_s. D shows the distinction between an isotropic elipsoid with high (large) trace and low (small). A high planar measure tends to indicate crossing fibers, spherical isotropy, linear anisotropy.

Use of tensor properties in this is unrelated to use in tractography. Rather they are measures of tissue structure entirely in their own right, unavailable by other MRI methods that additionally provide insight into tractography issues.

figure 2.4 B shows a tensor elipsoid and it's primary diffusion direction. Figure 2.4 A shows a directionally color coded map of primary directions. This, too, is a static map. We often show primary directions as color maps whose intensity is modulated by a tensor property, or as colored vectors whose length is scaled by a tensor property (e.g. linearity)

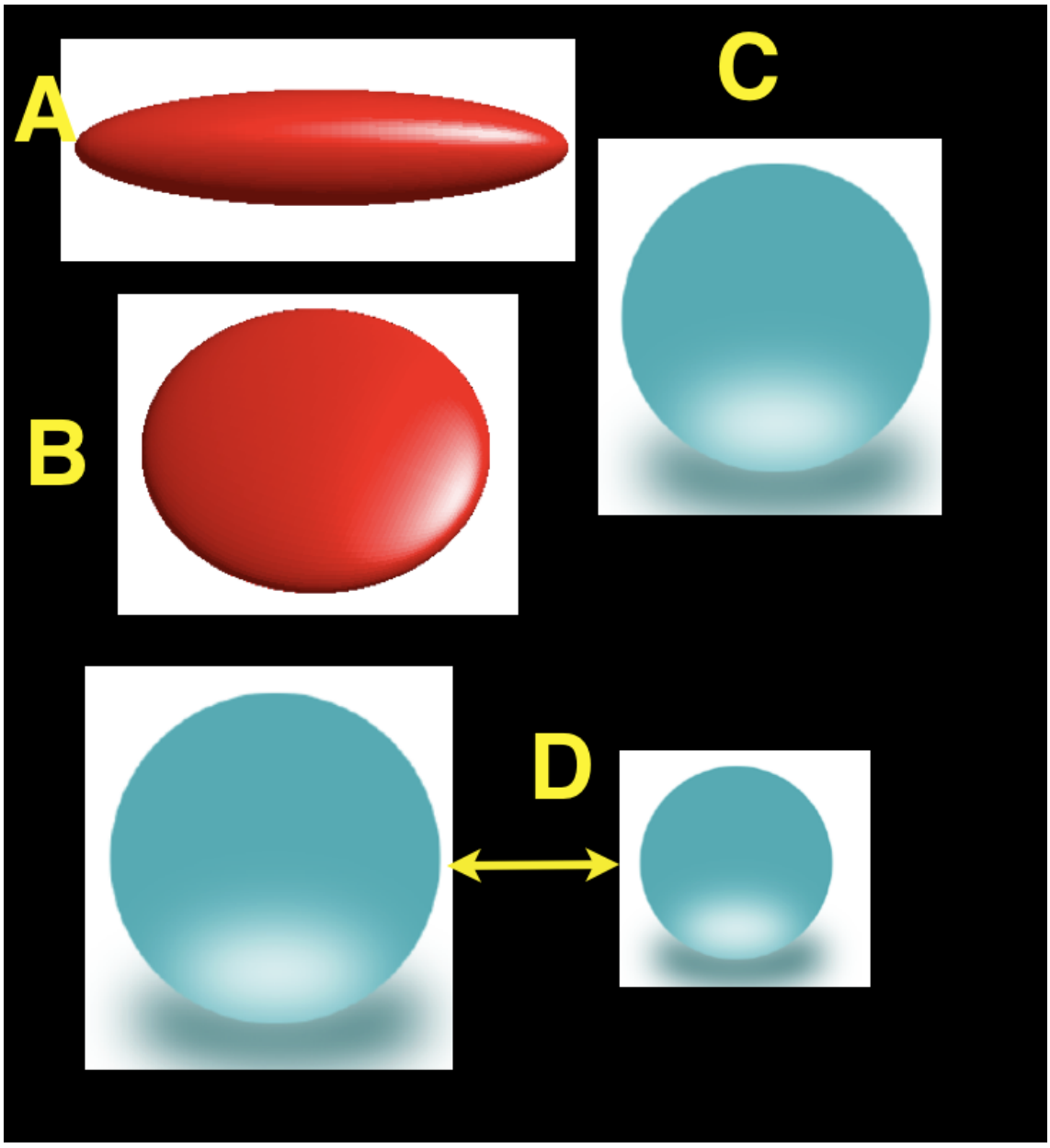

Figure 2.3: A a tensor elipsoid with a high c_l but low c_p and c_s. B high c_p. C high c_s. D two elipsoids with the same value of c_s (and c_p, c_l but a large TR on left and small on right (something is restricting diffusion on the right, either uniformly or in a way too complex to model and/or too small to measure with MRI at the acquisition resolution)

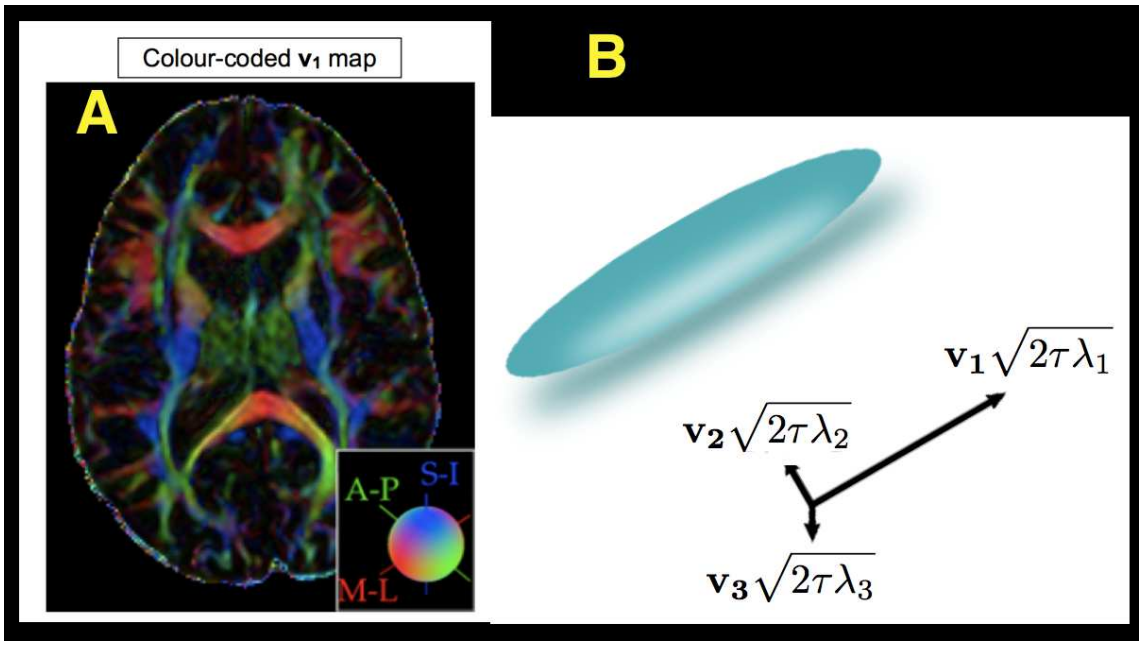

Figure 2.4: A: color coded map of principle ev v_1. B a very prolate elipsoid with large v_1 one might expect in e.g. corona radiata

2.2.3 Tractography

The topic of this thesis is the anatomy that affects tracking near the gray matter. Qball deterministic tractography is used briefly in places, but primarily FSL probabilistic local modelling and tracking is used (Behrens et al., 2003b, 2007) . Figure 2.5 A shows very briefly the local modelling strategy: rather than a tensor, a distribution of simple "ball and stick" models is fitted in each model via Bayesian inference on the MR signal. For each model the fraction of the MR signal modelled as anisotropic f is reflected in the size of the isotropic (ball) compartment $(1 - f)$. The angular dispersion reflects model uncertainty. We fit 3 distributions (representing 3 "crossing fibres") per voxel. Figure 2.5 B and C show a DTI elipsoid, and schematic of DTI tractography. C and D show the equivalent ball and stick distribution and statistical tracking over crossing fibres. rather than a single track, we examine the statistics of many thousands as they intersect a surface model of the cortical gray matter.

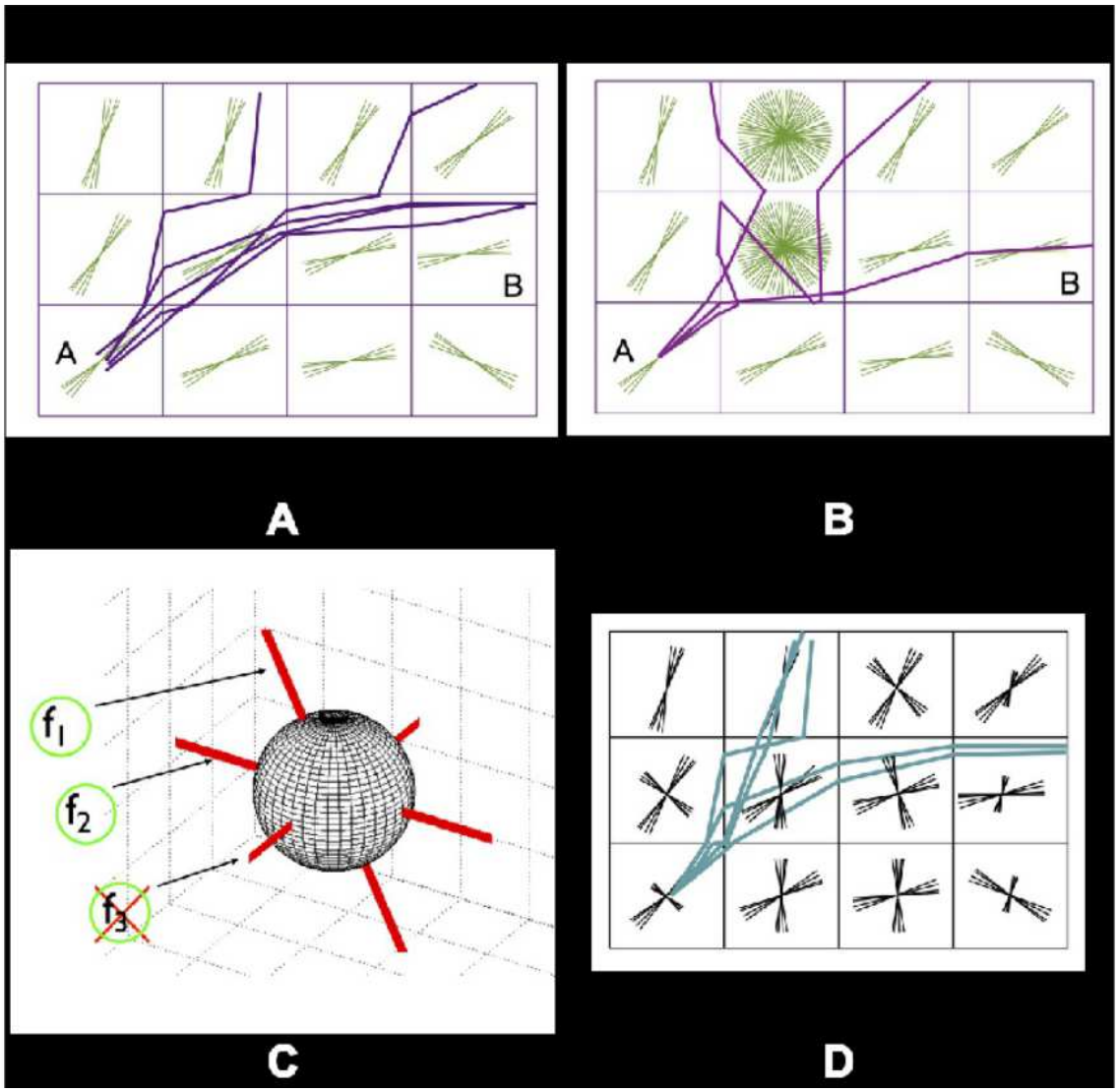

Figure 2.5: A shows a sample of streamlines through a field of single fibre models. B shows the propagation of uncertainty. C shows the ARD (automatic relevance detection) mechanism and the mean orientations of two distributions modelled, where f3 was too low to warrant a model. D shows sample streamlines in a mixed field of one and two fibre distributions

2.2.4 Surface Methods

A "surface" representation of the cortical sheet refers to a 2 dimensional mesh of vertices/nodes and edges between them. The mesh is folded in 3 dimensions to follow the sulci and gyri of the brain.

The richness of data available on surfaces, and richness of analysis possibilities in anatomical space for resultant data is extremely valuable. Tracking can be seeded from surfaces, or used as targets for tracking. Scalar maps can be presented, as well as functional data or anatomical tracer data.

In general (except in the case of flattened surfaces), a surface is topologically homeo-

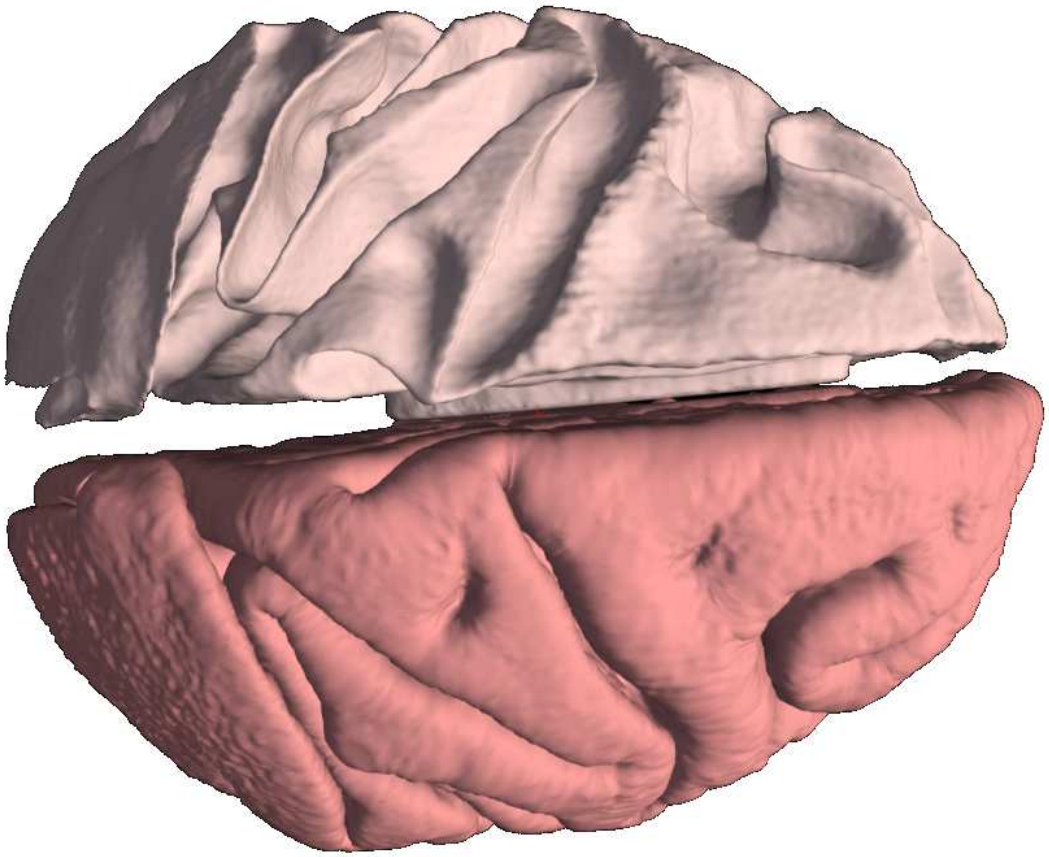

Figure 2.6: White and Pial surface of Case B from Freesurfer

morphic to a sphere; it is closed and does not contain overlapping edges or nodes ("crossovers"). Because it is two dimensional, it does not cover the entire cortical thickness but only a section through it, however data can be mapped between surfaces. Three primary types of surface are used here, a "white matter surface" which hugs the WGB boundary, a Pial surface which hugs the GM/CSF boundary (see figure 2.6), and a "midthickness" surface which runs through the GM midway between the WM and Pial (figure 2.8). White and Pial surfaces are be constructed with the "Freesurfer" software. The design of this software includes a large number of explicit assumptions and design choices, in particular that the input be a T1w 1mm isotropic scan of a human. Fortunately, it is an environment comprised of hundreds of programs joined by a shell code pipeline so it is possible to generate surfaces from ex-vivo Rhesus MTR with a custom pipeline and manual manipulation of the MRI to remove the hindbrain. Marmoset data was more challenging since the intensities of WM and GM overlap in this animal. To generate freesurfer surfaces, the scan of R (below) WM was manually segmented, and a volume constructed with GM,WM

and CSF values in the intensity values expected by the software, as well as stereotypical gradients expected in an MRI (figure 2.7. For marmoset P, the most intensively studied, the surfaces were generated by applying the methods in chapter3 to those of R.

Surfaces generated from a volume on freesurfer are on the same "mesh" meaning the nodes share an index (and can thus be vectorized for analysis) and a relation relative to each other in space. Because surfaces are homeomorphic to a sphere, they can be inflated to a sphere, or inflated to a lesser extent to open sulci and otherwise display data. Inflated surfaces are heavily used in this work

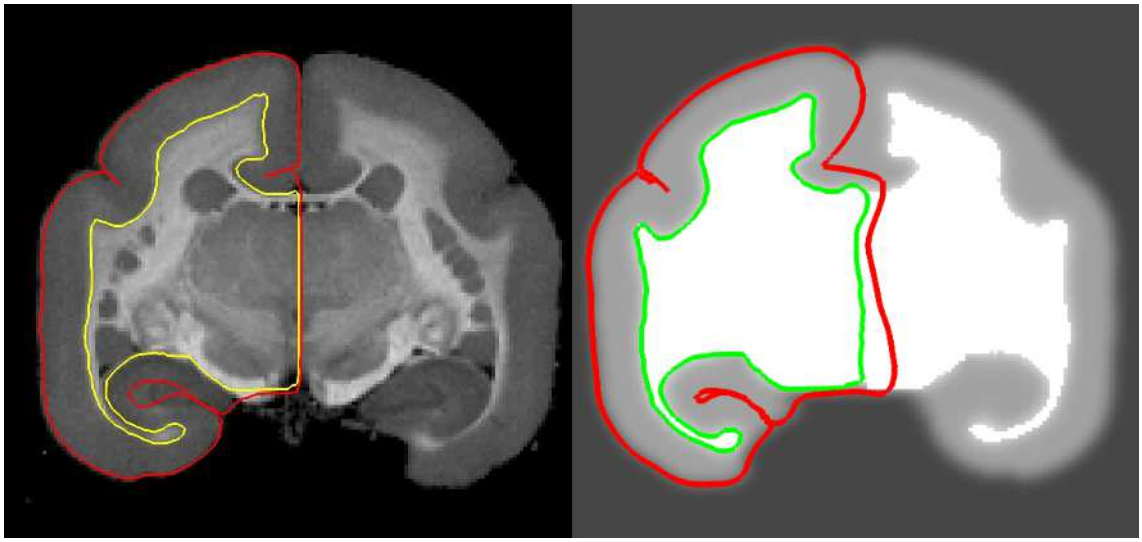

Figure 2.7: The artificial volume used to generate freesurfer surfaces for marmoset, and the final fit to the original MTR

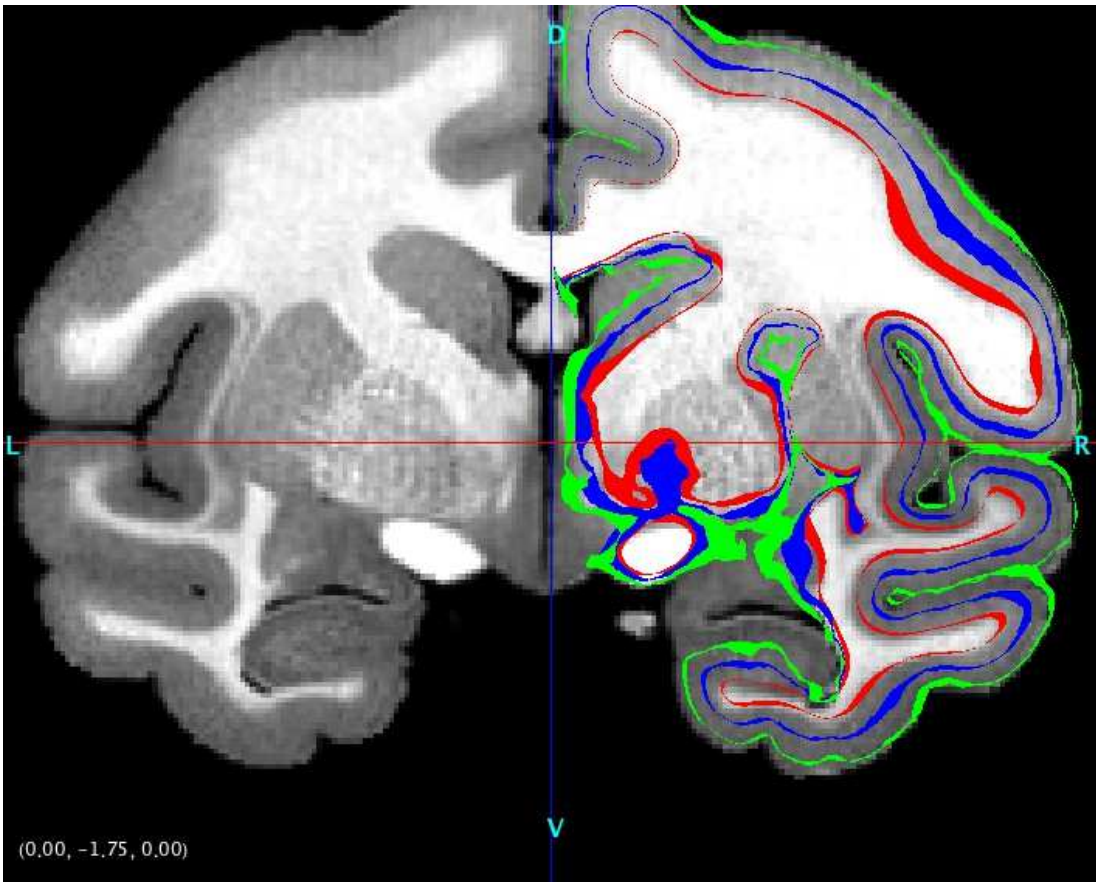

Figure 2.8: white, mid and pial surfaces that may be used for representation and intersection with volume data.

Surface Registration

Surface registration in Caret is shown in figures 2.9 and 2.10. The essence of the process is that on the atlas surface, and the surface to be registered, a set of named landmarks are drawn. These are lines that follow fundi of the hemisphere's sulci (in the human case, the major sulci are followed, but in the macaque it is generally possible to follow every sulcus). The atlas and target have the same named landmarks. Landmarks may be drawn anywhere on the surface however, and this is often useful in refining the registration and removing errors. Figure 2.9 shows the F99 atlas on the left (A), and a surface of Case B on the right (B), each with landmarks drawn. The surface is smoothed within the medial wall boundaries, since this facilitates registration and in general the surface is meaningless for subcortical data. Our own data is of sufficient quality that in both freesurfer and caret surface constructions, the thalamus, internal capsule, anterior commisure and optic nerve stub/ optic chiasm are accurately traced. These features are used for surface seeding. Registration proceeds with non-cortical tissue smoothed into a wall. Registration is single hemisphere. The bottom row of figure 2.9 shows these landmarks on spherical representa-

tions of the same surface (the edges and other data are removed, showing only the surface nodes).

Registration is accomplished by deforming the spherical representation of the target such that the landmarks align with the landmarks of the atlas sphere, and resampling the mesh. The process is bi-directional

Registration of this kind is non-linear - but it is also parametric. The landmarks are chosen by the researcher, who may alter them in order to achieve a result that appears most accurate. While this introduces a subjective element, it's the case that any automated procedure agnostic about anatomy. Figure 2.10 A shows A spherical form of the DB58 surface shown in D. The sulcal fundi and folding patterns of the cortex are shown on the sphere as dark regions. The landmarks are shown in their spherical form, but not that each landmark (color) is represented twice. The second version of each landmark is the pre-registration location of that landmark on the atlas surface, expressed in terms of the target. The algorithm deforms the target landmarks to match the locations on this sphere of the atlas landmarks. The result of the registration is shown in figure 2.10 B and C. In B, dark and light regions indicate where the sphere has been deformed positively or negatively to match the atlas. However; there has been a problem. The Red regions indicate that the registration produced overlapping nodes and edges. figure 2.10 shows the consequences of this on the registered midthickness surface which shows the Brodmann areas of the cortex; Where the nodes overlap, the data makes no sense and this surface is unusable.

Figure 2.10 D shows the final, correct registration result. This is obtained by adding and removing landmarks such that, by eye, the location of the Brodmann and other schemes make some kind of sense.

While this process may appear somewhat arbitrary, the results are surprisingly accurate and this permits the registration of e.g. tracer labelling used in chapter 4 or cortical parcellations from surface atlases.

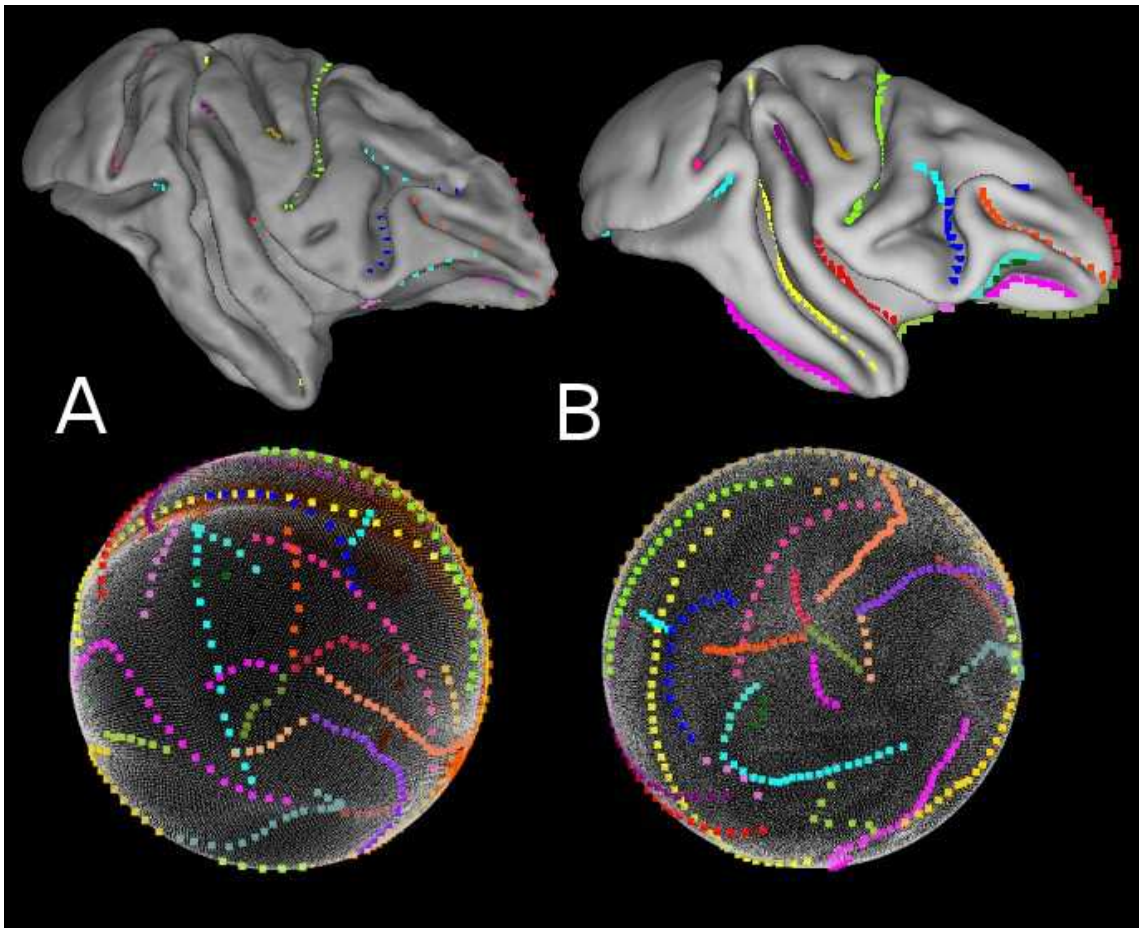

Figure 2.9: Landmark delineation on atlas and individual (CV3X) surfaces and their spherical representations

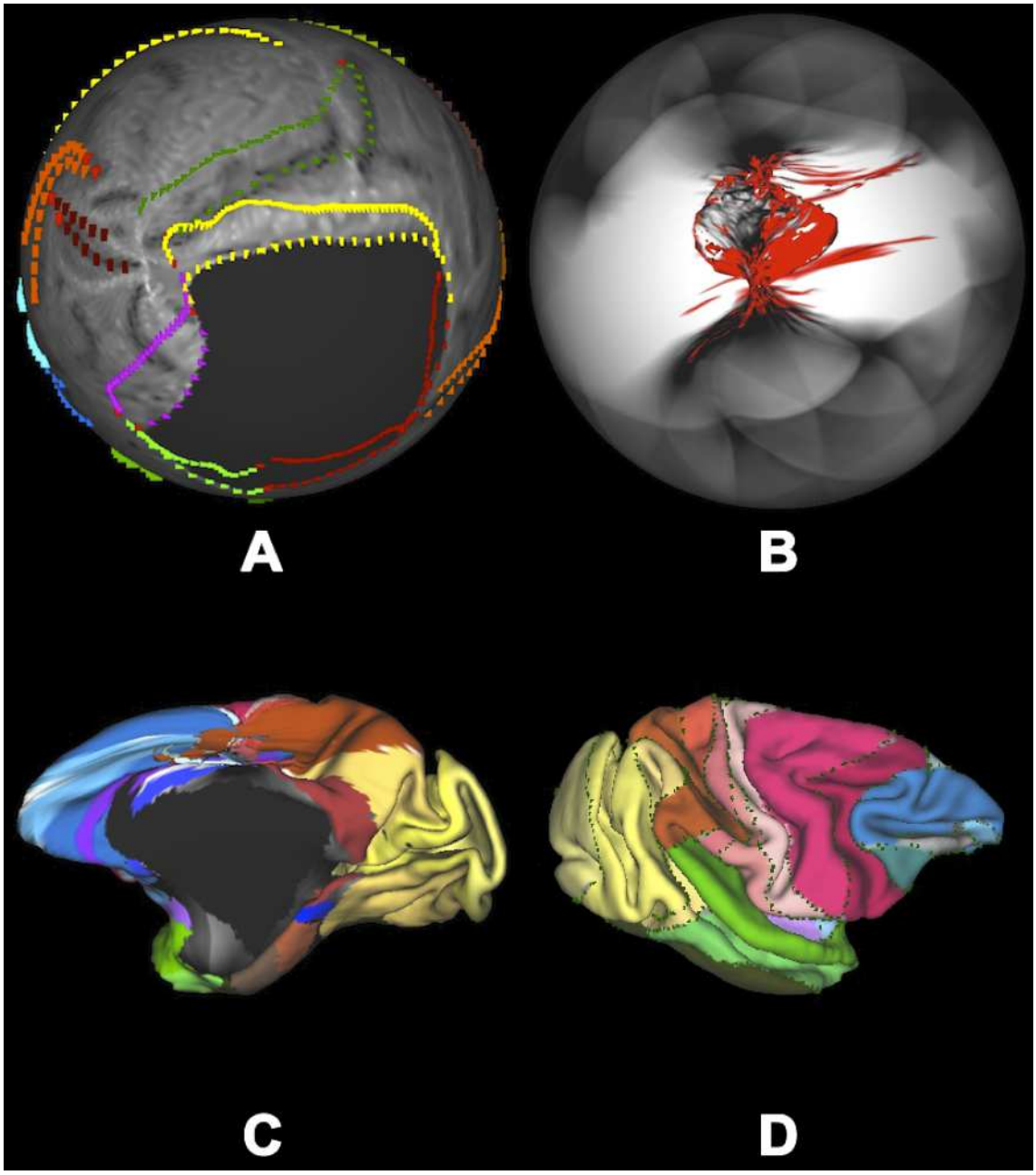

Figure 2.10: Landmarks of individual and atlas shown on a sphere of the individual (A). Some of these intersection, leading to sedge crossovers in the registration (B). The consequences for mapping are be shown in (C) and a fixed, complete registration in (D).

2.3 Structure Tensor Analysis of Histological Data

Structure Tensor Analysis of a two dimensional digital image operates in a conceptually analogous and mathematically similar way to the 3d diffusion tensor and its estimation. The structure tensor (equation 2.11) is a 4 element square matrix, defined over a region of the image. The image is subjected to a directionally weighted filter w along the x axis, then the y (figure 2.11 A). Equation 2.10 defines the spatial derivative of one image w.r.t another where g, h are images, $< g, h >_w$ is their weighted inner product and g is a gaussian weighting function defining a local neighbourhood around each pixel, so that Equation 2.11 then defines the structure tensor J as the partial derivatives of each image axis x, y under each gradient filter w.r.t the others, where f_x and f_y are the images of the partial derivates df/dx and df/dy respectively, that is the rate of change in each axis/gradient with respect to each other. This is similar to the diffusion tensor, but it is the rate of change of image properties that is measured, and these have a much less direct relationship to physical phenomena. The direction in which the structure is orientated is obtained using equation 2.12.

$$\langle g, h \rangle_w = \int \int_{\mathbb{R}^2} w(x,y) g(x,y) h(x,y) \mathrm{d}x \mathrm{d}y \tag{2.10}$$

$$J = \begin{bmatrix} \langle f_x, f_x \rangle_w & \langle f_x, f_y \rangle_w \\ \langle f_x, f_y \rangle_w & \langle f_y, f_y \rangle_w \end{bmatrix} \tag{2.11}$$

$$\theta = \frac{1}{2} \arctan \left(2 \frac{\langle f_x, f_y \rangle_w}{\langle f_y, f_y \rangle_w - \langle f_x, f_x \rangle_w} \right) \tag{2.12}$$

Although "anisotropy" (or "coherence") can be defined in a similar manner to the diffusion tensor, along with "Energy" (magnitude) (figure 2.12 we did not use this information for reasons described below. We used either a cubic spline or finite difference gradient function w and defined the image region as a single pixel. A Gaussian gradient with SD of 1 pixel was found to produce qualitatively similar but less precise results in terms of the final angle estimates.

The Gallyas histological Data required heavy pre-processing. First, tile overlap error from the microscope state had to be corrected by affine registration of the tiles and bilinear interpolation. Each tile had an artifactual color gradient, and this was found to be uncorrectable. To apply ST analysis, the data was converted to grayscale and also intensity inverted (so that myelin appeared bright, figure 2.13 D). Gallyas stains myelin in different

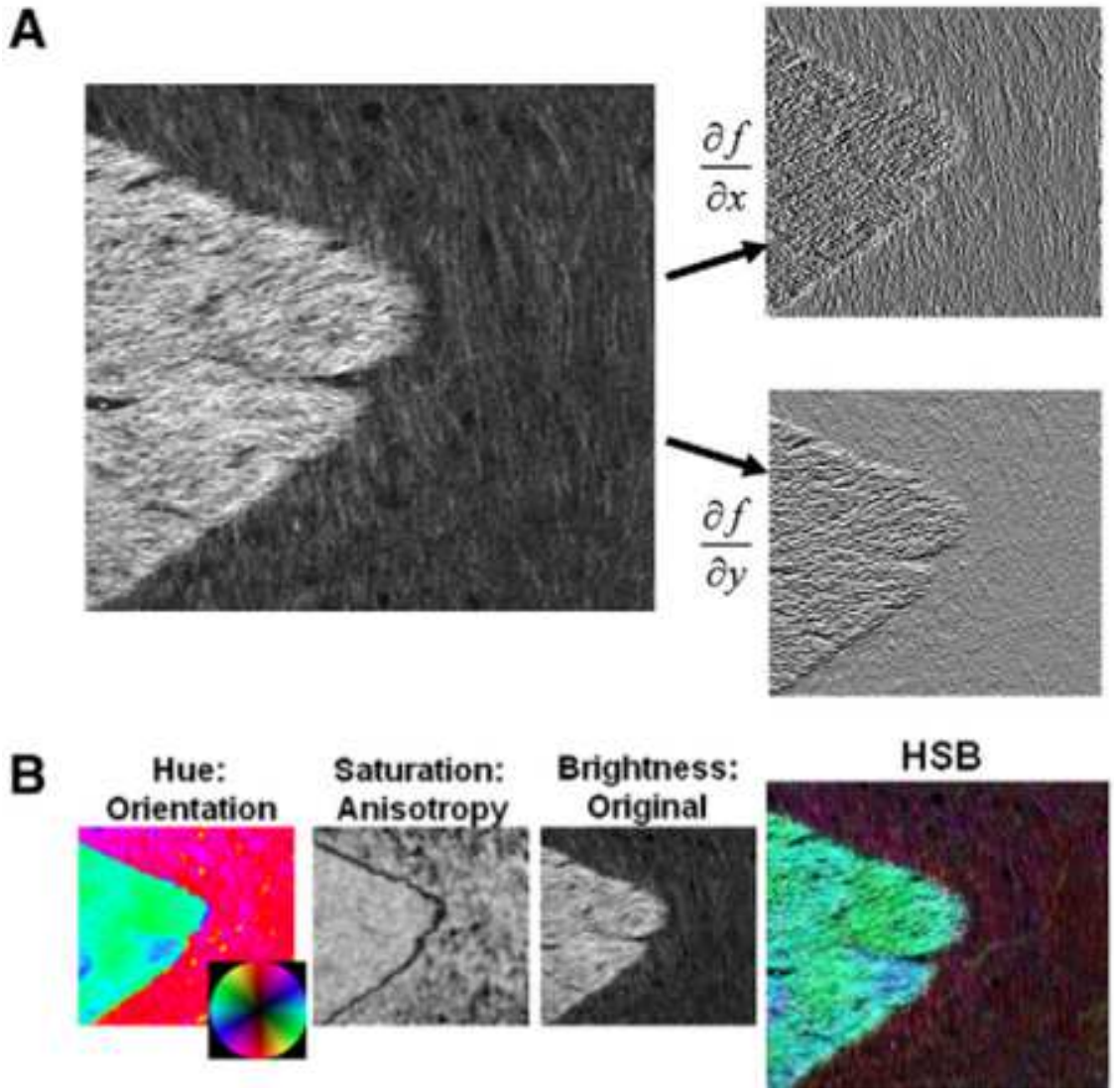

Figure 2.11: Elements of pixelwise structure tensor analysis, from ref budde and frank

ways; fine detail of axons is present in gray matter up to layer 1, but stain color can vary. Cell bodies (so it is thought, ref Gallays '78) are often stained a diffuse lighter brown, so some regions of gray matter have a clear, white background while in others axons are against a background closer to their own color. In general the light (or lighter) background and clear delineation of single axons in gray matter made it much easier for the technique to produce a clear result, certainly a different kind of result to that in white matter (2.13 A).

In the white matter, we relied on individual pixels, and a processing method to isolate fibre structure. In all cases (gray and white) processing was the same. the contrast was enhanced, and normalized over the entire image (giving a uniform gray appearance) using a fine windowed block-matching method with a small SD (Figure 2.13 B). Structure was enhanced, but at the cost of intensity variation. Brightness and saturation in figures is

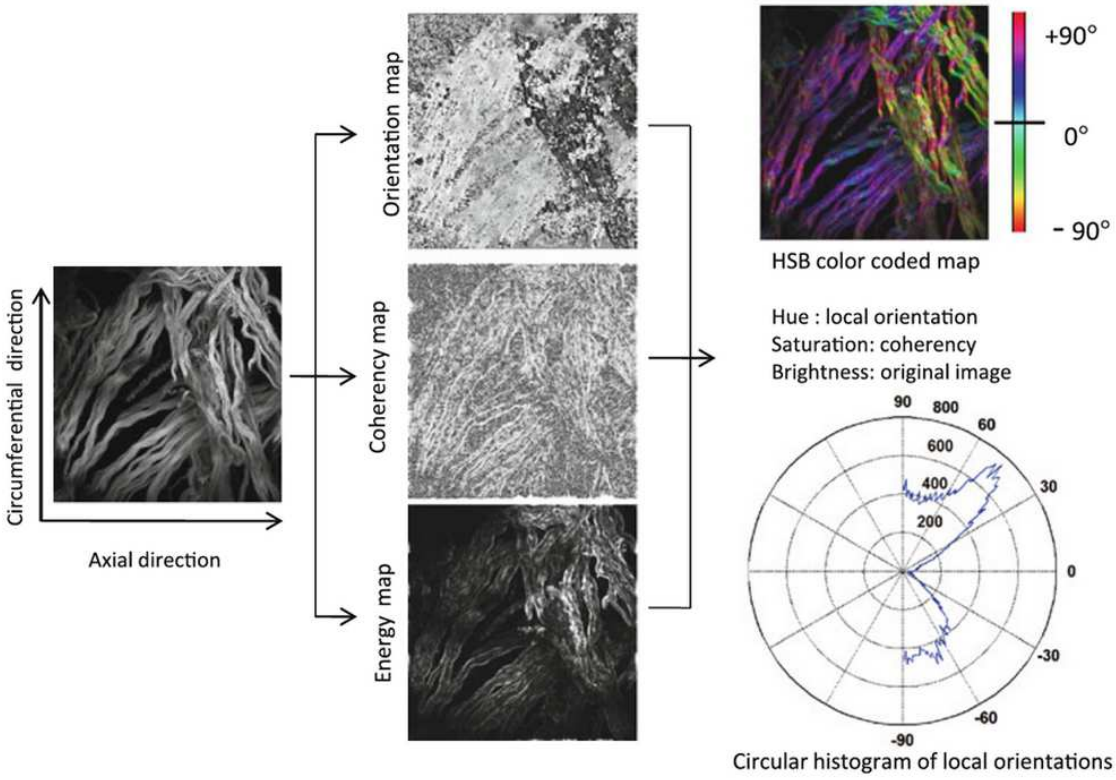

Figure 2.12: orientation distributions and other data calculated with orientationJ

supplied by a separate grayscale representation of the slide (2.13 D), with only hue coming from the ST analysis. The Resulting Hue from derived from ST of (2.13 B) and brightness, saturation from (2.13 D) yield images like (2.13 E) of detailed white and Gray (to 10x) information.

We used the method on a large scale, over entire ROIs as a direct comparator to DT directional information in the same region in the white matter.

We also made very heavy use, via various ImageJ (OrientationJ, ref, others) packages and custom MATLAB code, of angular distributions in small regions of an ROI (low right of figure 2.12, Figure 2.13 C in our data). We compared this to directional DT information in the exact same regions, but primarily to tensor maps in both the gray and white matter. We established many close relationships between tensor map properties, myelination patterns in terms of the peaks and kurtosis levels of ST angle distributions, and the exact locations and properties of GM tracking termination. All quantitative and directional analysis (Figure 2.13 C, D) derives from the preprocessing steps that end with figure 2.13 B. Other Data is for visual presentation.

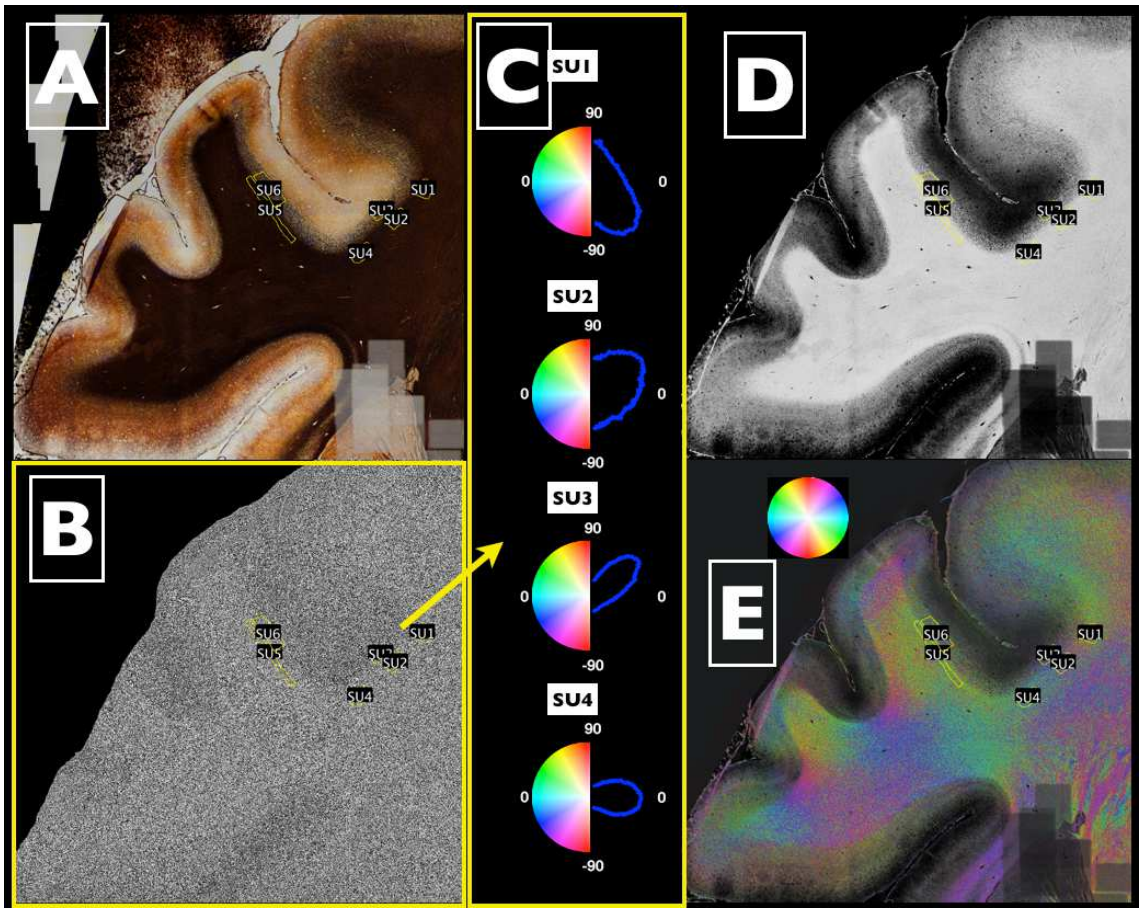

Figure 2.13: Histology processing: A original (affine stitched) Gallyas RGB. B, fine block matching contrast normalization of D, used in all ST calculations. C examples of Angle distributions in Gray and White matter, calculated from B in regions denoted (shown on other images also), D grayscaled, inverted for of A with brightness attenuated and non-brain tissue removed. E pixels of tensor structure analysis over the entire image B, colored by orientation with saturation and brightness provided by D

Because ST analysis is of pixelwise orientations, it is possible to apply ti nissl data too. Without further study, it's impossible to exactly what the orientation represents (in certainly represents the orientation of pyramids, with other cell types it is less clear). However, this does not stop the method from identifying clear cytoarchitectural and it is for this purpose, purely as a classification mechanism, that we employ it.

2.4 Data Sets And Analyses as applied In This Study

All MRI and Histological Data used in this research was provided by NIH [refs]. Two Rhesus monkey and Two Marmoset monkeys were scanned ex-vivo. Myelin and Nissl stained sections from one rhesus and one marmoset monkey were employed.

Two rhesus monkeys were sedated using ketamine (10 mg/kg i.m.), euthanized with

an overdose of anesthetic (60 mg/kg i.v.; Beuthanasia-D, Merck & Co) and then perfused transcardially, initially with 0.9% buffered saline followed by 3% paraformaldehyde in phosphate buffer (PB; pH 7.4).The brains were then extracted and immersed for 12 to 24 hours in 3% paraformaldehyde fixation solution. Gd-DTPA (Magnevist, Berlex Laboratories, Wayne, NJ) was added at 0.1% volume into the fixation solution. After the fixation, the brains were then incubated for 35 to 40 days in a phosphate buffered saline (PBS) mixed with 0.2% (Case B) or 0.1% (Case A) Gd-DTPA in order to reduce the longitudinal relaxation time (T1) (DArceuil et al., 2007; Wedeen et al., 2008). Similar procedures were applied for the marmoset monkeys.

The brains were transferred from the Gd-DTPA doped PBS into a sealable container constructed from a plexiglass tube (60 mm inner diameter) for scanning. The container was filled with the fomblin, a perfluorocarbon liquid, to closely match the susceptibility of the brain tissue (DArceuil et al., 2007). The brain was held in place tightly using either plastic rods or medical gauze. Scanning was performed using a 30 cm 7 Tesla scanner (Bruker, Billerica, MA) and a standard linear birdcage volume coil (72 mm inner diameter). A custom-design gradient coil (Resonance Research Inc.,Billerica, MA) allowed for a maximum gradient strength of 440 mT/m on each axis with a120 s ramp time. The diffusion data were acquired with a standard spin-echo diffusion-weighted (DW) echo planar imaging (EPI) sequence (DtiEpi) available in Bruker Paravision software. The diffusion encoding part consists of a pair of Stejskai-Tanner gradient pulses, with =6ms and = 14ms, and a b-value set at either 4800 s/mm2 (for Case A) or 4000 s/mm2 (for Case B). Various gradient tables were used: 60 directions (Behrens et al., 2007) in Case B, and 126 directions on vertices of a tessellated iconsahedral hemisphere (Tuch et al., 2002) in Case A. For scans with 60 gradient directions, the polarity of the diffusion gradients was inverted and the scans were repeated once, yielding a second equivalent set of data which are used as repeated measures in diffusion analysis. Additional image volumes (7 for Case A and 10 for Case B) were collected with b=0. The EPI sequence was used in three-dimensional (3D) acquisition mode in order to obtain isotropic high resolution images with high signal-to-noise ratio (SNR) (DArceuil et al., 2007; Wedeen et al., 2008).. Even echoes were phase encoded the same as the odd echoes and they were combined together in reconstruction to avoid EPI ghosting artifacts (Yang et al., 1996). To reduce echo time, the EPI train was acquired in 16 segments. Partial Fourier reconstruction was used in the EPI phase encoding direction to further reduce the echo time, with an over sampling factor of 1.3. The 3D image had an isotropic spatial resolution of 250 m, with

slightly different matrix sizes in the two animals (278x256x238 for Case A, 256x296x256 for Case B). Scan repetition time was 500 ms and echo time was 34 ms for Case A and 300 ms and 30 ms for Case B. Each diffusion direction took about 29 min (Case B) or 32 min (Case A) to acquire, with the whole diffusion data acquisition for Case A lasting about 71 hours. The data acquisition for Case A was stopped before the last 12 directions in the diffusion gradient table were finished due to scanner technical issues, so data set contained only 121 directions. Anatomical scans for magnetization transfer (MT) contrast (Wolff and Balaban, 1989) were collected using a FLASH sequence with and without magnetization transfer preparation. The repetition time was 25.3 ms, the echo time was 4 ms, and the flip angle was 20 degrees. The same field view and spatial resolution were used as in DWI scans. The MT preparation was achieved using a 12.5 ms Gaussian pulse with 540 degree flip angle. The offset frequency of the MT pulse was set alternatively at 2000 Hz and -2000 Hz to collect a pair of MT-weighted images. Such a pair was averaged to give a set of effective MT-weighted image data. For each MT-weighted pair, two control images were collected by turning off the MT pulse. About 10 hours were used to repetitively acquire the MT and control images overnight in order to obtain good signal to noise ratio in the final magnetization transfer ratio (MTR) images. The MTR images were derived as (Control_Image MT_Image)/Control_Image. The anatomical image acquisition was collected in a different scan session for Case A.

Marmoset data was collected in a similar fashion to Rhesus A in both P and R, however P was subsequently removed from the container, bisected along the midline and returned to a smaller container for closer coil proximity. For this scan a linear bircage coil of 25mm rather than 72mm was used. The bval was 4800s/mm^2 and the gradient table of 60 directions (Behrens et al., 2007) was used. The EPI train was acquired in 10 segments (rather than 6 with the rhesus). Spatial resolution in all reported marmoset scans was 150μm isotropic. The single hemisphere P scan had a matrix size of 256x160x140. Other parameters were comparable. Each diffusion direction was averaged 3 times in this scan and took 28mins to complete. One whole dataset thus took about 29 hours to acquire, however two identical scan sets were acquired over a 3 day weekend (yielding 6 averages per direction and 12 b0) as a single set. The SNR of the resulting combined data set is extraordinarily high, informally around 200 in a typical WM voxel. MT sets were acquired in the single hemisphere P sample at 75μm isotropic resolution

Case	Species	Dir	Res	Histol	MT	Notes
A	Rhesus	121	250μm	Gallyas,Nissl	250μm	Good SNR, Whole brain
B	Rhesus	60	250μm	-	250μm	Lower SNR, Whole brain
R	Marmoset	126	150μm	-	150μm	Good SNR, Whole brain
P	Marmoset	60	150μm	Gallyas	75μm	V High SNR, one hem

Table 2.3: table of MRI info

2.4.1 MRI Data Analysis Specific to this Study

DWI preprocessing: The dMRI data were preprocessed using TORTOISE software package (Pierpaoli et al., 2010) and corrected for eddy current distortions, and motion-like artifacts due to frequency drifts. The preprocessed data were reoriented to approximately parallel to ACPC line and exported to FSL raw data format. Data from Case A is further rotated to match the slice plane of the histology data by manually estimating a rigid body transform from the ACPC aligned FA map to coronal histology sections spaced through the hemisphere. The transform was then applied to the DWI set using spline interpolation (FLIRT, FSL). The rotated DWI data for monkey A was processed using FSL 5.1 bedpostx on an SGE cluster. 3 fibers were estimated with an ARD (Behrens et al., 2007) of 1. The number of MCMC burnin iterations was 5000, which provided lower model dispersion, and the rician noise assumption was used. Case B was processed using the earlier FSL 4.2 with 5000burnin iterations and without the rician noise model. SNR values measured at b=0 volume are 55 in corpus callosum, 69 in gray matter region near seed 1, and 57 in white matter region near the box in Fig. 1A. Using a cutoff threshold value of 0.01 for the FSL estimate of anisotropic signal fraction, we found that 90.7% white matter and 62.5% gray matter voxels contain two crossing fibers, and 25.9% white matter and 15.4% gray matter voxels contain three crossing fibers. Processing time on 64 AMD interlagos cores was 1-2 weeks per data set. The diffusion tensor was calculated using FSL dtifit, yielding the FA map. The principle eigenvector was used to create the directionally encoded color (DEC) maps in Fig. 1A and Fig. 6B, see also Fig. S1. Surface models. Models of the WGB and pial surfaces were computed using the magnetization transfer ratio (MTR) images. For Case A, the data was resampled to 290um to fit the Freesurfer size constraint of 256 cubic voxels and rotated to ACPC. The hindbrain and cerebellum were manually removed, and the WM was segmented using FSL FAST and manually adjusted to ensure topological constraints were met. A custom pipeline was developed to process the data with Freesur-

fer. The completed surfaces had roughly 210,000 vertices per hemisphere. The Freesurfer data was imported into the CARET software version 5.65 (Van Essen et al., 2001) using the initial steps in the pipeline developed in (Van Essen et al., 2012a). CARET5 was also used to compute inflated and mid-thickness (mean of WGB and pial) surfaces. In the case of Case B the MTR data was resampled to 500um to permit faster processing of VIC (see below) via a smaller surface mesh of around 70,000 vertices. In both cases resampling was for surface construction only, dMRI data and MTR data for presentation remained at 250um. Finally, all surface data was imported into the connectome workbench (version 0.83) software for subsequent DTI analysis and display, and linear transforms were applied to rotate the surfaces to the DWI data (Marcus et al., 2013) using workbench. Tractography. Tractography was performed using FSL probtrackx 5.1. In nearly all cases tracking was performed by defining sets of surface nodes on the mid-thickness surface in workbench. Surface nodes are simply coordinates. The coordinates were then used as seeds in the probtrackx program (FSL) using an output format that permits interoperation with the workbench software. Each seeded line in all cases was started from a random point within a radius of 125um of the seed coordinates, and initially followed only the direction of highest anisotropy within the gray matter, ignoring secondary fibers. In each monkey, a mask was defined by filling the pial surface of a hemisphere with voxels, and manually adjusting to fill gaps within the white matter and to ensure adjacent gyral walls did not touch, so that tracking could not proceed within regions of gray matter that are anatomically separated. Tractography experiments were performed only within the voxels defined by the masks. FSL locally modeled data within the defined masks were imported into the workbench software as fiber format files (Fig. 1). Tracking results were then imported into workbench format trajectory files for 3D visualization of sampled fibers (Figs. 2,6,7,S2). Tractography results were further transformed into dense connectome CIFTI 1 files. Files of dense connectome format form a matrix whose rows are the seed coordinates, and whose columns are each voxel within the mask. Files of the trajectory format contain the same data, but stored as a sparse matrix. Dense connectome matrix entries contain the number of times track lines from a given seed intersected a given voxel (the number of times the data in a voxel was sampled by tracks from a given seed). Using this dense connectome intersection matrix, we computed a quantity termed the volume intersection count (VIC). The count corresponds to a density of track lines throughout the brain following seeding at a single position, expressed as parts per million, of the 2.5 million voxels that were acquired in the brains hemisphere. Larger values empirically correlated with deeper white

matter penetration, since deep penetration allowed for tracks to reach more distant sites through the deep white matter fasciculi. We thus used VIC operationally as the measure of track line spread away from a surface seed to distant sites in the hemisphere. In Case A, a patch of around 10,000 mid-thickness surface nodes was defined around the IPS and CS. Dense connectome files were made by seeding 1000 track lines from each node. In addition, the entire cortical surface was seeded excepting the medial wall area (170,000 nodes) and a dense connectome file formed by seeding 200 lines per node. Computation of the latter took one week, 190GB of RAM and resulted in a dense connectome file of 170K seeds by the 2.5 million target voxels in the mask. This matrix was 1.5TB in size. In Case B, a mask of the entire cortex (58,000 nodes) was seeded with 1000 lines yielding a file 330GB in size.

2.4.2 Tracer Surgeries

Biotinylated dextran amine (BDA) was injected into the intraparietal sulcus of one monkey. Surgical procedures were carried out using standard sterile neurosurgical procedures. A large bone flap was removed over the dorsal aspect of the right hemisphere and the dura was opened and reflected medially to expose the lateral cortical surface. The banks of the intraparietal sulcus were carefully separated along its mediolateral length with a fine forceps and a small glass pipette attached to a vacuum pump. The fundus was visualized during gentle retraction and the BDA was injected through the pia to a depth of approximately 1.5 mm into the cortical sheet.The dura and skull were sewn into place and the skin was closed in anatomical layers. Postsurgical analgesics were provided as needed in consultation with the facility veterinarian. Following a survival period of 14 days, the animal was euthanized with an overdose of anesthetic (60 mg/kg i.v.; Beuthanasia-D, Merck & Co) and then transcardially perfused with 0.9% buffered saline followed by 4 l of 4% paraformaldehyde in phosphate buffer (PB; pH 7.4). Brains were removed from the skull, photographed, blocked in the coronal plane, and then cryoprotected through a series of glycerols (Rosene et al., 1986). Brains were quickly frozen in 800 C isopentane and stored until they were sectioned, at which time they were cut in the coronal plane at 50 m. Two 1-in-10 series were processed, one treated to visualize BDA (see below) and the other processed to visualize the BDA and then counterstained with thionin. The BDA series was stained using an avidin-biotin horseradish peroxidase technique (Reiner and Gamlin, 1980; Veenman et al., 1992). Endogenous peroxide was inhibited by a 30-min wash in 1% hydrogen peroxide. The tissue was then incubated for 4 hours at room

temperature and overnight at 40 C with a concentration of 0.5 g/ml of avidin horseradish peroxidase or streptavidin horseradish peroxidase conjugate (Molecular Probes Inc Eugene, OR) in 0.05M Tris buffer (pH 7.6). The chromogen reaction was conducted with 3,3-diaminobenzidine tetra hydrochloride reaction (DAB, Sigma Co., St Louis, MO) at a concentration of 0.05% with 0.03% hydrogen peroxide and 0.1-0.2% nickel sulphate in 0.05M tris buffer (pH 8.0) to intensify the staining. The reaction was monitored with a macroscope and stopped after 3-5 min to maximize fiber staining while minimizing background. Sections were then mounted, dehydrated, and coverslipped.

2.4.3 Preparation and analysis of histological data in this study

After the brain of Case A had been scanned a period of five months post mortem, it was removed from the fomblin-filled scan chamber and prepared for histological sectioning and staining. The brain was rinsed through multiple changes of 0.1M PB over the course of one week at 4 C, then cryoprotected in a 10% glycerol and 2% DMSO solution of 0.1M PB for 24 hrs followed by 20% glycerol and 2% DMSO solution of 0.1M PB for 60 hrs at 4 C, prior to being frozen and stored at -80 C in isopentane. The tissue then was sectioned at 50 m on a sliding microtome. Every tenth section was stained for myelin content using the Gallyas method (Gallyas, 1979). Digital images of the stained sections were taken utilizing a Zeiss AxioCam MRc5 digital camera, attached to a Zeiss ImagerZ1 microscope. The sections were stained at varying intensities, with lighter stains permitting better visualization of white matter fibers and heavier staining permitting better visualization of gray matter fibers. Visualization of individual fibers in Fig. 4 was aided by contrast limited adaptive histogram equalization of the section image. Fiber orientations in Fig. 6 were estimated in the following manner. First, the section image was converted to gray scale, inverted in its intensity, and subject to contrast limited adaptive histogram equalization. Next a pixelwise structure tensor estimation (at 1um per pixel) with a Gaussian gradient difference was applied. Pixels were colored according to their 2-D orientation, via the principal eigenvector of the 4 element structure tensor, using the software package ImageJ ((Van Essen, 2014; Budde and Frank, 2012; Rezakhaniha et al., 2011))(cites =VE chapter,budde and franke, orientationJ). The WGB was estimated by thresholding stain intensity and anatomical regions assessed with reference to position in the brain and (Lewis and Van Essen, 2000a).

2.4.4 FSL Results

Before continuing we first present the results of the FSL local modelling system for Case A, in terms of the mean_f for each of 2 modelled fibres, the mean dispersion, the mean orientations and how these compare to data derived from tensors. We compare Cases C and D (CV3X and DB58) with a data set derived from an invivo human scan. This scan was acquired on a 1.5T scanner, with b=1000, 30 gradients and 2.5mm isotropic voxels.

We argue might that because of the specific properties of the ex-vivo macaque data (high resolution, high bval, high SNR, low noise), the FSL system is implicitly modelling the sample properties to a much greater extent than acquisition uncertainty. Therefore, the properties of the model reflect anatomical properties via uncertainty (dispersion), even though in principle we cannot prove this.

Each model in each voxel remains that of a single direction of anisotropy, and it's dispersion is uncertainty regarding that direction. Within a voxel, kissing, fanning, and other patterns that constitute an inverse problem remain. but the resolution affords a fine grained picture of this that may reflect complex fibre anatomy over groups of voxels. But we cannot unfortunately say what, if anything, would be reflected in this way at this time.

Figure 2.14 shows the directions of the first and second distibutions of a the three fibre model of DB58 (C,D)(ARD=1 burnin=5000) used in this work. A and B show equivalent results from the 1.5T invivo comparator. In each case, the mean direction of the fibre distribution is shown in each voxel in the standard directional color scheme. The intensity of the colored voxels is modulated by the mean_f for the distribution in the voxel. The data is overlaid on structural scans. In the case of the human data, it was also subjected to an affine vector ("vecreg") registration procedure to represent it overlaid on a T1 scan of 1mm resolution.

In figure 2.14 A and C we see that in the macaque data, the mean fibre orientations are strong and coherent in the white matter. In the gray matter, the intensity is reduced because f is lower (meaning more of the signal is modelled by isotropy) but there is still a clear coherent structure, that reflects the orientations of large pyramidal axons running down the cortical columns in parallel. The human data shows much less white matter detail, and no clear GM detail. B and D show the second fibre model. In the human case, where a second fibre is found at all by the ARD process, it seems patchy and incoherent. most of the brain is not covered at all. The macaque data, by contrast, shows a clear pattern of orientations through nearly all the white matter, and a comparison of C and D shows that the orientations have a complementarity (NB the structural MTR of the

macaque data is slightly misaligned with respect to diffusion space)

An important property is the dispersion of the models about their mean. Even if the portion of signal modelled is low, if the models have low dispersion, we may regard them as reliable since 50 independent assessments of the likely direction of anisotropy are in agreement. Absent other factors, dispersion may reflect uncertainty from anatomical sources.

The FSL system will always produce very dispersed distibutions when it's unable to model anisotropy effectively; conversely low dispersion indicates and effective model. Even though the two model properties are correlated, dispersion is therefore a more useful comparator of first and second fibre properties in a region.

We summarize dispersion properties in figure 2.15. The top row shows dispersion of the first and second fibres for case B the second shows this data for Case A, while the third for the in-vivo control (30 gradients, 30 vols). The histograms of total dispersion for the first fibre in both macaque samples show very low dispersion across all the voxels. Case B may have slightly higher average dispersion, and this may be related to it's lower angular resolution or even SNR. The second fibre has two peaks. the Peak on the left shows low dispersion and this mainly represents WM models. The high dispersion on the right are models with very low f (a model is always fitted, even if f=0) .

By contrast, the in vivo control shows high dispersion even for the first model. The second model has a small region of low dispersion, but essentially the second fibre is modelled as isotropic over nearly all the volume.

In Case A we found 90.7% of WM voxels and 62% of GM voxels contained second fibers. 25.9% of WM and 15.4% of GM voxels contained 3rd fibers using a cutoff threshold of mean $f_n >= 0.01$

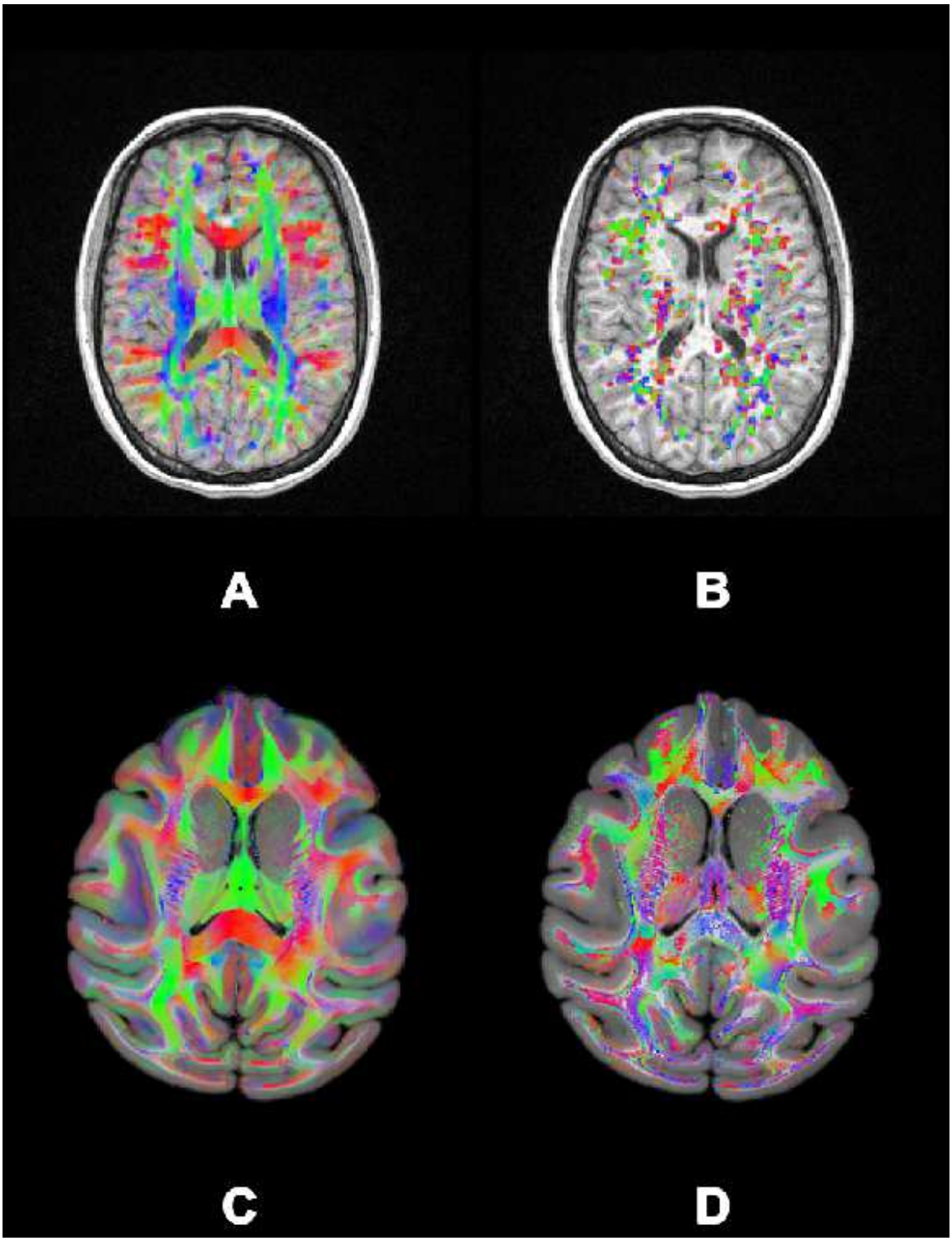

Figure 2.14: The first and second fibres, attenuated by the mean fraction of signal of signal modelled, overlaid upon a T1w image (A,B) and MTR (C,D). It can be seen that in the human data (A, fibre 1, B dyad 2) there is no modelling of the GM, and almost no viable second distribution at all (B). In DB58, the GM has is modelled well in the first distribution (A) though the second largely models only WM

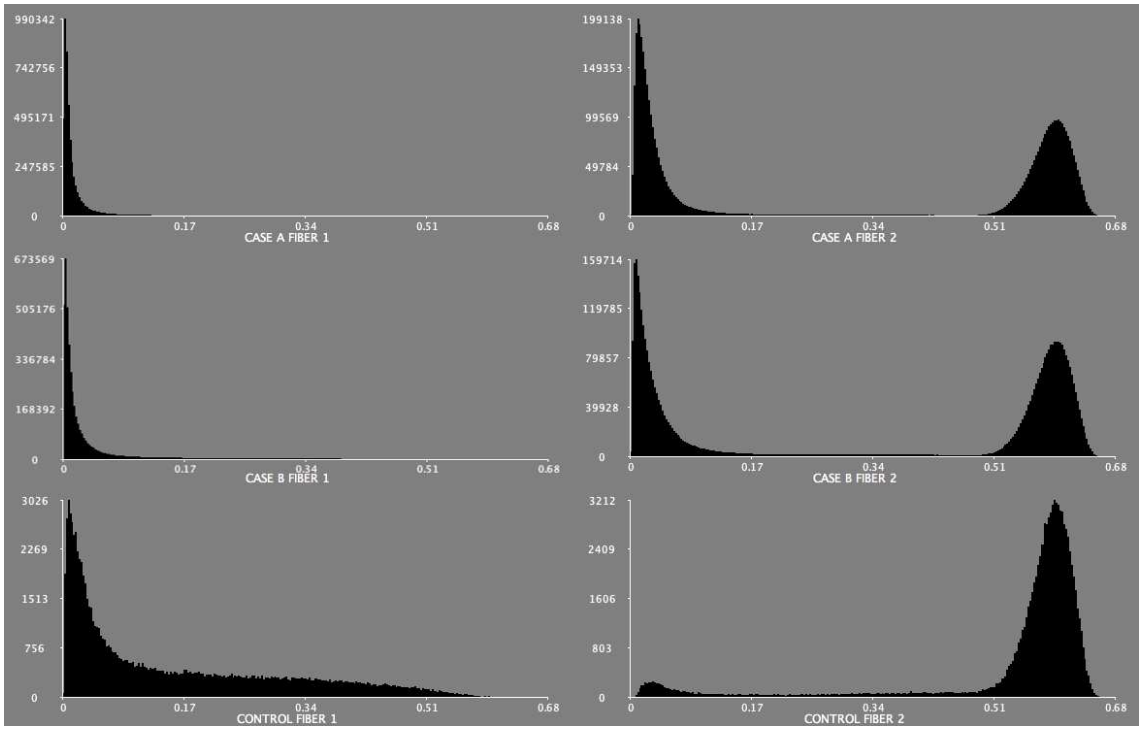

Figure 2.15: distributions of model dispersion in first and second fibres for both macaque samples and the human control data

2.5 Anatomical Terms and (selected) Rhesus Landmarks

Figure 2.16 A shows the major sulci visible in from the lateral aspect of the macaque. Glossary of terms (used) to follow

Monkeys are not all the same; The primary brain used in this work Case A lacks and IPCD, while in Case B the IPCD is so large it is sulcated. Case A has a very large arcuate spur, and the central sulcus extends very far laterally and makes a distinctive quasi-gyrus/sulcus which is analyzed very heavily because it produces atypical white matter and gray matter (axons turn back on themselves). The anatomical terms here for cortical tissue share some commonality but not identity with the work in chapter 3. This author tends to favour Brodmann derived/style numerical nomenclature simply because it is natural. This thesis does not contain work on anatomical connections of sufficient accuracy that conflicting cortical parcellation schemes or nomenclature are of importance. Brodmann has the benefit that it is cytoarchitecturally simple, and defined in human, marmoset and rhesus.

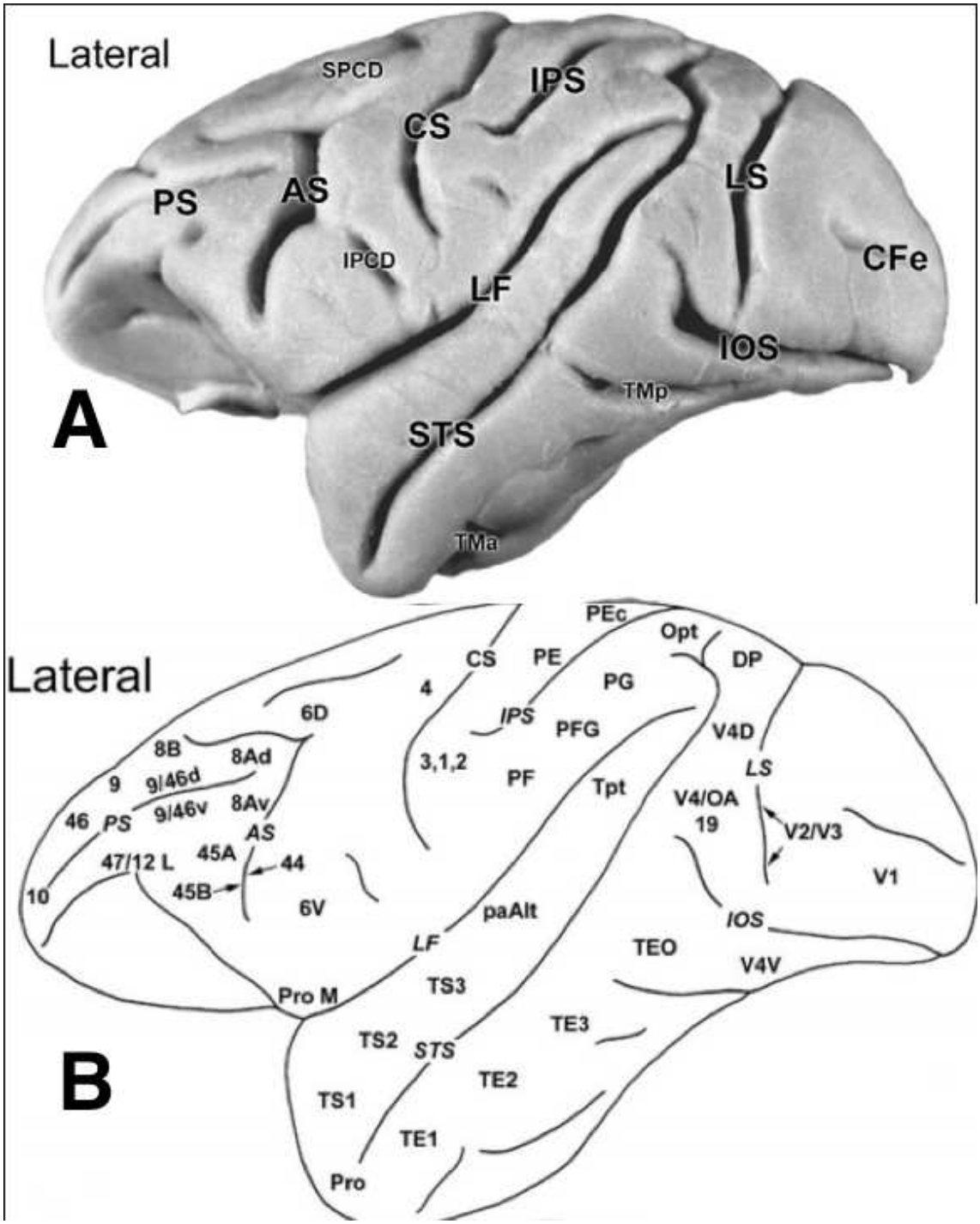

Figure 2.16: Major sulci and cortical regions in the macaque brain

Chapter 3

Accurate Labelling of Macaque Cortex

Abstract

A system for the construction of high resolution (250μm), 3D atlas of macaque cortex based on (Saleem and Logothetis, 2012) is presented. The atlas consists of a high resolution "surrogate" MRI of the atlas animal, together with labels. the labels reflect the histological properties of the scanned animal very accurately due to the properties of (Saleem and Logothetis, 2012). Highly accurate cortical surface models are also produced. The atlas is validated against the paper atlas at found to have near perfect correspondence to locations in the paper atlas. The 3D atlas improves over other efforts in terms of a resolution of the slice alignment problem during construction, and in fidelity to the histological properties of the brain due to the source material. In addition, the GPU based system forms the heart of a pipeline that is able to head extract and label MRIs of other animals in a highly accurate way, and produce high resolution "surrogate" scans and automatic surface models. We validate the system with histology and quantitative comparisons between multiple scans of the same animals. We produce the first histological and MRI atlas that is well formed and conforms to the 3D MRI of the subject from which it was made. We demonstrate that the registration pipeline is able to take a T1w scan of a macaque head, accurately extract the brain and label the cortex accurately with the Saleem Logothetis atlas (Saleem and Logothetis, 2012).

3.1 Introduction

In recent decades, neuroanatomical atlases have taken the form of large books of magnified photographs of sections, combined with corresponding outline drawings, depicting the stereotaxic coordinates of brain structures (Paxinos et al., 2008; Saleem and Logothetis, 2012). While this has provided an invaluable resource, inferring three-dimensional structure of the brain from a sequence of two dimensional images poses significant challenges. The cerebral cortex in particular is a structure whose complex three dimensional folds can result in very counter intuitive spatial relationships between regions when viewed as sections in a single plane. This problem is intensified when the angle of sectioning of subject does not precisely match the angle of sectioning in the reference atlas. Moreover, the stereotaxic atlas cannot account for differences between the atlas and an individual subject, a critical limitation. Recently, computational approaches have allowed for the extraction of cortical surfaces from MRI (Van Essen et al., 2001; Fischl et al., 1999) or histological section (Van Essen et al., 2001) data, and their conversion into folded sheets in stereotaxic space represented by sets of spatial coordinates. The topological relations of these coordinates permit their conversion to inflated or flat surfaces while preserving data relationships, permitting improved visualization of adjacent structures, and the presentation of fMRI, neurotracer and atlas data (Van Essen et al., 2011; Markov et al., 2014). The use of surface reconstructions have become commonplace in functional imaging, where activity depicted on surfaces (Hutchison et al., 2011) is often easier to interpret then on a series of sections. In both monkey and human estimated atlas data is widely available on reference surfaces (Van Essen et al., 2011, 2012a). One key advantage of surface based approaches is that subject data can be non-linearly resampled to a reference surface, providing anatomical parcellations on the subject and permitting subject cohorts to be displayed and analyzed in a common space. This resampling involves a non-linear deformation of the subject to the template via alignment of sulcal fundi delineated either manually or via estimation (Van Essen et al., 2012a) . While these procedures are superior to linear transforms of volume data, and typically non-linear volume methods, the landmark positions and algorithmic parameters combined with individual variation in brain shape can yield uncertain results, since the relation of cortical regions to cortical folds is uncertain. The need for accurate registration to an atlas is especially acute for non-human primate research which relies on the precise localization of electrophysiological recording sites, pharmacological inactivation, fMRI responses, and anatomical tracer injections with respect to cytoarchitectonic boundaries that are not visible in-vivo. It is particularly de-

sirable to have a high quality 3D volumetric atlas that can be used to automatically label in-vivo brain images by mapping the atlas onto the images by computer software. At present, there exist a few options for mapping macaque areas onto the brain , the most prominent of which is the use of the F99 surface and associated atlas data combined with landmark based surface registration. The F99 surface atlas itself is made from landmark registration to surfaces formed from imperfectly aligned histological. No easy way of labelling the voxels of the cortical thickness presently exists. Here we present and validate a 3D version of the Saleem and Logothetis atlas (Saleem and Logothetis, 2012). These data are unusually suitable for the construction of a 3D atlas, because the histological data was very carefully aligned to high resolution MRI data from the same animal. In constructing the 3D atlas the original MRI was enhanced in contrast and in spatial resolution (to 250um isotropic). The enhanced MRI and original is presented together with a GPU based non-linear registration algorithm that allows for highly accurate reconstruction of the atlas into 3D, and transformation of the 3D atlas to different brains (Gruslys et al., 2014). The accuracy of registration in labelling subjects is assessed directly via histological confirmation and consistency by comparing multiple scans of the same animals in different sessions and at different spatial resolutions. The generation of surface models in macaque is often very challenging, and our pipeline therefore deforms atlas surfaces to the subject animals, leaving a system in which all subjects are on a "standard mesh" and data from one animal or atlas freely displayed on another, or all subjects on the atlas reference itself without the need for spherical surface registration procedures. We also present a method of non-linear head extraction, also a hard problem in NHP as part of the pipeline. The pipeline requires little to no user intervention beyond installation and global configuration. This chapter describes the steps involved in converting the 2D atlas data from a high quality macaque brain atlas to a digital 3D atlas, as well as the pipeline for using software to transform the 3D atlas volume onto an individual macaque brain. The toolkit described here is based on the convergence of two previously published advances. The first is the Saleem and Logothetis rhesus brain atlas (Saleem and Logothetis, 2012), which provides the source MRI and histologically derived sections. The second is the GPU based non-linear registration software (Gruslys et al., 2014), which was modified to implement the algorithms described in section 3.2. We described the series of steps used to construct the 3D atlas volume by augmenting the registration software. In section 3.3 we demonstrate its application to labelling other animals and validate the approach.

3.2 Construction Of Atlas

The 3D reconstruction used 30 saggital diagrams of sections from the published atlas. After MRI scanning, the brain was carefully blocked in the stereotaxic plane of the MRI. The Axial (left hemisphere) and Coronal (right) planes of the animal were sectioned and stained for histological analysis. The saggital diagrams were drawn by the author from the contours of the MRI image of the left hemisphere. cytoarchitectonic boundaries were estimated from the axial and coronal histology. The saggital series are thus very closely aligned to the MRI, without the tissue shrinkage, distortion and minor damage associated with histological series, while still maintaining very close fidelity to the histological data of this exact brain. The first step in creating a 250um 3D atlas was to convert the saggital diagrams diagrams into a 3D stack. Each vector diagram had arbitrary spatial resolution in the saggital plane, but 1mm spacing between sections. To begin, we created a colouring scheme such that each area was manually assigned a unique colour label in the vector-based CVX source format (Figure 3.1). The coloured diagrams were rasterized and transformed into an RGB nifti volume of dimensions 1x0.25x0.25 mm volume of (Figure 3.2 A).

While ideally the 3D labelling should register perfectly with the original MRI volume of the atlas brain, and the interpolation from the axial and saggital colouring should provide a clear picture of areal designation throughout the cortex, in practice 2D section alignment from any section data is a formidable task. The unique nature of the saggital diagrams rendered this task possible in a way that still reflects the anatomy of the sample brain. In particular we had no need to implement slice to slice non-linear realignment see (Paxinos et al., 2008) which would cause decoupling of the label data from the brain's structure. Our manipulations treated the label volume as a whole, and only very minimal non-linear adjustment was used to fit the labels to the atlas MRI. Primarily, we enhanced spatial resolution and corrected alignment small alignment artifacts by applying anatomically motivated algorithms. To fine tune alignments and estimate a 250um isotropic volume we performed a number of additional corrective and enhancement steps. Issues included the treatment of image artifacts from the original MRI, the requirement that the atlas have higher resolution than the original MRI,the nature of the relatively large (1mm) between atlas sections, and the slight misalignments of 2D sections with respect to delineated cortical regions. The coloured rasterized nifti file representing the coloured atlas diagrams is shown in Figure 3.2 A as a 3D volume (dorsal) and in coronal 1mm slices. The finished atlas is shown in 3.2 B. The procedure for constructing the atlas is summarized in Fig. 3.3 and described in the following paragraphs.

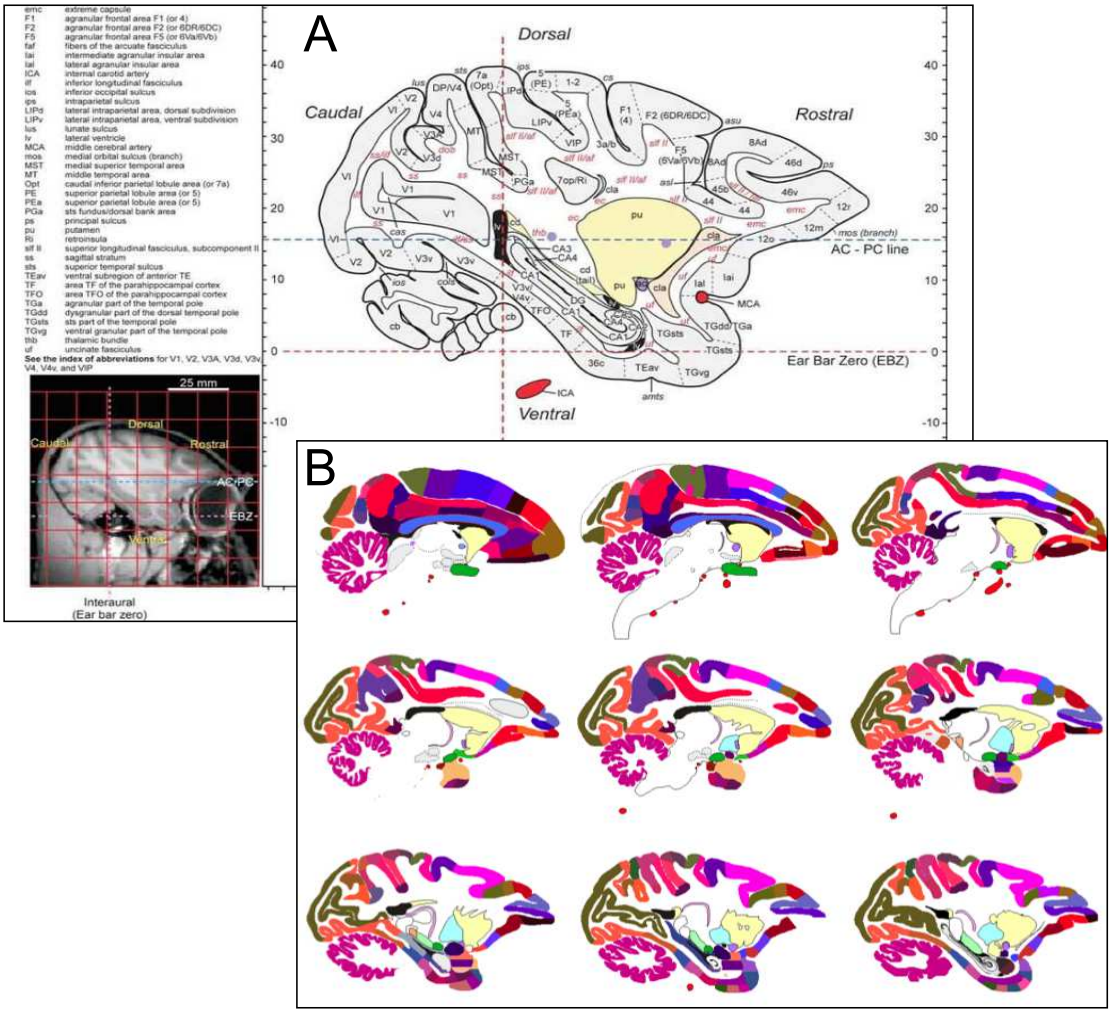

Figure 3.1: A an example page from (Saleem and Logothetis, 2012) showing terms, stereotaxic frame and MRI. B 9 coloured saggital diagrams

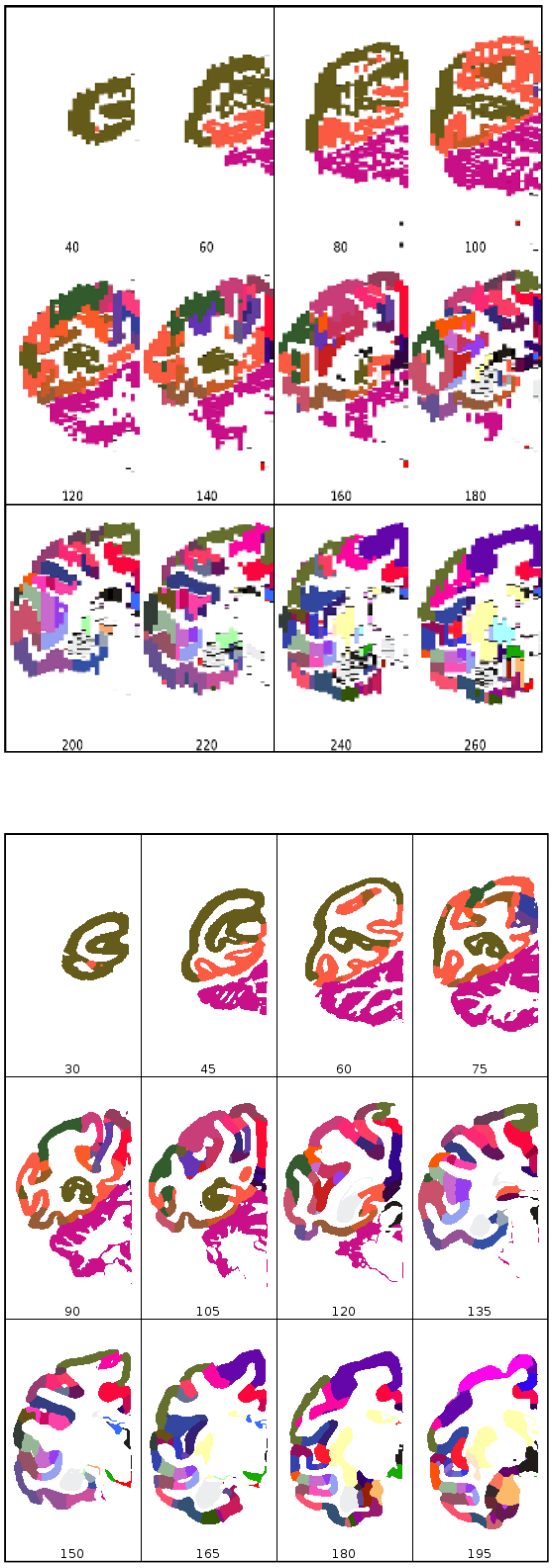

Figure 3.2: A shows the coloured saggital diagrams (Fig 3.1 B, rasterized to 250um per pixel, and stacked according to the stereotaxic coordinates. The right image shows a dorsal view of the stacked diagrams in 3D. The left pane shows selected sections resliced into a coronal view to demonstrate spacing and alignment issues. B shows the data after completion of the atlas 3D reconstruction presented here.

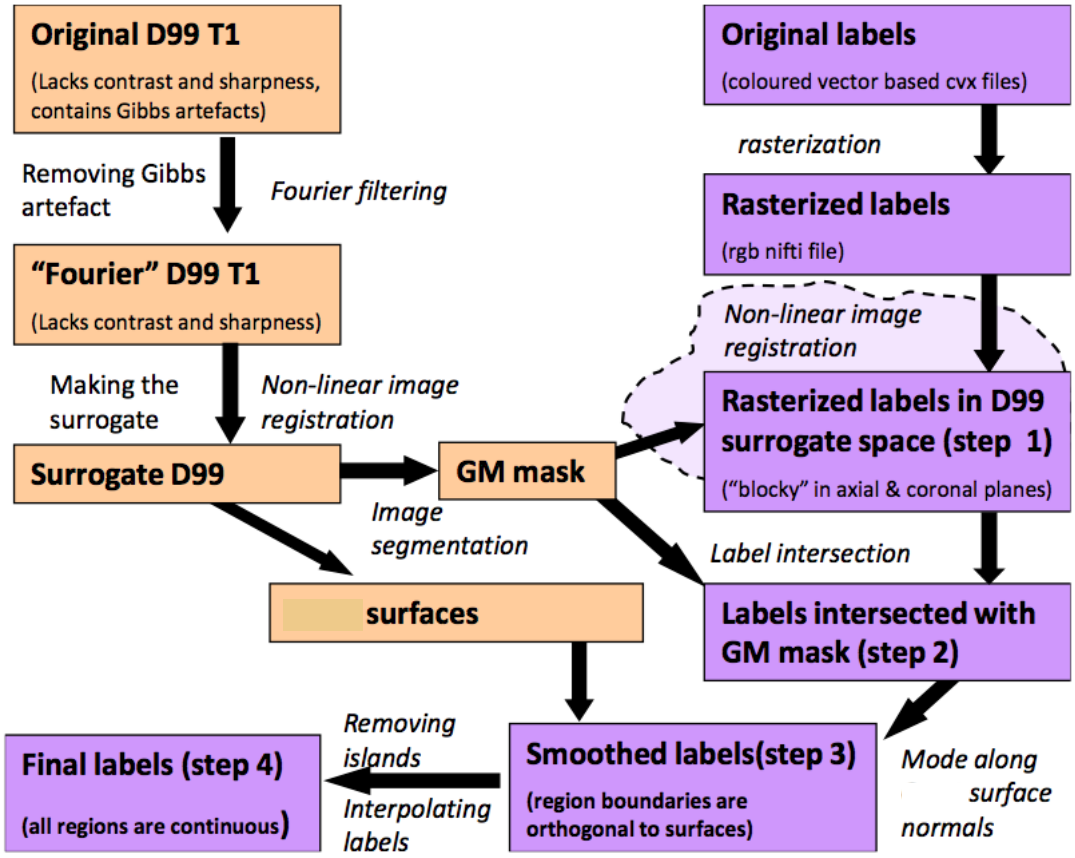

Figure 3.3: Flow chart of the 3D atlas construction pipeline

3.2.1 Artifact removal from original MRI images and creation of "surrogate" ultra high resolution MRI volume

In the original MRI 500μm in-vivo images from the atlas (Saleem and Logothetis, 2012) animal (see table 2.1 for summary of MRI data used in this chapter), Gibbs artifacts are quite prominent. Gibbs artifacts occur when the signal intensity of an object changes abruptly in space, and there is truncation of the discrete Fourier series representing the image. In this case the artifact manifests as bands of intensity (figure 3.4 A) While these artifacts do not affect the accuracy of the printed atlas, they pose severe challenges for the precise registration of the atlas animals brain to other macaque brains (Fig. 3.4 A), and to the fitting of the label volume. To overcome this obstacle, as well as to enhance contrast and resolution we created a surrogate atlas volume by very carefully non-linearly deforming a different animals very high quality MRI volume to the original atlas brain. This was done by first minimizing Gibbs artifacts from the original T1 contrast MRI volume of the atlas brain (Supplemental Methods, audrunas thesis, Fig. 3.4 B). Second, a very high resolution MRI image collected from an ex vivo brain, whose gray/white contrast was based on magnetization transfer (MT) contrast was then carefully non-linearly registered to the left hemisphere of the Gibbs corrected and upsampled atlas image. By deforming the 250μm MTR image of a second brain to the 250μm upsampled and contrast enhanced atlas T1 the white/gray and gray/CSF boundaries of the atlas brain are recreated in an image with low noise and brain like properties (figure 3.4). This newly registered MT volume thus serves as a surrogate for the original anatomical MRI, with very high spatial resolution (250 um isotropic), excellent gray/white tissue contrast, and very high SNR Fig. 3.4 C). These properties are effectively impossible to obtain in-vivo. These properties render the surrogate MRI volume more suitable to register with other brains than the original, and to fit the labels, permitting the 3D atlas to have a higher spatial resolution with more accuracy than simply upsampling. The process of creating the surrogate preserved the original gross anatomy of the atlas MRI. This was assessed by eye, and by the generation of the white and pial surface representations for the atlas using the surrogate volume and the custom use of the freesurfer software. Fig. 3.4 E) shows slices of the 250um surrogate with the white (yellow) and pial(red) surfaces overlaid. Fig. 3.4 D shows these same surfaces in the same stereotaxic space overlaid upon the lower quality MRI data printed in (Saleem and Logothetis, 2012). The GM and WM contours of the surrogate and original closely match. Since the WM and pial surfaces generated from the surrogate closely match the scan as published in (Saleem and Logothetis, 2012) the surrogate may be regarded as

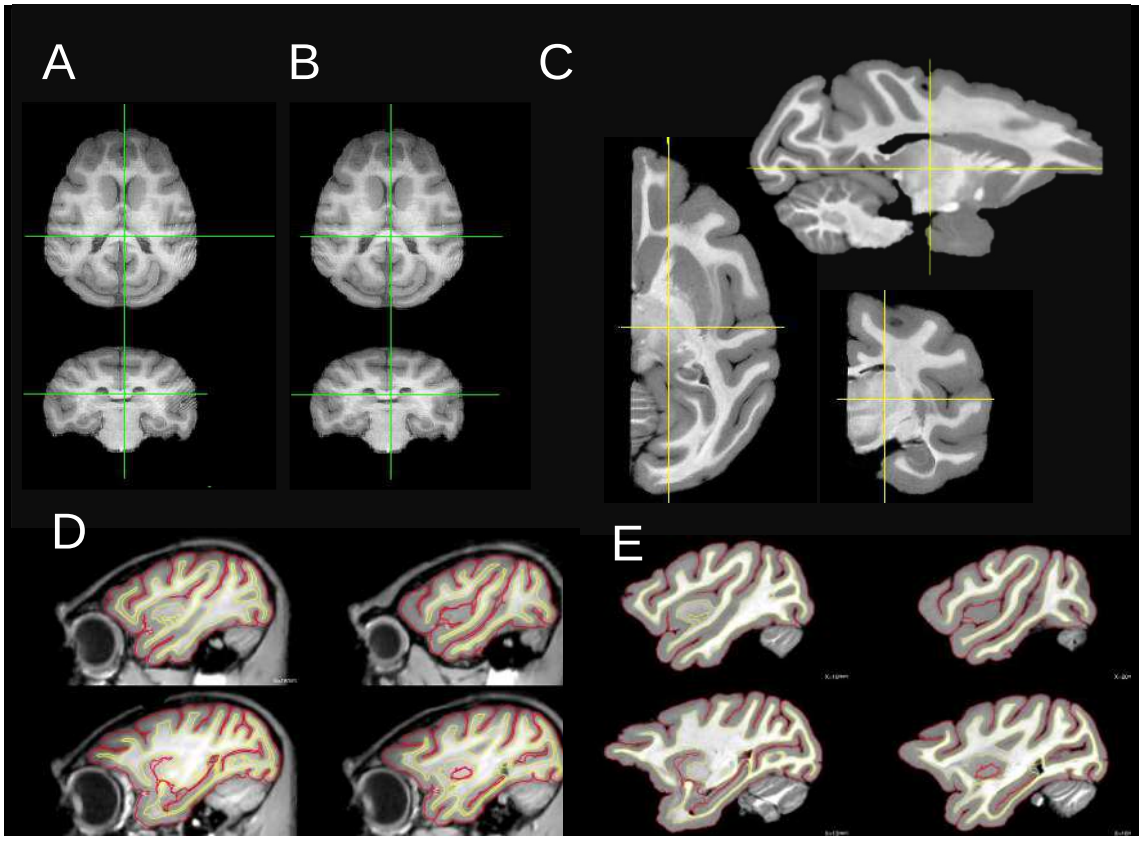

Figure 3.4: A the original MRI. B the original with Gibbs removed (right hemisphere only). C the 250um surrogate Atlas MRI (see text). D, E demonstration that the White and pial boundaries of the surrogate (E) and published MRI (D) are the same for the same coordinates

a high quality, high resolution version of the original

3.2.2 Reconstruction of 2D sections to high resolution 3D atlas

. The distance between saggital sections in the atlas was 1mm, and inter-section alignment was imperfect. This posed challenges for creating a smooth 3D volume at an isotropic resolution of 250um. Assembling a volume based on coloured saggital sections appeared rough and in some cases inaccurate when resliced into coronal or axial sections (Figure 3.2 A). To create self-consistent, accurate, and high-resolution 3D volumetric labels 3.2 B), four sequential steps were required. The conceptual requirement, and initial design of these steps was designed by the present author. Each step was implemented by Audrunas Gruslys as an extension of the Ezys software, both of us adjusted the conceptual requirements to reach the desired goal of each step. For example the original requirement (that cortical regions be continuous) and concept for removing "islands" used surface normal vectors (figure 3.6 A top row) this led to problems solved by gruslys (figure 3.6 A bottom row)

1. Affine and nonlinear section alignment. The assembly of the anatomical volume from coloured diagrams began with optimizing alignment using a combination of manual landmark constrained affine transformations and very small non-linear adjustments to the label stack as a whole. (Fig 3.5 A and B). This process led to a coarse map of areal boundaries. However, these steps do not address misalignment or spacing.

2. The next step used a rotationally invariant interpolation method, constrained within a gray matter mask to increase the resolution to 250um isotropic while ensuring preservation of atlas properties . During this procedure, voxels labelled as being in the cortex, but lying outside of the gray matter mask, were discarded. In the same vein, unlabelled voxels within the gray matter were assigned a value based on the labelling of their neighbours in 3d [slightly subtler: rotational invariance, other wise result differs depending on how the non-isotropic volumes are resliced]. This procedure led to a complete labelling that was restricted to the gray matter (Fig 3.5 C). However, while the spatial resolution was enhanced, the effective gap remained 1mm, and alignment errors are not resolved, in some cases appearing as islands of high resolution voxels, invading the wrong cortical space. The next steps were applied to estimate 250um isotropic resolution, and remove residual alignment artifacts via algorithms that draw inference from the data available and from general anatomical principles, enhancing but preserving the source data.

3. Assignment of cortical boundaries based on radial vectors. Given lower spacing in

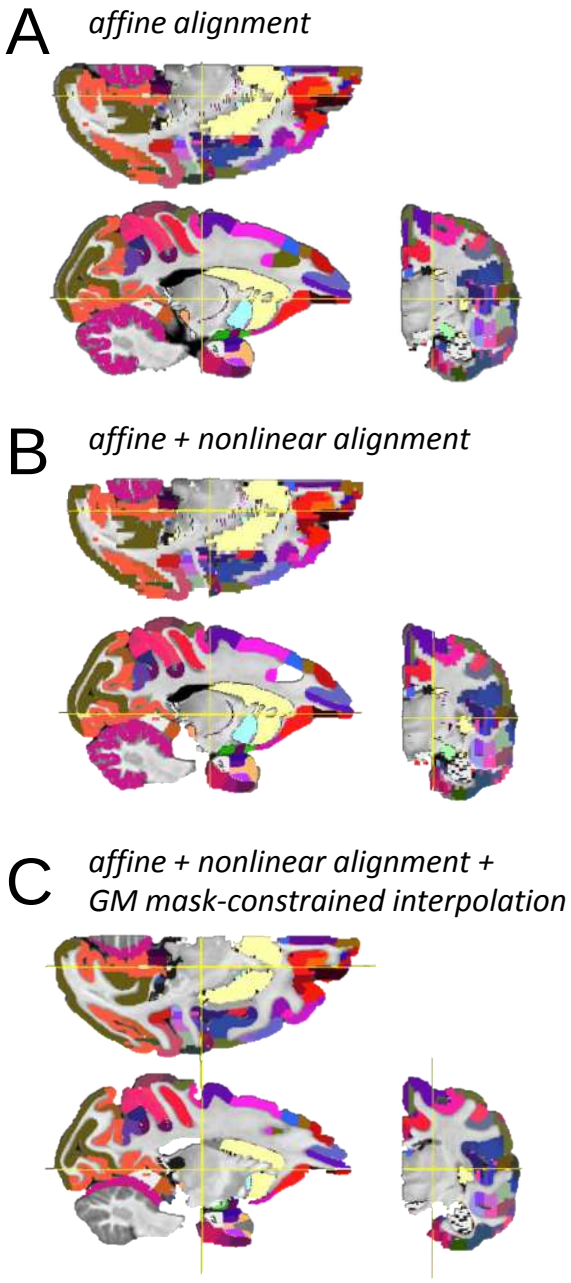

Figure 3.5: A affine alignment of 3D labels to surrogate via manual control points. B Very moderate nonlinear deformation with respect to control points. C upsampling via rotationally invariant interpolation within GM mask

one dimension than the others, we assumed that where cortical boundaries required inference of missing information, the shortest vector in the space of non-crossing vectors along the radiation from the white to the pial surface was the most principled source of missing information. We used the vectors normal to the WM surface as a starting point to estimate a set of shortest, non-crossing paths within the cortical thickness that allowed us to constrain areal assignments within the high-resolution gray matter mask. This procedure ensured that cortical boundaries aligned along cortical columns, and inferred missing information. This process began with an assignment of a vector direction, at each point on the white matter / gray matter boundary, that radially met the pial surface without any two such vectors intersecting (Fig 3.6, Supplemental Methods). For each such unique path within the 3D gray matter , the labels were set to the most abundant label ID encountered along that path.

4. Removal of areal islands and fine labelling. In the final step it was necessary to remove small islands of voxels from one region enclosed within another, that corresponded to local ambiguity or uncertainty unresolved by the algorithm in the previous step. Given the anatomical assumption that cortical regions in the atlas are unique, homogeneous and contiguous, that is cannot contain one another (plainly regions are grouped, but that is unimportant here), we resolved this final issue. These islands corresponded to small regions of a given area that had the same label ID as another area, but was spatially removed from it. The existence of such islands reflects, in part, the inherent difficulty in assigning strict areal boundaries based on cytoarchitectonics, and, in part, the errors associating with steps (1) to (3) above. We took the strategy of removing these islands if they were small and filling them in according to the neighbouring areal assignments. Specifically, we discarded discontinuous regions of a particular label ID that were less than one quarter the size of the parent region, filling in the removed island region with the surrounding areas label ID. The island removal algorithm was used in earlier processing steps with a criterion that islands be very small.

Following these steps, the labelled surrogate brain (Fig. 3.7 A) exhibited complete labelling restricted to the cortex, with clear, radial divisions between adjacent cortical areas. This volume mapped directly onto the original MRI data (Fig. 3.7 B), indicating that the use of the high-resolution surrogate volume was successful. The accuracy of the reconstruction method was then verified by comparing the resliced volume to the

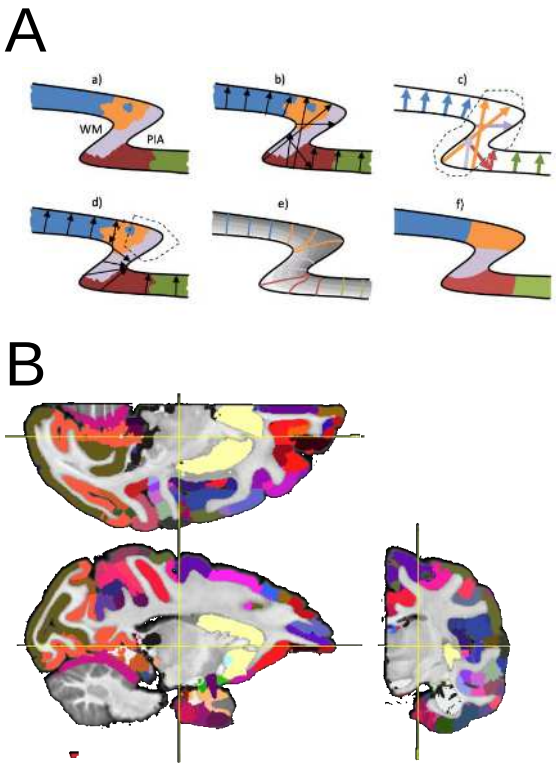

Figure 3.6: A the process by which misaligned 1mm spaced data was estimated to aligned 250um isotropic data. B The result

original section diagrams. This volume is thus ready for registration to the brains of other individual macaques, in order to serve as a guide for any of a number of research applications for which accurate knowledge of areal boundaries is desirable. Fig. 3.7 C shows the folded cortical map rendered as a 3D volume, and Fig. 3.7 D shows an example of one application, presenting a comparison of this volume to a map of cortical thickness computed from the surrogate brain. We found that in the saggital plane any region was never more than -/+0.5mm from the published diagrams (as is expected from the 1mm spacing) but the values tended to be lower, meaning the data properties were not only preserved but enhanced. In the axial plane, good agreement was shown even though those atlas data were never incorporated directly into the atlas (because of tissue distortion, saggital drawn from MRI of both hems also)

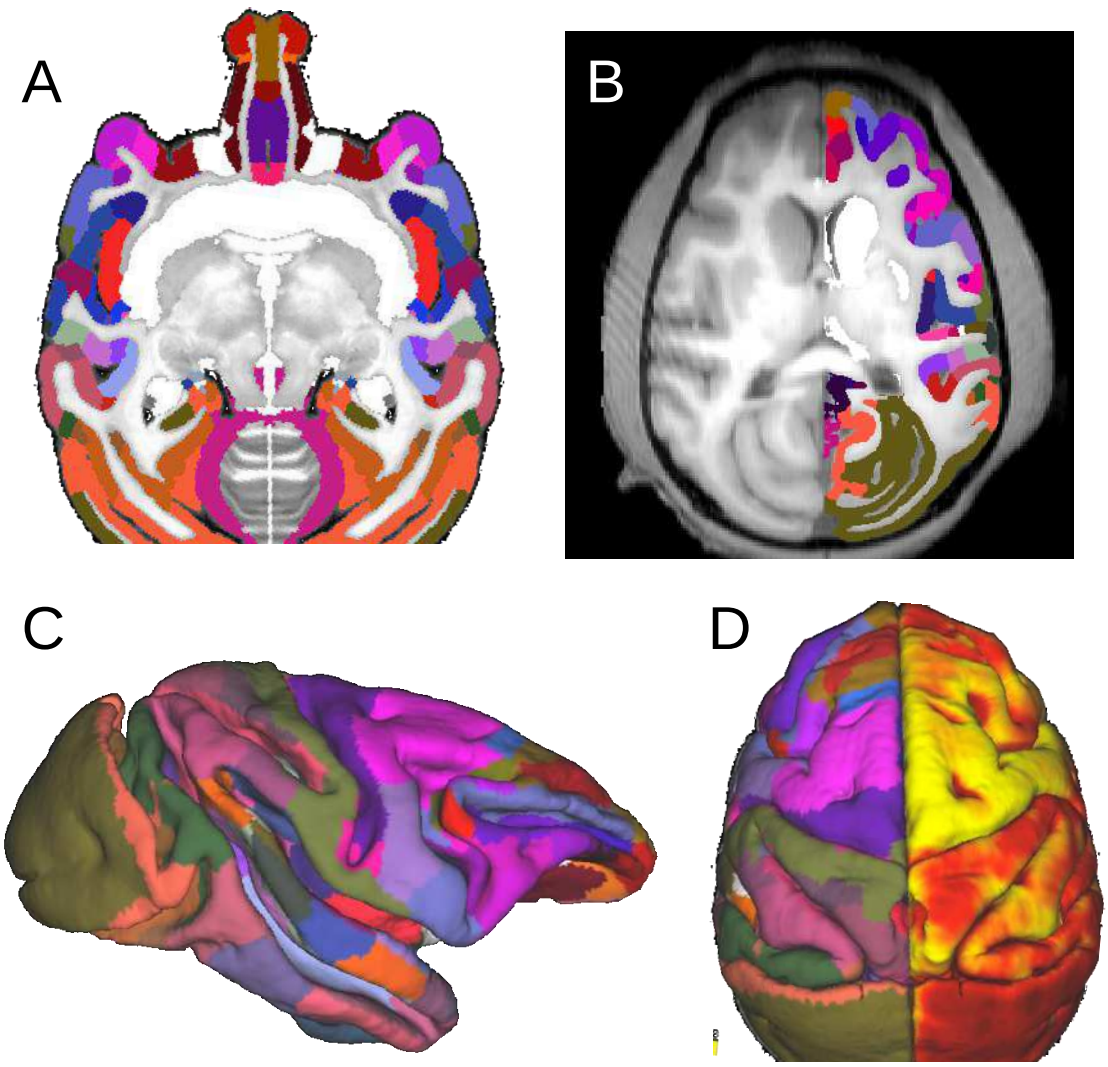

Figure 3.7: A the mirrored surrogate and labels. B the labels accurately fit the original publication. C midthickness surface. D Pial surfaces, labels and thickness.

3.3 Mapping The Digital Atlas Onto Other Brains

The second component of the macaque digital 3D brain atlas toolkit uses the GPU based non-linear registration system as part of a processing pipeline that accurately, efficiently, rapidly and very simply maps the 3D atlas onto the MRI anatomical volumes of other individual monkey subjects. The system takes a T1 weighted scan and performs the following steps, each of which used the Ezys software, Python, Matlab and shell code together with functionality provided by specific command line binaries from the FSL group of programs and Freesurfer programs for tasks like intensity correction. Given the atlas, different programs may be substituted and applied. We did find the GPU accelerated Ezys nonlinear transformer yielded better results than other programs.

1. Automated non-linear brain extraction
2. calculation of rigid body transforms from the scan to the atlas stereotaxic space and the inverse
3. resampling to 250μm, intensity correction of the extracted brain
4. non-linearly registration of the atlas surrogate to the subject, saving the forward and inverse transforms
5. application of the transforms to the atlas labels
6. application of the transforms to the atlas white and pial surfaces

The output is

1. Labelled subject scans in atlas and original space
2. Extracted subject brains in atlas and original space
3. Subject surface representations in atlas and original space
4. Linear and non-linear transform information to and from atlas space
5. A high contrast, 250um "surrogate" of the animal in atlas and original space for display and assessment of the transform accuracy

Of particular note is the rapid, automated construction of standardized mesh surface representations at the white and pial surfaces which are often challenging to produce in macaque using standard software. Automated, accurate brain extraction is also of

considerable benefit. The pipeline is not species specific, given an appropriate atlas for a species. The labelling is high resolution. We next assess its accuracy by comparison to tissue from labelled animals, and then its consistency by comparing multiple scans of the same animals.

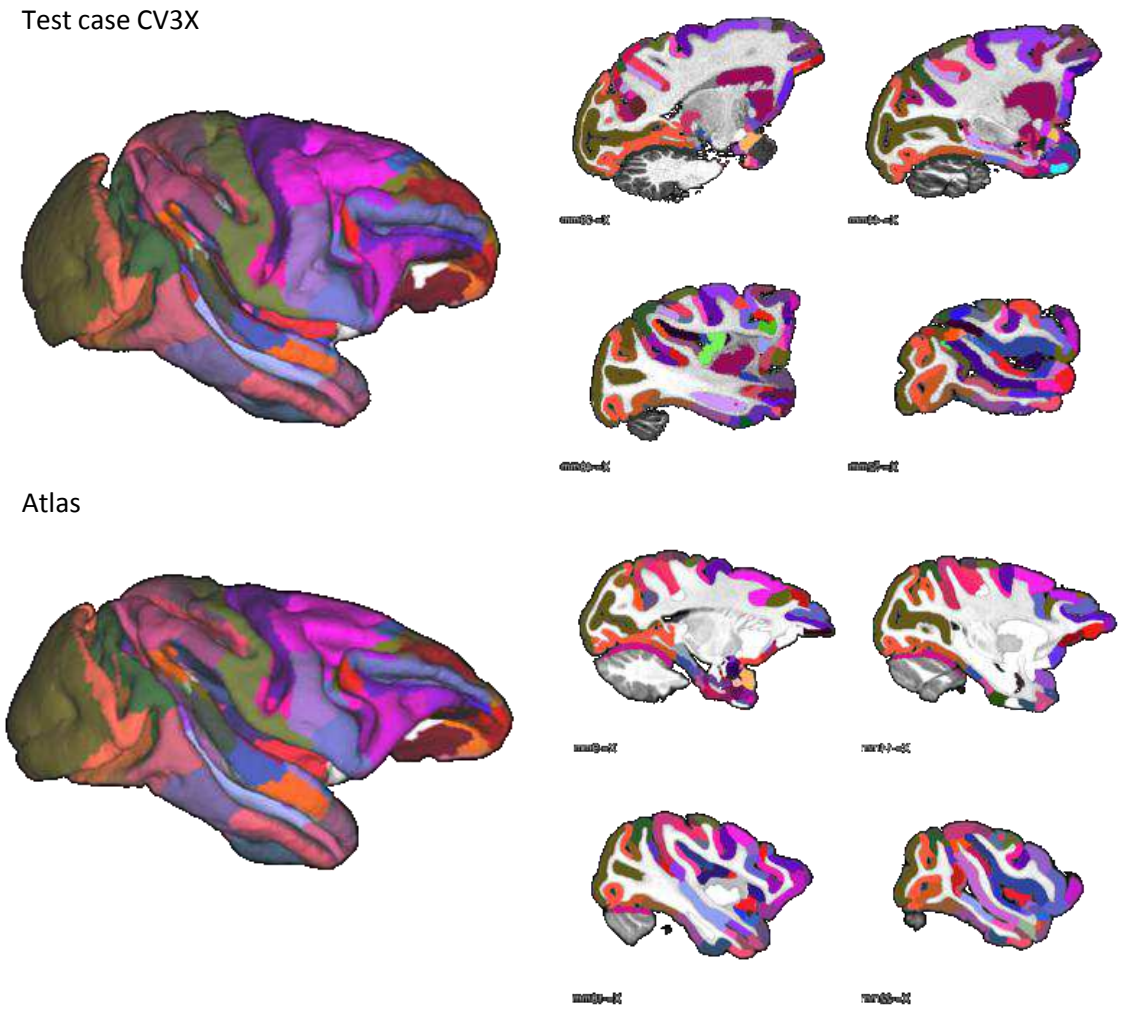

Figure 3.8: BOTTOM An atlas surface and 4 saggital slices. TOP the atlas data transformed to a subject, presented in it's own spatial frame

3.3.1 Validation of digital labelling against histological sections

For validation against histology, two subjects "T" and "DB58" used in previous studies were scanned and compared to myelin and to nissl histology. Details of all subjects used in this section are shown in table 2.1. Subject "T" ("trinity") was previously used in lesioning studies not reported in this thesis. It was scanned in-vivo at 500um isotropic. The brain had undergone a number of surgeries and electrode placements. Nevertheless,

the automated pipeline was able to extract the brain and label it. Figure 3.9 shows a slice of the original scan (A), the "surrogate" from the pipeline (note the "repair" of the lesioned tissue) B, the surface outlines (C) and full labels (D). The second subject was "DB58" an ex-vivo subject used in subsequent chapters on diffusion imaging, and for the creation of the surrogate D99 brain above.

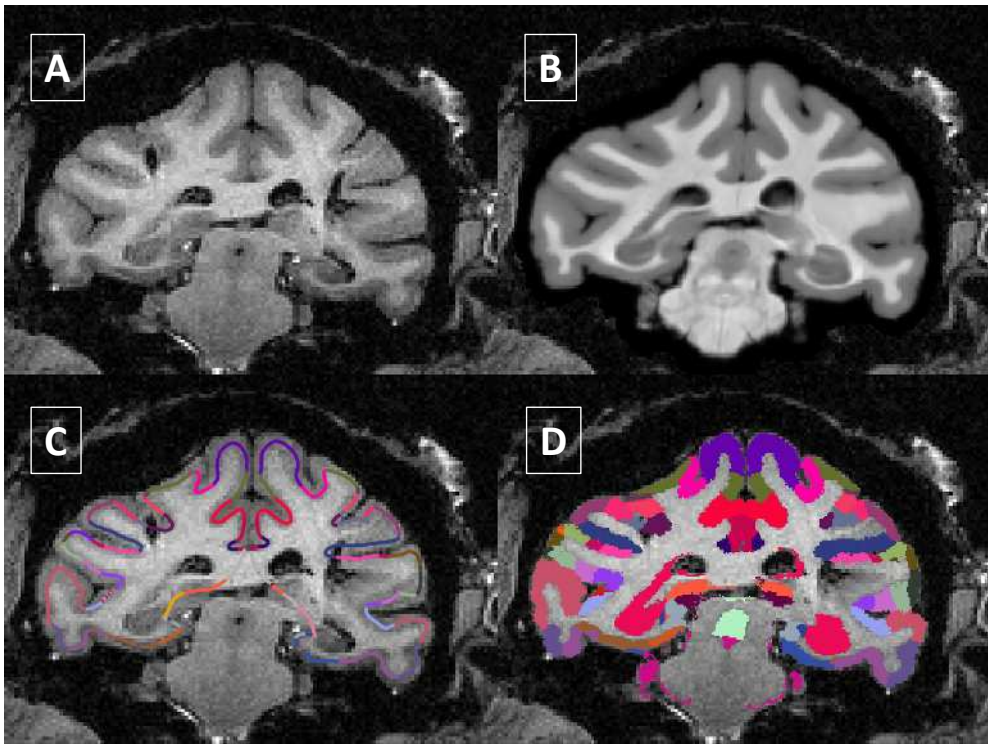

Figure 3.9: A Original T1 slice (note lesions, exaggerated by 500um, B 250um Surrogate of subject T, note lesions filled and higher contrast and definitions , C Surface outlines of the anatomical regions on the T1 slices, D 250um atlas label voxels

The accurate labelling of a lesioned scan is of great utility, in surgical planning and assessment. the generation of surface representations of a lesioned brain is something not typically possible since surface software requires an unbroken cortical sheet. Since we deform rather than generate surfaces de-novo we are able to produce accurate surfaces of the lesioned brain. Figure 3.10 top shows the right white matter surface. The ablation of V1 is visible, as are the influence of electrode tracks on the lateral bank of the IPS. The bottom shows the left midthickness surface. The pronounced deformation of the post-central gyrus is visible, and nearby electrode influence. While the surface representations are not reliable for electrode localization due to the 2 dimensional nature of surface representations they are nonetheless useful guides in tandem with the 3D MRI. Figure 3.11 A shows a region of nissl histology from subject T, and the atlas labels C, yellow box in B. The slice in figure 3.11 B has been carefully matched to the Nissl slice in the top right of 3.11

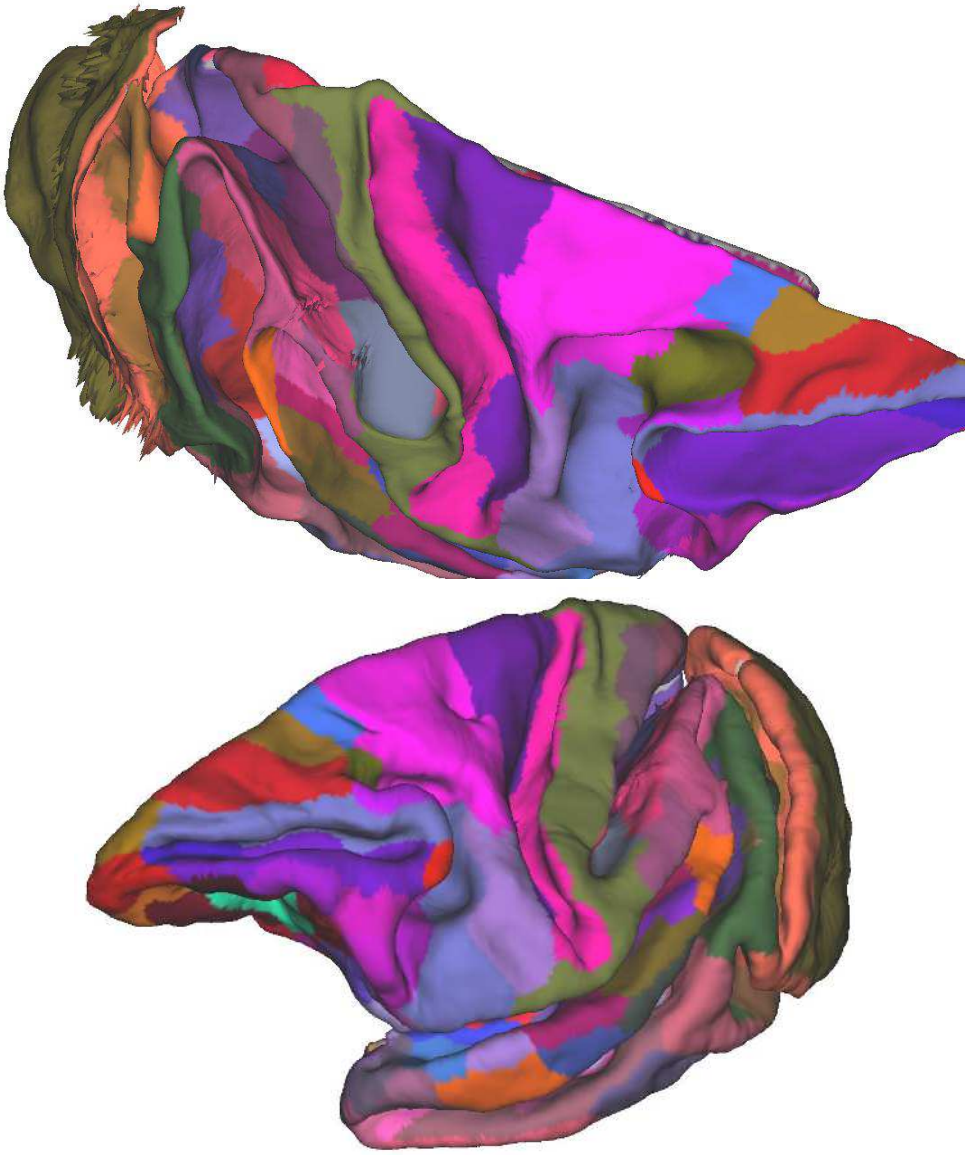

Figure 3.10: Trinity surfaces from lesioned scan, showing ablations, electrode tracks, labels

A. Comparing A and C shows surprisingly good agreement in regions where low res Nissl is a good indicator (see caption).

Subject DB58 was scanned ex-vivo for MTR and later for high resolution Gallyas myelin histology. Figure 3.12 shows fine grained, spatially accurate labelling confirmed by myeloarchitecural properties and transitions.

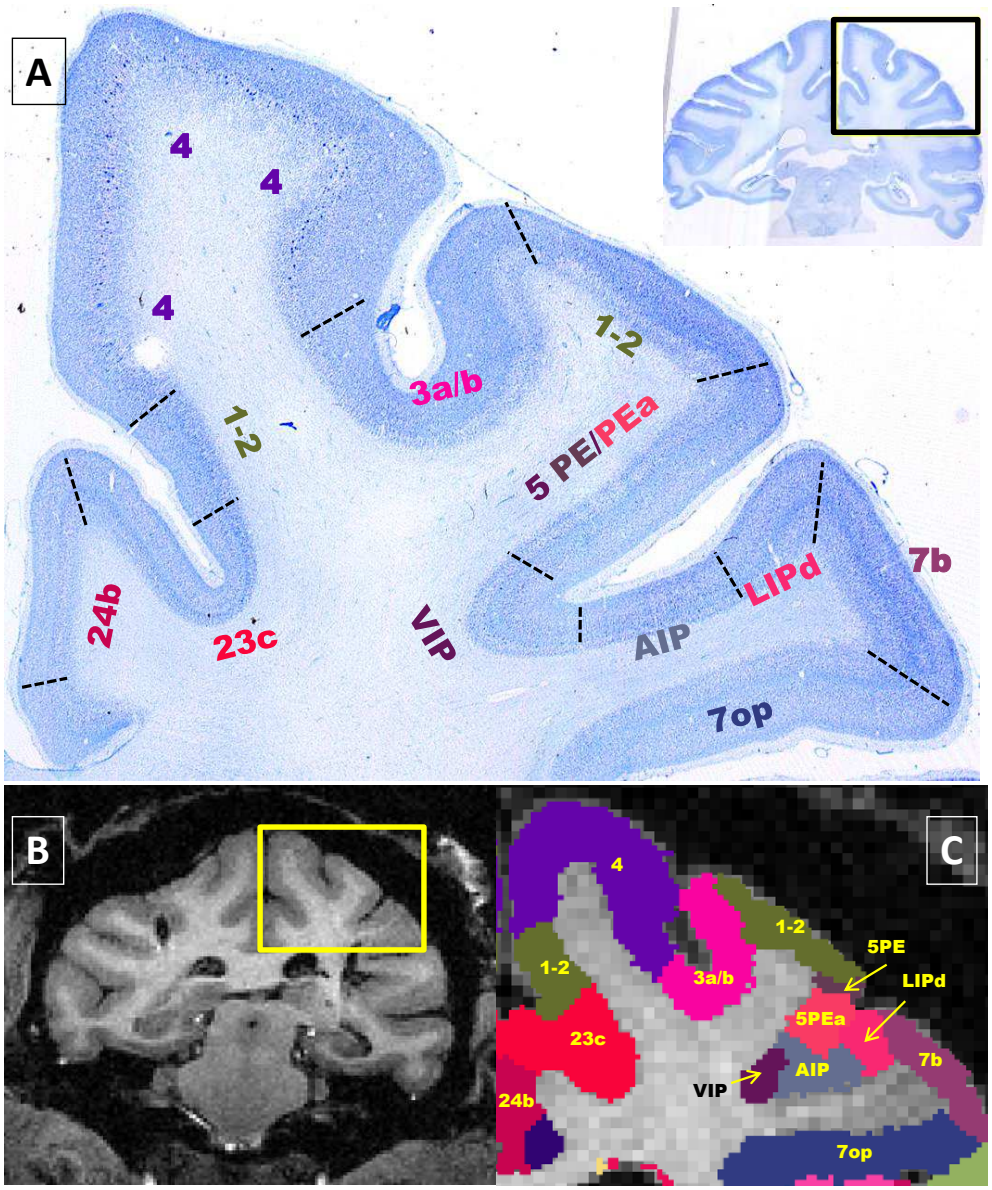

Figure 3.11: Histology to labelling comparison. The histology images are low resolution. Nevertheless regions are recognizable by their transitions and in some cases cytoarchitecture.

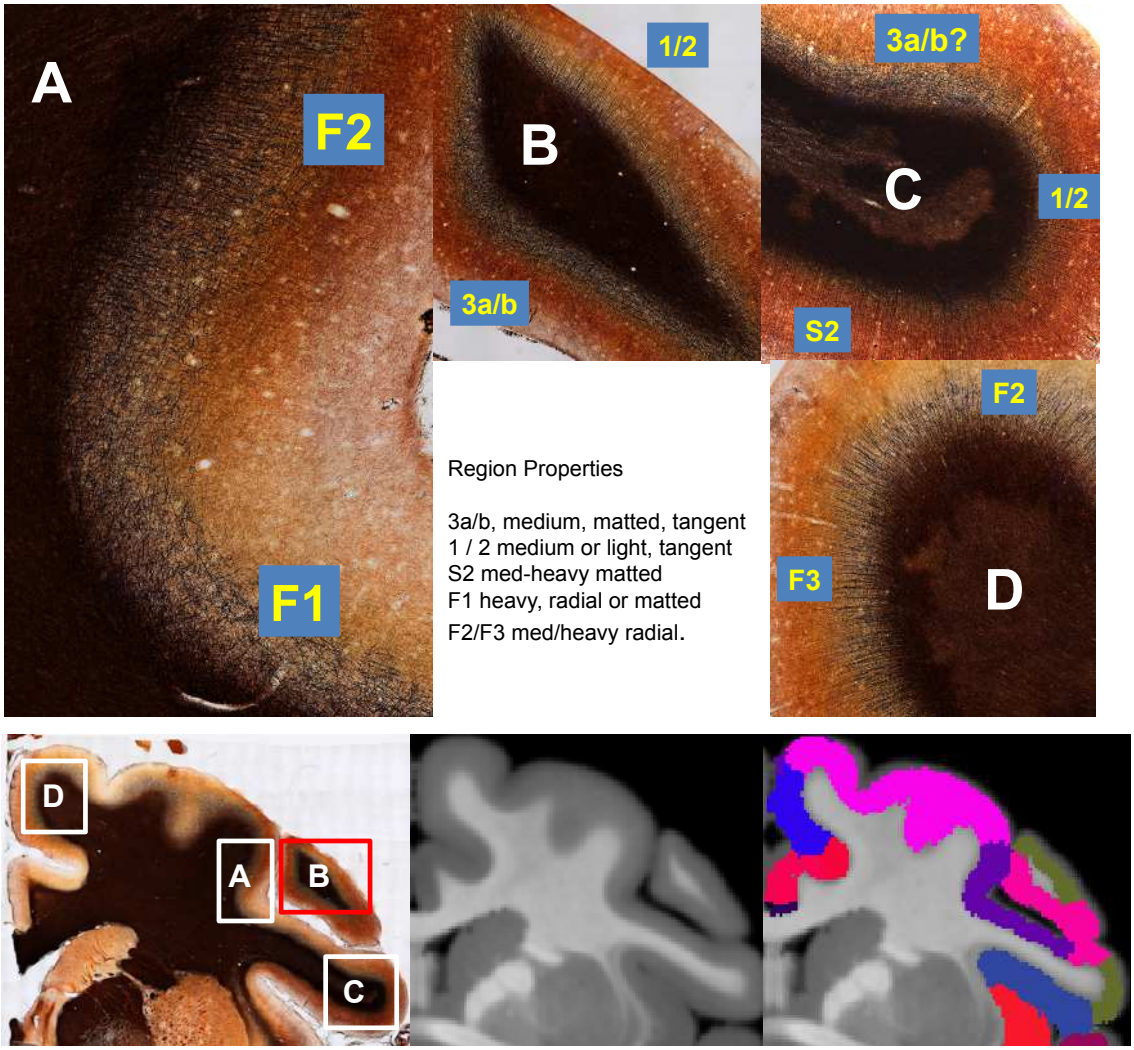

Figure 3.12: Regional myelin properties in the center of the figure are from (Lewis and Van Essen, 2000b), region 1/2 is lightly to medium myelinated with radial fibres. This can be seen in C, B. B shows detailed labelling accuracy , almost precisely delineating 3a/b and 1/2 in a tiny area. The bottom row shows the histology region from which A-C are zoomed. The center shows the MRI and the bottom right shows the labelling and its accuracy

3.3.2 Consistency in the mapping software

MRI scans vary in noise, spatial resolution, bias field and artifact. In transforming the atlas to a subject scan, the question arises "are we labelling the brain, or the scan". how robust is the system to measurement noise and different properties of scans? To address this two subjects were scanned multiple times on different days with different voxel sizes. We used scans of two in-vivo naive animals not used elsewhere in this thesis to invistagte these questions. Five scans of animal A ("POSH"), 4 at 500um 1 at 330um were obtained. Four scans of animal B ("PUFFIN") 3 at 500um and 1 at 370um were obtained (see table 2.1). Each of those scans was labelled using the atlas and mapping software. The result of mapping the atlas should be the same within each animal and across each animal i.e. where there is variation between the anatomy of the animals, it should be the same in comparing the mapping result of any scan.

To compare scan results, we used the surface representations generated by the atlas mapping pipeline. Each surface has the same mesh of about 16000 coordinates. if the pipeline is effective, the nodes should all have the same spatial coordinates at a given index for a given animal. In assessing consistency we analyze the differences in these coordinates. Figure3.13 shows two input scans and two output surfaces per animal as an example. Assessment consisted of calculating the unsigned distance in mm for each coordinate point between each scan and each other scan within an animal. Five scans were obtained for animal A, so ten comparisons are made since absolute (unsigned) distances are pairwise symmetric. We then take the mean and variance of these distances, which is a vector of 16000 in each case. The same procedure is applied for scans of animal B (6 comparisons), and between each scan of A and each scan of B (10 comparisons). Figure 3.14 bins the vectors of mean distances between each coordinate and vectors of standard deviations between each coordinate. Both the mean distances and standard deviations are very low and peaked within animals. The distribution of distances between animals are higher and more distributed, however the standard deviation is low and peaked, indicating the differences are consistent.

Figure 3.15 shows where those the distances are in 3D atlas space (note the scale is larger comparing between A and B). B's slightly more distributed distances and standard deviation are localized to the ventral occipital pole. In general the distances are small within a subject, between 0 and 0.2mm, maximum of 0.5mm, and with very low std dev. The distances between scans (10 comparisons) show large distances (up to 2.5mm) in specific anatomical regions, the occipital cortex, and parts of frontal cortex. The standard

deviation is low, indicating that a comparison of any two scans yields a similar result. In principle two scans of the same brain should yield surface representations that are identical after applying the pipeline. Any differences are the result of scan variation or pipeline error. Since the mean and standard deviation are low within different scans of the same animals (fig 3.15 top two rows, fig 3.14 left two columns) we can conclude that the pipeline accurately transforms "the animal" rather than "the scan". The same figures show mean and standard deviation in pairwise comparisons between different scans of different animals. Specific regions are transformed in a consisent way between animals regardless of scan. In this way we have eliminated noise and shown it is "the thing scanned" that our pipline transforms, rather than the scan itself.

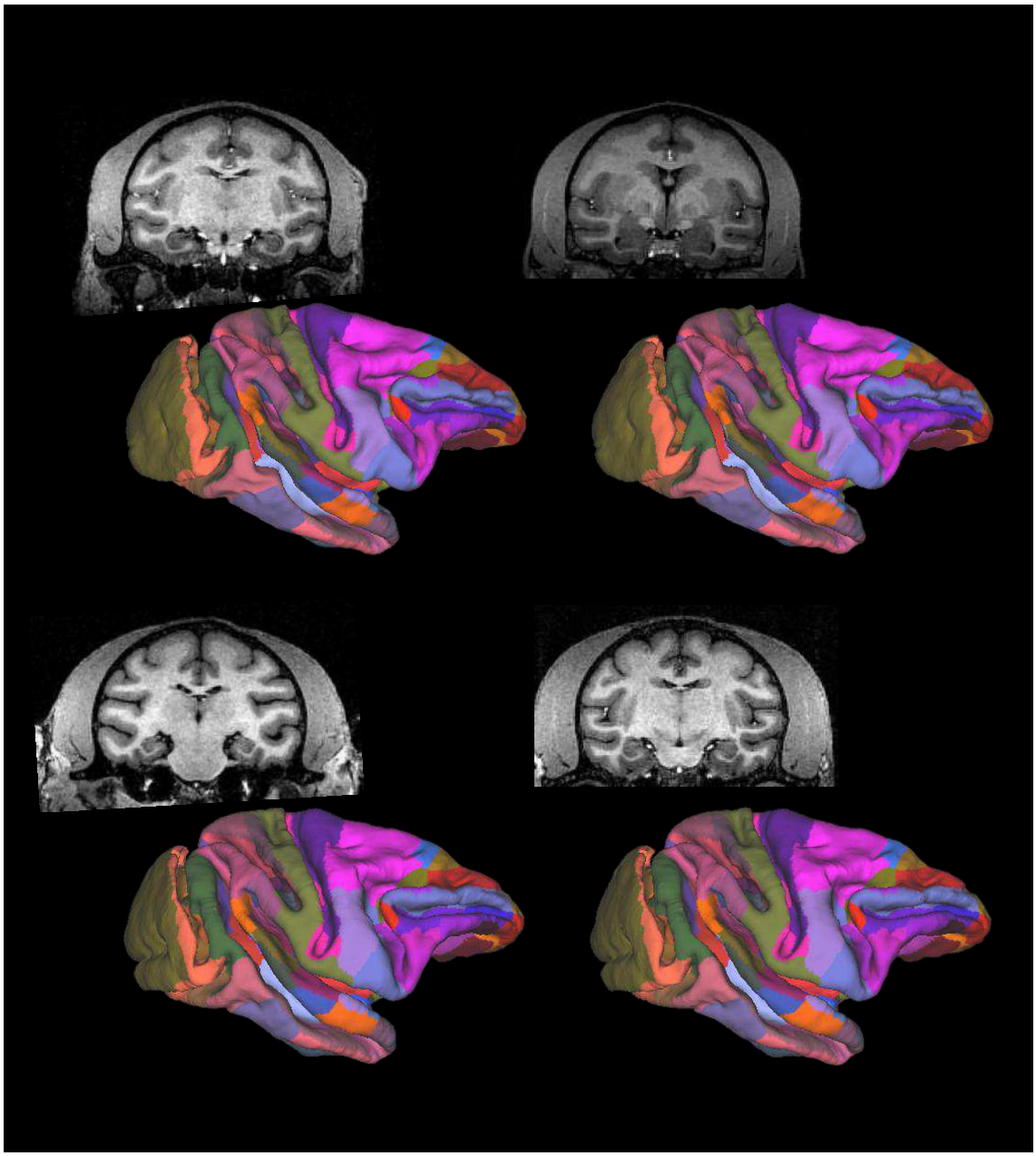

Figure 3.13: example of two scans of animal A and of B. surface coordinates are used to analyze their similarity by computing the distance between equivalent coordinate pairs

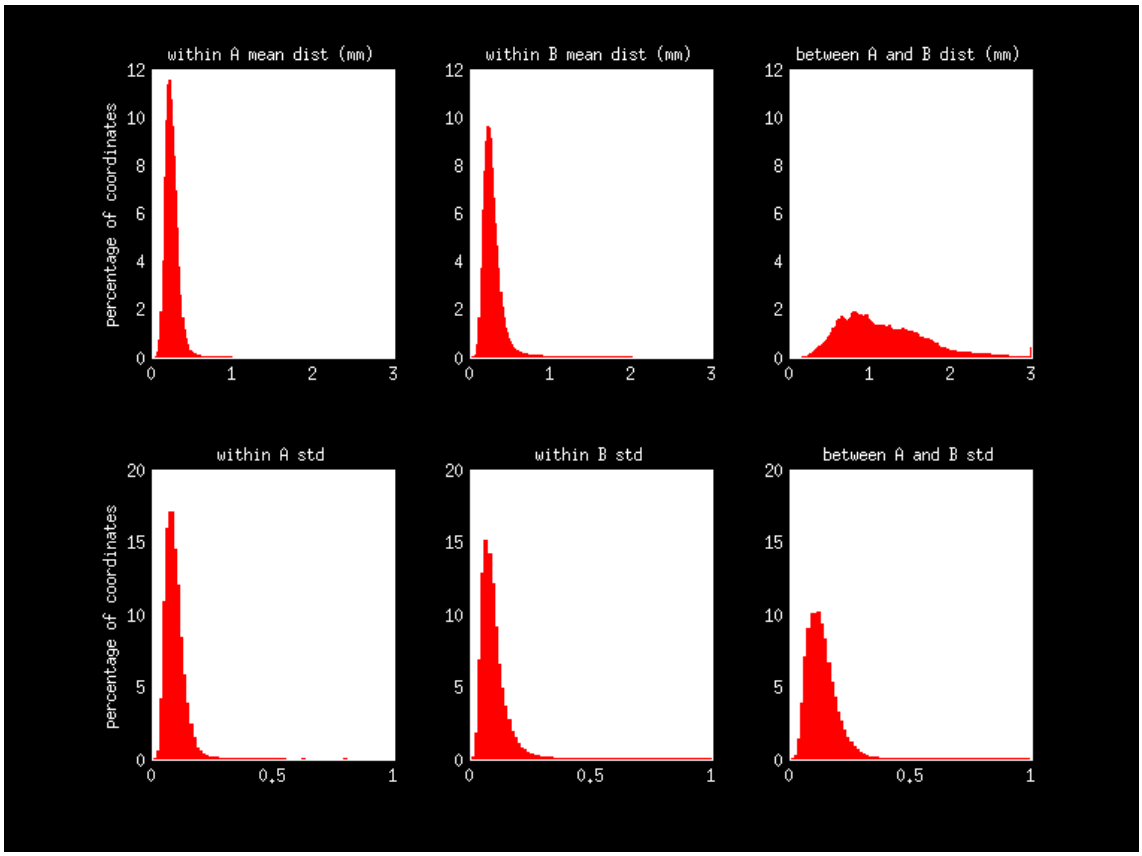

Figure 3.14: Top row shows the mean distance between each coordinate point in each scan of animal A (5 scans, 10 comparisons) of animal B (4 scans 6 comparisons) and between each scan of animal A and animal B (10 comparisons). The bottom row shows the standard deviation. Within Animal A the distances are lower than within B, but more coordinates have a high standard deviation. These are seen in the occipital pole in figure 3.15. The distances between scans of A and B are larger and more varied, but their standard deviation is low suggesting that scans within each animal are comparable, and differ to the other animal in the same way.

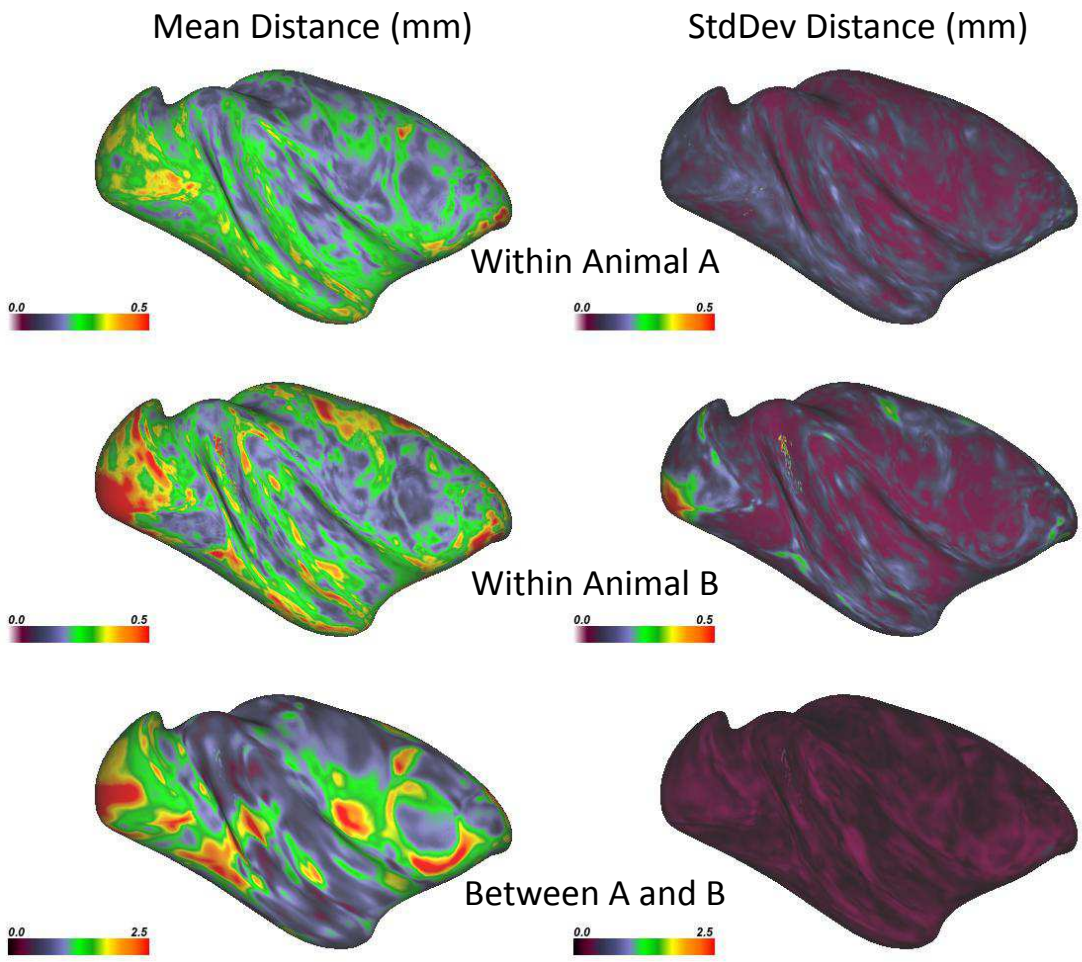

Figure 3.15: As figure 3.14 but showing the spatial distribution of distance variation. notice animal B variation is clustered around V1. the Scale of the distances between scans of A and B versus intra subject scans is much larger (see figure 3.14) Although there are many scans and two animals the statistics are presented on an inflated atlas surface in our mesh system for simpler comparison

3.3.3 Summary

We have presented the construction of a high resolution 3D cortical derived from histology aligned to MRI data from the same animal. Thus, the atlas truly conveys the underlying architecture of the cortex. We have demonstrated a method of non-linearly labelling scans of other animals. We showed that the histology of the labelled animals confirmed that the labelling was accurate, though further work is required in this area. We demonstrated that differing scan properties did not affect the system. It is robust to scan differences and accurately labels the brain itself. Further work on validating the system is in progress for preparation of a publication and software package.

Chapter 4

Tracer and dMRI Tractography Compared

Abstract

The properties of GM and WM seeded tractography in Rhesus and Marmoset are compared to results from tracer studies. The observed behaviors of tracking are hypothesised to have a general pattern in terms of false positives and false negatives. To explore this generalized pattern, tracking to and from the entire GM is analyzed in a series of scalar maps on the entire cortical surface. Each map is designed to tease out a scalar spatial property of the tracklines from each seed point, so that in sum they provide a good picture of tracking behaviors over the entire cortical sheet. These maps are discussed in comparison to other scalar metrics of cortical shape discussed in chapter 1. The chief result is that access to deep WM from GM seeds tends to be greater at outfolding regions, and limited at infolding regions. In the lisencehpalic marmoset access to the deep WM is limited over most of the cortex. A comparison to the explanation of "gyral bias" outlined in Chapter 1 is described. The variety of novel maps employed leads to an explantion of the observed tracking patterns in terms of superficial white matter. This explantion subserves the cortical properties of the "gyral bias" explation, and also accounts much more fully for the tracking behaviors over the cortex. This suggests that superficial white matter accounts for the pattern of false positives and negatives over the brain. Measures like cortical shape are proxy explations for gyral bias rather than primary explanations. Their ultility lies in partially prediciting

local fiber patterns and hence partially predicting tracking behaviors, rather than predicting tracking behaviors themselves. The structure of superficial white mattter accounts fully for false positives and negatives in tracking to and from the cortex. Finally, the role of dMRI spatial resolution is examined with respect to tracer comparisons, with the result that false positives and negatives are influenced by partial volume at low resolution effects over the superfical WM in a way that exaggerates false positives in tracking rather than ameliorates false negatives from the high resolution case.

4.1 Introduction

Cortical connectivity is typically assessed using invasive tracer methods. A tracer injection involves exposing the brain and injecting a compound into a location in the brain. The animal is then recovered from surgery. This tracer compound travels from the injection site either from synapse to cell body (retrograde) or from cell body to synapse (anterograde). Retrograde tracers label the afferent soma providing information about the regions afferent to the injection site.

In the macaque tracer studies have revealed no bias in connectivity related to folding (Van Essen et al., 2013; Markov et al., 2014). Inputs and outputs are distributed over the cortical sheet, in the banks of sulci, fundi and gyri. Axons may follow a very complex path e.g. projecting from a bank, turning sharply, entering a fasiculus, exiting sharply and terminating on a distant fundus.

diffusion tractography is bidirectional (does not distinguish afferent and efferent). More seriously, tracking algorithms use only local anisotropy information, and even where local information exists that relates to the presence of sharp turns, tracking always favours the straightest path. There is insufficient local information to trace the length of a fiber that takes sharp turns. Tractography methods are described in section 2.2.3.

In both human and macaque experiments seeding the white matter globally to assess cortical penetration have found that tractography terminates overwhelmingly on gyral crowns (Van Essen et al., 2013).

As discussed in chapter 1 (Van Essen et al., 2013) gives 3 main reasons why this might be

so in dMRI

1. reconstructed local fiber orientations on walls and fundi are tangent to the cortical column. We examine this in the following chapter, but also here in figure 4.10 E,F and in the marmoset in figure 4.13 D

2. as mentioned, the assumption that tracking follows the path involving the least angular deviation (straightest line)

3. the "wedging" effect of cortical folding. in fundi, the radial axis of the cortex from pia to WGB radiates inward, while at crowns outward. For each region of the WGB the cortical volume is much larger at gyri than sulci.

In this chapter we initially attempt in section 4.2 to validate the capacity of tractography to accurately determine cortico-cortical connectivity via comparison to the "gold standard" of neurotracer data (Lewis and Van Essen, 2000a; Schmahmann and Pandya, 2006), seeding primarily in GM but also WM and subcortical structures, and examining GM terminations and WM trajectories. Comparison to published tracer experiments used surface registration to map tracer injection results to the diffusion animal, and comparisons with photomicorgrpahs and atlas data.

After examining specific tracer comparisons, we further examine cortico-cortical connectivity estimates in section **??** with dMRI and tracking behavior by generating surface based scalar measures over the entire cortical hemisphere which represent aspects of global patterns of cortical connectivity and tracking behaviors with special attention to sulci, gyri and cortical folding. Using a novel method we assess tracking from the gray matter into the white (rather than the other way around) and connectivity from all GM loci to all other loci. Section 4.4 analyses these same surface based methods in the lisencephalic marmoset brain.

Finally, section 4.5 examines the effect of the spatial resolution on GM terminations

4.2 Tractography Compared to Tracer Results

In this section we compare tracking behavior to tracer data from 3 studies via 3 methods, each of which assesses qualitatively a different aspect of tracking behavior with respect to tracer behaviors.

- In section 4.2.1 we use tractography to segment (Behrens et al., 2003a) the corpus callosum by cortical target, and compare this to aggregate tracer derived results from (Schmahmann and Pandya, 2006)

- In section 4.2.2 we seed 1000 tracklines from an estimate of a single autoradiographic tracer injection ((Schmahmann and Pandya, 2006) case 5/6) and compare the results in GM and WM via photomicorgrpahs from (pandya) aligned to the diffusion animal.

- in section 4.2.3 we compare 3 retrograde tracer injection GM labellings and injection sites (Lewis and Van Essen, 2000a) to the equivalent dMRI tracking. The tracer data was mapped to the diffusion animal by SVD surface morphometry (see chapter 2)

- Finally, in section 4.2.4 we summarize and note that there are overlapping and stereotypical patterns in GM terminations regardless of seed origin and seed type.

4.2.1 Corpus Callosum Connectivity

Figure 4.2 shows the corpus callosum segmented via probabilistic tractography according to the number of terminations from each voxel in the CC to a midthickness surface divided into 7 subdivisions roughly as (Schmahmann and Pandya, 2006). the comparison to a large extent there is agreement with pandya but it is a large central structure such that the properties of the experiment are not unlike the segmentation of the thalamus (Behrens et al., 2003a), who's methods we follow here.

In (Behrens et al., 2003a), voxels of the thalamus were seeded with n tracklines and the number of these that intersected with masks of cortical areas was recorded, a long with the proprtion with respect to those which intersected at least one mask. The intent of FSL local modelling and probabilstic tractography is to produce a distribution of paths from a seed such that the most likely path can be inferred with respect to measurement and other noise. Each voxel thus contains data on the liklihood it intersects with each mask. The most likely path can be used to form a hard segmentation of the set of seed voxels.

Like the thalamus, the CC is located centrally in the brain and has clear properties. Commisural fibers radiate outwards from this central point, and intersect the target masks without following long intracortical fibres or needing to deviate from a complex rostro-caudal path with crossing properties We expect the primary (first fibre, DTI first EV)

direction to be followed for the most part through the field from seed to mask.

Since by definition the CC is represented by commisural fibres, and these are represented by the largely by the first fibre distribution, tracks from each voxel were initiated from the first fibre only, though they are free subsequently to follow the second fibre where appropriate. 2000 tracks were seeded from each voxel in the seed mask, and their intersections with each of the 7 cortical surface classification masks were recorded for each seed.

In the second panel of figure 4.2 the seed voxel set is colored by the mask color that received the largest number of intersections from each seed voxel. These results broadly match the segmentation in (Schmahmann and Pandya, 2006), however there are some differences. Notably, in there is a portion at the rostral end of the CC classified as predominately connecting to the superior temporal region. Likely this is due to a slight mistake in extending that mask too far dorsally into the insula. Connectivity to the occipital lobe is falsely represented at the rostral portion of the CC. Likely, this is due to these tracks following the optic radiation from the front of the brain. The results may be broadly compared to figure 4.1 tracer composite results.

Further panels of figure 4.2 show the results for each mask in more detail. The color bar ranges from 0 to 1, and represents the fraction of tracks hitting the specified mask, as a fraction of those hitting any mask. These are in quite close match to the data in (Schmahmann and Pandya, 2006), except for the over representation rostrally of the superior temporal region, and the over representation rostrally of occipital connectivity.

In general, these results are in good agreement with (Schmahmann and Pandya, 2006) though we note that methods differed in strategy, quite apart from the use of tracer rather than DWI methods. However, segmentation of a central structure such as the thalamus or CC by DTI tractography radially along the principle direction of anisotropy to another structure surrounding it is perhaps the simplest task we might assign to tracking.

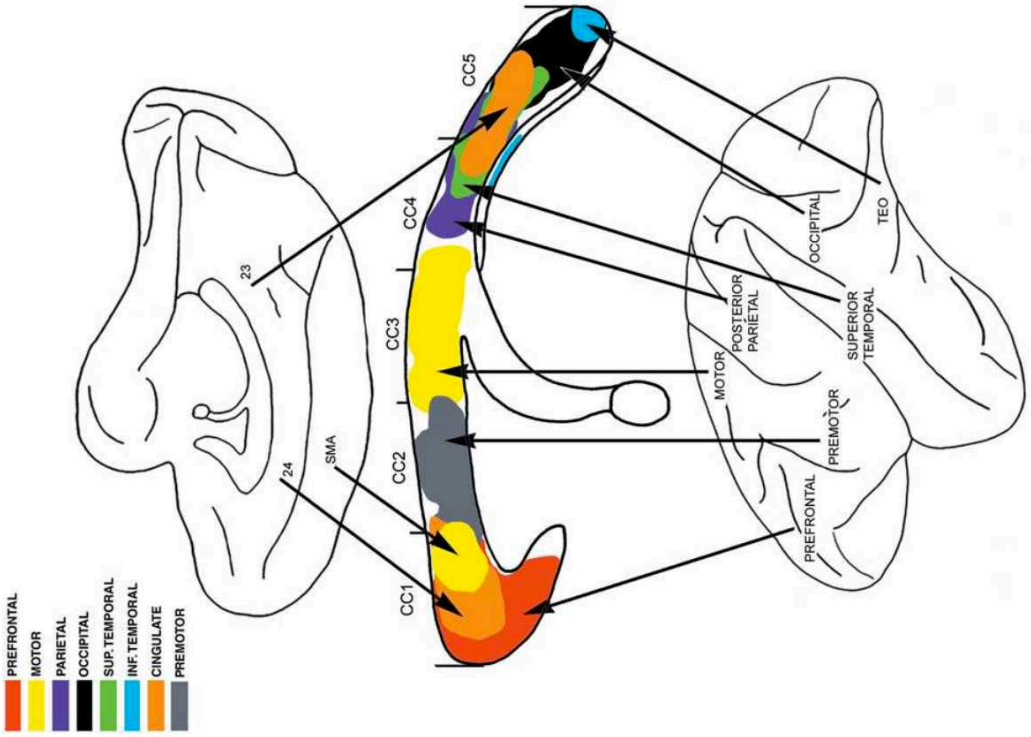

Figure 22-3
Composite summary diagram of the topography in the midsagittal plane of the corpus callosum of axons derived from the major lobar regions of the cerebral hemisphere of the rhesus monkey. The lateral view of the cerebral hemisphere (below) and the medial view (above) depict the region of origin of the fibers traversing the corpus callosum, color-coded according to the legend at top left. The designations CC1 through CC5 refer to the five rostral to caudal sectors of the corpus callosum described in the text. The detail of the topography within the callosum of fibers derived from the individual cases is represented in the preceding figures.

Figure 4.1: Composite tracer estimates of CC connectivity. Note we merge Premotor and Motor in Figure 4.2, and these tracer results contain overlapping regions laid on top of each other

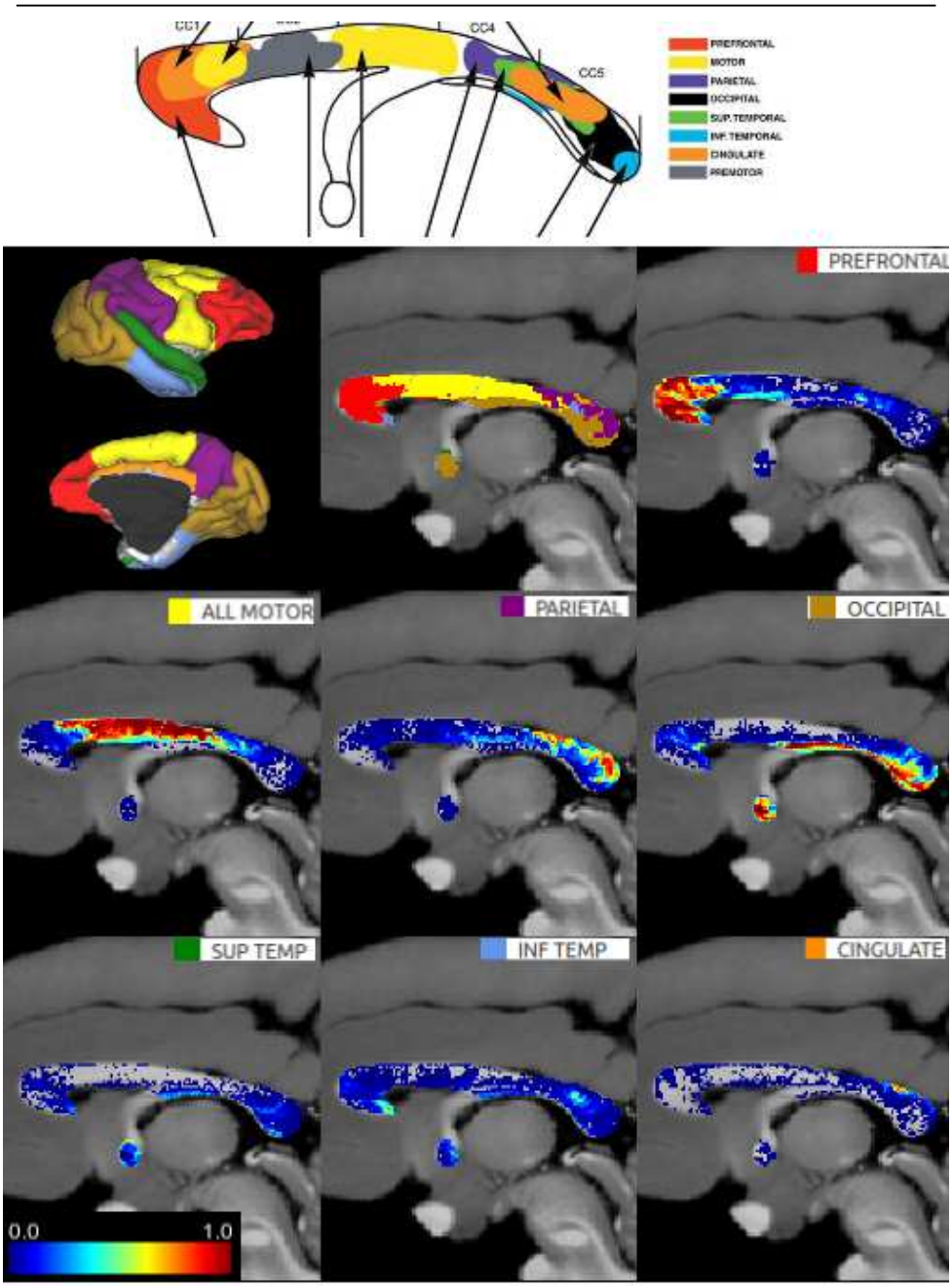

Figure 4.2: the inferior temporal label accidentally impinges on fronto-insular cortex, hence the labelling at the rostral end of the CC. the occipital label includes some inferior temporal. The most noticeable discrepancy is the lack of connectivity to cingulate cortex compared to the tracer. Partly this may be the relatively small surface area labelled as cingulate. But also, callosal anisotropy tends strongly towards the medial and dorsal aspects of motor cortex, (can show DTI trackvis)

4.2.2 Autoradiographic WM Tracer Comparison

Figure 4.3 shows Pandya case 5/6 in 7b/7op comparison of WM trajectory and GM terms to pandya case 5 brain. There is good agreement in the trajectory of tracks in the WM, however many GM terminations are absent (terminations shown on surfaces in figure 4.3 E). Gyral terminations appear favoured while sulcal or wall terminations tend to yield false negatives as may be expected from the gyral bias points 1-2 in section 4.1 above

Figure 4.3 shows a rough comparison of 250um FSL tractography to the results from an anterograde autoradiographic (Cowan et al., 1972) tracer injection in a different animal ((Schmahmann and Pandya, 2006) case 5). (Figure 4.16 further explores this approach with respect to spatial resolution). The tractography results were plotted as surface intersections (Fig 4.3 E) and presented additionally as coronal MRI sections (A-D).

The comparison shown in Figure 4.3 is qualitative in that it is from a different brain, and no attempt has been made to thoroughly register the data.

It will be seen that high resolution 'simulation' of tracer results shows good agreement in white matter. However it is critical to note that it almost exclusively captures gray matter terminations only at cortical outfolds. Fig 4.3 A-D show FSL tractography from a gray matter seed Group (Black patch in E) in the crown and dorsal and ventral banks of the inferior parietal lobule at 250um, compared (F) to the roughly equivalent anterograde autoradiographic results from Pandya (Case 5) Our seed region covered more area than just case 5: the region in Case 6 was also included on the ventral bank of the rostral IPL. A further difference is that diffusion results will be expected to show tracks that are both afferent and efferent to the seed region, while the tracer method was anterograde. Despite this, and despite the differing cut planes of the tracer sections and MRI data, there is a striking congruence between the autoradiographic axon labelling and the FSL tracking results, especially within the white matter. However gray matter terminations, especially far from the seed/injection tended to occur only at cortical outfolds. The figure shows gray matter terminations in outfolds of insula and the fronto-parietal operculum. Many clear termination patterns in the tracer results are absent on the walls of sulci, on the operculum's ventral bank and within fundi.

Intuitively the the reason for this may be the strategy used by (Behrens et al., 2007)

and more generally in tractography discussed in point 2 in section 4.1 above, chapter 1 and Chapter 2. It follows the straightest line possible given local information, so that sharp turns are seen as undesirable. Our high res data has favourable modelling properties (low artifact, high SNR) so that dispersion is low and sharp turns are statistically very unfavourable in practice within white matter. As discussed this tractography approach is anatomically sensible for fiber tracking bundles, but not for tracking between gray matter regions since those involve smaller number of axons which enter and leave the gray matter often at sharp angles, and enter and leave fibre bundles also at sharp angles. Axons entering or leaving the gray matter of cortical out folds are often (though not always see section 5.4.1) an exception to this.

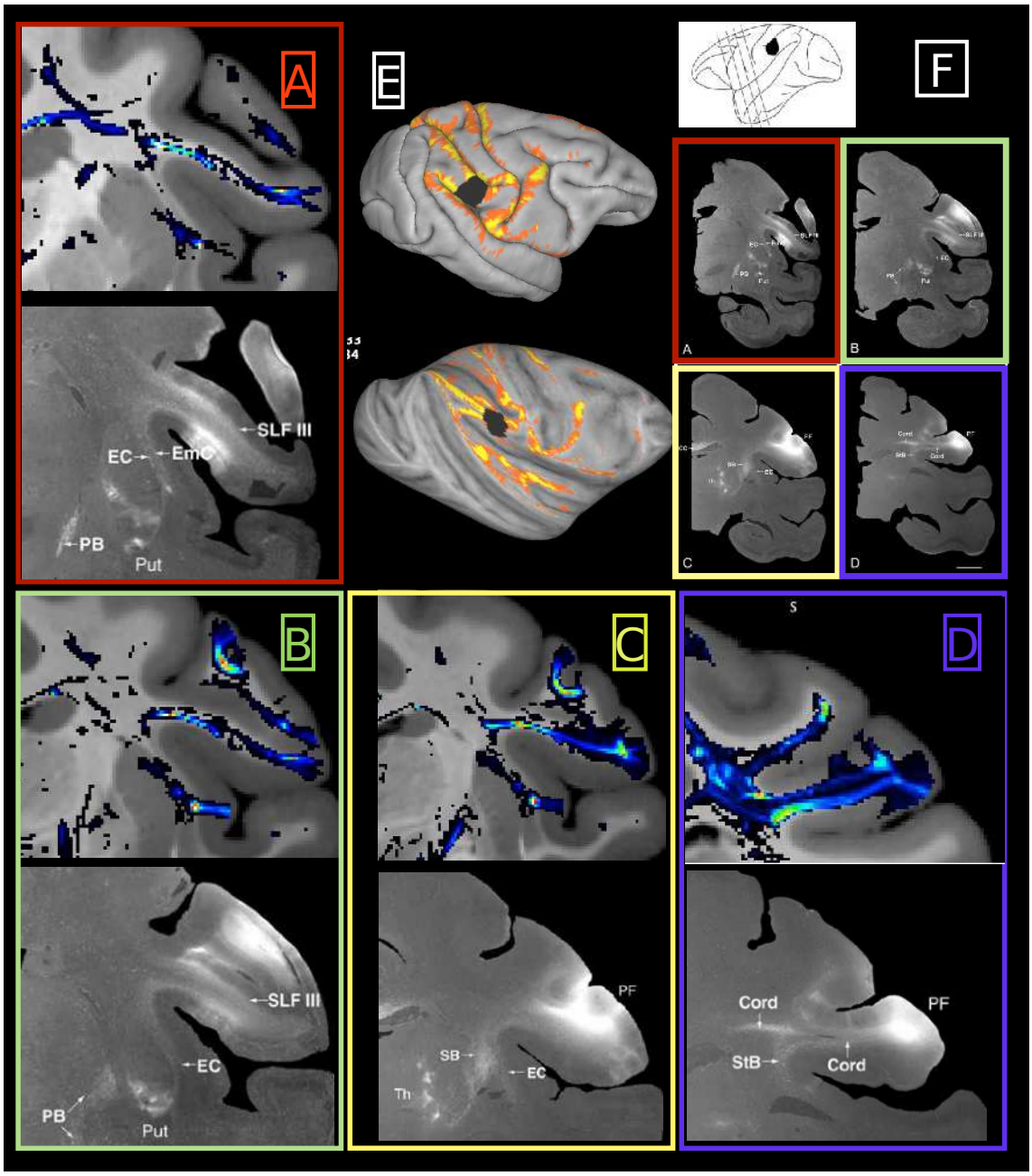

Figure 4.3: High Resolution "Simulation" of tracer shows good agreement in WM, but only captures GM terminations at cortical outfolds. A-D show FSL tractography From a GM seed group (Black patch in E) in the crown and dorsal and ventral banks of the IPL at 250um, compared (F) to very roughly equivalent anterograde autoradiographic results from (Schmahmann and Pandya, 2006) (Case 5) Labelling runs anti-clockwise from A

4.2.3 Cortical Tracer Labelling Comparisons

Tracer studies are principally interested in connectivity between GM regions (rather than paths through WM). Figure 4.4 compares tracking intersections to retrograde tracer labellings. Three retrograde injection sites and the resulting tracer labellings the study from (Lewis and Van Essen, 2000a) were registered by landmark constrained spherical surface deformation from the F99 surface atlas to our DTI Case A midthickness surface using the CARET program (version 5.65), so that both the injection sites and labellings were transfered from the atlas to our case as sets of surface nodes with metric values assigned. Surface registration is described in section 2.2.4. The positions of the sites and labelling contain an inherent inaccuracy from the registration process and from anatomical differences between the source and target animals but are qualitatively accurate. The nodes of the registered injection sites were used to select rows from the midthickness square connectivity matrix B (figure 4.6 B, section 4.3.1) i.e. to seed tractography and display the resulting track intersections from the exact locations of the registered tracer injections.

On the right side of figure 4.4 on each surface node, the sum of the intersections from tracks seeded within the blue seed patch is displayed, which is exactly equivalent to tracking from those node. In this way tracking from any set of nodes to the cortical surface can be performed with one dataset.

Figure 4.4 A shows retrograde tracer labelling from MSTdp, on the ventral bank of the STS near the tempero-parietal junction. Labelling can be seen through most of the STS, the length of the IPS and medial parietal and occipital lobe, the lunate sulcus as well as in pre-frontal cortex around the arcuate cortex and gyral dorsal premotor regions.

By contrast in figure 4.4 B, the “equivalent” tracking from the tracer injection region shows targeted intersections with the fundus of the STS, and gyral outfolds adjacent to the seed site. No intersections away from the tempero-parietal junction or STS are observed.

figure 4.4 C shows retrograde labelling from the crown of the IPL, in 7b. the IPL and rostral IPS are heavily labelled, as is much of premotor and prefrontal cortex. Sparser labelling is visible in the temporal lobe.

Figure 4.4 D shows long range tracking intersections, however they do not really agree with the tracer. Intersections are sparser, more targeted and almost exclusively on gyri. Many tracer labelled regions are not intersected. Those regions that are intersected are not always labelled by the tracer (however since the tracer is retrograde only this does not necessarily indicate a false positive, see anterograde results from the similarly located injection in figure 4.3)

Figure 4.4 E shows retrograde labelling from the fundus of the IPS (CaseB, VIPl in (Lewis and Van Essen, 2000a)) the temporal, parietal and occipital lobes are widely labelled, as is PFC. by contrast figure 4.4 F shows tracking intersections limited to a small region immediately around the injection site.

In summary the evidence from these 3 cases show a qualitative difference between the surface mapped tracer estimates and the tracking results. In none of the 3 cases can GM to GM intracortical tracking reasonably be said to have approximated the tracer labelling in extent. Tracking is dominated by false negatives, and appears delineated by folding patterns, with distal sulci avoided entirely, and long range intersections avoided.

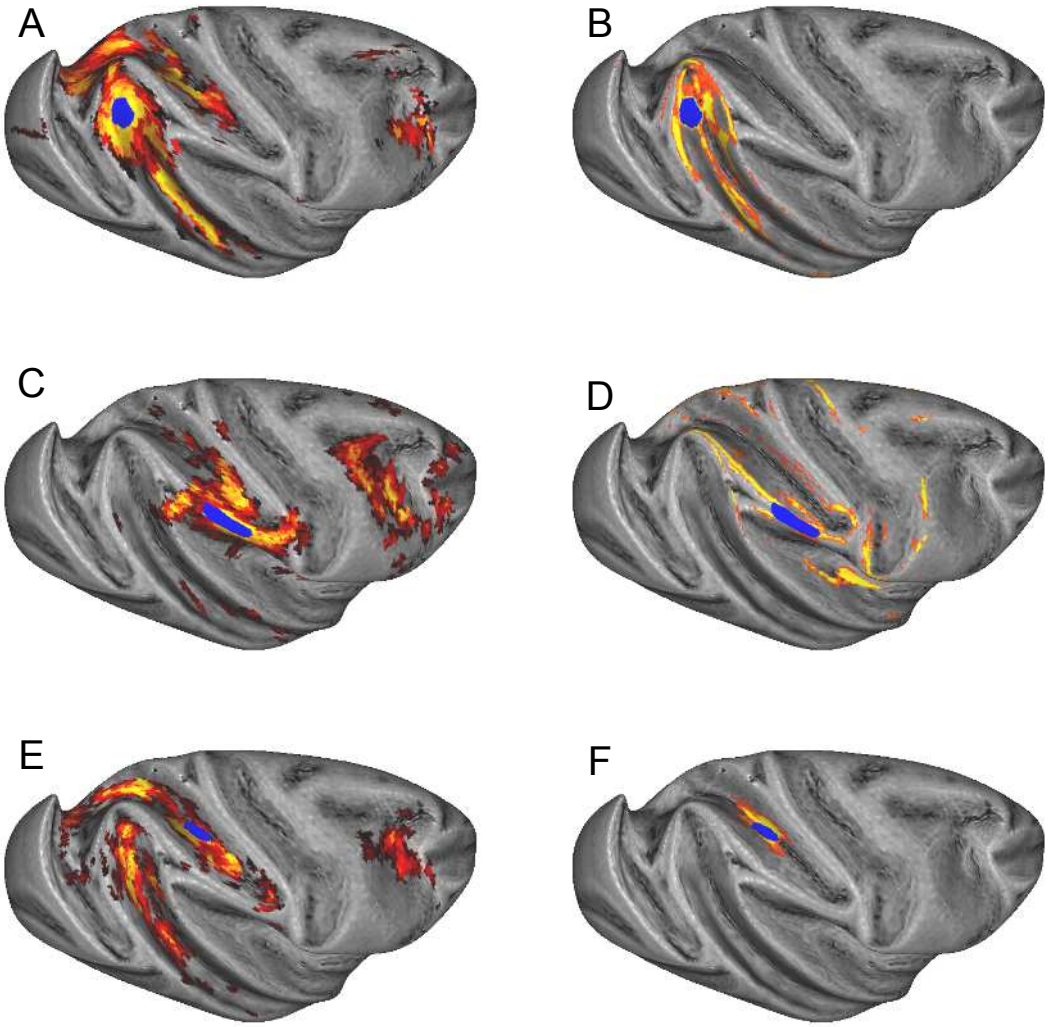

Figure 4.4: A,C,E represent retrograde tracer injections (Lewis and Van Essen, 2000a) (injection sites in blue) in MSTdp, 7B and VIP registered to the present case A by SVD from the F99 atlas using landmark constrained spherical surface registration in the CARET program (5.65) see section 2.2.4. B,D,F show the midthickness surface seeded tractography and GM penetration from those same sites. The MSTdp tracer results (A) show widespread labelling in the STS, fundus of the IPS and posterior parietal, in addition to FEF and inferior arcuate region. The tracking results are more much local to the seed. The 7b injection (C) labels the IPL, lateral IPS, some insula and heavily in the arcuate and prefrontal cortex. The tracking (D) avoids all sulci, following gyral ridges. The VIP injection (E) widely labels IPS, STS, arcuate, which the tracking is restricted purely to the seed site. B, D, F show GM intersections with a minimum threshold of 10 tracklines

4.2.4 GM Terminations are Similar for Diverse Seeding Strategies

A notable feature of all these experiments with tracking is the preponderance of gyral terminations. Figure 4.5 shows seeding from the corpus callosum to the GM (A) similar to the experiment in section 4.2.1, a large voxel set representing SLF3 fiber which runs within the lateral WM of the fronto-parietal operculum. This seed patch may extend somewhat into medial WM and the pathways from the extreme or even internal capsule but majoritively represent the SLF3 which was hard to track due to an idiosyncratic fold at the frontoparietal junction (B), and a GM seed patch in 7b, running along the radial vectors from Pial to WGB and representing the most anatomically accurate seed region, containing the least ambiguous WM starting point (since the WM subjacent to the GM has crossing fiber representations (C) similar to section 4.2.2. In each case, the terminations appear to overlap. This pattern appears correlated to the curvature shown in (D).

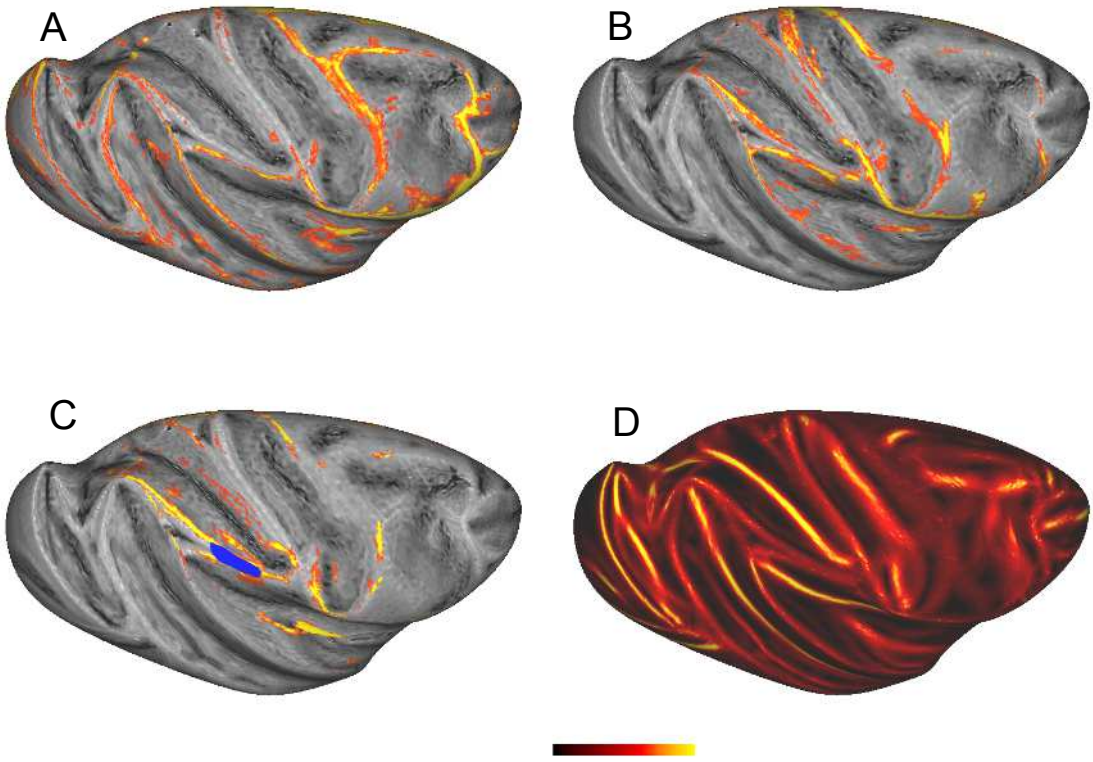

Figure 4.5: **A.** Seeds from Corpus callosum (see figure 4.2 and 5.7), **B.** from 20,000 voxels inside the white matter representing the SLF3 long fiber, **C.** from figure 4.4 D Case 5 all show similar termination patterns, despite the very different seeding. Terminations appear restricted to regions of low concavity **D.**. See figure 5.7. A, B, C show GM intersections with a minimum threshold of 10 tracklines

4.3 Global DTI Cortico-Cortical Connectivity and Cortical Shape

In section 4.2.4 we noted a similarity in termination patters regardless of seed site or type of seed (WM or GM). Regions of infolding were rarely terminated on, outfolding often were. This is consistent with observations on gyral bias in dMRI when seeded in white matter . To more fully explore this pattern, in the section we develop and apply measures of regional penetrability from and to the cortical gray matter in the Rhesus. The same measures are applied in the Marmoset in section 4.4.

4.3.1 Mapping Methods

Tracks seeded from each surface vertex of the midthickness GM (see section 2.2.4 for surface construction methods) can be used two form two kinds of matrix. Matrix type "A" has seed vertices as columns and every voxel within the tracking mask as rows. Each cell contains the number of times a voxel v was intersected by a track seeded from a surface vertex n. The resulting data can then be analyzed. Matrix type B has surface vertices as both rows and columns. The cells of this (transposable) matrix contains the number of times a surface vertex a was intersected by tracks seeded from a vertex b. This is illustrated in figure 4.6.

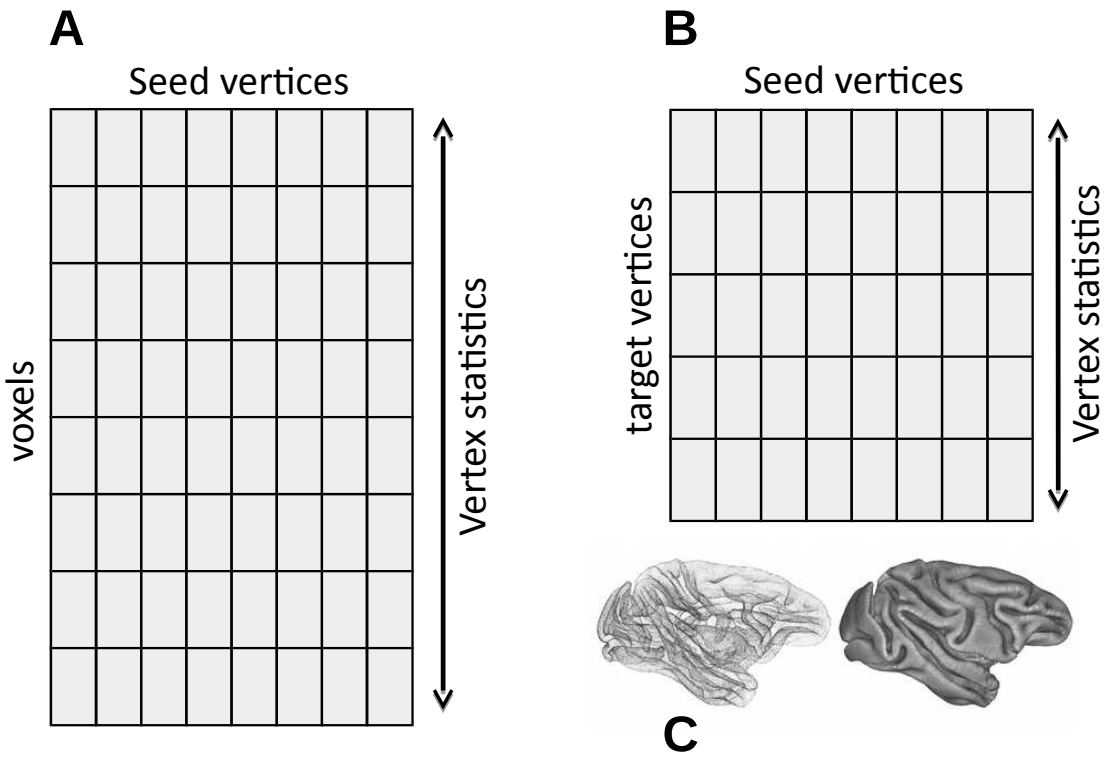

Figure 4.6: matrix methods for PVI, other maps

4.3.2 Grey Matter to Gray Matter Connectivity Maps

Figure 4.7 assesses cortico-cortical connectivity using the Matrix B method. 1000 lines were seeded from each midthickness node (excluding medial wall), and the number of intersections with every other node recorded. For each seed the number of track intersections with every point (including itself) is recorded in a square matrix (figure 4.6 B) whose columns are seeds and whose rows are targets, but can be transposed.

The left column of the figure contains summary data about afference (the pattern of intersections to a node from all others). The right column contains information about efference, that is the pattern of node intersections resulting from seeding at a point.

Figure 4.7 **A.** shows the total number of intersections each node **received from any source (afference)** (the sum of the rows). **A.** shows a high total number of intersection to gyral ridges. reducing to intersections from unique afferent seeds (binarising the matrix) enhances this pattern **C.** So that both the total number of intersections to gyral regions, and the number of unique sources is high, suggesting these regions are genuinely highly reachable from the rest of the cortex.

Figure 4.7 **B.** shows the total number of intersections tracks seeded from (efference) a node made **to any target node (including itself) (efference)**. **B.** Appears to show a high total number of trackline intersections when seeding from the fundus of the IPS and other sulci, as well as parts of the occipital pole (V1). However When this data is reduced to intersections to unique targets (**D.**) the apparent emphasis on efference from the fundus disappears, leaving higher values on gyral banks and ridges in the posterior part of the brain.

Dividing the number of unique sources by the total number of intersections (**E.**, **F.** yields a normalized measure of efferent and afferent cortico-cortical reachability that incorporates information about both the frequency of intersections and the extent of cortex from which nodes are reached or themselves can reach.

Afference is dominated by gyral ridges, with some afference to sulcal walls. Efference shows a similar pattern, with greater emphasis on sulcal walls.

None of these measures gives a complete picture. Summation yields no information about

the variety of source or target nodes. The sum of unique nodes yields no information about how likely an intersection is. The latter divided by the former gives information about both, but is normalized locally. The normalized measure viewed in the context of the binarised matrix yields a strong picture of GM to GM connectivity. **E.** and **F.** (always between 0 and 1) provide a direct way of comparing (rather than measuring) the overall ipsilateral cortico-cortical afference and efference of each node and over the brain. In both efferent and afferent cases, values on sulcal fundi are low. Gyral crowns tend to be more reachable and diverse walls, ridges and crowns in the posterior part of the brain tend to (have more efference)

Efference is dominated by the caudal part of the brain. Rather than reflecting the reachability of gyral frontal cortex, this likely reflects the strong anisotropy (and anatomical connectivity) of cord and commisural projections from motor cortices, which are not recorded in figure 4.7. This can be demonstrated using the methods in section 4.3.3.

Overall, GM to GM connectivity is dominated by gyri but not in a simple way. Gyral ridges tend to be favoured over gyral crowns. Some sulcal walls show both efference and afference.

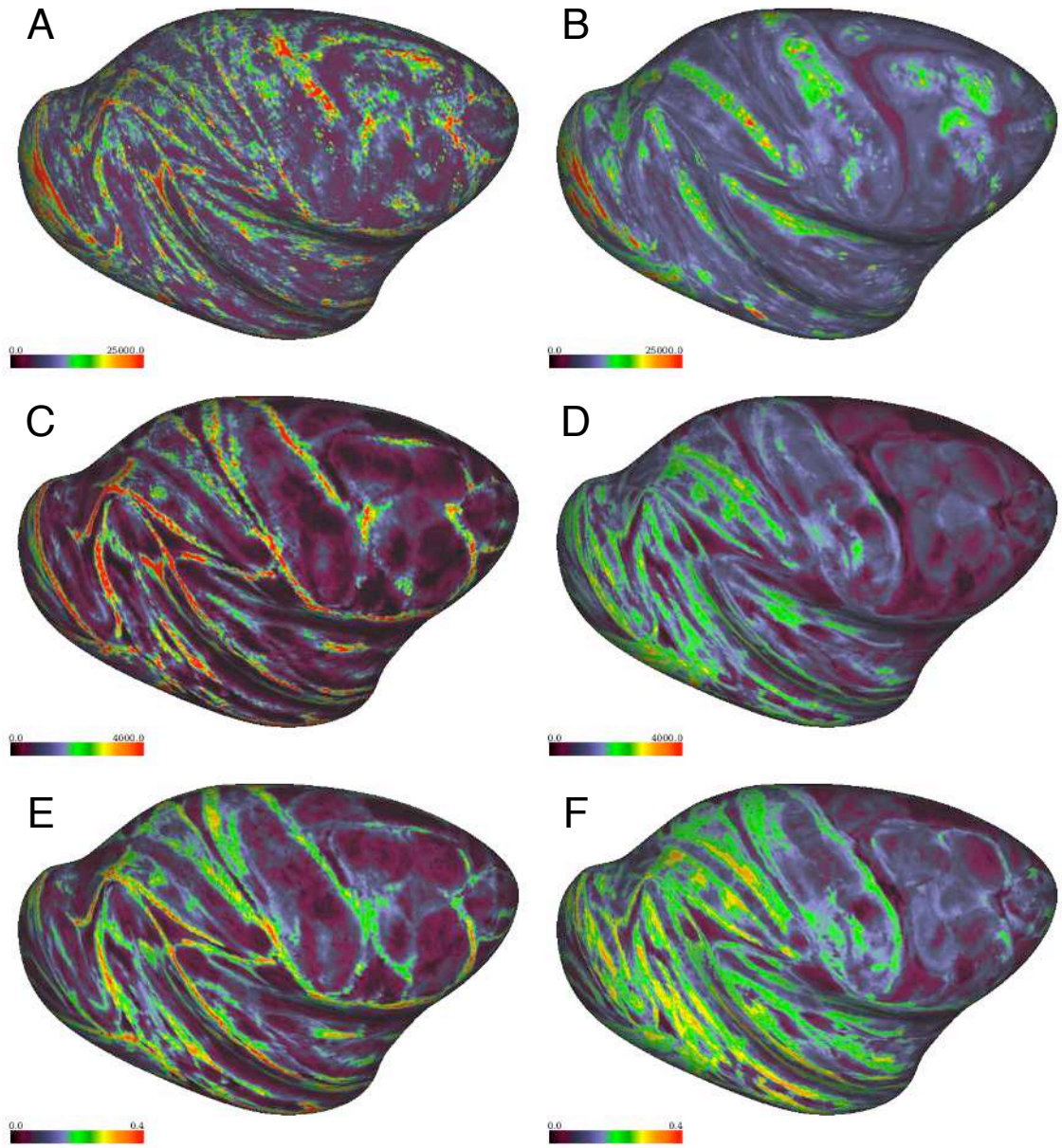

Figure 4.7: GM surface to surface seeding: Each point on the midthickness gray matter surface is seeded with 1000 lines. For each seed the number of track intersections with every point is recorded in a square matrix (figure 4.6 B) The left column shows afference (figure 4.6 B) , the right column efference (Transpose of the matrix figure 4.6 B) on very inflated surfaces. The top row (A,B) shows the total afferent or efferent trackline intersections (sum of columns). The middle row (C,D) shows the total afferent or efferent intersections from unique seed points (sum of binarised columns). The bottom row (E,F) shows unique intersections divided by total intersections. See text

4.3.3 Gray Matter to White Matter Maps

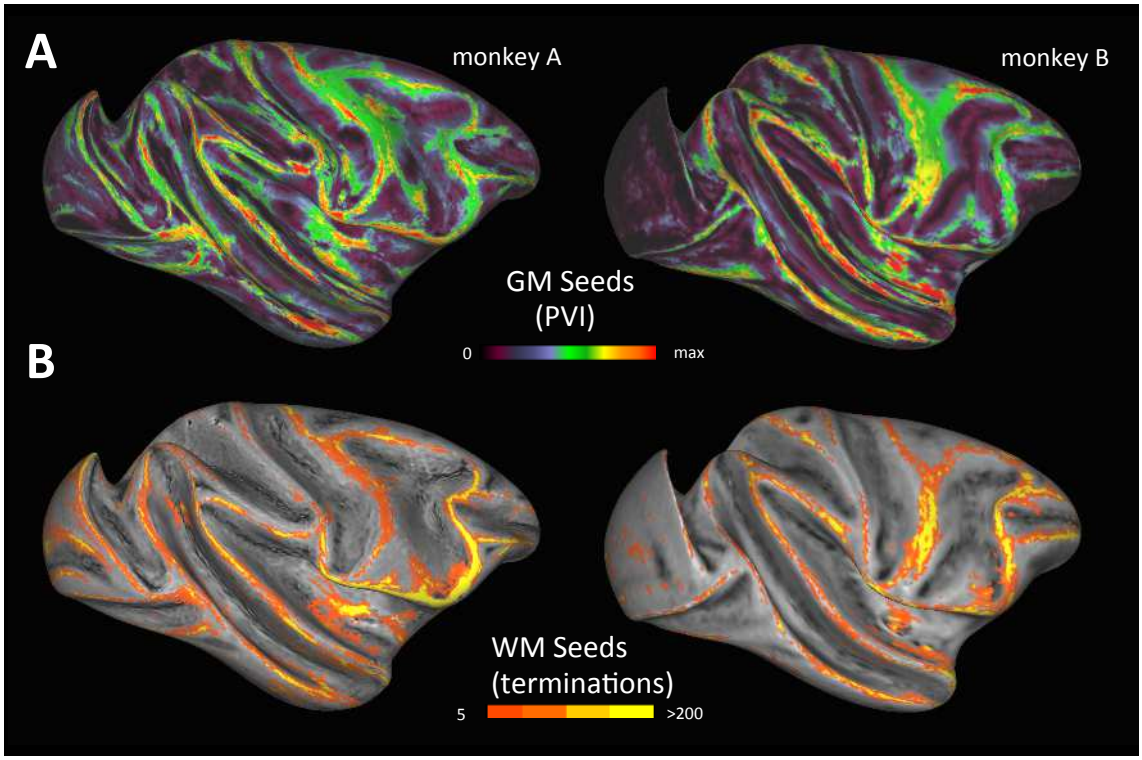

Figure 4.8: in and out the same. 2 animals. pvi. seeding as yellow in above figure. the termination values are qualitative, so they relate to PVI non-linearly. but sorting the nodes into ten interval by PVI value, we can take the mean termination and mean PVI in those intervals. more than 63% of termination occurs in nodes within the top 10% of PVI values. More than 79% of termination occurs in nodes within the top 20% of PVI nodes. remember we have bar graphs of that.

Figure 4.8 shows in both macaque samples a method of estimating how much of the brains cortical volume can be reached from a given point within the gray matter. Figure 4.6 A shows a schematic of a matrix of surface nodes by voxels "Matrix A". This was in practice implemented by a CIFTI 1 dense connectome file (see chap methods). Each entry in the matrix corresponds to the number of times a voxel is intersected by a given seed vertex. Using this dense connectome intersection matrix, we computed a quantity termed the **percent voxel intersection (PVI)**. For a given seed point the PVI is defined as

NV =The number of voxels

NT =The number of tracks sent per vertex

x_iThe number of intersections in voxel i

$$PVI = \frac{\sum_{i}^{NV} x_i}{NV \times NT} \tag{4.1}$$

The PVI is expected to statistically converge as NT is increased (and dispersion in the

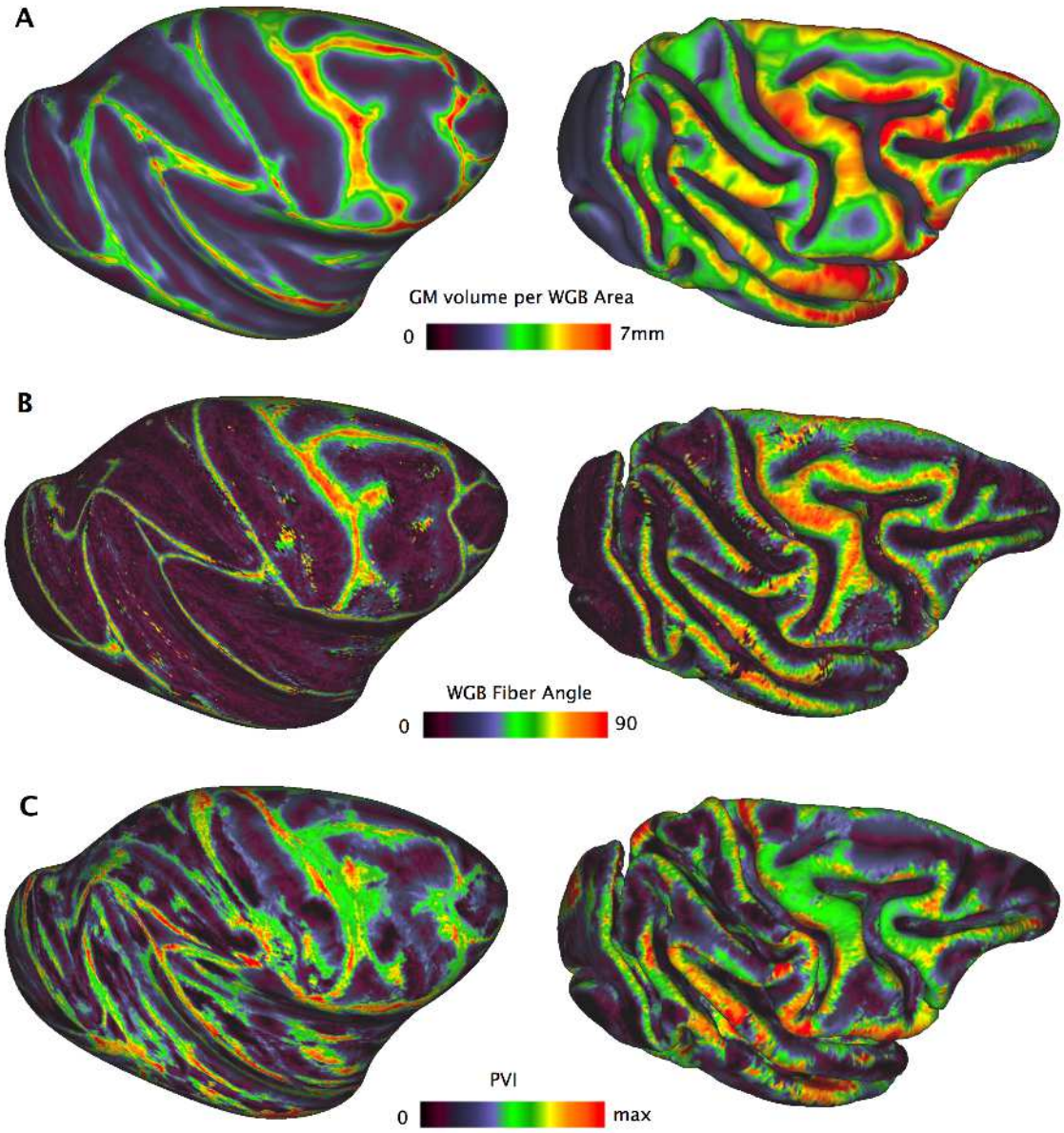

Figure 4.9: **A.** cortical volume per mm^2 of WM surface indicating "wedge" (see figure **??** and radial orientation. **B.** largest (of f1,f2,f3) fiber angle at WGB into WM. **C.** PVI measure. Left column inflated, right midthickness. The PVI pattern is similar but not the same as the wedge volume and first or second fiber dot products into the GM.

FSL models in each voxel lowers). For two major paths from a seed vertex that tracks may follow, PVI may be expected to give a weighted mean. Track length and voxels intersected by a single track do not have a one to one correspondence, but are intuitively correlated values. Under this assumption PVI reflects expected track length. The mean number of voxels intersected by all tracks from a seed is $PVI \times NV$ a quantity related (but not equal) to the expected track length from a seed.

The PVI thus reflects the density of coverage of track lines throughout the brain following seeding at a single position, expressed as a fraction of the approximately 2.5×10^6 voxels that were acquired in the brains hemisphere (excluding subcortical structures caudal to and including the midbrain).

PVI is operationally a measure of track line spread away from a surface seed to distant sites in the hemisphere. Unlike the methods used in figure 4.7 PVI measures interactions in 3D with the entire hemisphere (GM and WM) at a resolution of $250\mu m^3$ rather than GM to GM intersections. PVI is an imperfect measure of underlying penetrability because low values may result from short and focused fiber bundles into deep WM with low dispersion or from tracks failing to enter deep WM (both involve a small set of voxels intersected many times). Trajectories are not known and may or may not project into deep WM. Larger values empirically tend to correlate with deeper white matter penetration since deep penetration allows tracks to intersect many more voxels. Chapter 5 examines the relationship between the PVI measure and specific track trajectories. Adjunct PVI derived measures are shown in figure 4.10 that permit disambiguation in the PVI measure. In monkey A the entire cortical surface was seeded excepting the medial wall area (170,000 nodes) and a dense connectome file formed by seeding 200 lines per node. In monkey B a sparser mesh (around 60,000 excluding medial wall) was used and 500 line per node.

The PVI is shown in figure 4.8 A, and is similar in both macaques with gyri having higher values than sulci overall. Figure 4.8 B shows the track intersections from a seed region including the Corpus callosum and internal capsule. While this is necessarily qualitative the pattern of tracking intersections from deep white matter to cortex shows a similarity to the PVI measure of penetration into the white matter, though the pattern evident in the WM seeded **B.** (similar to that shown in chapter 1) is less complex and nuanced than the GM seeded PVI measure, in the sense that the track terminations in GM from the

WM matter seeds tend to concentrate heavily on gyral crowns while avoiding other regions entirely, while the PVI displays a richer distribution of values on crowns, ridges and some sulcal walls. The subtler patterns when seeded from GM suggests heterogeniety in WM, possibly near the GM, corresponding to complex superficial white matter structures, ufibers, neighbourhood fibers, crown fibers and regions where superficial WM is absent. While deep white matter contains structural heterogeniety this is not reflected on the GM maps in figure 4.8 since the GM intersections are essentially superpositions of the results from the set of WM seed voxels while the PVI reflects a measure from exactly one seed vertex into that set of voxels.

Figure 4.9 shows the wedge, the dot product of the largest fiber into the WM, and the PVI. The first two of these correspond to the explantion for "gyral bias" in section 4.1. The PVI does not match any other map exactly, calling the explanation for "gyral bias" in section 4.1 into question as a complete account. The wedge volume indicates gyrification, but this does not exactly predict PVI. Fiber orientations also fail to predict PVI. Further factors may influence the tracking behaviors, i.e. superficial WM stucture which losely matches the hypothesis in section 4.1 but not in detail.

Figure 4.10 expands the PVI method to measure more specifically the properties of the trackline trajectories. The central inset shows a small coronal portion of the FA map. The cyan band represents the midthickness surface from which all tracks are seeded. The red line represents the WGB. The green line represents a an inner WM surface surface **IWM** formed by linearly contracting the WGB into the WM. Self intersection limits the degree to which the WGB can be contracted. the IWM represents a loose boundary surrounding the deep WM. Figure 4.10 **A.** repeats the PVI measure with the additional constraint that tracks which intersect the IWB are completely discarded from the analysis (the IWB is an FSL **exclusion mask**). Figure 4.10 **B.** repeats the PVI measure with the additional constraint that tracks which **do not** intersect the IWB are completely discarded from the analysis (the IWB is an FSL **waypoint mask**). Figure 4.10 **C.** repeats the PVI measure, but first binarising the matrix A (figure 4.6 A) so that it is the number of unique voxels intersected as a proportion of the total. This is a measure of track dispersion from the seed "percent voxel spread" **PVS**, defined for a given seed point as.

$$PVS = \frac{\sum_{i}^{NV} m_i}{NV} \tag{4.2}$$

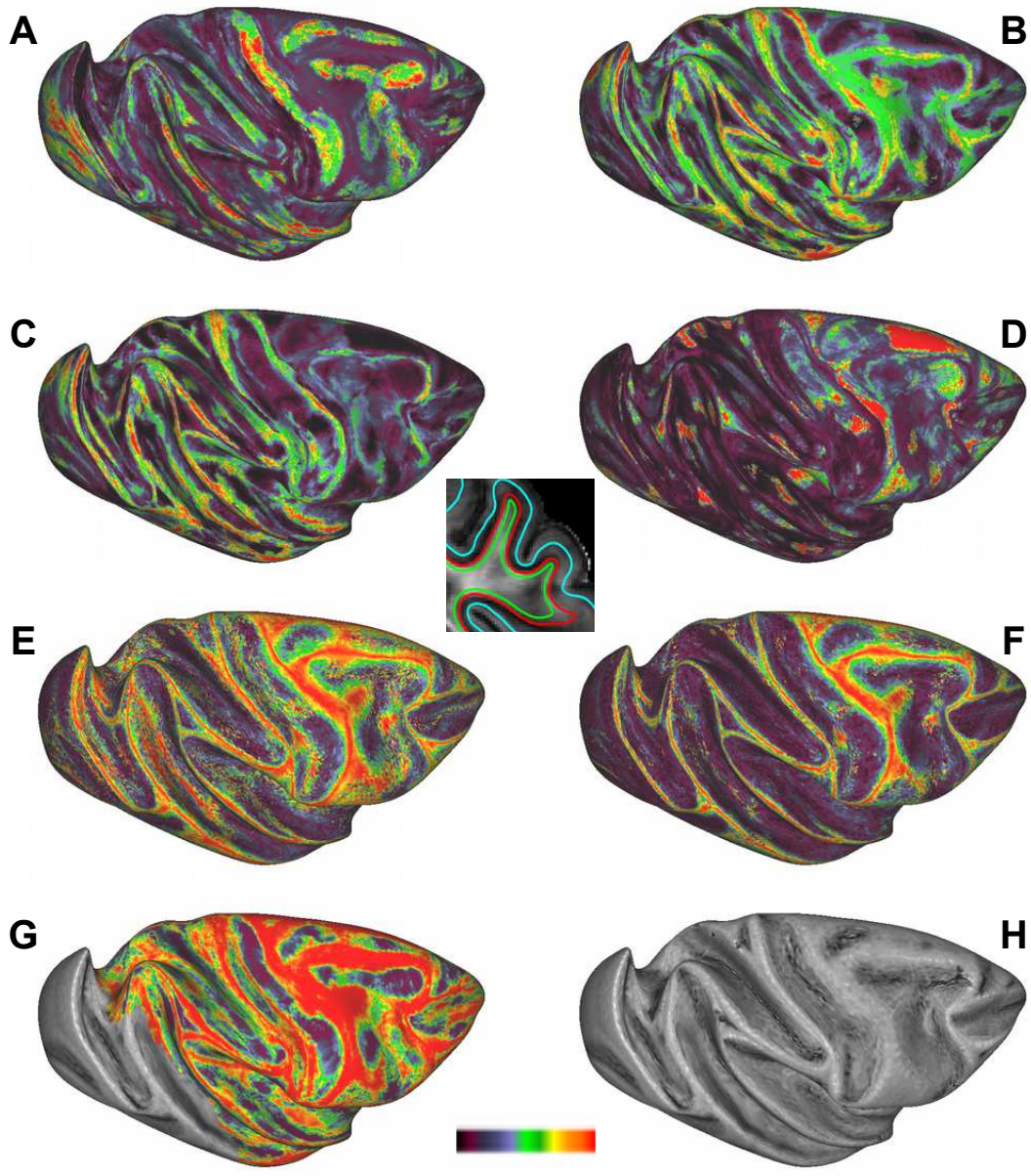

Figure 4.10: The central inset shows the outline of three surfaces on a coronal region of somato-sensory cortex. The cyan surface is at the cortical midthickness, the red at the WGB, the Green at the Deep WM boundary. **A** shows PVI tracks must NOT pass deep WM (green), **B** PVI but tracks MUST pass green (note map is the same as just "PVI"), **C** Number of unique voxels used in PVI (i.e. the percent spread of tracks from a seed "PVS"), **D** PVI divided by PVS, **E** dot product into GM, **F** into WM, **G** of 2000 seeded tracks, how many pass the deep WM boundary

where $m_i = 1$ if $x_i > 0$ else $m_i = 0$

and other values are as defined for equation 4.1

PVS ranges from 0 to 1 where 1 means every voxel was intersected by at least one track seeded from the vertex. Smaller values indicate a smaller number of unique voxels intersected, thus a smaller spread. If each track from a seed follows an identical path, $\frac{PVS}{PVI} = 1$. The more tracks follow differing paths, the larger $\frac{PVS}{PVI} > 1$, where the largest value is $\frac{1}{PVI}$. Taking $\frac{PVI}{PVS}$ thus gives high values where the PVI may be low as a result of low track dispersion rather than low penetrance, however it does not guarantee penetrance is high since it is a ratio. With reference to other data in figure 4.10 $\frac{PVI}{PVS}$ can reveal further information about track behaviour.

Figure 4.10 **D.** shows $\frac{PVI}{PVS}$ (note this is the inverse to figure 4.7 in which unique intersection are divided by the total intersections and is not related to that measure). Figure 4.10 **E.** and **F.** show the fiber orientations of the largest fiber into the GM and WM respectively from the WGB. Figure 4.10 **G.** shows a simple approach. For 1000 lines seeded per vertex, the number that intersect the IWB is recorded. No measure of track behavior is recorded other than intersection with IWB. The occipital lobe is omitted for computational reasons. 4.10 **H.** shows the curvature for reference.

The $\frac{PVI}{PVS}$ measure helps show that the low frontal connectivity is due to callosal connectivity. A picture is formed in which tracks seeded sulcal regions enter the WM but remain close to cortex (figure 4.10 A). The number of unique voxels sampled is lower in large frontal gyral regions (figure 4.10 C) some of which have high PVI values and some lower (figure 4.10 B). The manipulation in figure 4.10 D) Yields information about regions whose PVI value may be low due to a low PVS, which may be disambiguated with reference to figure 4.10 A. All the PVI related maps show patterns of WM penetration quite distinct to the fiber orientations into GM or WM from the WGB or cortical curvature (4.10 E,F,H). Figure 4.10 G crudely shows where deep WM penetration does or does not occur.

Figure 4.11 relates the PVI, PVS and $\frac{PVI}{PVS}$ measures to the cortical curvature. in each case, a 2D histogram is formed of curvature values to metric values. The color indicates the height of the histogram bins. discuss

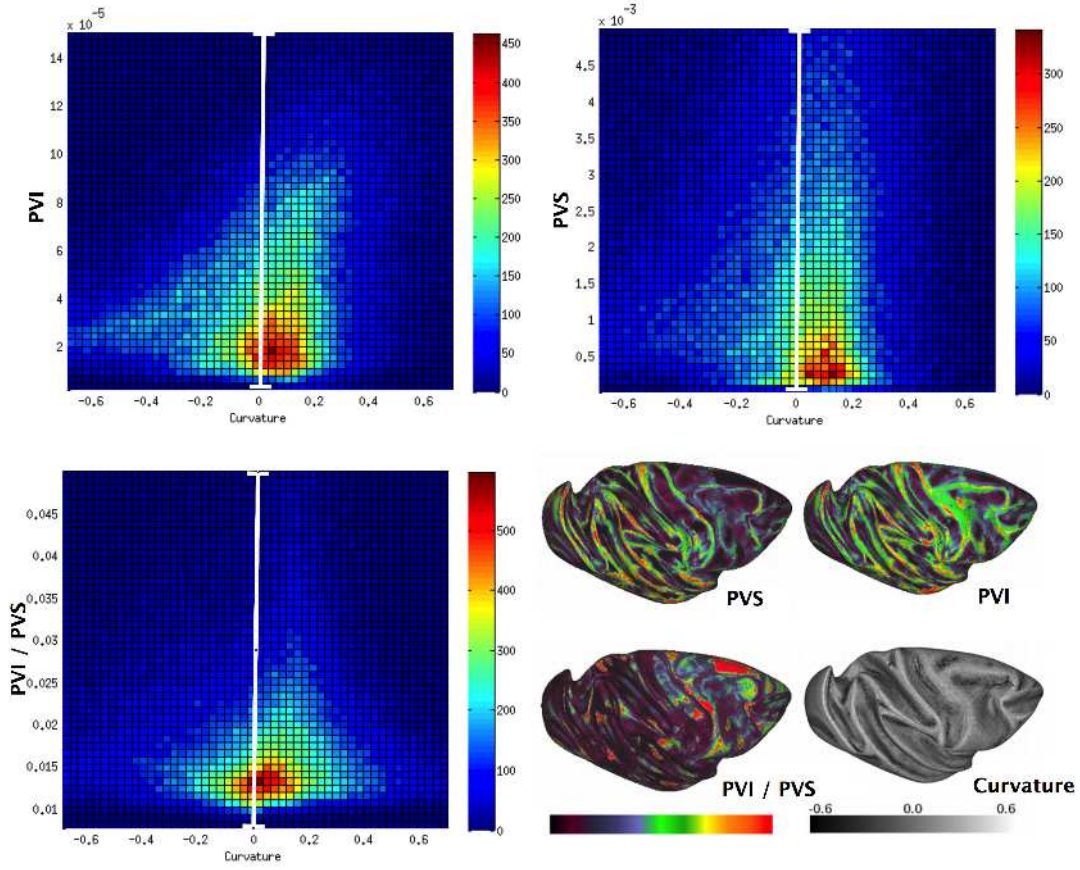

Figure 4.11: 3d histograms. the vector of curvature values binned against the other measures. positive curv gives higher spread (neg curv almost no spread). positive curv gives higher PVO, only positive curv yields very high pvo values although neg can give significant PVO (note the slope). PVO/PVS same pattern, but less pronounced more centered on 0 curv

4.4 Global DTI Cortico-Cortical Connectivity in Marmoset

The lisencephalic marmoset brain contains much fewer outfolding regions than the rhesus brain, however we may consider the entire cortical surface as behaving as an outfold or an infold dependent on the underlying WM anatomy. In this section we repeat some of the explorations in the preceding sections with the marmoset for comparison.

Section 4.2.3 compared tracking intersections to retrograde tracer labels mapped via surface registration methods. No such tracer data exists for the marmoset, so we estimated the injection zones from two cases in 4.12 as midthickness surface patches similarly to figure 4.4 and took the trackline interactions. Estimations of the two retrograde tracer injections (Fast blue and Fluoro Emarald) are shown in figure 4.12 from (Burman et al., 2008). The tracking intersections have some similarity but in that there is more coverage of the lateral bank of the frontal lobe in **C.** than **D.** and tracks do not intersect caudally. To an extent the difference between the tracer and tracking results may be due to error in the estimation of the injection site. However, in both cases tracks are drawn heavily to the outfolds at the midline and gyri around the sylvian fissure (the only outfolding regions available) and these are false positives since the tracer does not label the temporal lobe at all. In principle this may reflect efferent projections from the (retrograde) injection sites. However false negatives are clearly visible in both cases. In explaining these false negatives in terms of superficial fibers we can look at the PVI and dot product of the fibers nearest to the WGB (figure 4.13 **B.** and **D.** respectively). Regions of large fiber angle are mostly found at regions of large fiber angle. To a good approximation these coincide with regions of high PVI. These regions of large angle and large PVI tend to account for positives, both genuine and false. Low PVI and low angle tend to account for false negatives. Given the fiber angles and PVI both measure properties at the WGB primarily, and hence interaction of tracking with superficial fibers we can reaonably infer that these fibers domination the GM intersections in figure 4.12. figures 4.14 4.15 repeat figure 4.7 in the marmoset for completeness.

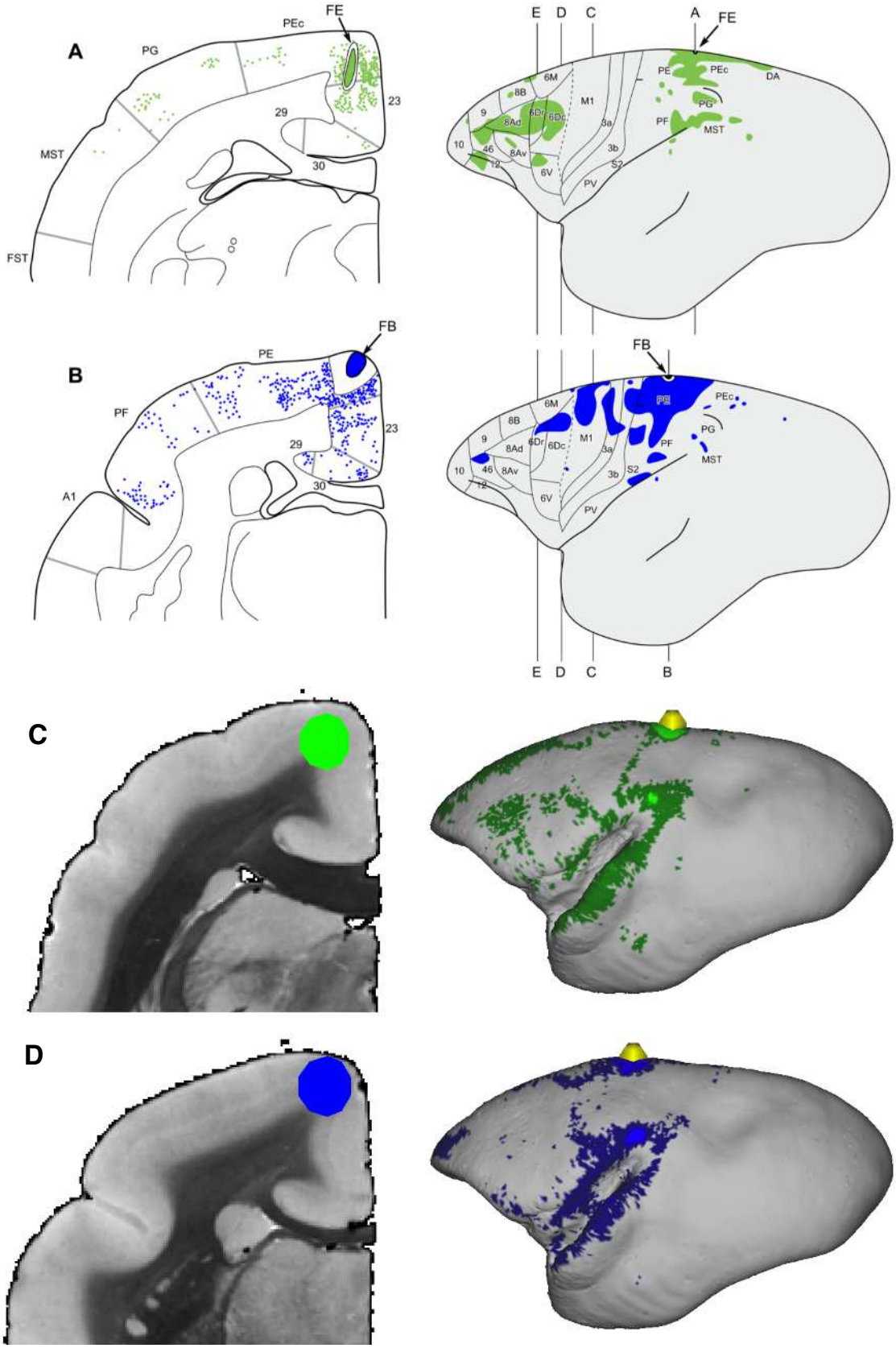

Figure 4.12: **A.**, **B.** retrograde tracer injection sites and labelling from (Burman et al., 2008) figure 8. **C.**, **D.** estimated equivalent tractography from midthickness seed patches (rough location of patch center shown as colored circles on sections and yellow spheres on surfaces). See text

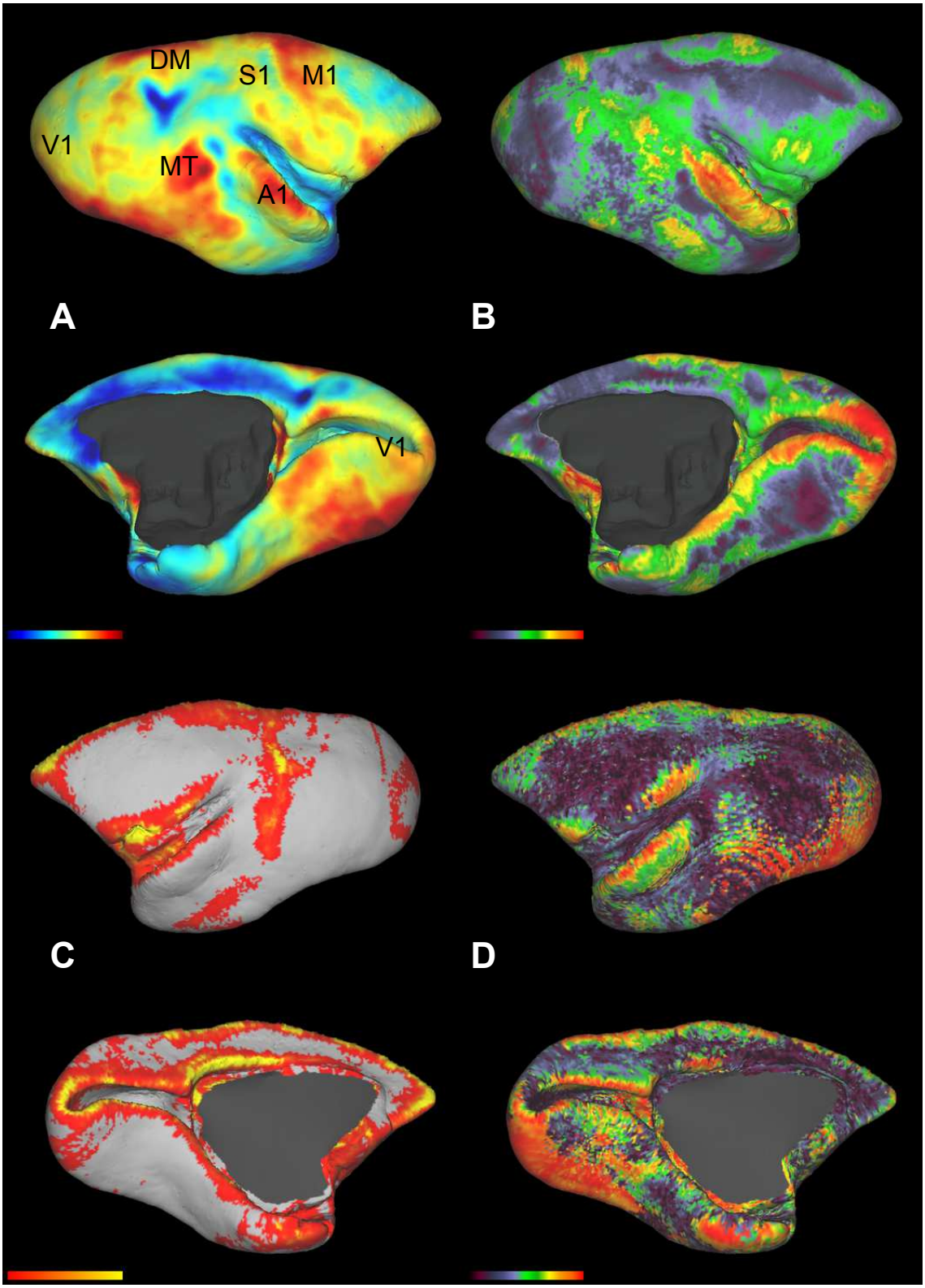

Figure 4.13: **A** cortical regions by myelin map (MTR), **B** PVI measure across marmoset cortex, **C** Tracking seeded at the callosum penetrating cortex, **D** Dot product of WGB with nearest superficial WM fiber

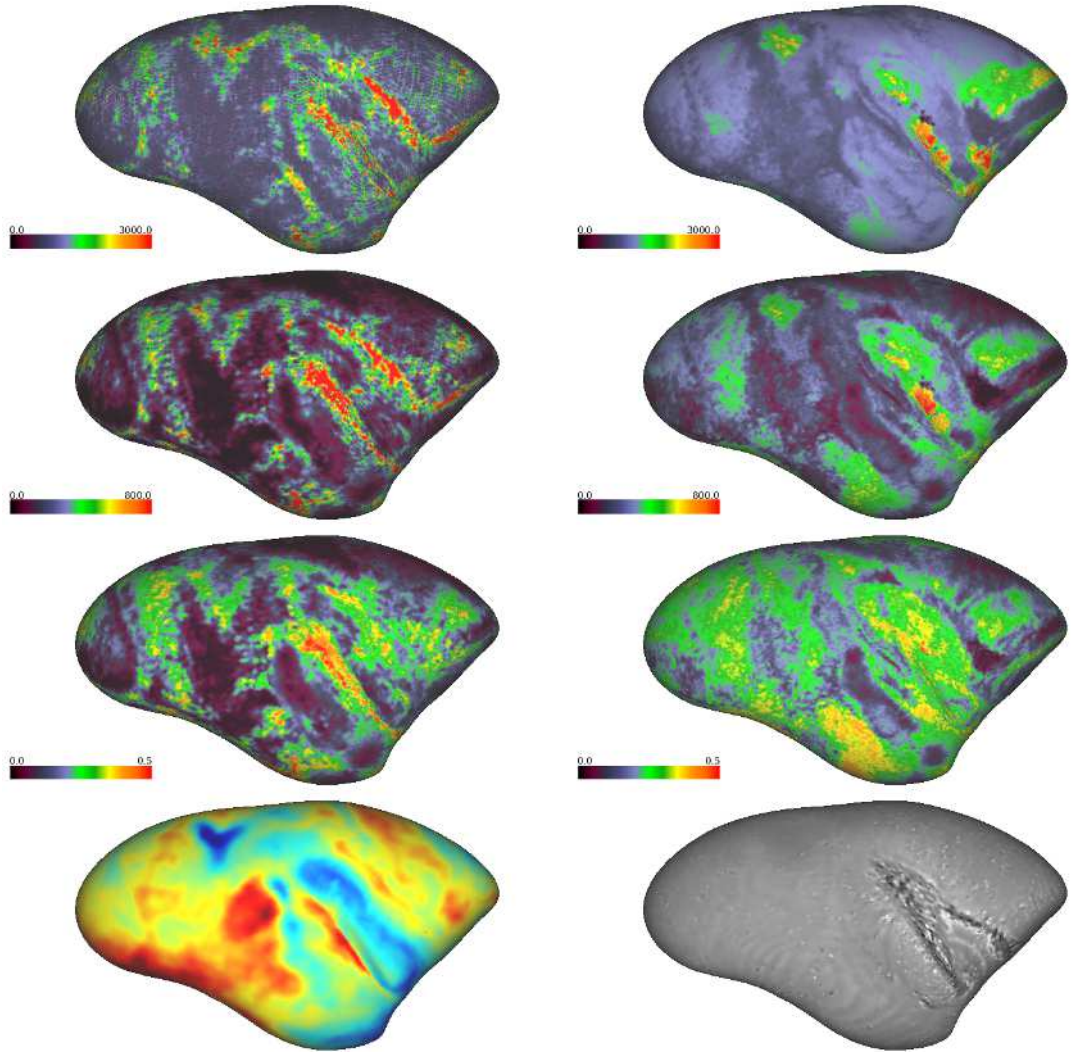

Figure 4.14: as figure 4.7 but inflated marmoset (bottom row for orientation) GM surface to surface seeding: Each point on the midthickness gray matter surface is seeded with 1000 lines. For each seed the number of track intersections with every point is recorded in a square matrix (figure 4.6 B) The left column shows afference (figure 4.6 B) , the right column efference (Transpose of the matrix figure 4.6 B) on very inflated surfaces. The top row (A,B) shows the total afferent or efferent trackline intersections (sum of columns). The middle row (C,D) shows the total afferent or efferent intersections from unique seed points (sum of binarised columns). The bottom row (E,F) shows unique intersections divided by total intersections.

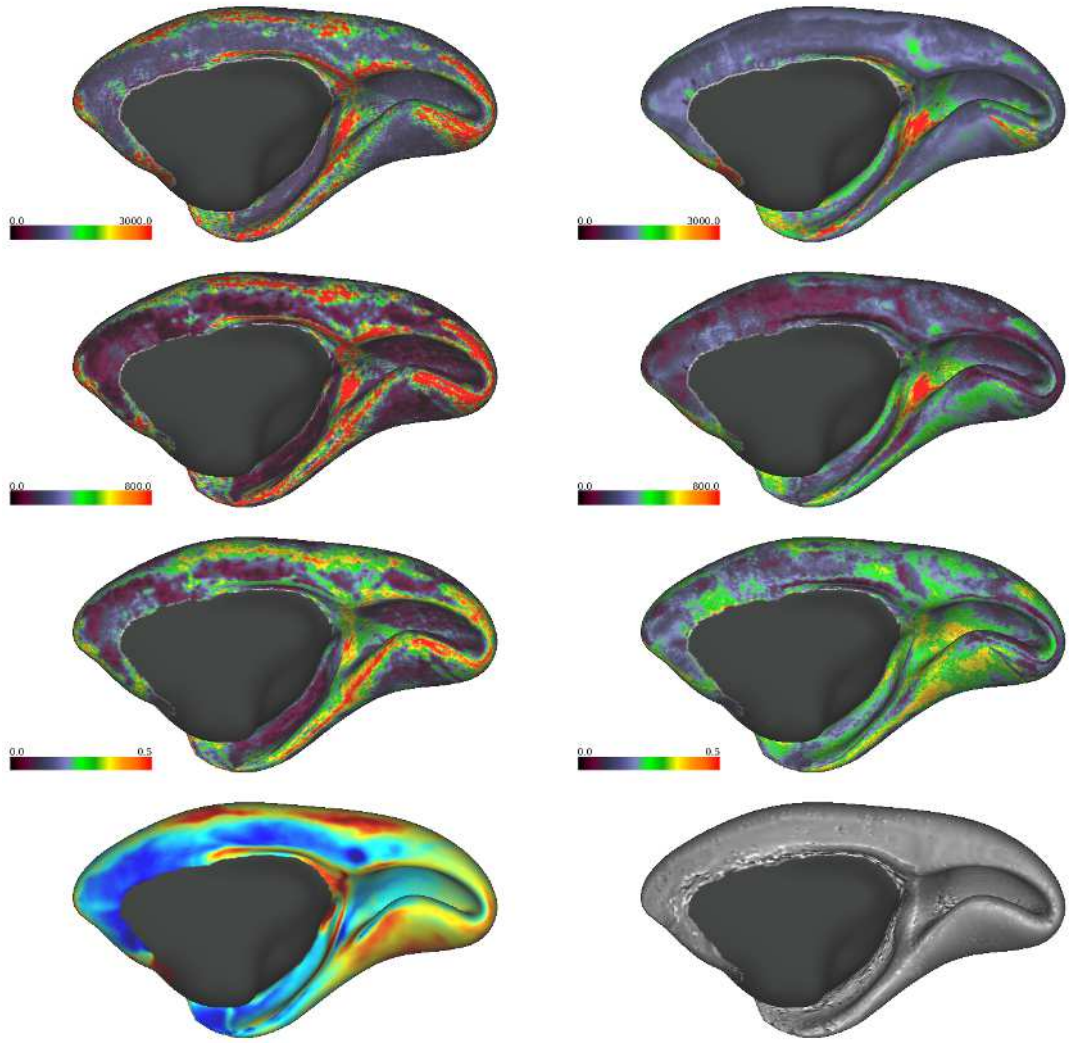

Figure 4.15: as figure 4.7 but inflated marmoset (bottom row for orientation) GM surface to surface seeding: Each point on the midthickness gray matter surface is seeded with 1000 lines. For each seed the number of track intersections with every point is recorded in a square matrix (figure 4.6 B) The left column shows afference (figure 4.6 B) , the right column efference (Transpose of the matrix figure 4.6 B) on very inflated surfaces. The top row (A,B) shows the total afferent or efferent trackline intersections (sum of columns). The middle row (C,D) shows the total afferent or efferent intersections from unique seed points (sum of binarised columns). The bottom row (E,F) shows unique intersections divided by total intersections

4.5 Spatial Resolution

Whether FSL tractography favours terminations at outfolds for algorithmic or anatomical reasons or a combination, it is important to note that in this thesis very high spatial resolution is employed, not typically available in-vivo. We here explore some of the preceeding behaviors while varying spatial resolution. High resolution is less susceptible to partial volume effects and is inherently to be preferred, since more accurate measure is preferable to less. However it is an empirical matter as to how spatial resolution influences tracking terminations. Therefore, we conducted tracking experiments in which we sought to vary only spatial resolution and nothing else.

Downsampling of diffusion data by enclosing 8 high resolution voxels (eg 250um) within one lower (500um) resolution voxel and averaging the intensity is theoretically equivalent to an acquisition at the lower resolution. The scan time remains constant so the downsampled data will receive a boost in SNR of sqrt(8). Downsampled data is equivalent to the source data and simply another way of interpreting it.

On the left, outlined in blue, Figure 4.16 shows the experiment in figure 4.3 repeated at 250,500 and 1000um. The Gray matter track termination densities are shown on flattened representations of the 3d mid thickness surface model. Additionally, we seeded from a mask at the corpus callosum (green, on the right). The seed was manually delineated on 250um data and was four saggital slices thick. The tracking seed voxel sets for the IPL were generated identically by a specification of 250um above and below the 3d mid-thickness surface. At lower resolution the reference volume resolution was varied which forced a resolution change in the seed group. The corpus callosum seed was simply downsampled with nearest neighbour interpolation. At 250um 5000 lines per voxel were seeded, at 500um 40,000 and at 1000um 32000 since there would be roughly 8 times fewer seed voxels for each downsampling and we wished to retain the overall number of tracks. The resulting FSL track result voxel sets were then divided by 1, 8 and 64 respectively. In addition, tracks were started from a random point within a radius of 100um, 200um and 450um from the voxel center respectively. Other parameters for tracking and FSL local modelling were identical (including the integration step of 62.5um). Data was mapped identically in all cases using the FSL surface projection program, taking the largest value between the pial surface and mid-thickness. The step over which data was mapped took the value of the datas resolution. Interpreting the number of trackline intersections at different resolutions still presents a challenge: We simply used Carets display to threshold each at 2% of their minimum and 96% their maximum: values over 96% are displayed, but mapped

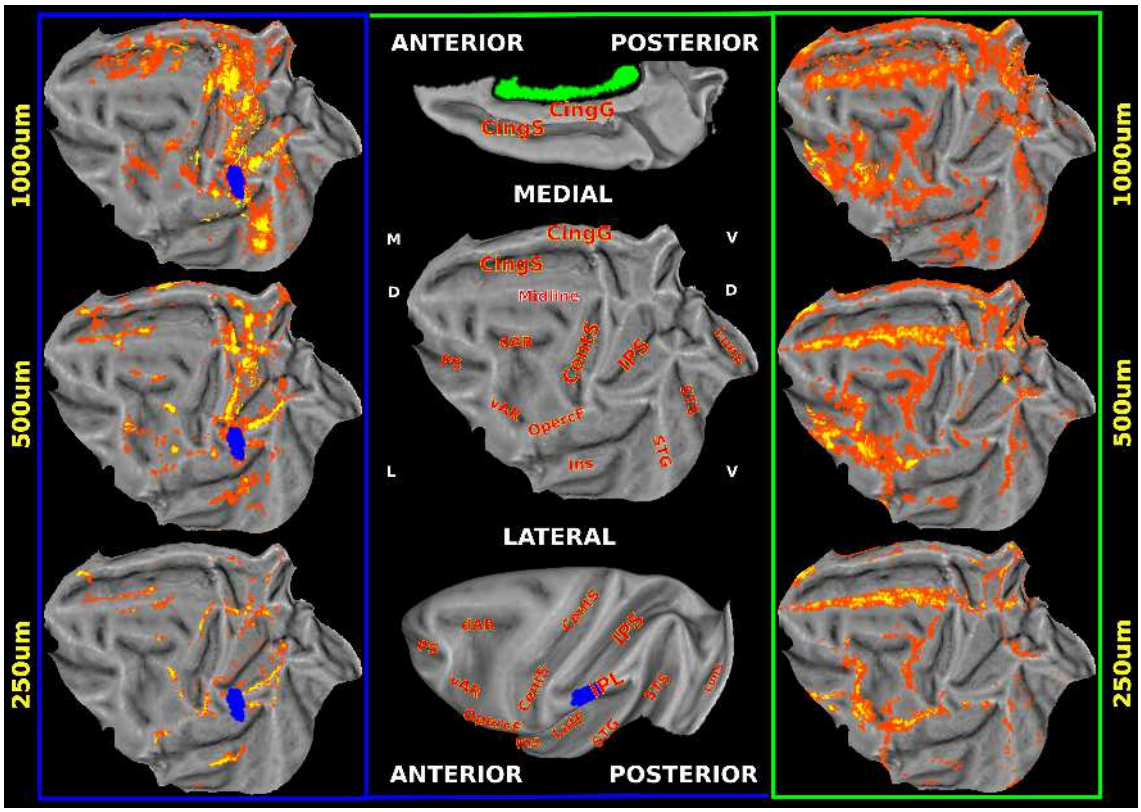

Figure 4.16: 2 experiments from above (CC and 5/6) repeated at different resolution. Gray Matter Tractography Results Differ in Their Termination Patterns Due to Partial Volume Effects at Low Res and the possible Influence of white matter anatomy

as 96%. Tracks vary in number but we show high intensity in yellow, lower in orange. In this way, we minimized the effect of all factors other than spatial resolution because the brain is the same, in the same stereotaxic coordinates, and identical or near identical procedures are applied at all resolutions to ensure other factors are controlled for. The over all result is that partial volume or other effects yield an enormous difference between high and low spatial resolution. At all resolutions, the results may reflect the influence of subsistene fibers and gray matter myeloarchitecture, as well as tracking algorithm and other model limitations. At high resolution these latter effects, which reflect anatomical truth, dominate partial volume effects which may be effectively absent. The Middle column of Figure 3 provides the anatomical orientation for the flatmaps and seed locations. The rostral IPL gray matter seed results are in blue on the left, and the corpus callosum result in green on the right. The spatial resolution increases down the page. The IPL seed produces very specific results at 250um. The results are less dominated by terminations near to the seeds than at lower resolutions. The primary terminations are in the IPL itself, the fronto-parietal operculum at the ventral tip of the central sulcus (SII, other somatosensory regions), the rostral tip of the postcentral gyrus, ProM, regions on the

caudal and medial aspect of the crown of the precentral gyrus, insula, and some medial regions including one pronounced termination in medial pFC. With a single exception these patterns occur at outfolds. This exception occurs in motor cortex on the bank of the frontal lobe, ventral to the spur of the arcuate sulcus and just caudal to the principle sulcus. All these pattern are supported by the tracer data (Pandya and Cipollini 1999). However those studies show data that our model is missing, and there is a clear pattern in where things are missing. We might expect from Lewis et al (2000 fig 7) more terminations on the convexity of the IPL, as well as in the arcuate and principal sulci. In general, the model tends to ignore regions of infolding where known connections to the rostral IPL reside.

In the absence of a same-brain tracer experiment, the evidence from literature is strong that at 250um we have little trouble from false positives. But we find an anatomically consistent and predictable pattern of false negatives.

At 500um the results are superficially similar, but simply less targeted. There are even terminations (around arcuate and premotor) that appear to add information. These may be right or wrong: there is an inevitable discrepancy in seeding. However the premotor bank termination appears to arise at the cost of the known ProM termination. Moreover, the gray matter is thin here and what appears a premotor GM intersection may be white matter tracks close to the surface. At 500um the exact locations of terminations differ significantly, to the extent of being different cortical regions. At 500um the Tracks tend to terminate much more heavily in parietal regions near the seed. At 500um the result is less precise, and in disagreement with the higher resolution data.

At 1000um all fidelity to tracer data is essentially gone. Gray matter seeding here shows some similarities, but in general remains within the parietal lobe and disagrees very substantially with the high and medium resolution data. This data, however, terminates heavily in the wall of the intraparietal sulcus (IPS), fundus of the superior temporal sulcus (ST, and widely on the bank of the superior temporal gyrus (STG). It fails to follow the anatomical pattern shown clearly at 250 and still at 500. The data at 1000um shows terminations in the IPS that might be expected given the literature. However, given the dominance of false positives we are forced to conclude these could easily be false positives (even though they may be correct). At 1000 gray matter terminations that are the result of accurate tractography can't be distinguished from those that aren't. All terminations are suspect.

The purpose of seeding the corpus callosum (CC) is not to replicate tracer findings, but simply to spread tracks widely through the brain and examine this issue of termination patterns and folding geometry. The seed is unambiguous, and the terminations are not examined in terms of the connectivity of the CC Generally we expect a lot of terminations on the medial frontal lobe, premotor cortex, motor cortex, prefrontal. And that is what we see. But the high resolution data terminates with great precision, and always on outfolds. This is less the case at 500um, and not the case at 1000um.

The difference in termination patterns between the IPL and CC seeded cases result from the fact that the IPL seed requires more sharp turns to meet any cortical target. The CC seeded case often requires no sharp turns just a radiation from a central point. The patterns at different resultion for the IPL case result from partial volme effects interacting with sharp turns.

In sum, we find that the high resolution data produces accurate, but incomplete results. Lowering resolution to 1000um produces highly questionable results.

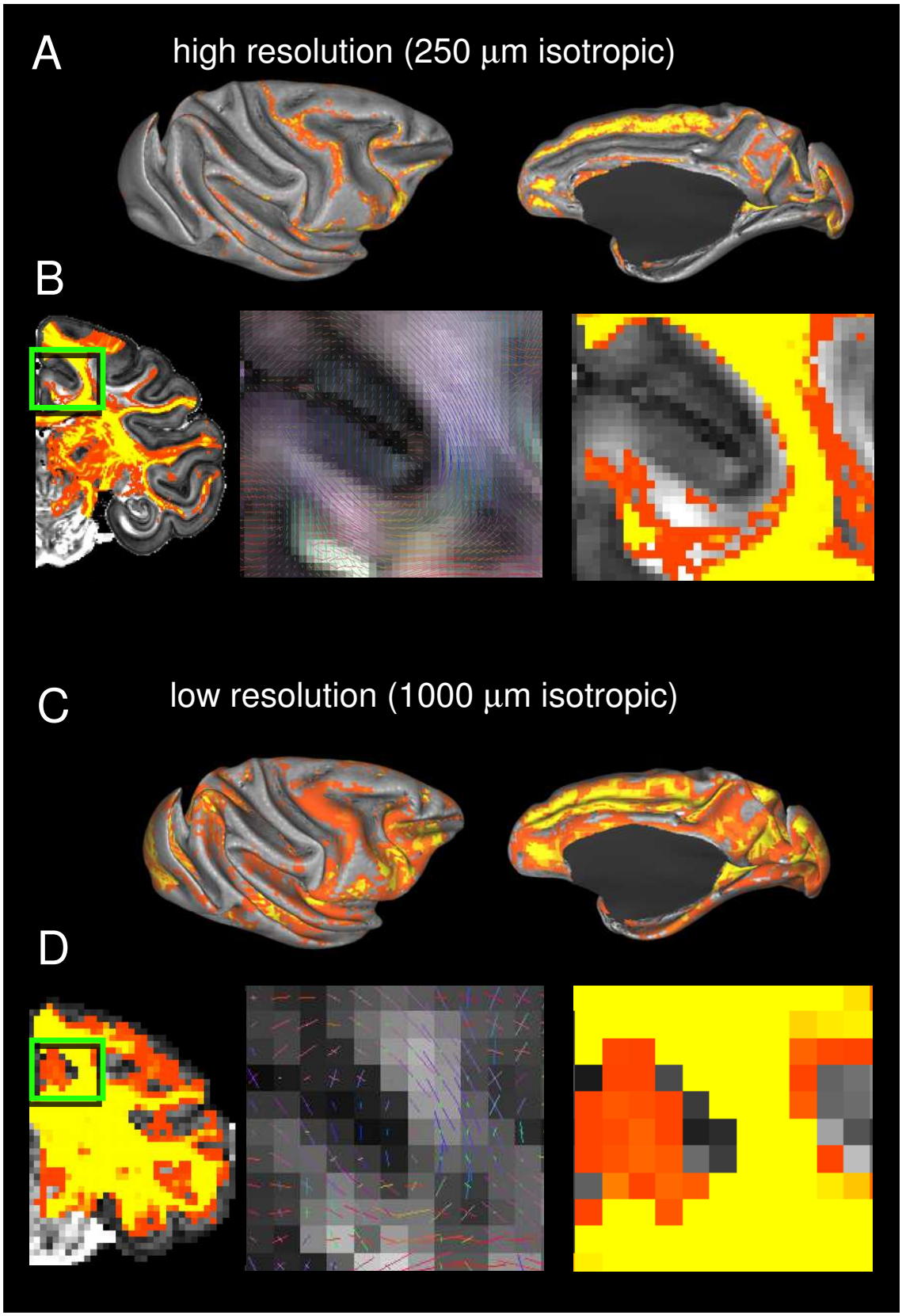

Figure 4.17: High res, low res, surface, cingulate sulcus

4.6 Summary

In this chapter we began by comparing GM seeded tracking to tracer data in 3 distinct ways: segmentation of the corpus callosum, a loose comparison to an autoradiographic tracer in WM, and surface registered retrograde tracer data. In each case we found false positives and negatives such that the tracer results were not reliable replicated. We determined that regardless of seed type (GM or WM) or location, terminations occurred within a set of cortical locations, primarily gyral ridges. To further explore this we developed a series of global scalar maps of GM to GM and GM to WM connectivity. These maps of afference and efference between GM regions, and of various penetrability measures into WM roughly corresponded to the "gyral bias" seen when seeding from WM suggesting that "gyral bias" is related to factors other than those outlined in chapter 1 since in the case of PVI and related maps, tracking is from GM into WM and the maps are not affected by these factors to the same extent. The maps but exhibited more variability and subtlety than "Gyral bias" suggesting an anatomical factor, though they did not overlap with cortical wedging or fiber orientations at WGB. We then repeated a similar exploration in the marmoset brain, discovering again an emphasis on outfolds in our maps but also subtlety, given the smooth lisencephalic brain. Finally, we repeated some of the rhesus experiments at a range of spatial resolutions since this is a key factor in in-vivo dMRI.

The following chapter seeks the anatomical substrate for these phenomena.

Chapter 5

Local Fibers and DTI

Abstract

Following from Chapter 4 this chapter seeks to determine the mechanism by which maps such as the PVI derive their properties. On the one hand, we explore this using dMRI itself. We also employ histology from the same brains as scanned. We determine the relation between tracking and tissue properties, and note myelin patterns in GM and the composition of local fibers. We discuss local fibers along gyri. The principle finding here is that the PVI map properties are principally defined by the local fiber architecture of the brain since these fibers limit accessibility of GM seeded tacks to deep WM. We also examine tracking, histology and anatomy in the marmoset brain again focused on superficial white matter and find results that reflect the findings in the rhesus brain. Finally, we focus on a sepcific region in detail, the IntraParietal sulcus (IPS) in the rhesus. By bringing all the methods together, with the addition of a tracer injection, We characterize the relation of dMRI to anatomy in great detail at the sulcus. Finally we analyze the structure of the local fibers at the IPS region using histology, image processing, tensor maps and tracking to develop a hypothesis about how they may subserve the function of the lateral parietal lobe.

5.1 Introduction

This chapter looks at the dMRI and histology evidence for local fibers as the primary explanation for gyral bias and the impenetrability of many regions of cortex when seeded from the cortical GM, seeking to shed light on the underlying anatomical structures and

their dMRI correlates that yield the tracer comparison and scalar tracking measure results from the previous chapter.

In the previous chapter we saw the effect of seeding from sulci and gyri in two primate species. In this chapter we explore histological tissue samples and compare to diffusion MRI. In the previous chapter showed

1. Gyral bias in agreement with previous results when seeding from WM (Van Essen et al., 2013)

2. Gyral bias exists when seeding from GM as well, using the PVI measure of GM to WM penetration (and variants), tracer "simulations", GM to GM maps. GM to GM maps and tracer simulations show resolution dependent properties.

3. The pattern does not match the wedge metric, the fiber angles at WGB and since GM seeded the "straight line" aspect of tracking algorithms cannot be the primary reason. What is the anatomical reason the PVI measure looks the way it does?

4. Marmoset is lisencephalic yet low PVI. Why, anatomically?

In this chapter we

1. Ask what is the anatomy underlying the findings of the previous chapter?

2. Compare histology and DTI derived tissue properties carefully

3. we demonstrate dMRI that our dMRI modelling is sufficient to capture the anatomy as far as current methods permit (figure 5.2 ,5.3, 5.22.

4. in section 5.3 We examine the tracking behaviors underlying the PVI map in detail by selecting 4 seed points and examining the tracking qualitatively and quantitatively in 3D (figures 5.4, 5.5.) We note the DTI evidence for 2 superficial fiber structures (seeds 1,3,4) which are examined later in section 5.6.

5. in figure 5.6 we show and discuss the correspondence between these tracking behaviors from specific seed points and their corresponding representations on the whole brain PVI scalar map.

6. In figure 5.7 we note that the gyral bias pattern exhibited when seeding from the WM appears in the DTI evidence to be related to a band of high anisotropy subjacent to the central sulcus, but absent at the opercular tip of the postcentral gyrus.

7. In section 5.4 We show the fiber architecture at the arcuate sulcus and the dorso-medial premotor cortex. We compare this to GM seeded tracking behaviors at the AS and PMc (figures 5.8, 5.9) and at 3 other sulci (figure 5.8)

8. in section 5.4.1 we demonstrate and explore the existence of superficial fibers running the length of a gyral crown. We note that if local fibers exist to join cortical regions on the sheet via the shortest route (As discussed in chapter 1 (which is unchanged by cortical folding) then it follows local systems should exist wherever the distance between regions has not been shortened by folding, yet connectivity is desirable including crowns and even fundi (e.g. CS).

9. in section 5.5 A similar dMRI and histological analysis of local fiber architecture is applied to the marmoset.

5.2 Diffusion Data And Tissue Properties: Initial Comparison

An example of a local dMRI data slice, along with corresponding histological sections from the same brain (see chapter 2, see section 2.3 for structure tensor methods), are shown in Fig 5.2, which features a region surrounding the rostral opening of the intraparietal sulcus (IPS). The maps in Fig 5.2 A show the local three-dimensional diffusion orientation as colored line segments superimposed on a gray scale map of fractional anisotropy (FA). The cyan curve is an estimation of the WGB determined using a separate magnetization transfer contrast MRI scan see chapter 2. The high signal-to-noise ratio of the acquisition made it possible to determine at least one diffusion orientation, and often more than one, throughout the gray matter despite the lower anisotropy of gray matter. Across the brain, the principal diffusion orientation in the cortical GM was nearly always perpendicular to the WGB (see figures 5.3 and 4.10 for fiber model angles w.r.t. the WGB over the whole brain), with the exception of the deepest cortical layers in some regions.

This regularity was in sharp contrast to the principal diffusion orientation in the superficial white matter, operationally defined here as a zone deep to the infragranular cell layers of the cortex and within 1 mm from the WGB (corresponding to < 4 voxels in the current datasets) (in chapter 1 the literature suggested a typical local fiber bundle might have an average diameter of 0.5mm). The principal orientation of the computed diffusion direction in this superficial white matter region varied widely relative to the overlying WGB plane,

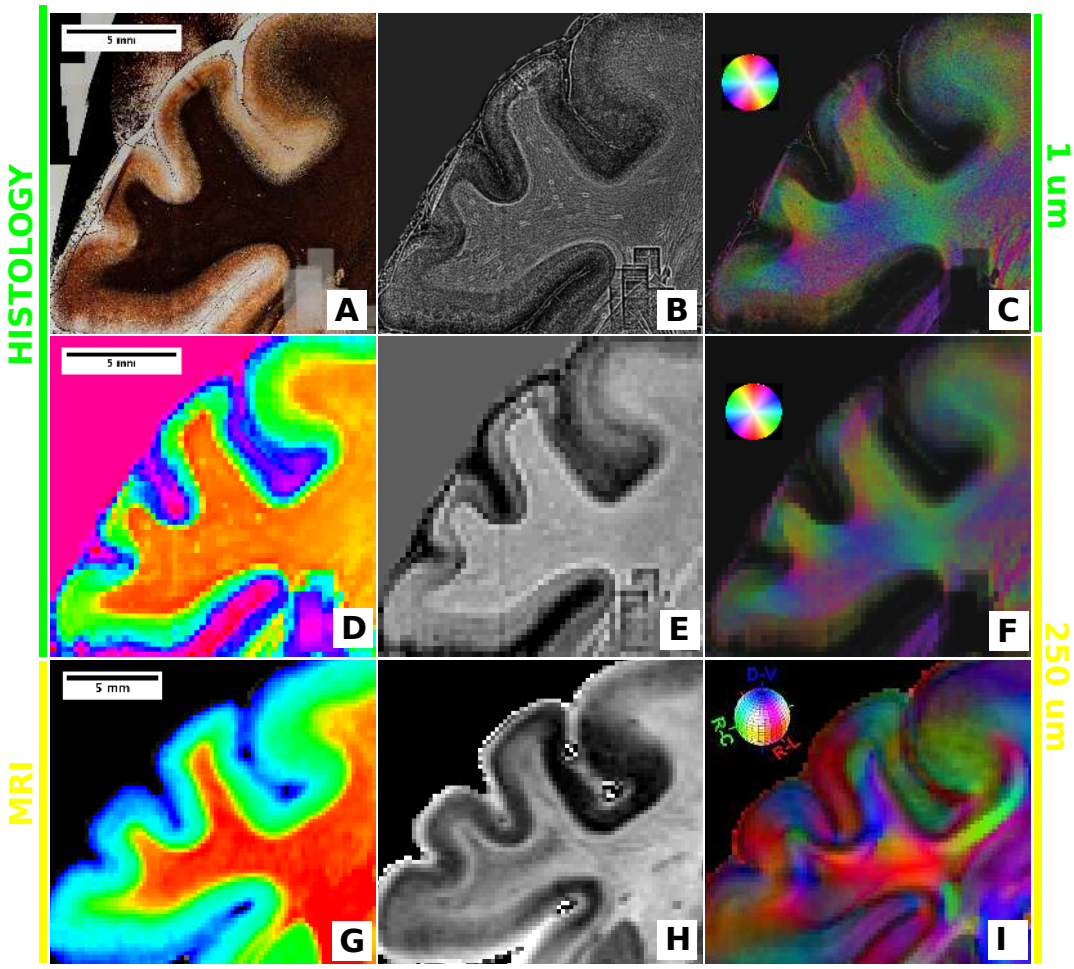

Figure 5.1: **A** digitized myelin stained section (at about 1um per pixel). The banks of the post (left) and pre (right) central gyri are in the top right, with the CS fundus below. the rostral tip of the IPS is to the left, an individual unnamed small fold at the fronto-parietal junction far left. Motor cortex is top right, with 3a/b on the postC bank, 1/2 on the crown. **B** The data in A, grayscaled an subjected to local contrast enhancement this has the effect of lower contrast in matted myelin and in relatively homogeneous regions, but raising in local fibers. C) the structure tensor analysis, discussed in more detail in chapter 2. D,E,F as A,B,C but downsampled to 250um per pixel. D is colored by myelin intensity. G shows 250um MTR data from this region, colored by myelin intensity . Myelin is lower around local fibers both in D and G. H shows the MD in inverted grayscale (high diffusivity is dark). Local fibers are generally brighter than deep WM even though myelin is lower (discuss why, many fibers in complex configuration restrict rate of diffusion. I) the DEC map for this region showing the large CS ufiber, crown fiber.

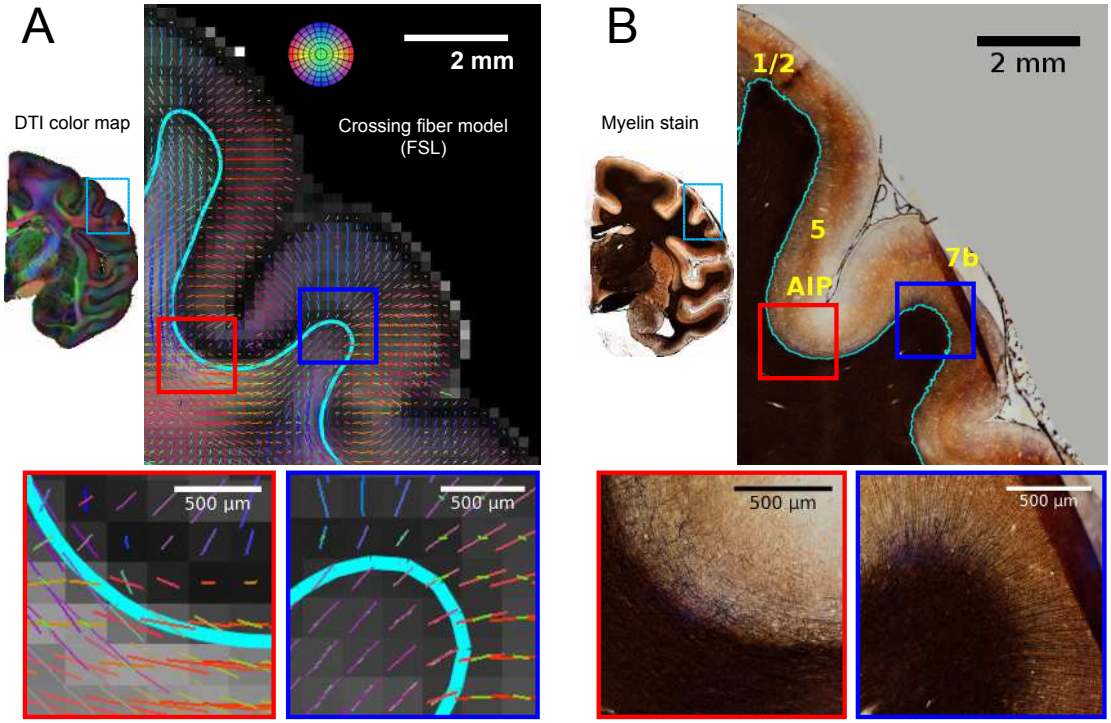

Figure 5.2: Examples of diffusion MRI and histological data sets used in this study. A. dMRI data collected at 250m isotropic resolution showing an entire coronal slice colored by dominant direction (DTI principal eigenvector) top left, the main inset on right focusing on a region in and around the intraparietal sulcus (IPS) and inferior parietal lobule (IPL). The colored lines in each voxel correspond to the FSL crossing fiber mean model orientation. The lines are overlaid upon the FA map. The cyan contour is the white matter gray matter boundary (WGB) derived from MTR and surface reconstruction .The red and blue areas show magnified subregions of the IPS and IPL shown with greater magnification in the insets bottom row. The blue inset shows magnified region of the IPL showing the orderly and radial trajectory of principal orientations flowing from the white matter into the IPL. The red inset shows Magnified region of the IPS in which the orientation of the white matter fibers is not continuous with that in the gray matter. B Myelin stained sections corresponding to the same subregions (of the same brain) as in A. Coronal slice of the same region, showing the darkest staining within the white matter. main inset as in A. In this panel the cyan contour estimates the WGB based on a discontinuity in staining intensity. The blue panel shows Magnified view of the myelin fibers radiating into the appearing to match the DTI orientations seen in equivalent DTI. Red panel Magnified view of the sulcus myelin pattern, showing a lack of radial penetrations as well as matted fibers positions of the low FA shown in A

and thus relative to the diffusion orientation of the overlying cortex (see figure 4.10 E, 5.3). This range of relative diffusion orientations is exemplified in the red and blue insets magnified in Fig 5.2 A. The principal fiber orientation in the blue magnified region, from the gyral crown of the inferior parietal lobule (IPL), is nearly perpendicular to the WGB, and hence largely parallel to the gray matter diffusion orientations. The secondary fiber orientation, while not parallel to the first is again near parallel to the WGB. By contrast, the principal fiber orientation in the red magnified region, from the adjacent fundus of the IPS, is nearly parallel to the WGB and hence perpendicular to the overlying cortex. The secondary fiber orientation is near parallel to the first in-plane, but runs more rostro-caudally (green). The angles of the first, second and third fibers to subjacent to the WGB and relative to it (dot product) are shown in figure 5.3. The myelin stained sections in Fig 5.2 B highlight fiber features that contribute to the measured diffusion orientation and FA information, including the matted pattern of myelinated fibers in the cortex of the sulcus that gives rise to the regions of particularly low FA. Such matted fibers have been observed previously in the vicinity of sulci (Lewis and Van Essen, 2000b; Preuss and Goldman-Rakic, 1991), and are visible in figure 5.1 A, B and E. Figure 5.10 examines the histological structure of GM myelin and superficial WM in this same area of lateral somatosensory cortex.

Second and some third fiber orientations were robustly found in the superficial white matter on sulcal walls and fundi, less so in gyri. Figure 5.3 shows this via the angle of the first, second and third fibers with respect to the WGB. See also section 5.6 figure 5.17 which determines the number of second and higher fibers in the GM and WM and in the superficial WM also showing their angles relative to WGB. It is notable from figure 5.3 B (showing the angle and existence of secondary fibers found below WGB) that secondary fibers tended to be found within sulci but not always on gyri, perhaps reflecting a strong direction of principle anisotropy in these regions due to radial efference and afference into GM (figures 5.8, 5.9) or lower myelin content at gyral crowns

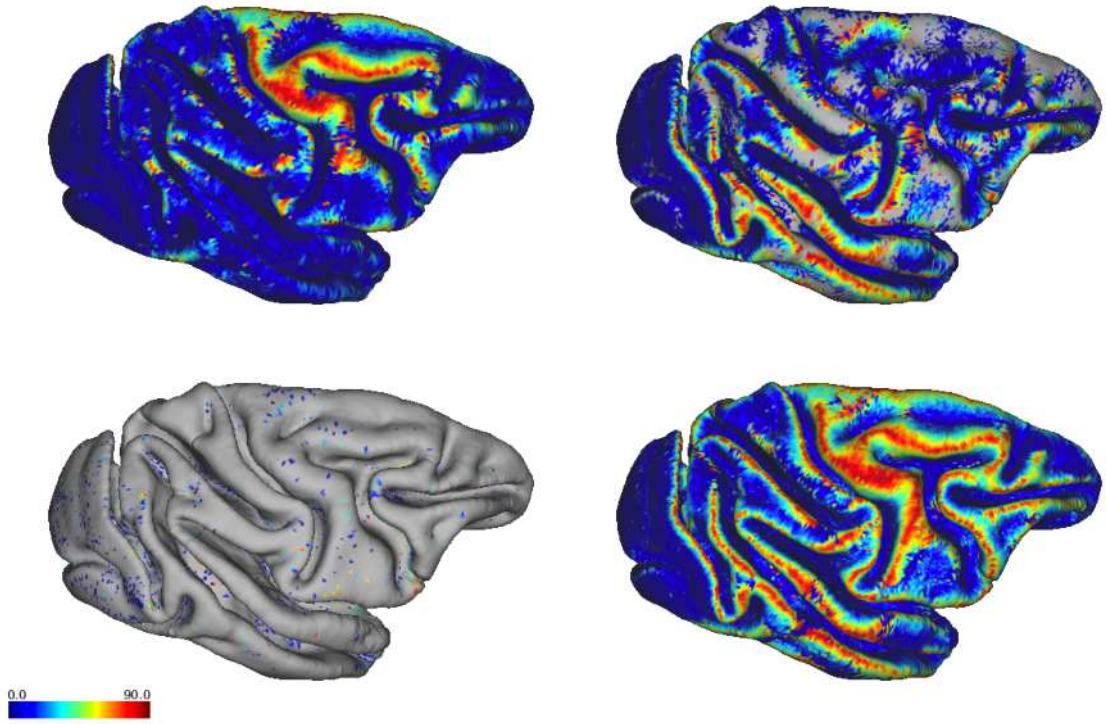

Figure 5.3: first second third dot products (f>0.01) and max dot product. superficial WM is more radial on gyri, but has fewer second fibers.

5.3 Relationship of Representative Tracking Behaviors To Derived Scalar Maps

The previous chapter showed a pronounced similarity in GM terminations regardless of GM or WM seed strategy or location. A measure was presented that showed a similar spatial pattern of penetrability into deep WM (PVI). The overall pattern of GM to GM afference (figure 4.7 E) bore striking similarity to the PVI measure (figure 4.9 E) This pattern was shown not to be co-extensive in a simple way with cortical curvature, "wedging" or DTI fiber angles over the macaque (figure 4.9) or marmoset (figure 4.13) brain. The profound differences in local diffusion orientation at the WGB in figure 5.2 A, and the tissue properties in B shed some initial light on these results in terms of more direct data from within the volume of the brain. To further explain the properties of the PVI measure and other diffusion data maps from the previous chapter (e.g. figure 4.10), we next investigated in detail specific instances of dMRI tractography from the cortex into the deep white matter that as an ensemble give rise to those summary scalar measures, in order to provide a concrete linkage from the 3D structure of the brain and dMRI scans to the scalar map methods and in order to directly assess tracking behaviors. Long-range cortical connections involve axons from a given cortical position passing through

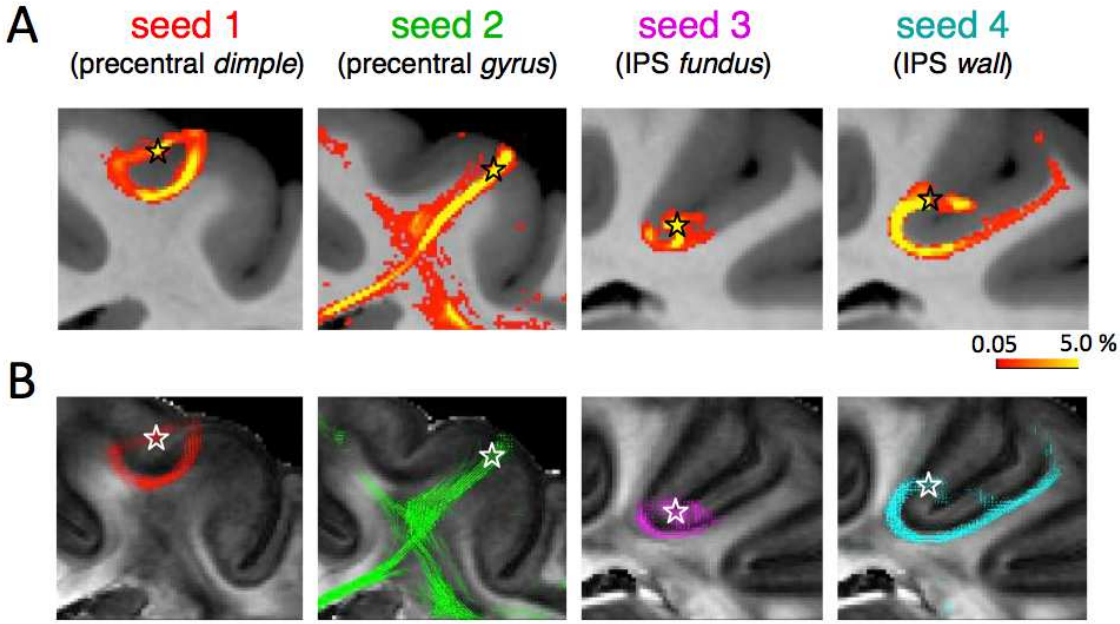

Figure 5.4: Equivalent gray matter seeding in both macaque datasets. Seeding is from two pairs of nearby positions, demonstrating that the precise positioning of gray matter seeds determines the success of tracking into the deep white matter. **A.** FSL track line density derived from four different seeds. Seeds 1 and 2 are less than 2mm apart in the dorsal motor region, whereas seeds 3 and 4 are less than 1mm apart in the intraparietal sulcus (IPS). In each case, 5000 probabilistic track lines were seeded from a single surface coordinate within the middle thickness of the grey matter. The color map indicates the percentage of the track lines that reached a given voxel. Despite the physical proximity and, in the case of seeds 1 and 2, functional and cytoarchitectural similarity of the seed regions, the track lines emanating from the four example seed locations varied markedly in their white matter penetration. Track lines emanating from seeds 1, 3, and 4 became trapped in local fiber systems and failed to enter the deep white matter. Probability tracks were overlaid on MTR maps. **B.** Tracks from each seed in A, shown as the dominant orientation in each voxel reached by probabilistic tracking, overlaid on FA maps. These show seeds and context for the 3D representation in figure 5.5.

the superficial white matter into the deep white matter and then on to a distant cortical or subcortical structure. The accurate detection of such connections using tractography requires that projections can be followed in contiguous voxels based on the local diffusion profile measured at each position. Capitalizing on the reliable diffusion orientation in the gray matter voxels of the present datasets, we were able to initiate tracking using pure gray matter seeds. In investigating specific instances of tracking behavior, we found that throughout the cortex track lines emanating from gray matter seeds always successfully crossed the WGB into the white matter. However, we found that despite the uniform entry of track lines into the superficial white matter, the subsequent fate of individual tracking attempts seemed strongly determined by the structure of the local fiber systems.

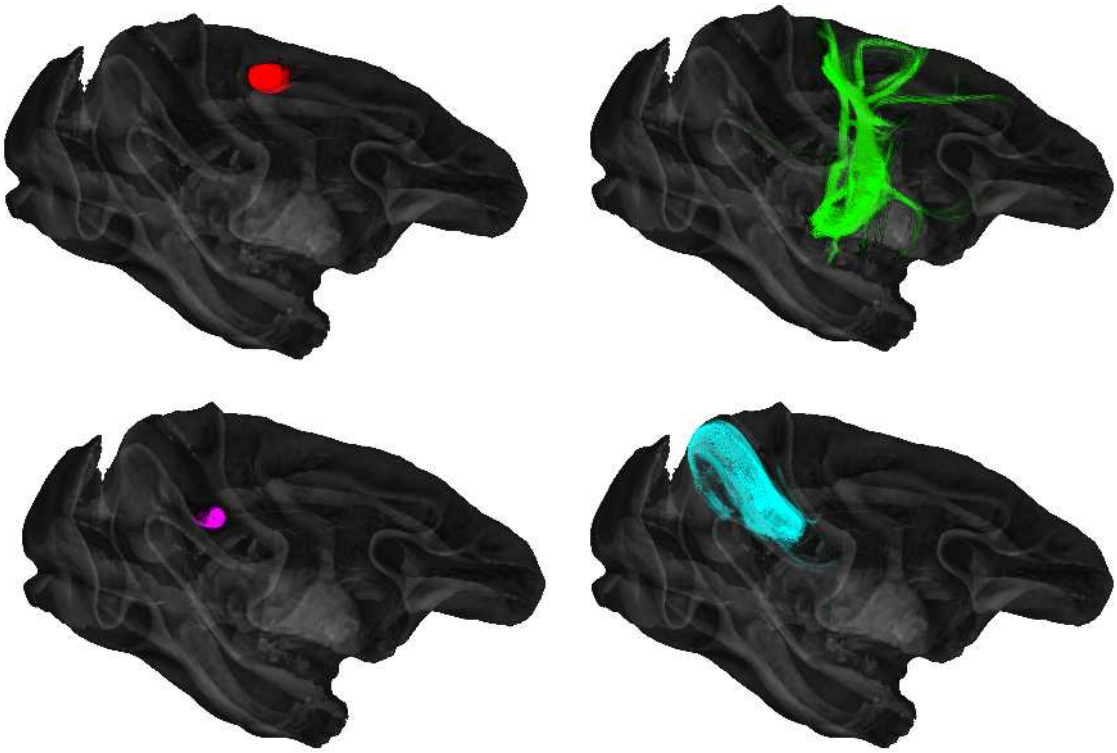

Figure 5.5: Tracking from seed 1 (red), 2 (green), 3 (magenta), 4 (cyan) in 3D from figure 5.4. Seed 2 shows fairly widespread coverage of the deep WM, 4 shows more limited tracking near the sulcal walls. 1 and 3 are restricted to the fundi of the SPCD and IPS respectively.

Specifically, track lines frequently became trapped within the particular types of superficial white matter and thus failed to reach the deep white matter or distant cortical targets. This observation is exemplified in four seeds from the dorsal motor cortex and intraparietal sulcus in both macaque data sets (Fig. 5.4), which were representative of sulcal and gyral locations in many other regions of the cortex. Although previous macaque anatomical studies have shown that each of these cortical positions gives rise to long-range axonal projections , we found that the resulting track lines in most cases failed to escape the local white matter environment. In fact, of the four seeds shown in this example only seed 2, on the precentral gyrus, extended beyond the superficial white matter and into the deeper white matter. In the brain of the second animal, the same gray matter seeds showed similar regional differences in their track line patterns, again with only seed 2 showing some deep white matter tracking. Figure 5.6 shows the PVI measure presented in the previous chapter. The seed points in the IPS (seeds 3,4) and PCG (1,2) are marked as stars, showing the underlying behavior of tracking giving rise to the PVI. seeds 1 and 3 have low values (36.8 and 23.2 ppm), while 2 and 4 have large values (143.9 and 75.6 ppm). The measure shows a larger value for seed 2 than 4, but not in a way that unambiguously

reflects the greater diversity of track trajectories from seed 2 or their penetration into deep WM. The ancillary measures in figure 4.10 showing track spread (PVS) and PVI scaled by PVS (PVI/PVS) help complete this picture. Overall low PVI shows failure to enter deep white matter, while higher PVI is suggestive of deep WM penetration but may indicate behaviors seen in seed 4 (looked at in more detail in section 5.6). Taking the PVI value for seed 2 as a conservative threshold for penetration into deep WM, we find only 24% of seeds have a PVI greater or equal to it, suggesting only those seed points lead to deep WM penetration. However, correcting for PVS yields a somewhat larger value by including gyral regions with focused callosal and cord connectivity e.g. dorsal motor regions patterns. The patterns were similar in both monkeys. The intermediate PVI value and trajectories for seed 4 reflect the "neighbourhood" superficial fiber system at the IPS connecting the SPL and IPL (Schmahmann and Pandya, 2006). The local fiber anatomy at the IPS is explored in detail in section 5.6 using both dMRI and histological data.

The Tracking from the four specific seed regions chosen indicate that the properties of the superficial white matter play the defining role in whether tracking proceeds into the deep white matter to potentially estimate long range connectivity, or is instead trapped near the seed region. Figures 5.4,5.5 and 5.6 indicate that the PVI method produces a scalar metric over the cortex that reflects whether long range penetration of tractography is viable from a GM seed location, and by proxy information about the anatomy of the superficial white matter. The PVI and other scalar maps, as well as the analysis in figure 5.4 and 5.5 concentrate on penetrability into deep WM when seeding from the cortical GM. Gyral bias has been typically (Van Essen et al., 2013) examined when seeding from the deep WM to the GM. Figure 5.7 seeds 1000 lines from each of 20,000 white matter surface nodes surrounding the corpus callosum, optic tract, thalamus and other forebrain structures, and the internal capsule. From these WM (in particular the Corpus callosum and internal capsule) and other subcortical structures, in the entire cortical GM is anatomically reachable. Seeding every WM voxel is not computationally feasible. The pattern of intersections with the WM surface and midthickness GM is shown lower left. A negligible number of tracks reach sulcal walls and fundi as expected. The slice upper left shows GM terminations on outfolds. the zoomed regions to the right show a crown and a fundus. At the fundus, tracks stop well short of the WGB line, and a large band of high anisotropy is visible (white arrows). This suggests that a superficial WM fiber structure, rather than any other factor, is the primary or most fundamental reason why tracks fail to terminate in the GM of the fundus. We next examine the superficial white matter tissue

itself in the context of tracking behaviors.

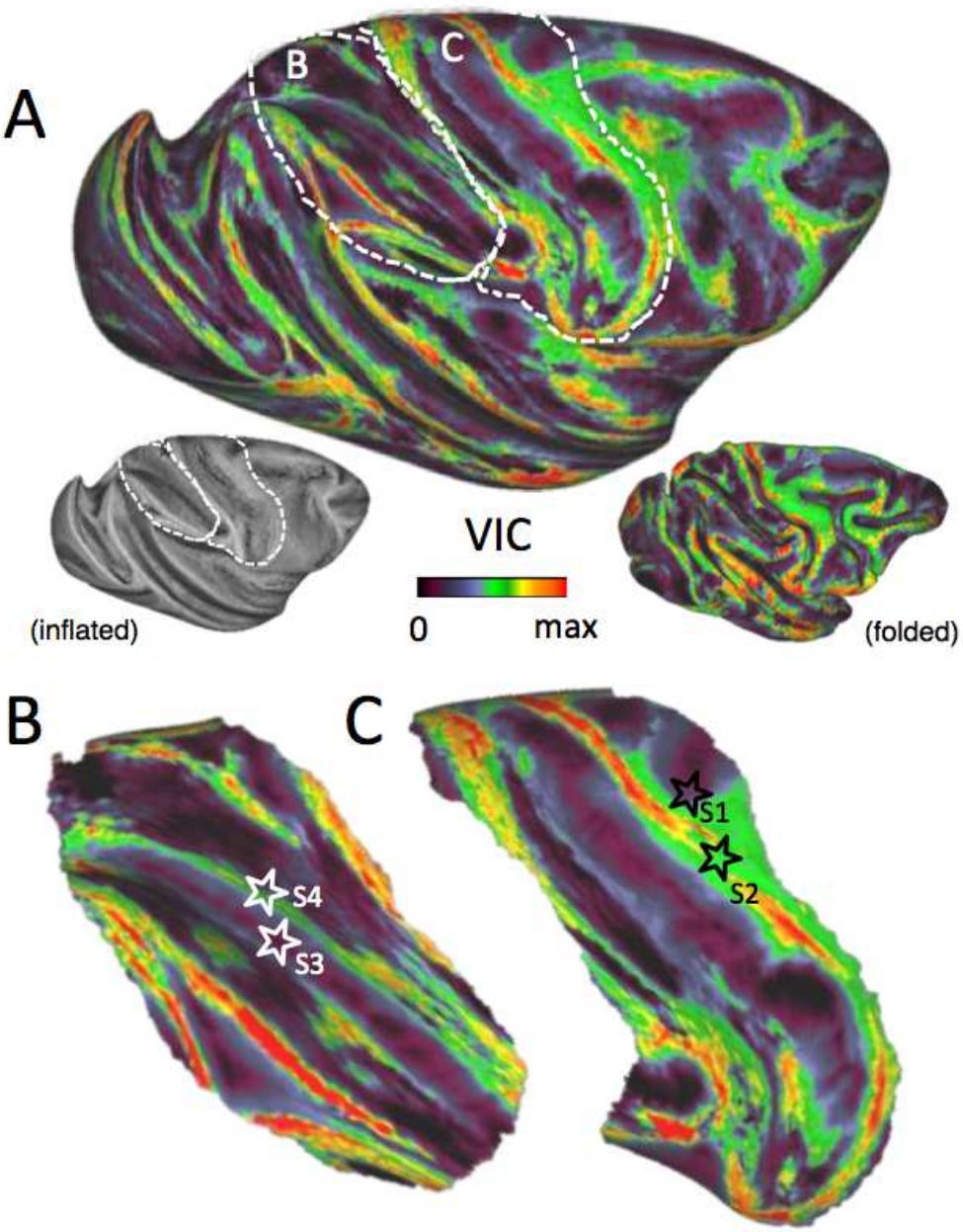

Figure 5.6: **A.** Map of PVI from the gray matter of an entire cerebral hemisphere. The PVI is a normalized measure of how many voxels the track lines reached from a given gray matter seed. As such, it indicates the success of tractography from a given cortical position in forming long tracks. Each cortical surface node was seeded 200 times and the number of voxel intersection events was recorded. The PVI index reflects both the number of voxels that were reached and also how often they were reached over multiple instantiations of the probabilistic tractography (see section 2.4.2 Methods). **B.** Intraparietal sulcus region, including the positions of seeds 3 and 4 from Fig. 5.4 (white stars), seeded 1000 times. C. Central sulcus region, including the positions of seeds 1 and 2 from Fig. 5.4 (black stars), seeded 1000 times.

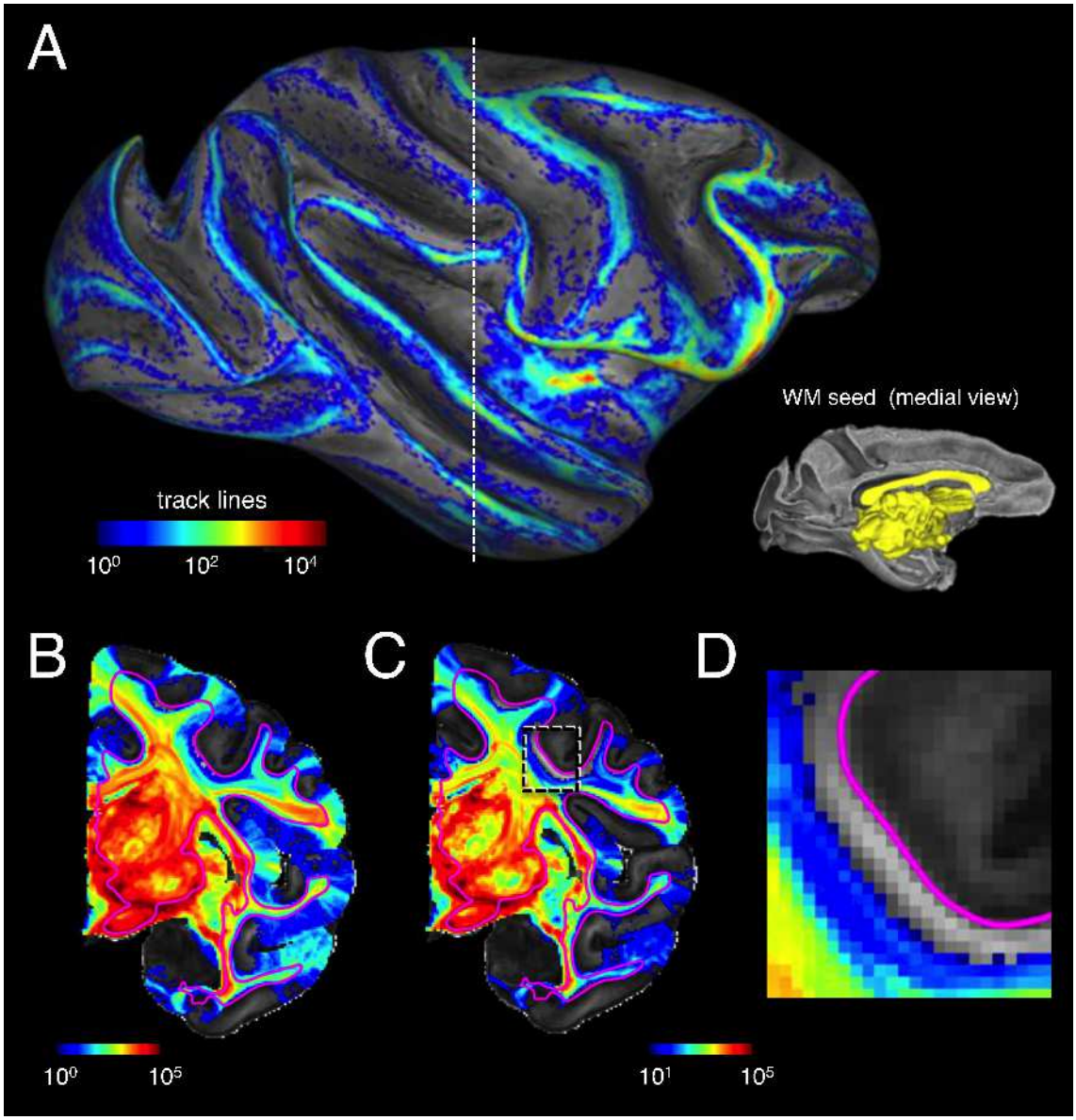

Figure 5.7: . Penetration of track lines into the cortex following white matter seeding. **A.** Cortical labeling of track line penetration following massive white matter seed that includes the internal capsule and corpus callosum (yellow region in inset). **B.** Seeding resulted in a massive spread of track lines across the hemisphere but a rather limited and heterogeneous penetration into the gray matter. In this figure, there is no threshold in the probabilistic tracking, thus areas without color did not receive a single track line following the massive white matter seed.**C.** Same as **B**, but with a threshold of 10 track lines, allowing for visualization of a large portion of the cerebral cortex for which long-range tracking is almost nonexistent. **D.** Magnification of a portion of the central sulcus with the same threshold as **C.** This region of white matter, approximately 1mm wide running just below the WGB, along with the overlying cortex, is devoid of any afferent track lines. Together, this analysis shows that even with massive white matter seeding, significant portions of the gray matter do not register long-range inputs.

5.4 Superficial Fiber Structures and Tracking Behaviors

Thus far, the evidence that the structure of the superficial white matter acts as the primary barrier to diffusion tractography entering the deep white matter or leaving it to terminate in the GM has been inferred from the patterns in diffusion imaging itself. Here we reify these anatomical structures by showing tissue sections from the same brains scanned and analyzed with dMRI. Later in section 5.6 we explore these fiber structures in detail in the IPS region. Figure 5.8 A shows GM seed patches in sulci. Each patch contained 800-1500

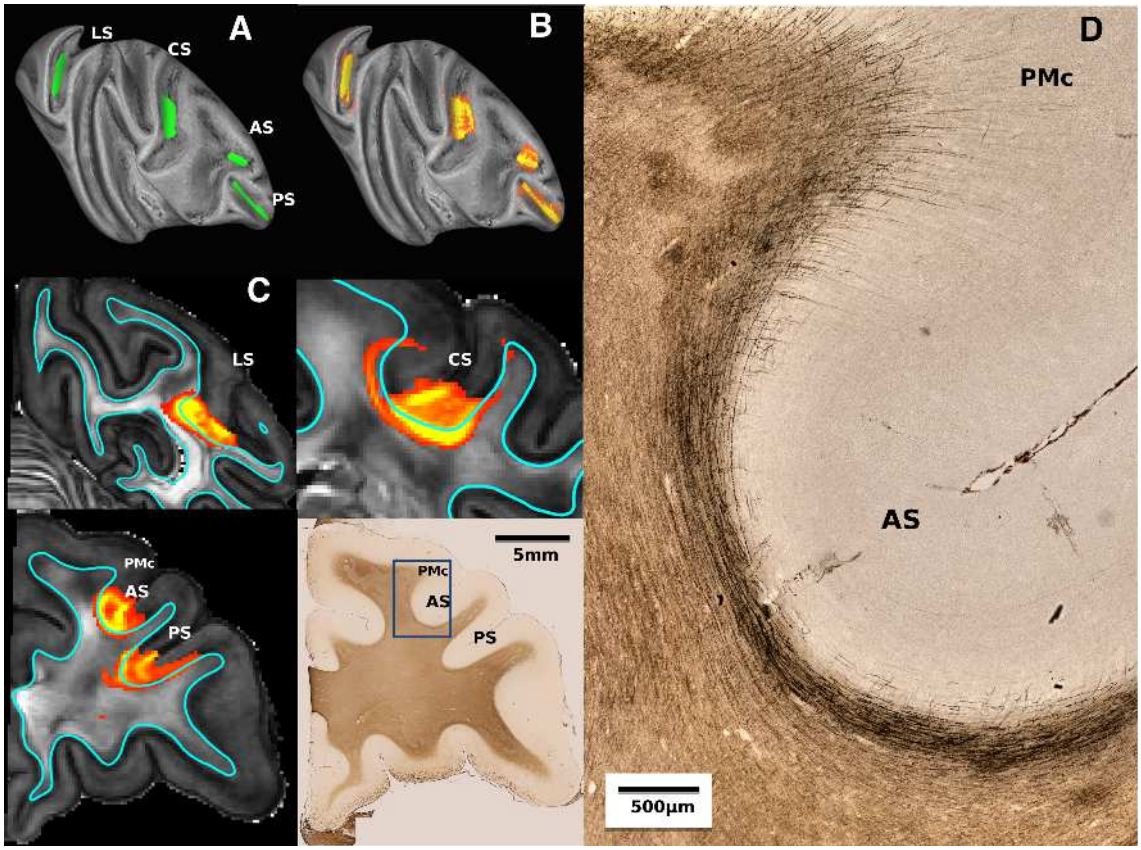

Figure 5.8: Examples of broader gray matter seeding in sulci. Despite the larger seeding regions, the track lines are restricted due to the impenetrability of the dense U-fiber bundles in the superficial white matter. **A.** Larger seed regions in four prominent sulci. **B.** Track lines from these seed regions remain restricted to the local sulcus environment and fail to produce labeling elsewhere in the cerebral cortex despite the known long-range projections. **C.** Visualization of the white matter distribution of the track line spreading for each seed in **A**, together with myelin-stained histological slide corresponding to two of the seeds. **D.** Magnified view of myelin stained histological section in the vicinity of the arcuate sulcus featured in the histological section in **C**. Stained fibers in the superficial WM surrounding the sulcus are generally parallel to the white matter/ gray matter boundary, whereas those at the adjacent gyrus are primarily radial in their orientation. This difference in local fiber structure is the primary driver of to the penetration bias associated with gray matter seeding, and with "gyral bias" more generally. (Abbreviations: LS, lateral sulcus; CS, central sulcus; AS, arcuate sulcus; PS principal sulcus; PMc, caudal premotor).

nodes, and 5000 lines were seeded from each node. From the resulting tractography, the sum of all tracks intersecting the GM surface is shown in fig 5.8 B. Within the brain, the density of tracklines is shown on a representative slice of MRI in figure 5.8 C. Of the millions of seeded tracks, a negligible number enter the deep WM. Figure 5.8 D shows a blow up of contrast enhanced Gallyas stained tissue at the arcuate sulcus and dorsolateral premotor cortex, in a gyral crown region. The light staining reduces the visibility of GM axons in order to show WM structure more clearly. nevertheless, radial myelination is visible in PMc while at the fundus tangent or matted myelination is evident. subjacent to the fundus a band of myelinated axons parallel to the WGB is prominent. This local fiber is the anatomical feature preventing tracking into the deep WM. In section 5.6 it is shown via tracer injection that fibers pass through these structures.

Figure 5.9 shows the relationship of local fibers/radial myelin in more detail in this region. Figure 5.9 A shows a region of radial GM myelination on the cingulate gyrus, the superficial white matter also appears radial and directed towards the GM. 5.9 B shows the GM and superficial WM in the arcuate sulcus (see figure 5.8 D and description). These regions are shown as green (A) and magenta (B) insets on the entire section (E). Figure 5.9 C shows GM seeding of tractography from within the gyral region shown in A. On the slice, tracklines appear to enter the deep WM. The rostrocaudal extent of this tracking is shown as green tracklines in a 3D inset, tracks reach as far as the parietal lobe. Figure 5.9 D shows the equivalent for the sulcal seed. tracks are limited to the superficial WM. The radial myelin and radial superficial WM structures provide an intuitive explanation for why diffusion models the GM and WM fiber structures well and permits tracking along them in the vicinity of the seed. Similarly the pattern of local fibers in the sulcus gives an intuitive explanation as to why local water diffusion favours pathways within the superficial WM, tangent to the GM radiation. We note from figure 5.3 that the superficial white matter around gyral regions often lacks a secondary distribution of anisotropy. Since the FSL model is parameterised to account for as much of the anisotropic signal as possible within the first model ("ARD"=1) and only model secondary fibers where signal remains unexplained, we may conclude that the radial myelination is often co-existent with strong radial WM projections, and in many gyral regions lacking a second distribution, the first fiber in superficial WM is orthogonal to the WGB. The lower left of figure 5.10 shows an enhanced, processed analysis of high magnification Gallyas showing the white matter axons at the edge of the frontal operculum (a region with complex folding in this animal) are indeed very coherent and radial, as are the GM axons in the raw Gallyas in the upper

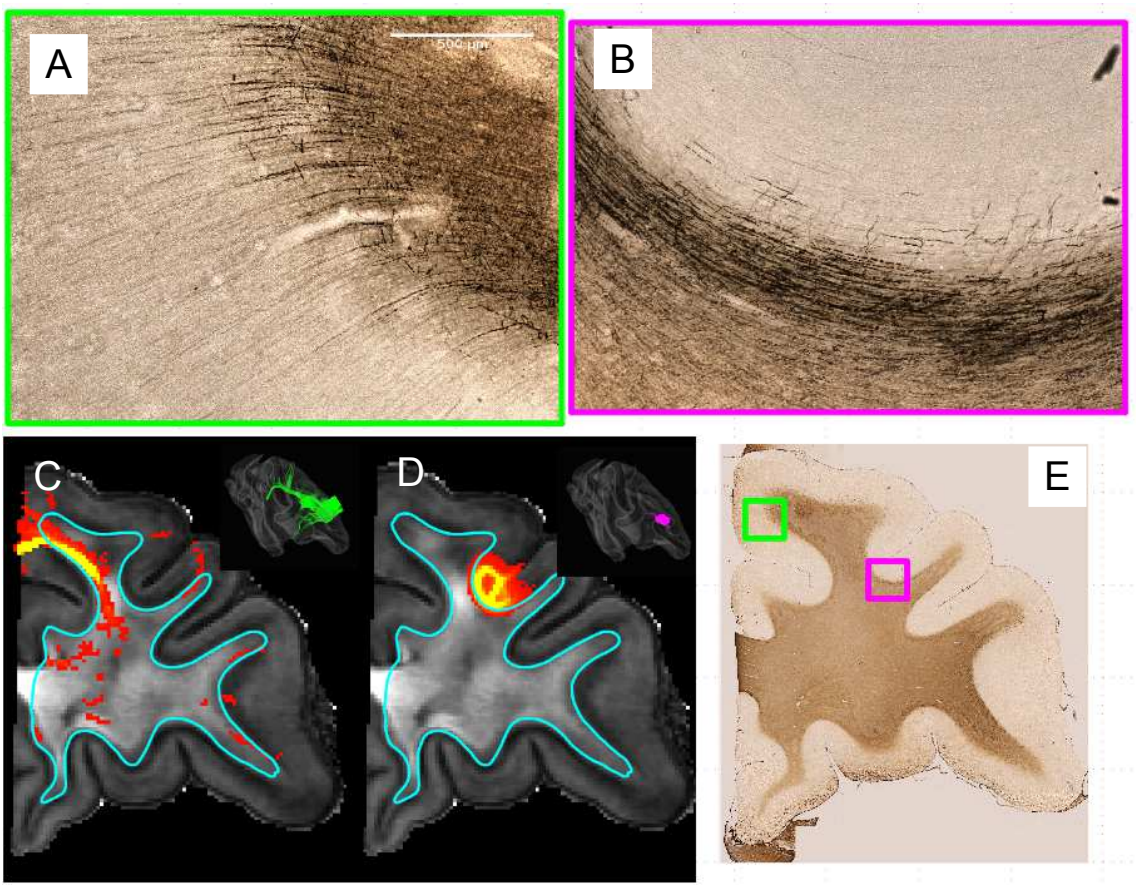

Figure 5.9: **A.** radial myelin in GM and WM on PMC, **B.** U-fiber on arcuate. **C.** GM seeded tracking from the region approximating that in **A** spreads into deep WM, and also caudally and ventrally (green inset) **D** As with figure 5.8, seeding in the Arcuate sulcus is restricted to the local fiber system (magenta inset). **E.** The histological slice corresponding to **C** and **D**, with the regions for **A** and **B** outlined in green and magenta respectively

pane of figure 5.10 S6.

Taking all distributions into account, regions where superficial WM orientations are orthogonal to WGB tend to be gyral crowns and ridges, notably not all crowns (section 5.4.1. As noted in section 4.3.3 figure 4.9 the pattern of fiber orientations in superficial WM does not fully account for our patterns of penetration into deep WM however, but it may accurately reflect regions of radial myelin in GM and subjacent WM. Figure 5.10 shows in the upper half, tracking and terminations from the thalamus and CC. At each of the labelled regions, Gallyas histology is shown. S6 and S5 contain radial myelin, somewhat complicated by the small caudally oriented fold this animal exhibits at the lateral extreme of the central sulcus. Nevertheless the axons are radial, and correlate to tracking terminations. S7 at the rostral tip of the IPL shows clear radial axons (as in figure 5.2). Regions S8 and S2 show no tracking intersections, and matted myelin. S8 on the IPS fundus is described in figure 5.2. Region S2 lies on the wall of postcentral gyrus

in somatosensory areas 1/2. The highly matted myelin is marked.

In the lower part of figure 5.10 the white matter subjacent to the cortex in region S2 is examined by image processing and enhancement. In contrast to the radial axons in the WM at S6, at S2 a dense, complex thatch of small fibers in a band is clearly visible. This shows the architecture of the local fiber to be comprised of many small axons in a complex arrangement along the wall. While local fibers and matted GM axons appear together frequently, they do not always. No causal relation is posited between the two in this research.

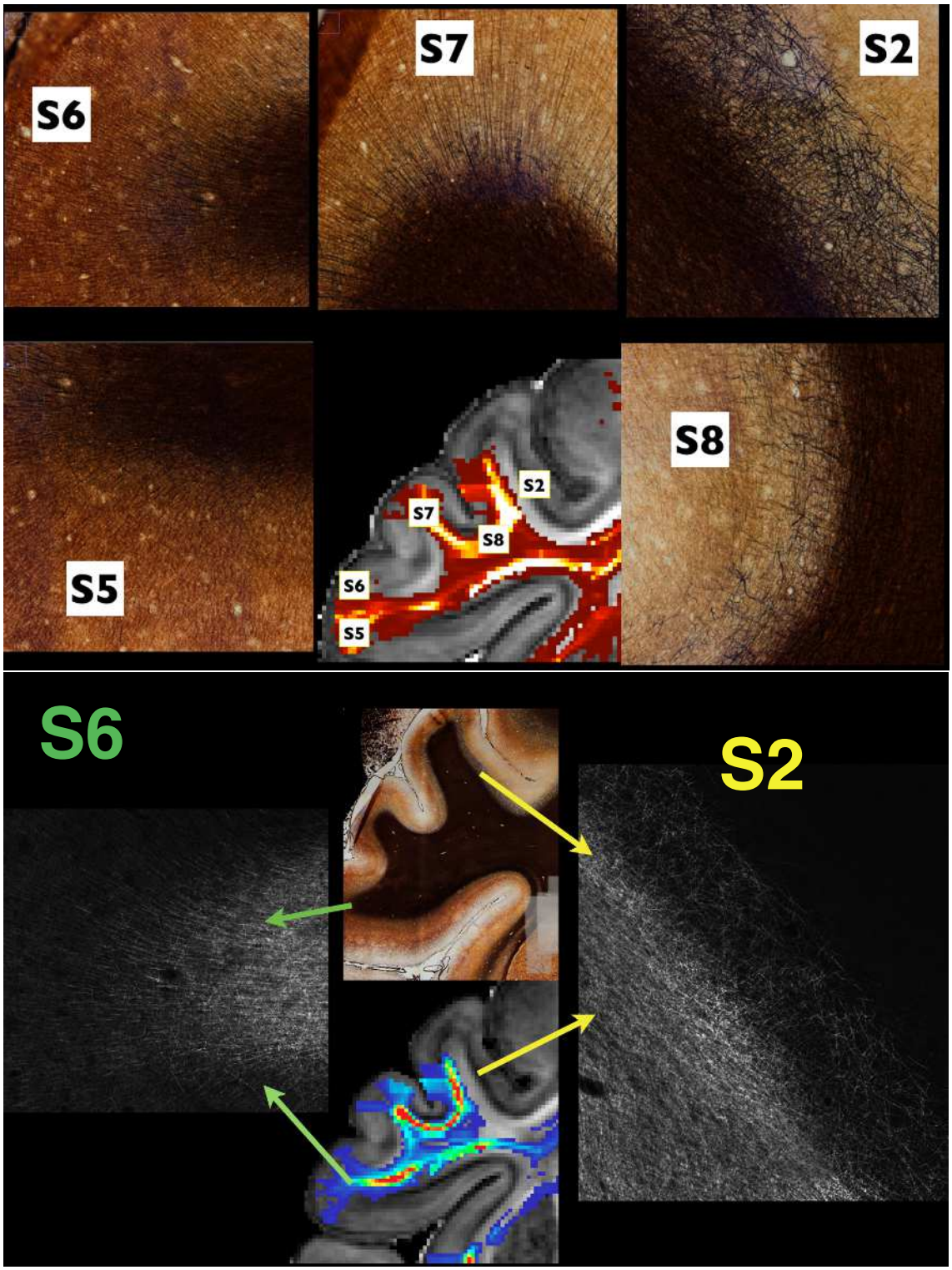

Figure 5.10: **TOP:** 5 Myelin stained regions of the GM/WM boundary (10x magnification). Each corresponds to the FA map in the lower central panel. The MR data contains representative WM tracking to the GM. At S2 and S8 we see no penetration into GM. S2 lies on a gyral wall with dense, matted GM myelination. S8 on a fundus. S5,6,7 show penetration into GM and radial myelination on or near outfolds. **BOTTOM:** Regions S2 and S6 grayscaled and processed with CLHE contrast enhancement. S2 shows the presence of a distinct band of WM fibers beneath the WM with a tangled pattern of axons compared to the subjacent WM. S6 more clearly show the radial projection of axons into GM in a way that is congruant with the WM myelin: S2 ufiber visible, s6 radial WM. grayscaled, reciprocal CLHE

5.4.1 Crown Fibers

Local association u-fibers running subjacent to the cortical sheet are well known (Schmahmann and Pandya, 2006) and see figure 5.20. In chapter 1 we noted that under a theory of cortical folding such related to axonal tension (Van Essen et al., 1997) between functionally related regions, convolutions form as axons projecting between regions of tissue that strongly associate (e.g. V1 and V2) create physical tension forming a gyrus or operculum (V1 and V2 are on posterior and anterior sides of the occipital operculum/pole). Thus, the distance between V1 and V2 is minimized. Importantly, no axonal paths hugging the sheet are ever lengthened. ufibers between gyri are thus the shortest straight line path (whether or not there is folding).

It might follow then that the region of the sheet corresponding to the long axis of a gyral blade/crown would also retain subjacent fibers as the shortest path between cortical regions lying on the crown itself. For exactly the same reason that local fibers are the most efficient way to connect regions on the walls of adjacent gyri, local fibers may be the most efficient way to connect regions separated by the long axis of a gyral crown. Such fibers might form barriers to tractography.

We have already noted that the PVI measure and other scalar maps assessing penetration into the WM from the GM in section 4.3 showed tracking from many gyral crowns or more generally regions of zero or positive curvature failed to penetrate into deep WM. Figure 5.11 shows histological, MRI, tracking and PVI surface scalar map from the crown of the IPL. Seeding tracking on the IPL reveals a long, local fiber Figure 5.11 B, A. Figure 5.11 F and I show that the crown of the IPL where the seed patch is located has low PVI, although the ventral ridge of the IPL has a much higher PVI. Figure 5.11 D and E show the FA map and myelin histology as coronal sections, outlining the crown and ridge regions. Figure 5.11 E and F show the Primary diffusion orientation is distinct at the crown, almost orthogonal to the rest the gyral WM. H analyses the myelin histology using the pixelwise structure tensor method (at 1μm per pixel). The tissue also appears to show an orthogonal fiber structure in the superficial WM of the crown. The dorsal and ventral ridges show axons orientated radially into the GM.

Figure **??** Shows the first, second and largest fiber angles pointing into the WM with respect to the WGB, and PVI map. Note that while the fiber orientations were calculated from the WGB surface, but the PVI from the mid, the orientation data displayed on the mid impinges onto a slightly larger area of surface. The data shows that the primary fiber is parallel to the WGB on the IPL crown. A secondary fiber exists that is orthogonal to

the WGB but only on the ridge. This is in congruence with a local fiber explanation for low PVI.

In figure 5.13 we show that the crown fiber is a discrete, continuous entity in WM. The coordinate space of the brain such that the 3 axes were defined with respect to the crown of the IPL gyrus (figure 5.13 top left). The primary diffusion vectors were then rotated into this coordinate space. Thus transformed, it is clear the crown fiber is a discrete bundle running the length of the IPL crown superficial WM and dominating anisotropy.

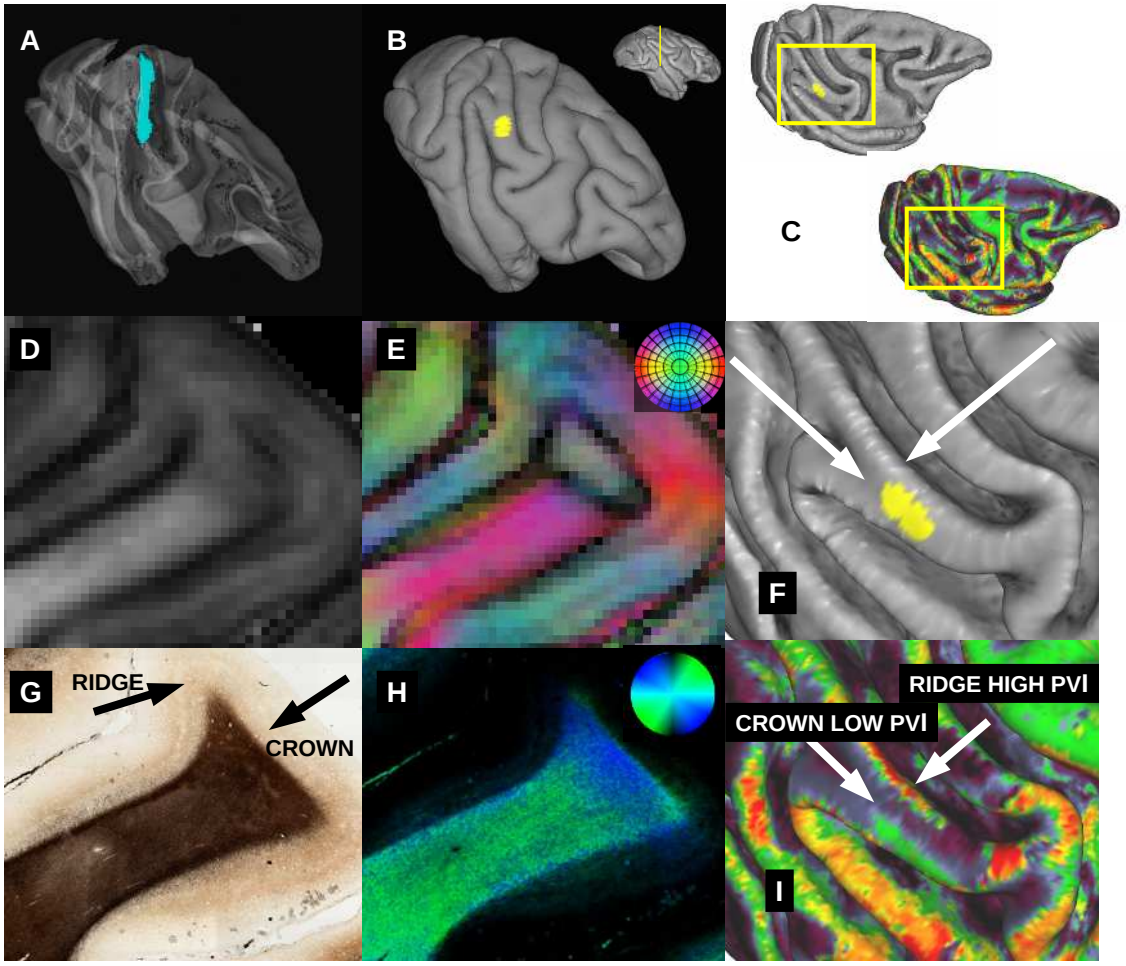

Figure 5.11: Example of gyral region in which tracking is restricted by crown fibers. A. Track lines emanating from the gyral seed are trapped within the local environment, but in this case running along the gyral crown. B. Position of seed location in the ventral IPL (yellow) and the slice plane of the dMRI and histology sections in C and D (dashed line). C. Surfaces showing cortical curvature (upper) and PVI maps, with the detail region shown in F. and I. outlined as yellow boxes. D,E. Maps of fractional anisotropy, and directionally encoded color (DEC) maps in the region shown in B illustrate a clear directional compartmentalization, reflecting the dense bundle of longitudinal fibers running along the gyral crown. These crown fibers result in track lines propagating along the gyrus (white arrow) but act as an impenetrable barrier for track lines entering the deeper white matter (black arrow), similar to the effects of U-fibers in fundus regions. F. Detail of cortical surface in the IPL region showing the seed patch on the gyral crown and the gyral ridge (upper arrow). G,H. Histological section of the same tissue (in the same area) reveals a similar compartmentalization of the white matter. While the myelin stained section (left) reveals a largely uniform appearance of white matter at the crown, analysis of fiber orientation (right) shows that the fibers in the crown do not have the same radial orientation as the deeper fibers, similar to the DEC map. Orientation analysis used the principal eigenvector of the four-element structure tensor (see Supplemental Methods). Black and white arrows indicate the same orientation compartments as in E. I.PVI map at the region highlighted in C. and F. showing the heterogeneous penetration of track lines from gray matter positions along the gyrus, in this case the IPL. While the PVI values along the gyral ridges are relatively high, indicating that those regions can participate in long-range cortical connections, those along the gyral crown are much lower, reflecting the barrier posed by the longitudinal crown fiber system.

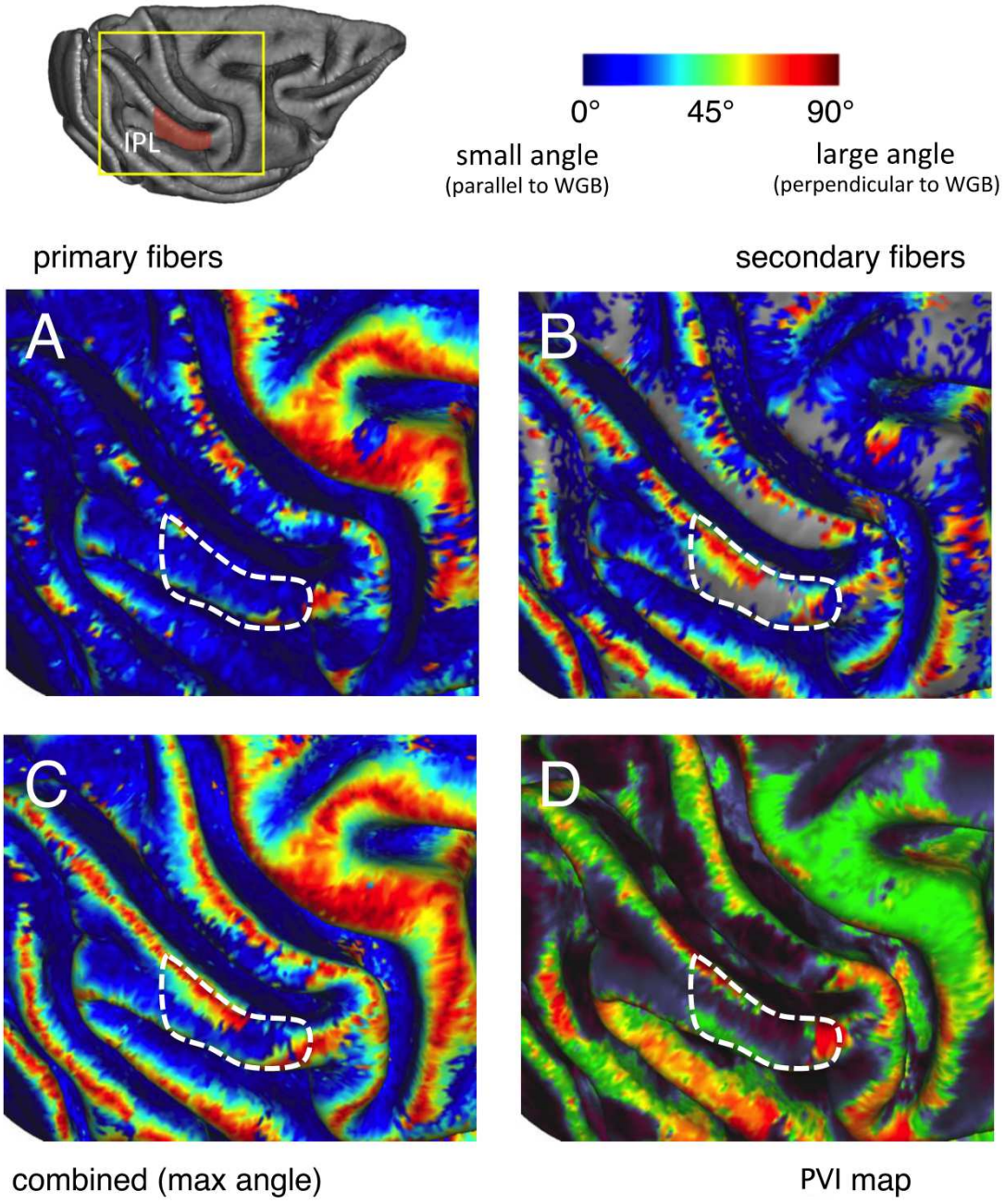

Figure 5.12: Angular (dot product) composition of superficial white matter voxels associated with the crown fiber bundle. The colors in the first three maps correspond to the fiber angle relative to the local WGB surface. **A.** Relative angle of the primary fiber in each voxel. **B.** Relative angle of the secondary fiber in each voxel, with blanks where no secondary fiber could be found with f>= 0.01. **C.** Maximum of the primary and secondary angles for each position. Note that there are many positions for which the maximum angle in the superficial white matter is parallel to the WGB. **D.** Comparison of same region with the VIC map, corresponding to the penetration success of cortical seeding.

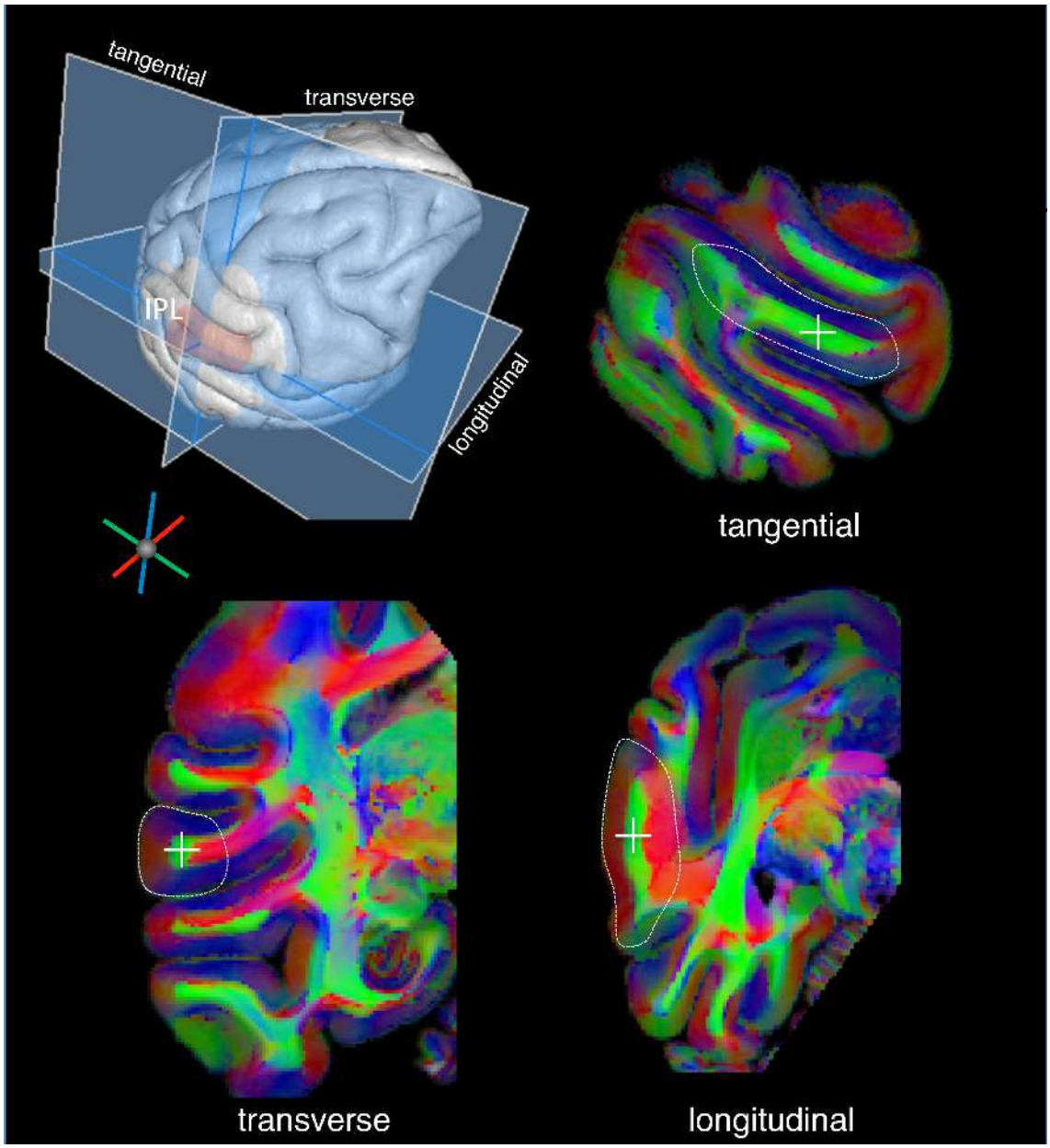

Figure 5.13: Diffusion data rotated so that Crown of IPL defines the coordinate space. Visualization of the crown fiber bundle featured. The dense fiber bundle running parallel to the inferior parietal lobule is here shown from three different angles. Colors correspond to standard directional encoding (DEC) derived from principal DTI direction measured at each voxel. The data rotation permits clear visualization of the fiber as having a consistent "rostro-caudal" (green, with respect to the rotated coordinate frame) orientation in all three planes along the IPL crown

5.5 Superficial Fiber Structures and Tracking in the Marmoset

In sections 5.4 and 5.3 we examined seeding into the WM from GM and from the WM to the GM in rhesus. While the picture of local fiber architecture that emerged was complex, it remained the case that gyral crowns exhibited greater penetrability than sulci, suggesting a very loose correlation with folding properties as described in chapter 1.

The marmoset brain is largely lisencephalic, although it does posses a sylvian fissure and superior temporal gyrus, as well as outfolding regions at the midline, frontal operculum and pronounced folding within occipital lobe. Large portions are lisencephalic nevertheless. In figure 5.14 We show the results of seeding a surface patch of roughly 500 nodes with 5000 lines in the data set R. The 150μm summed track density are displayed in figure 5.14 A on top of coronal slices of the 75μm Magnetization weighted scan of the animal. Tracks are visible in GM, however in WM they stay near GM in a band. This band of WM is visible as a distinct intensity difference in the anatomical scan. figure 5.14 B shows seeding from the corpus callosum. In this case, tracks rarely enter GM or the outer band of WM (explaining the result in figure 4.13 C).

Figure 5.15 Shows these two white matter bands clearly in DTI from scan R. Nissl histology from another animal shows the orientation of oligodendrocytes is strikingly different in the inner and outer WM bands. We may conclude that the marmoset GM contains superficial WM across the entire cortex. Quite possibly because without path shortening by folding, the cortex is essentially a sheet in which the shortest distance is a straight line. The central white matter may contain longer distance fibers (e.g. LGN to V1)

Figure 5.16 examines this further. The diffusion data for R was carefully rotated to a myelin histology slice. A,B and C show the 2D structure tensor analysis, raw histology and 75μm upsampled DEC map in the same slice of R. D,E and F show the boxed regions zoomed in. in D, an inner and outer set of orientations is clear. in E (which has been locally contrast enhanced), the raw histology clearly shows a band of superficial WM with distinct properties to the deeper WM. in F, the DTI shows and inner fiber oriented rostrocaudally, and an outer dorsoventrally. In G we performed a Q-Ball analysis of the DWI data in R at 150μm. using deterministic tracking we placed a seed in this outer, local fiber system. tracks remained local. moving slightly into the deep, the tracks showed a dense formation of long range tracks.

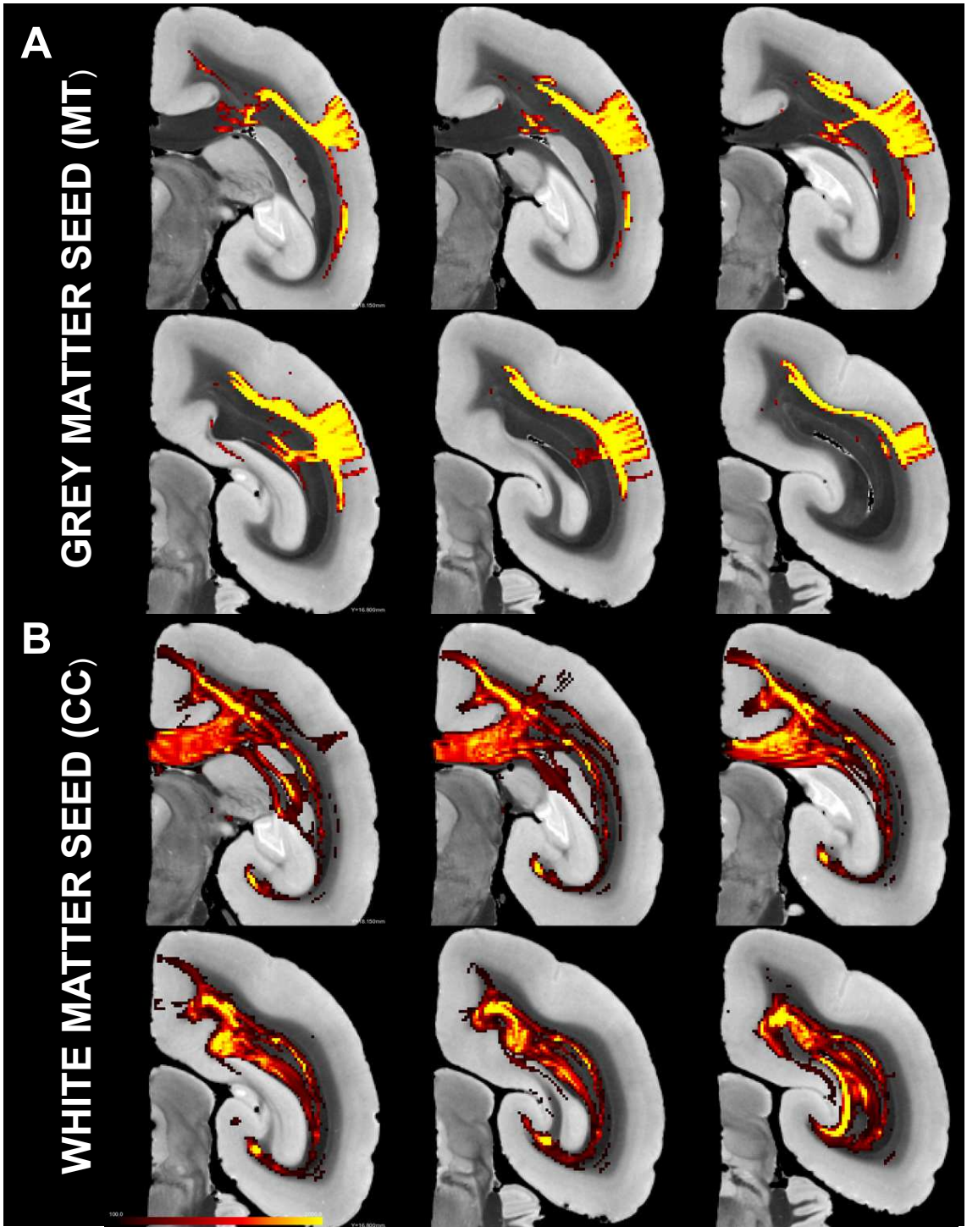

Figure 5.14: **A.** Six coronal slices in marmoset parietal and temporal lobes. The structural MR is magnetization transfer weighted acquired at 75μm running Left to right, top to bottom from rostral to caudal. Overlaid is FSL tractography from a GM surface patch in roughly in area MT, from the same brain (diffusion data at 150μm, see section **??** methods). Note the tracks that enter the WM tend to remain in a band subjacent to the GM. **B.** the same regions, seeded in the corpus callosum. Tracks remain in deep WM avoiding the superficial WM and GM.

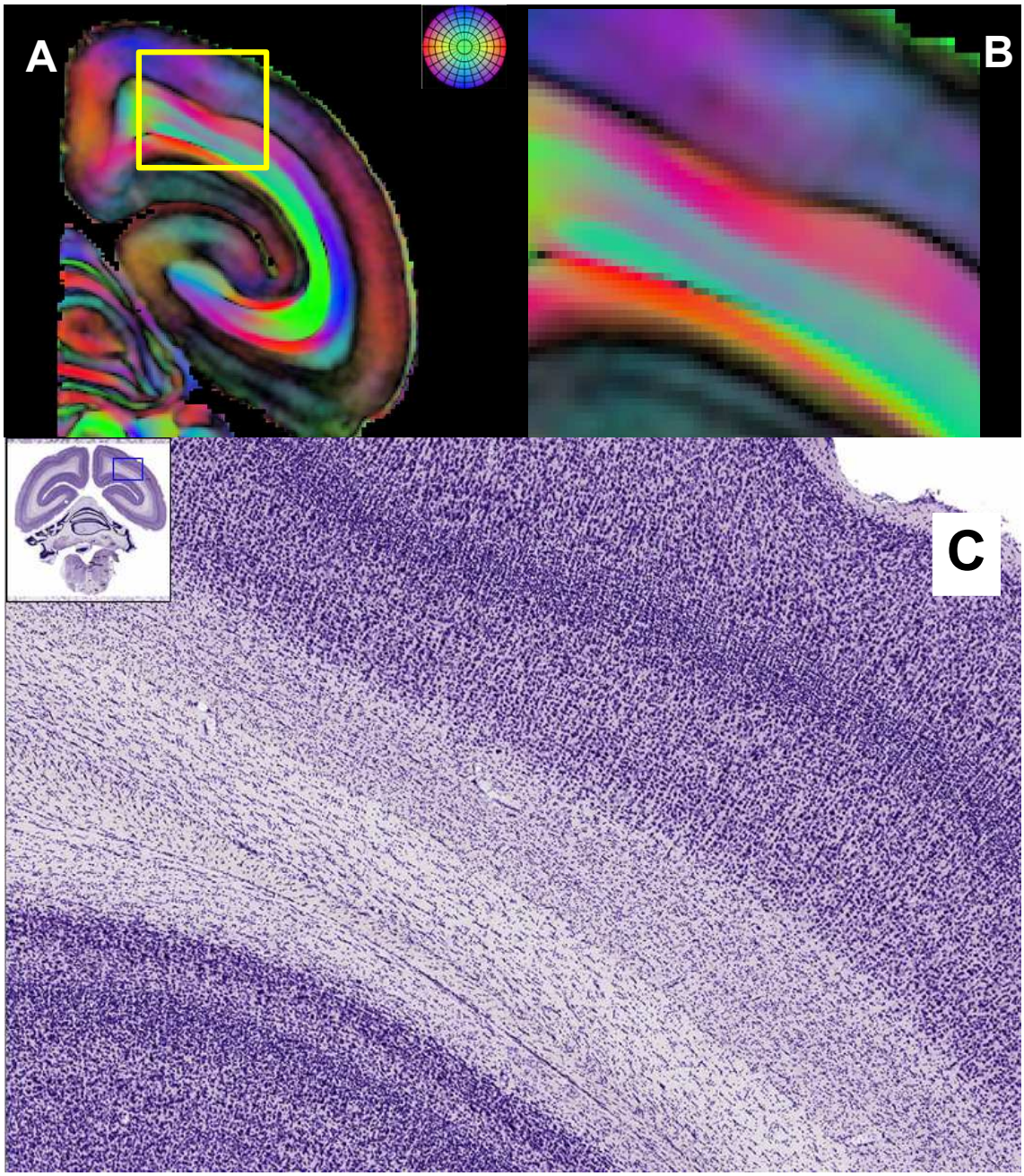

Figure 5.15: **A** Coronal section of the FA map of marmoset DTI in striate and extrastriate cortex (150um isotropic upsampled to 75um) colored by the primary eigenvector. While the directionality of anisotropy varies, and the white matter contains subtlety, a clear structure of an inner rostrocaudal fiber and outer medio-lateral/dorsoventral local fiber is evident. **B** inset showing a dorsal local fiber, ventral local fiber and inner long fiber. especially the ventral local fiber exhibits variation and subtlety. **C** A similar nissl stained region from a different animal. The beading patterns in WM indicate the slight dorsomedial curve of the heavily myelinated central long fiber system in this dorsal region. The beading in the dorsal local fiber is consistently mediolateral, but more diffuse, perhaps indicating more but smaller caliber axons. The complexity of the ventral u-fiber is mirrored in the DTI and nissl beading.

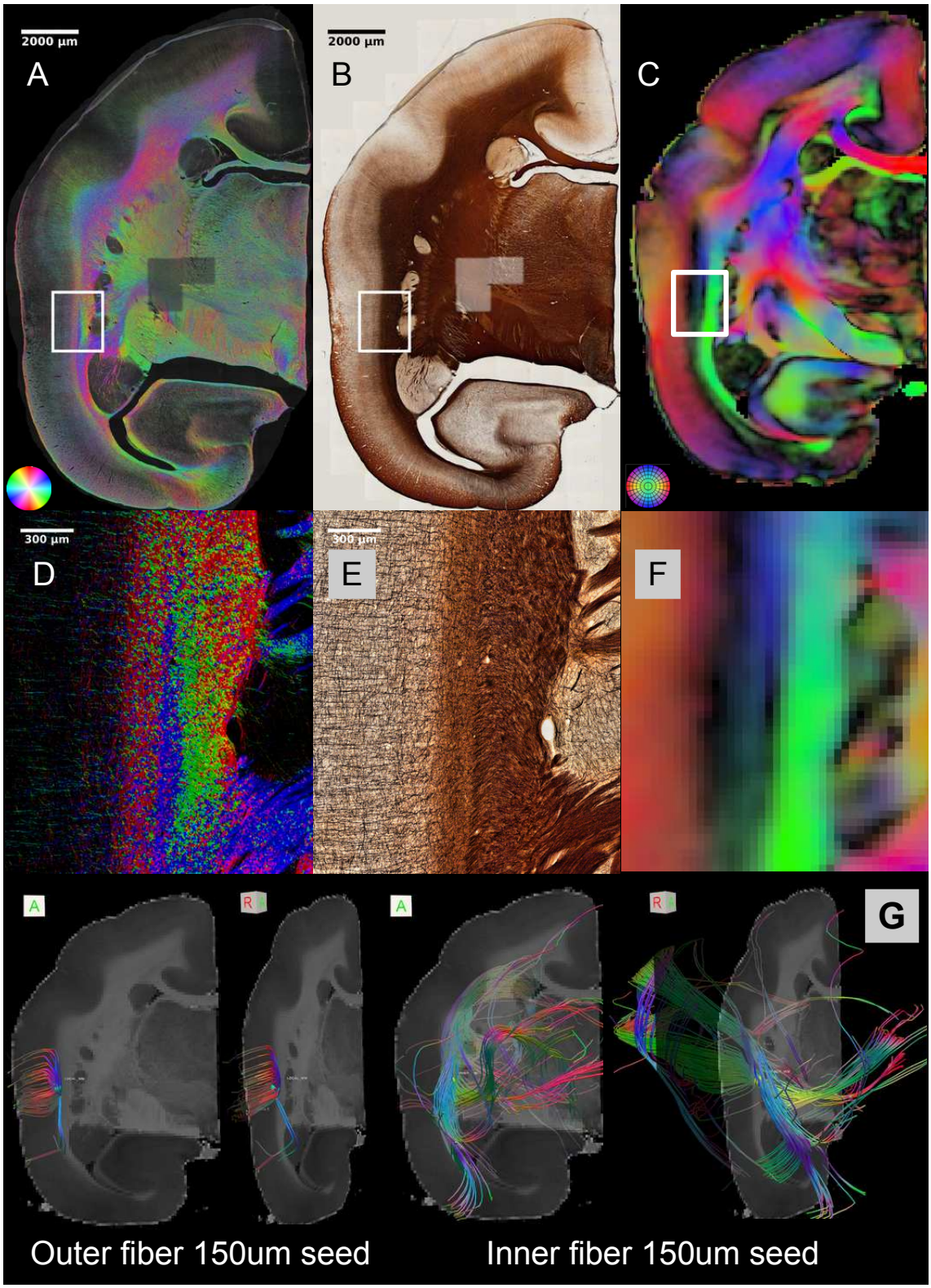

Figure 5.16: **B** Coronal, myelin stained section of marmoset. **A** pixelwise structure tensor analysis of B (1um per pixel) **C** The Linear map in the same tissue, colored by the primary eigenvector of the DT (150um upsampled to 75um). D-F show insets revealing two fiber systems, one close to the GM one deep. The DTI shows near orthogonal 3D anisotropy. The stain shows the fibers as distinct. The ST (2D) shows orientations at right angles (green v red) in the two fibers. **G** seeding a small region (75um radius sphere) in the outer and inner fiber regions of a Qball reconstruction and tracking shows the extent to which one is a large, long fiber system, while the other is local. The DTI and Histology data is carefully matched for precise rotation and location.

5.6 Anatomy and Diffusion at the IPS

In this section we first make a final examination of the dMRI issues at a local fiber region (the IPS), and demonstrate that it does not adequately model the connectional anatomy, though does model local fiber systems. We finally then discuss the local fiber anatomy in this region in detail, and what it's relationship with brain function may be.

5.6.1 Diffusion Tracking and Anatomical Tracing in the IPS

In Section 4.2.3, figure 4.4 **E** and **F** we showed long range retrograde GM labellings from an injection roughly in the area shown in figure 5.19. Our explanation for the failure of high resolution tracking has been related to local fibers. In this section we finalize this conclusion. In figure 5.17 we show the low PVI on the fundus of the IPS (seed 3). We show that at the fundus, in many areas 3 distinct fibers are found by the FSL system, all are parallel to the WGB suggesting anisotropy is strongly dominated by local fibers.

Figure 5.18 confirms that tracks pass through the local fibers in the approximate location of 5.21. the issue lies with dMRI.

Finally, referring back to discussions of spatial resolution figure 5.19 demonstrates the inadequacy of varying seed placement and inaccuracy of low resolution.

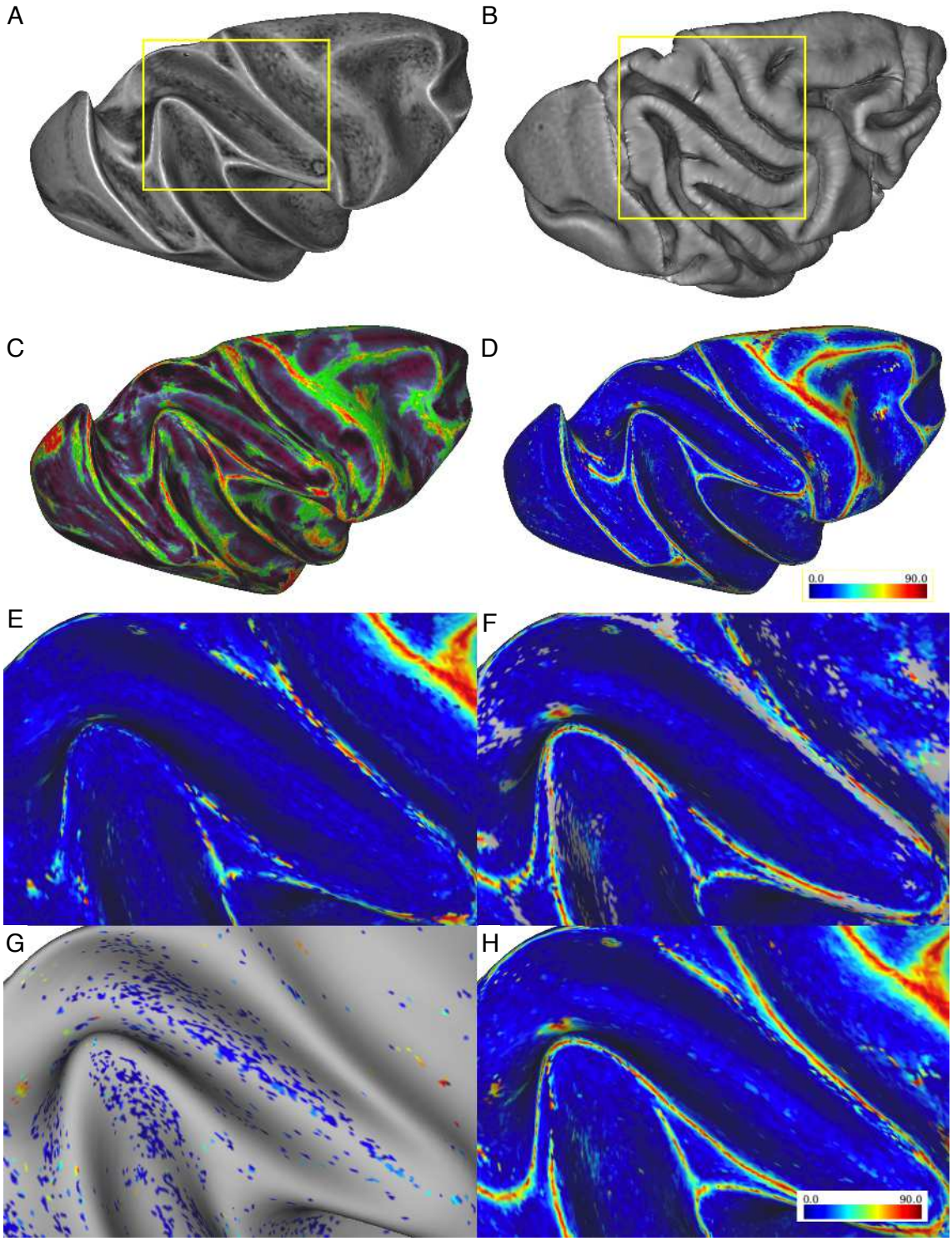

Figure 5.17: A.,B Inflated and Folded surfaces with the inset location (E-H) shown in yellow. C. PVI measure. D. The largest (of fiber 1,2,3) angle between the surface at WGB and the nearest fiber. E - H As D., for each of fibers 1,2,3 and the largest in the IPS region (see A) At the fundus all three modelled fibers are parallel to the WGB. This suggests the difficult modelling of 4 or 5 diffusion directions may be necessary to model projections from the fundus into deep WM. It is not guarunteed even then.

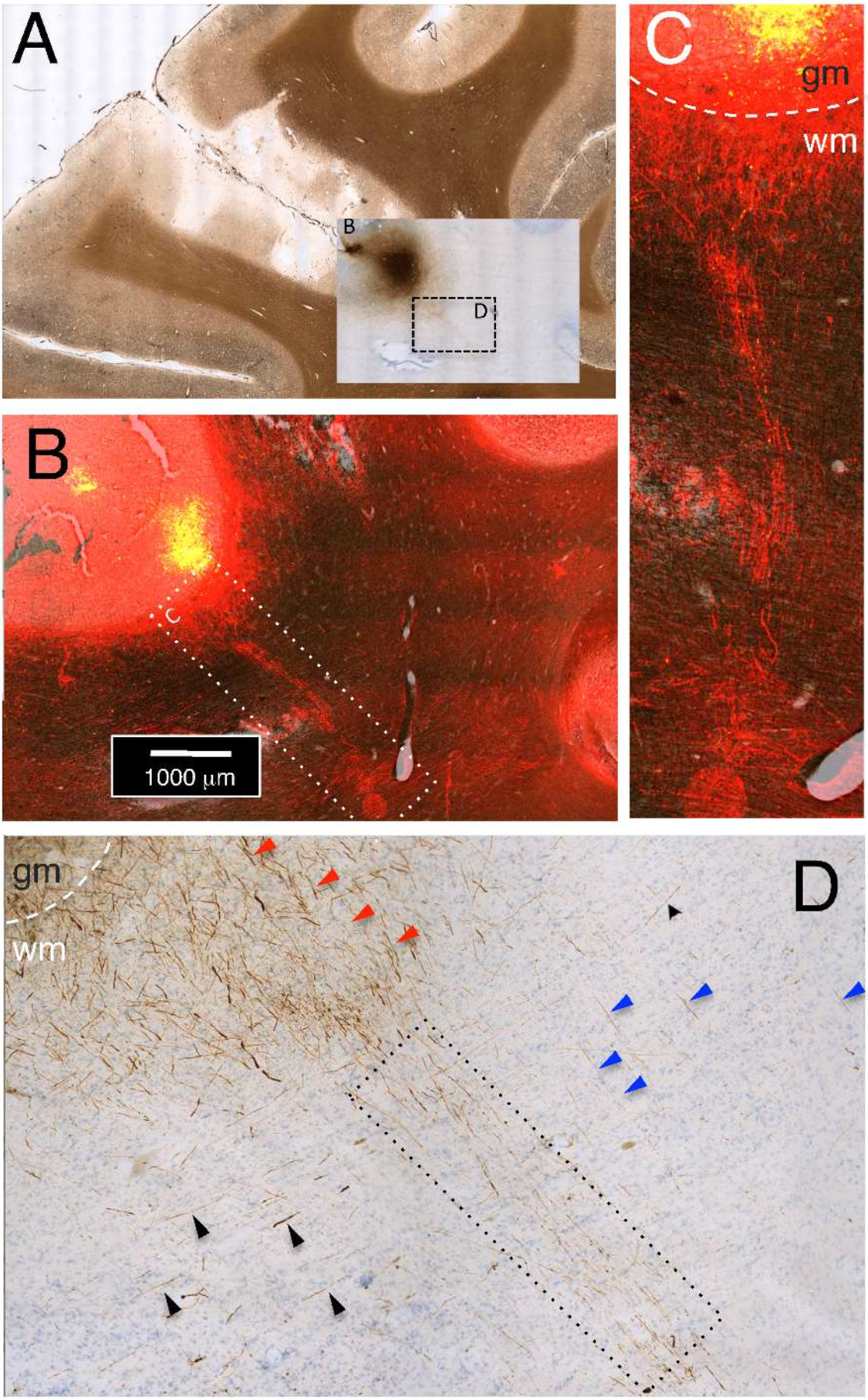

Figure 5.18

Figure 5.18: (BDA), an anterograde tracer, into the intraparietal sulcus (IPS). A. View of BDA injection site at the fundus of the IPS. Inset is BDA staining on Nissl section, shown superimposed on myelin-stained background. B. Magnified view of fundus depicting fluorescently immunolabeled BDA superimposed on myelin-stained background. Dotted rectangle highlights group of labeled fibers projecting from fundus to deep white matter, crossing the superficial white matter. C. Magnified view of dotted rectangle in B. White dashed line indicates the white-gray matter boundary. D. BDA-labeled white matter fibers from IPS fundus injection, magnified from inset in A. A group of labeled fibers projects radially through the superficial white matter into the deep white matter (red arrowheads, dotted black rectangle). In addition, sparse fibers oriented parallel to (blue arrowheads) and perpendicular to (black arrowheads) the penetrating fiber group are also visible

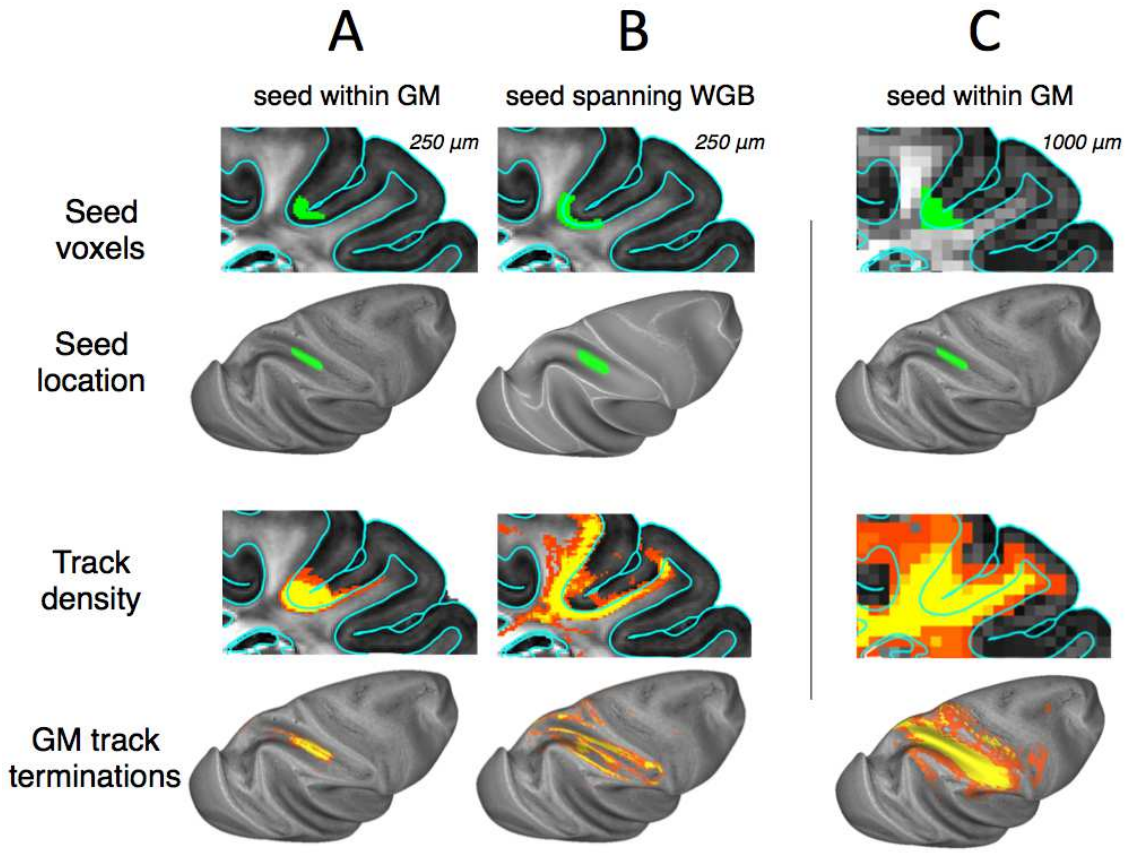

Figure 5.19: Effect of gray matter seeding strategy and spatial resolution on penetration of track lines into the deep white matter. The top two rows show seeding strategy and bottom two rows show distribution of track lines. A. A slab of voxels (rather than surface coordinates used elsewhere in this study) was used to create a tractography seed region in the fundus of the IPS. Voxels were selected within a region projected 250m above and below the cortical mid-thickness. Examination of the resulting track density and track termination plots revealed that this large seed led to minimal labeling away from the IPS, consistent with the results shown in Fig. 2. B. Shifting an equivalent slab to straddle the WGB led to more widespread labeling, particularly on adjacent gyri. C. In a 1mm isotropic dMRI dataset, downsampled from the 250m dataset, voxels projected using identical 250um methods and parameters to A resulted in a yet broader spread of track lines. Note that the increased spatial distribution in B and C was not an improvement in the accuracy of projections emanating from the overlying cortex but simply reflected a seeding of superficial white matter tracts projecting broadly.

5.6.2 Local Fiber Anatomy at the IPS

Figure 5.20 shows and describes histologically derived characterizations of the local and neighbourhood fibers from (Schmahmann and Pandya, 2006).

Figure 5.21 Shows in the same animal the seeding from the corpus callosum (yellow) which does not reach the GM, as well as seeds 3 and 4 which capture the two local fibers at IPS: neighbourhood and local. These are subsequently shown histologically.

Figure 5.22 Shows that via dMRI, we can see that the local and neighbourhood fibers have different properties: the local fiber passes under the fundus orthogonal to the line of the sulcus. the larger Neighbourhood fiber travels obliquely across the fundus, covering the walls of the IPS as it moves mediolaterally between the IPL and SPL.

Figure 5.23 uses a combination of scalar DTI maps, MTR, DTI and structure tensor processing of tissue to support the ideas introduced in figure 5.22

Finally, the argument for the structure of the neighbourhood fiber is concluding using ST, tracking and DTI evidence to clarify further and more visually figure 5.23

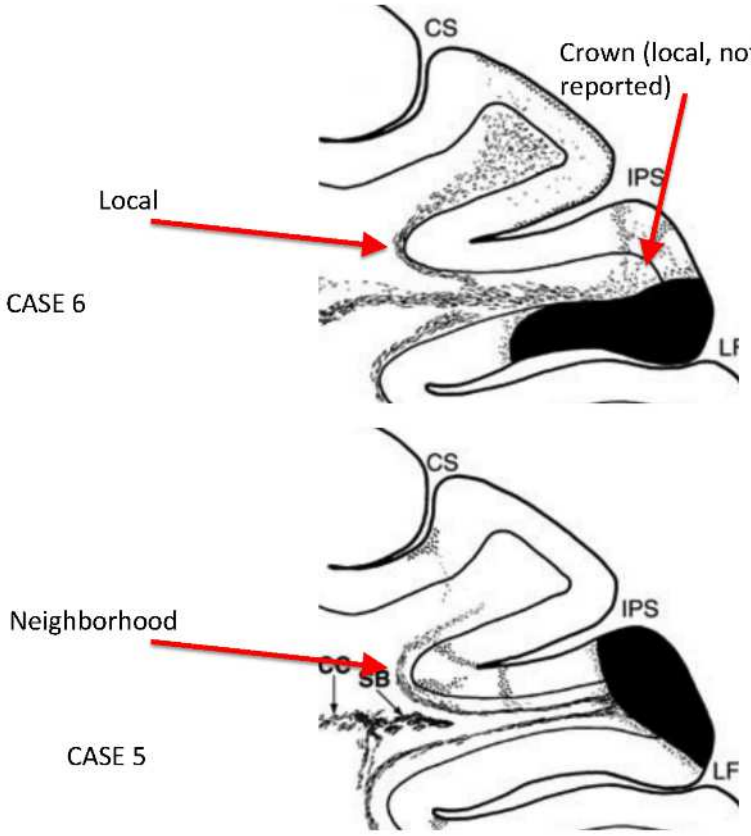

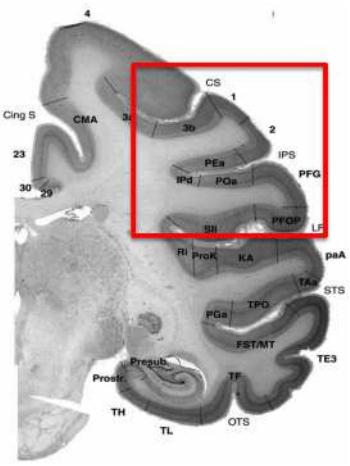

Section 93

Association Fibers

Local Association Fibers

From the injection site fibers travel within the white matter subjacent to the lower bank of the IPS and provide discrete columns of termination in areas POa and IPd (Scs. 93, 97).

CASE 5

Neighborhood Association Fibers

Distinct terminations are conveyed via the white matter of the superior parietal lobule to areas 1 and 3b in the lower bank of the central sulcus (Scs. 93,97). Also, columnar terminations are seen in area Ri in the depth of the Sylvian fissure, conveyed by the white matter near the injection site (Sc. 93).

Association Fibers

Local Association Fibers

Adjacent to the injection site, terminations are noted in a columnar manner in areas PF and PFG in the inferior parietal lobule and in SII in the parietal operculum (Scs. 89, 93, 97).

CASE 6

Neighborhood Association Fibers

Neighborhood connections are conveyed by fibers traveling around the depth of the IPS to terminate in the first layer in areas 2 and 1 in the superior parietal lobule (Scs. 89, 93, 97).

Figure 5.20: from (Schmahmann and Pandya, 2006)

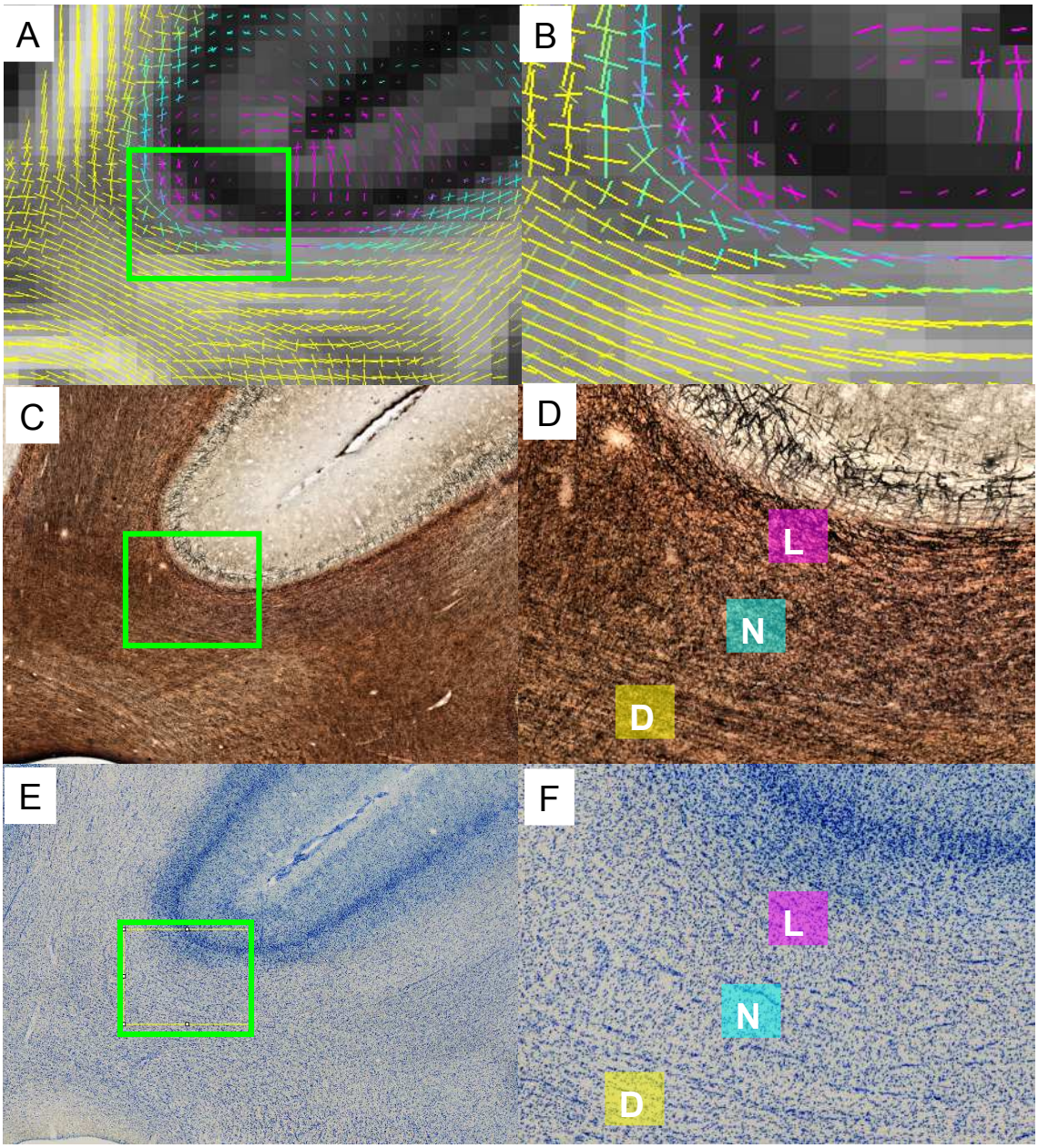

Figure 5.21

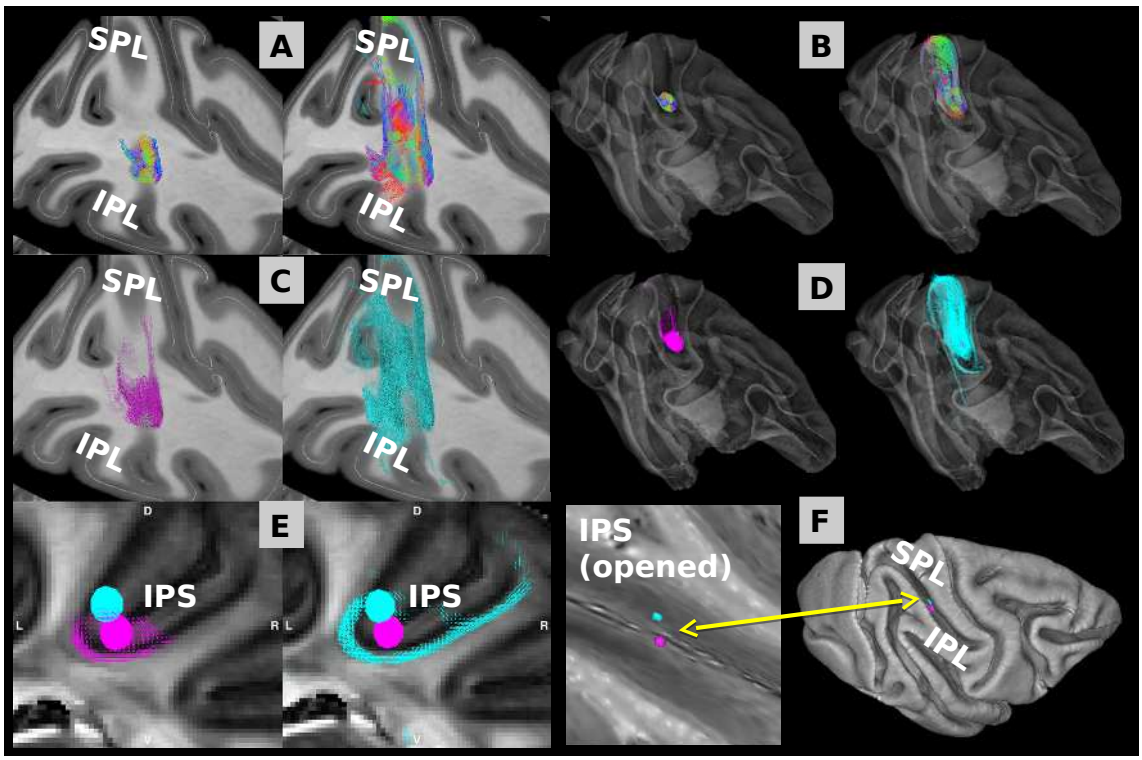

Figure 5.22: The local, u-fiber (seed 3) appears from DTI evidence to cross under the fundus orthogonally to it. By contrast, the larger Neighbourhood fiber crosses the fundus obliquely, following the sulcal walls and running medio-laterally from the SPL to the IPL. This is in keeping with observations in (Schmahmann and Pandya, 2006). **A.** color coded tracking from seeds 3 (left) and 4 (right). Colors are with respect to the histological coordinate frame. **B.** as **A.** in the context of WM outline. **C.,D.** as **A,B** but colored by seed. **E.** seed locations and tracks on coronal slices. **F.** seed locations on the surface model.

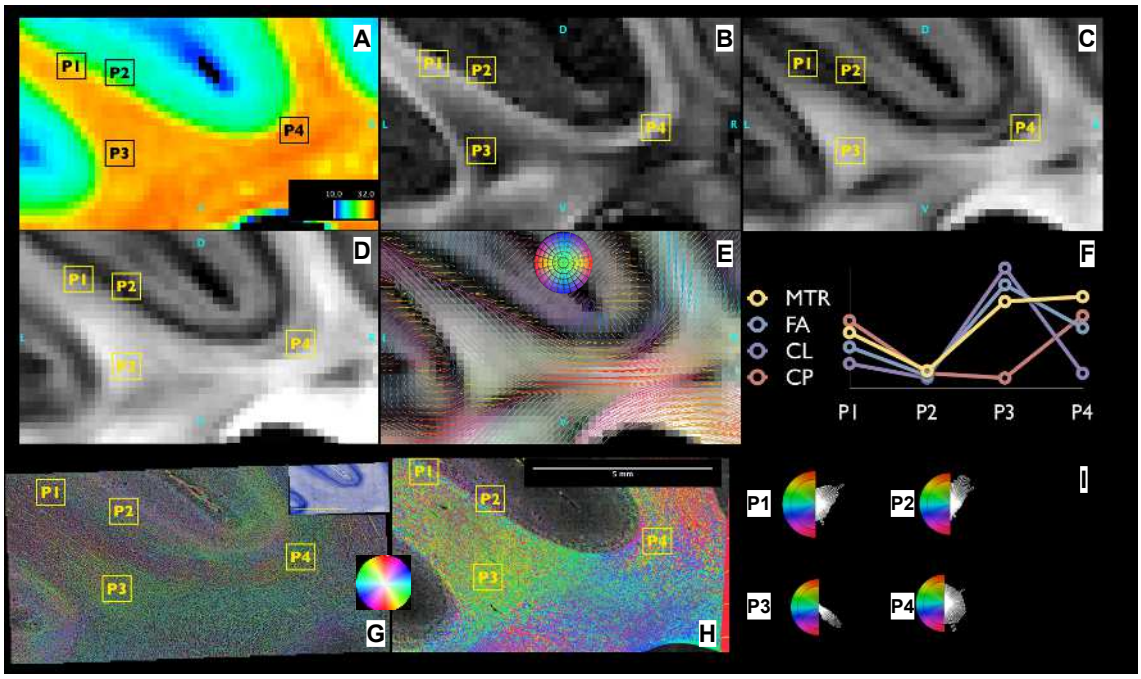

Figure 5.23: Four points are shown in MRI (A-E) and ST processed histology (G cell bodies, H fibers). P1 in the ufiber on dorsal bank of the IPS. P2 adjacent GM. P3 in deep white at entrance to IPL. P4 in local fibers at fundus. A MTR. B planar. C linear. D FA. E DTI. F relative values of A to D. G nissl. H myelin ST. I angle distributions in H

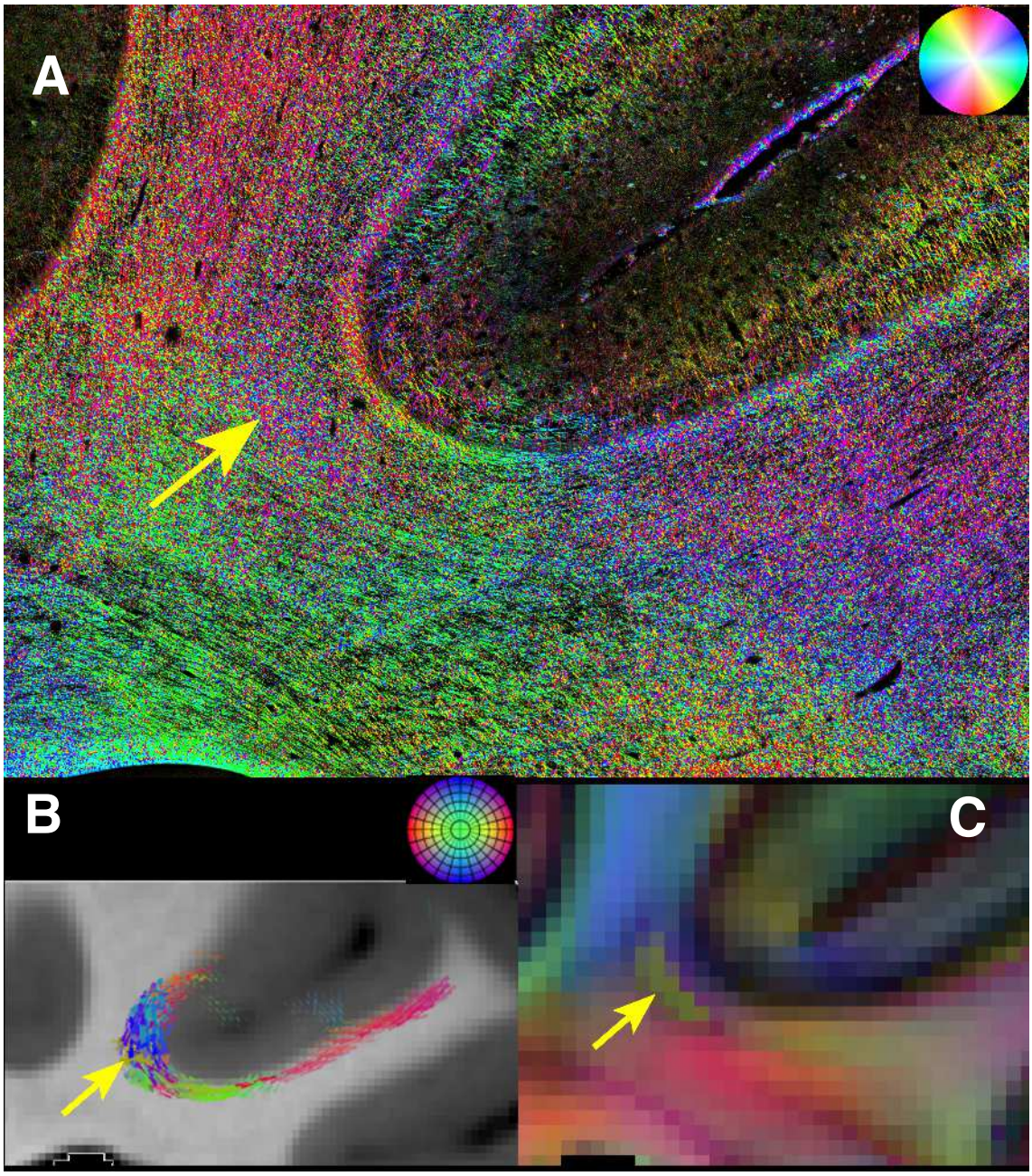

Figure 5.24: **A** pixelwise structure tensor analysis of Gallyas stain in IPS (see methods). The tight, rope like band of the u-fiber is visible subjacent to LVI. It is most sharply defined at the fundus, where by eye it's orientation is most coherent. In the central white matter of the precentral gyrus (left) a coherent group of ascending axons is visible. Each gyral wall exhibits a local fiber. From the bottom left, coherent fibers run from the corpus callosum in a large swath to the mouth of the IPL gyrus. Fibers can be seen passing through this deep commisural bundle at right angle towards the fundus. The neighbourhood fiber system is visible as a more diffuse curve of fibers running subjacent to the u-fiber. The yellow arrow denotes the region of low anisotropy, where the N-fiber is at it's most complex (P4). the mix of angles from figure 5.23 is visually evident. In **B** the tracking trajectories sampled (limited only to the dominant model) are diffuse and varied at this location. **C** notes the complexity in DEC map.

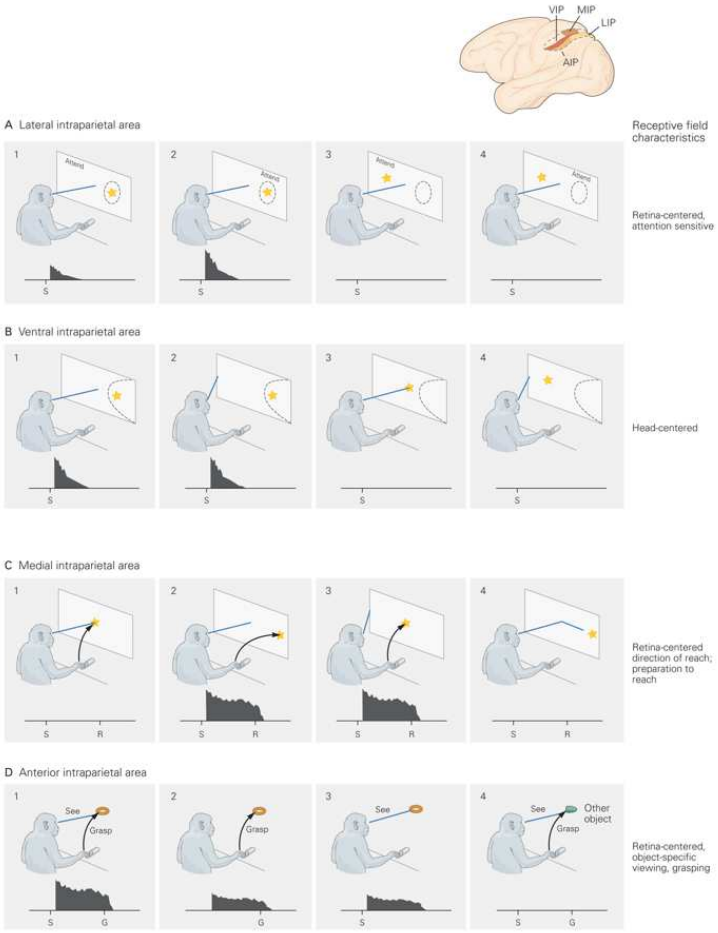

Figure 18-6 (Opposite) Neurons in the parietal cortex of the monkey are selective for the location of objects in the visual field relative to particular parts of the body. Each histogram represents the firing rate of a representative neuron as a function of time following presentation of a stimulus. In each diagram the line emanating from the eyes indicates where the monkey is looking.

Figure 5.25: The regions on the banks of the IPS perform related visual functions. The N fiber serves to link them ventrolaterally, hence it is oblique. from (Kandel, 2013).

A picture may have emerged of the local fiber anatomy around the inferior parietal lobule in which the structure and orientation of the neighbourhood fiber bundle serves to join the IPL and SPL but also the visual regions on the banks of the IPS mediolaterally, hence it crosses the fundus obliquely to join e.g. LIP and VIP efficiently (figure 5.25) . The local fiber directly joins across the fundus, orthogonal to it connection regions directly across from each other in the IPS, IPL and lateral postcentral gyrus consistent with e.g. (Rizzolatti et al., 1998). The crown fiber then serves to link regions on the IPL crown, the visually dominated multimodal motor area 7A to the more lateral somatosensory multimodal region 7B.

5.7 Summary & Conclusion

In this chapter we examined the evidence that superficial white matter structures are the primary or ultimate (after other issues described in chapter 1 have been resolved) reason for "gyral bias" and the failure of tracking to cover much for the cortex. We first examined the properties of tissue and scan data from the same locations. Subsequently we examined in detail the tracking behaviors that appear underlie the gyral bias. We next examined the GM and WM histology surrounding local fibers in detail and with respect to tracking behaviors. We noted the existence and properties of superficial fibers running the length of gyral crowns as well as in fundi.

We then showed that despite, or perhaps because of, its lisencephalic cortex the marmoset white matter consists in a thick superficial WM layer, surrounding deep rostrocaudal fibers. Thus, the folding pattern of a brain is not a reliable indicator of "gyral bias". Bias in tracking results to GM is ultimately due to local fibers, not folding itself as seen in the marmoset and in e.g. crown fibers in Rhesus. Local fibers are, we suggest, "remnants" of the white matter subserving the cortical sheet prior to the ontogenetic process of folding which we ascribe to the tension based theory of morphogenesis (Van Essen et al., 1997) as described in chapter 1. The tight coupling between tracking penetrance into GM from WM and superficial WM structures suggests that tracking from the thalamus or other central stucture like the Corpus Callosum e.g. Figure 5.14 B will be restricted in penetrating the cortical GM by superficial WM and tend to remain in deep WM.

Finally we turned to a detailed examination of the local fiber systems at the IPS. We noted that even with 3 directions of local model, paths through the IPS local fiber systems could not presently be modelled. We showed by tracer injection on this fundus that axons to pass directly through. We discussed some potential problems in modelling this with dMRI in principle. seed placement strategies and spatial resolution were briefly examined in the context of this analysis of IPS fibers. Finally, we applied dMRI and histological analysis combined with known literature data to characterize the trajectories of the IPS superficial fibers with respect to anatomical regions and cortical landmarks. We suggested that the specific shape and structure of the local, neighbourhood and crown fibers in the IPS/IPL region may subserve compact efficient local intra-connectivity between the various visual association, visuomotor and somato-motor regions in the lateral parietal lobe of the rhesus monkey in a way that might lead to insights into the visuo-motor processing of this region.

Chapter 6

Conclusion

We began by investigating the extent to which tracer result could be replicated with tractography. To the extent it could not we accounted for that by the notion of "gyral bias" and it's accompanying explanations. We found these explanations did not entirely account for cortical penetrability patterns using the scalar maps we developed in this thesis ("PVI") to assess penetrability of tractography from the GM into the WM and investigated superficial white matter as an overriding anatomical factor.

We investigated the superficial WM via tracking and histology and described novel micro and meso scale properties as anatomical structures in detail, including entirely new anatomical structures. We demonstrated via a range of approaches that local fibers are likely the primary determining factor in the viability of cortico-cortical dMRI tracking.

Further, we found that folding was not only an unreliable correlate of local fiber structure and "gyral bias", by repeating our analysis in the marmoset brain we showed it need not be correlated to folding at all in a primate brain.

We found that in high quality data with a modern modelling technique, even where 3 directions of anisotropy are resolved, they all follow the local fiber, making WM effectively impenetrable from cortex. Tracer evidence showed that deep fiber projections do cross this structure. While the density of long projections per cortical region or per mm^2 facing WM may vary, the evidence is strong that they are widespread in all regions.

Local models of fiber fanning or further advances may well permit a trackline to traverse a local fiber. However, a problem remains. Long range axons impinge on cortex by

passing through local fibers. For an afferent trackline, what is the basis for deciding when to cross? If some axons remain the local system for some of their length, how can the point of exit be detected? How are we to track the connections subserved by the many axons of the local fibers themselves, and determine when a connection enters or leaves the bundle into deep WM or back into cortex. Consider the local fiber linking the SPL and IPL, which not only suffers this problem but also means that long, neighbourhood and local systems form a complex mesh and which to track at what point is a difficult problem regardless of the local model employed or spatial resolution obtained.

Point **3.** in section 1.3.1 of chapter 1 refers to the "orientation continuity assumption" of tracking algorithms. While dMRI supports "crossing fibers" via many local models, tracking algorithms proceed by choosing to integrate via the orientation that minimizes the deviation from their current path ((Behrens et al., 2007). As a consequence, sharp turns as in figure 1.2 **C** will still not result in tracking terminations because even if the local models spatially resolved the turns they would be avoided unless they minimized angular deviation. And if the algorithm does not employ the "orientation continuity assumption" then the issues above come into play: when to turn, which local diffusion orientation to follow, conceptually which fiber structure to follow and when to enter or leave it.

This is symptomatic of a wider conceptual issue. Long range intracortical axons follow complex paths with many sharp turns, entering and leaving bundles and regions of tissue (Schmahmann and Pandya, 2006) given any local model in a voxel, it is impossible to track a connection from to/from a site because the actual axons make so many sharp turns. With only local diffusion information as your guide for tracking (i.e. in a voxel) there is no way of knowing when the turns happen. Because something will be turning in every voxel. How can you know when the specific path you are tracking turns or does not? You cannot know in principle. There is no information about that. the problem is especially acute re local fibers but it generalizes to all tractography. Because actual anatomical connections follow such complex paths (e.g. see figure 5.18 which shows many sharply turning axons from a tracer injection in addition to a central group projecting from the fundus), there is not enough information to work out their paths using only local diffusion patterns. It is impossible in principle. the issue of local fibers, even when tracking could be developed that passes through them is in a way just a special, very acute case of general in-principle problem in all tractography.

However, diffusion imaging yields more than orientations. The Gaussian diffusion tensor can provide information about the rate and the manner in which water diffuses (e.g. figure 5.23. Taken as e.g. a moving spatial window of diffusion information in a region around the track head, perhaps combined with a non-markovian property the track might infer information about it's anatomical context on which to base turning decisions. Plainly such decisions would retain a statistical aspect. Plainly such an algorithm would involve anatomical prior knowledge or at least supervised learning which might call into question the validity of the results. Plainly the design and implementation of such an algorithm is quite formidable, if models from diffusion MRI data can even provide the anatomical information required. Information from MT and other contrasts, surface (folding) and fMRI information may all play a role, fMRI and dMRI is already a research subject.

In terms of pure anatomy, this thesis explored local fibers in detail as important structures in their own right. We found local fibers to be complex in structure, trajectory and in location, rather than simply "U-fibers" under the cortex of adjacent gyri . Some evidence from both diffusion and available histology points to a fiber running the mediolateral length of the central sulcus fundus, terminating along the length with another larger ufiber running orthogonally and linking the sensory and motor cortices. In the parietal lobe diverse local fibers were found. This diversity makes predictions based on folding patterns or cortical wedging very hard, even if known local fibers can be tracked.

In section 5.4.1 we described a "crown fiber", a local fiber running the length of a gyral crown, previously unreported. In the context of the anatomical and developmental hypothesis of the formation of local fibers and cortical folds put forwards in Chapter 1 that guided much of this research conceptually as a matter of neuroscience, the existence of this fiber is not surprising: it is a "leftover", a thick bundle of many local axons required to connect adjacent or near adjacent regions with a close functional relationship not brought closer in proximity by folding. Similarly, the finding that the majority of marmoset cortex surrounds a local fiber system may be seen as stemming from the notion that cortical regions have not drawn closer by folding during morphogenesis. That is, local fiber connections between cortical regions are the rule, and folding and the formation of adjacent walls of a gyral blade with short axons the exception.

If that is true, as we have argued in depth, the structure and composition of the local fiber systems may provide physical clues that aid in the understanding of how parietal regions interact functionally. In the Rhesus parietal lobe we investigated the properties of interacting local fiber systems in the context of the cortical regions and spatial relationships involved. Plainly white matter structure gives clues as to function in the form and location of fasiculi; local fiber bundle organization in relation to folding, distance, composition and so on may also provide clues to how locally related regions are organized in e.g. processing hierarchies.

Moreover, further and more earnest research into the principles of cortical morphogenesis and white matter structure morphogenesis in mammalian brains may well provide the spatial context required to develop algorithms that can plausibly trace the many efferent and afferent paths from a cortical site from only MRI derived data.

While this work does not examine in-vivo acquisition and tracking explicitly, the primary implication is one of spatial resolution. Fig 5.19 and section 4.5 discuss this issue. The data here were aquired by high field scans lasting several days to achieve a resolution of 0.25mm. At 0.25mm 64 times as much data is present as at 1mm, which is roughly what is possible in vivo at present. Figure 5.19 shows a pattern of false positives at lower resolution because of partial volume effects in the thin local fibers. Higher resolutions may require prohibitive scan times, although a mixture of high spatial resolution data with lower resolution high SNR data may be a viable strategy. In general the issues in ex-vivo data would seem in principle the same, although false positive rate is hard to know at lower resolution as discussed in section 4.5.

Bibliography

Alexander, A. L., Lee, J. E., Lazar, M., and Field, A. S. (2007). Diffusion Tensor Imaging of the Brain. *Neurotherapeutics : the journal of the American Society for Experimental NeuroTherapeutics*, 4(3):316–329. 22

Basser, P. J., Mattiello, J., and LeBihan, D. (1994). MR diffusion tensor spectroscopy and imaging. *Biophysical Journal*, 66(1):259–267. 3

Behrens, T., Berg, H., Jbabdi, S., Rushworth, M., and Woolrich, M. (2007). Probabilistic diffusion tractography with multiple fibre orientations: What can we gain? *Neuroimage*, 34(1):144–155. 7, 26, 38, 39, 40, 84, 154

Behrens, T., Johansen-Berg, H., Woolrich, M., Smith, S., Wheeler-Kingshott, C., Boulby, P., Barker, G., Sillery, E., Sheehan, K., Ciccarelli, O., et al. (2003a). Non-invasive mapping of connections between human thalamus and cortex using diffusion imaging. *Nature neuroscience*, 6(7):750–757. 3, 80

Behrens, T., Woolrich, M., Jenkinson, M., Johansen-Berg, H., Nunes, R., Clare, S., Matthews, P., Brady, J., and Smith, S. (2003b). Characterization and propagation of uncertainty in diffusion-weighted MR imaging. *Magnetic Resonance in Medicine*, 50(5):1077–1088. 26

Brodmann, K. (1909). *Lokalisationslehre der Grosshirnrinde in ihren Prinzipien dargestellt auf Grund des Zellenbaues*. 1, 2

Budde, M. D. and Frank, J. A. (2012). Examining brain microstructure using structure tensor analysis of histological sections. *NeuroImage*, 63(1):1–10. 43

Burman, K. J., Palmer, S. M., Gamberini, M., Spitzer, M. W., and Rosa, M. G. (2008). Anatomical and physiological definition of the motor cortex of the marmoset monkey. *The Journal of Comparative Neurology*, 506(5):860–876. 102, 103

Catani, M., Jones, D. K., Donato, R., and Ffytche, D. H. (2003). Occipitotemporal connections in the human. *Brain*, 126(9):2093–2107. 4

Chen, H., Zhang, T., Guo, L., Li, K., Yu, X., Li, L., Hu, X., Han, J., Hu, X., and Liu, T. (2013). Coevolution of Gyral Folding and Structural Connection Patterns in Primate Brains. *Cerebral Cortex*, 23(5):1208–1217. 6

Cowan, W., Gottlieb, D., Hendrickson, A., Price, J., and Woolsey, T. (1972). The autoradiographic demonstration of axonal connections in the central nervous system. *Brain research*, 37(1):21. 2, 84

Crick, F. and Jones, E. (1993). Backwardness of human neuroanatomy. *Nature*, 361(6408):109–110. 3

Dauguet, J., Peled, S., Berezovskii, V., Delzescaux, T., Warfield, S. K., Born, R., and Westin, C.-F. (2007). Comparison of fiber tracts derived from in-vivo DTI tractography with 3d histological neural tract tracer reconstruction on a macaque brain. *NeuroImage*, 37(2):530 – 538. 4

Dejerine, J. J. (1895). *Anatomie des centres nerveux*, volume 1. Rueff. 8

Dyrby, T. B., Sgaard, L. V., Parker, G. J., Alexander, D. C., Lind, N. M., Baar, W. F., Hay-Schmidt, A., Eriksen, N., Pakkenberg, B., Paulson, O. B., and Jelsing, J. (2007). Validation of in vitro probabilistic tractography. *NeuroImage*, 37(4):1267–1277. 4

DArceuil, H. E., Westmoreland, S., and de Crespigny, A. J. (2007). An approach to high resolution diffusion tensor imaging in fixed primate brain. *NeuroImage*, 35(2):553–565. 38

Felleman, D. J. and Van Essen, D. C. (1991). Distributed Hierarchical Processing in the Primate Cerebral Cortex. *Cerebral Cortex*, 1(1):1 –47. 2

Fischl, B., Sereno, M. I., and Dale, A. M. (1999). Cortical Surface-Based Analysis: II: Inflation, Flattening, and a Surface-Based Coordinate System. *NeuroImage*, 9(2):195–207. 51

Gallyas, F. (1979). Silver staining of myelin by means of physical development. *Neurological Research*, 1(2):203–209. 43

Gruslys, A., Acosta-Cabronero, J., Nestor, P., Williams, G., and Ansorge, R. (2014). A New Fast Accurate Non-Linear Medical Image Registration Program Including Surface

Preserving Regularisation. *IEEE Transactions on Medical Imaging*, Early Access Online. iv, 52

Hutchison, R. M., Leung, L. S., Mirsattari, S. M., Gati, J. S., Menon, R. S., and Everling, S. (2011). Resting-state networks in the macaque at 7T. *NeuroImage*, 56(3):1546–1555. 51

Jbabdi, S., Behrens, T. E., and Smith, S. M. (2010). Crossing fibres in tract-based spatial statistics. *NeuroImage*, 49(1):249–256. 4

Jbabdi, S. and Johansen-Berg, H. (2011). Tractography: Where Do We Go from Here? *Brain Connectivity*, 1(3):169–183. 4

Jbabdi, S., Lehman, J. F., Haber, S. N., and Behrens, T. E. (2013). Human and Monkey Ventral Prefrontal Fibers Use the Same Organizational Principles to Reach Their Targets: Tracing versus Tractography. *The Journal of Neuroscience*, 33(7):3190–3201. 4

Kaas, J. H. (2012). The evolution of neocortex in primates. *Progress in brain research*, 195:91–102. 2

Kandel, E. R. (2013). *Principles of Neural Science*. McGraw Hill Professional. 151

Kitamura, K., Nakayama, K., Kosaka, S., Yamada, E., Shimada, H., Miki, T., and Inoue, Y. (2008). Diffusion tensor imaging of the cortico-ponto-cerebellar pathway in patients with adult-onset ataxic neurodegenerative disease. *Neuroradiology*, 50(4):285–292. 4

Kleiser, R., Staempfli, P., Valavanis, A., Boesiger, P., and Kollias, S. (2009). Impact of fMRI-guided advanced DTI fiber tracking techniques on their clinical applications in patients with brain tumors. *Neuroradiology*, 52(1):37–46. 4

Lewis, J. W. and Van Essen, D. C. (2000a). Corticocortical connections of visual, sensorimotor, and multimodal processing areas in the parietal lobe of the macaque monkey. *The Journal of Comparative Neurology*, 428(1):112–137. 6, 43, 79, 80, 87, 88, 89

Lewis, J. W. and Van Essen, D. C. (2000b). Mapping of architectonic subdivisions in the macaque monkey, with emphasis on parieto-occipital cortex. *The Journal of Comparative Neurology*, 428(1):79–111. 70, 118

Mantini, D., Hasson, U., Betti, V., Perrucci, M. G., Romani, G. L., Corbetta, M., Orban, G. A., and Vanduffel, W. (2012). Interspecies activity correlations reveal functional

correspondence between monkey and human brain areas. *Nature Methods*, 9(3):277–282. 2

Marcus, D. S., Harms, M. P., Snyder, A. Z., Jenkinson, M., Wilson, J. A., Glasser, M. F., Barch, D. M., Archie, K. A., Burgess, G. C., Ramaratnam, M., Hodge, M., Horton, W., Herrick, R., Olsen, T., McKay, M., House, M., Hileman, M., Reid, E., Harwell, J., Coalson, T., Schindler, J., Elam, J. S., Curtiss, S. W., and Van Essen, D. C. (2013). Human Connectome Project informatics: Quality control, database services, and data visualization. *NeuroImage*, 80:202–219. 41

Markov, N. T., Ercsey-Ravasz, M. M., Gomes, A. R. R., Lamy, C., Magrou, L., Vezoli, J., Misery, P., Falchier, A., Quilodran, R., Gariel, M. A., Sallet, J., Gamanut, R., Huissoud, C., Clavagnier, S., Giroud, P., Sappey-Marinier, D., Barone, P., Dehay, C., Toroczkai, Z., Knoblauch, K., Essen, D. C. V., and Kennedy, H. (2014). A Weighted and Directed Interareal Connectivity Matrix for Macaque. *Cerebral Cortex*, 24(1):17–36. 6, 51, 78

Molnr, Z., Blakey, D., Bystron, I., and Carney, R. S. E. (2006). Tract-Tracing in Developing Systems and in Postmortem Human Material Using Carbocyanine Dyes. In Zaborszky, L., Wouterlood, F. G., and Lanciego, J. L., editors, *Neuroanatomical Tract-Tracing 3*, pages 366–393. Springer US. 3

Mori, S. and van Zijl, P. C. M. (2002). Fiber tracking: principles and strategies a technical review. *NMR in Biomedicine*, 15(7-8):468–480. 3

Mufson, E. J., Brady, D. R., and Kordower, J. H. (1990). Tracing neuronal connections in postmortem human hippocampal complex with the carbocyanine dye DiI. *Neurobiology of Aging*, 11(6):649–653. 3

Nie, J., Guo, L., Li, K., Wang, Y., Chen, G., Li, L., Chen, H., Deng, F., Jiang, X., Zhang, T., Huang, L., Faraco, C., Zhang, D., Guo, C., Yap, P.-T., Hu, X., Li, G., Lv, J., Yuan, Y., Zhu, D., Han, J., Sabatinelli, D., Zhao, Q., Miller, L. S., Xu, B., Shen, P., Platt, S., Shen, D., Hu, X., and Liu, T. (2011). Axonal Fiber Terminations Concentrate on Gyri. *Cerebral Cortex*, 22(12):2831–2839. 6

Op de Beeck, H. P., Haushofer, J., and Kanwisher, N. G. (2008). Interpreting fMRI data: maps, modules and dimensions. *Nature Reviews Neuroscience*, 9(2):123–135. 1

Paus, T., Toro, R., Paus, T., and Toro, R. (2009). Could sex differences in white matter be explained by g ratio? *Frontiers in Neuroanatomy*, 3:14. 11

Paxinos, G., Huang, X. F., Petrides, M., and Toga, A. (2008). The rhesus monkey brain in stereotaxic coordinates with DVD. 51, 53

Perelman, P., Johnson, W. E., Roos, C., Seunez, H. N., Horvath, J. E., Moreira, M. A. M., Kessing, B., Pontius, J., Roelke, M., Rumpler, Y., Schneider, M. P. C., Silva, A., O'Brien, S. J., and Pecon-Slattery, J. (2011). A Molecular Phylogeny of Living Primates. *PLoS Genet*, 7(3):e1001342. 3

Pierpaoli, C., Jezzard, P., Basser, P. J., Barnett, A., and Di Chiro, G. (1996). Diffusion tensor MR imaging of the human brain. *Radiology*, 201(3):637–648. 3

Pierpaoli, C., Walker, L., Irfanoglu, M., Barnett, A., Basser, P., Chang, L., Koay, C., Pajevic, S., Rohde, G., Sarlls, J., and others (2010). TORTOISE: an integrated software package for processing of diffusion MRI data. 40

Preuss, T. M. and Goldman-Rakic, P. S. (1991). Architectonics of the parietal and temporal association cortex in the strepsirhine primate Galago compared to the anthropoid primate Macaca. *The Journal of Comparative Neurology*, 310(4):475–506. 118

Rakic, P. (1988). Specification of cerebral cortical areas. *Science (New York, N.Y.)*, 241(4862):170–176. 13

Reiner, A. and Gamlin, P. (1980). On noncarcinogenic chromogens for horseradish peroxidase histochemistry. *The Journal of Histochemistry and Cytochemistry: Official Journal of the Histochemistry Society*, 28(2):187–191. 42

Rezakhaniha, R., Agianniotis, A., Schrauwen, J. T. C., Griffa, A., Sage, D., Bouten, C. V. C., Vosse, F. N. v. d., Unser, M., and Stergiopulos, N. (2011). Experimental investigation of collagen waviness and orientation in the arterial adventitia using confocal laser scanning microscopy. *Biomechanics and Modeling in Mechanobiology*, 11(3-4):461–473. 43

Rizzolatti, G., Luppino, G., and Matelli, M. (1998). The organization of the cortical motor system: new concepts. *Electroencephalography and clinical neurophysiology*, 106(4):283–296. 151

Rosene, D. L., Roy, N. J., and Davis, B. J. (1986). A cryoprotection method that facilitates cutting frozen sections of whole monkey brains for histological and histochemical processing without freezing artifact. *Journal of Histochemistry & Cytochemistry*, 34(10):1301–1315. 42

Saleem, K. S. and Logothetis, N. K. (2012). *A Combined MRI and Histology Atlas of the Rhesus Monkey Brain in Stereotaxic Coordinates*. Academic Press. 15, 50, 51, 52, 54, 57

Schmahmann, J. and Pandya, D. (2006). *Fiber pathways of the brain*. Oxford University Press, USA. 2, 9, 79, 80, 81, 84, 86, 122, 131, 145, 146, 148, 154

Schmahmann, J. D., Pandya, D. N., Wang, R., Dai, G., D'Arceuil, H. E., de Crespigny, A. J., and Wedeen, V. J. (2007). Association fibre pathways of the brain: parallel observations from diffusion spectrum imaging and autoradiography. *Brain*, 130(3):630–653. 4, 10

Schz, A., Braitenberg, V., Miller, S. R., and others (2002). The Human Cortical White Matter: Quantitative Aspects of Cortico-Cortical Long-Range Connectivity. In *Cortical areas: unity and diversity*, pages 377–385. Taylor Francis. 11, 12, 14

Seehaus, A. K., Roebroeck, A., Chiry, O., Kim, D.-S., Ronen, I., Bratzke, H., Goebel, R., and Galuske, R. A. W. (2013). Histological Validation of DW-MRI Tractography in Human Postmortem Tissue. *Cerebral Cortex*, 23(2):442–450. 3

Smith, S. M., Vidaurre, D., Beckmann, C. F., Glasser, M. F., Jenkinson, M., Miller, K. L., Nichols, T. E., Robinson, E. C., Salimi-Khorshidi, G., Woolrich, M. W., Barch, D. M., Uurbil, K., and Van Essen, D. C. (2013). Functional connectomics from resting-state fMRI. *Trends in Cognitive Sciences*, 17(12):666–682. 1

Sporns, O. (2013). The human connectome: Origins and challenges. *NeuroImage*, 80:53–61. 2, 3

Sporns, O., Tononi, G., and Ktter, R. (2005). The Human Connectome: A Structural Description of the Human Brain. *PLoS Comput Biol*, 1(4):e42. 3

Stephan, K. E. and Kotter, R. (1999). One cortex - many maps: An introduction to coordinate-independent mapping by Objective Relational Transformation (ORT). *Neurocomputing*, 26-27:1049–1054. 2

Tardif, E. and Clarke, S. (2001). Intrinsic connectivity of human auditory areas: a tracing study with DiI. *European Journal of Neuroscience*, 13(5):1045–1050. 3

Thomas, C., Ye, F. Q., Irfanoglu, M. O., Modi, P., Saleem, K. S., Leopold, D. A., and Pierpaoli, C. (2014). Anatomical accuracy of brain connections derived from diffusion MRI

tractography is inherently limited. *Proceedings of the National Academy of Sciences*, page 201405672. 5

Tootell, R. B. H., Hadjikhani, N. K., Mendola, J. D., Marrett, S., and Dale, A. M. (1998). From retinotopy to recognition: fMRI in human visual cortex. *Trends in Cognitive Sciences*, 2(5):174–183. 1

Tsao, D. Y., Moeller, S., and Freiwald, W. A. (2008). Comparing face patch systems in macaques and humans. *Proceedings of the National Academy of Sciences*, 105(49):19514–19519. 2

Tuch, D. S., Reese, T. G., Wiegell, M. R., Makris, N., Belliveau, J. W., and Wedeen, V. J. (2002). High angular resolution diffusion imaging reveals intravoxel white matter fiber heterogeneity. *Magnetic Resonance in Medicine: Official Journal of the Society of Magnetic Resonance in Medicine / Society of Magnetic Resonance in Medicine*, 48(4):577–582. 38

Van Essen, D. et al. (1997). A tension-based theory of morphogenesis and compact wiring in the central nervous system. *NATURE-LONDON-*, pages 313–318. 10, 11, 12, 131, 152

Van Essen, D. C. (2014). VAN ESSEN CHAPTER. 43

Van Essen, D. C., Drury, H. A., Dickson, J., Harwell, J., Hanlon, D., and Anderson, C. H. (2001). An Integrated Software Suite for Surface-based Analyses of Cerebral Cortex. *Journal of the American Medical Informatics Association : JAMIA*, 8(5):443–459. 41, 51

Van Essen, D. C., Glasser, M. F., Dierker, D. L., and Harwell, J. (2011). Cortical Parcellations of the Macaque Monkey Analyzed on Surface-Based Atlases. *Cerebral Cortex*, page bhr290. 51

Van Essen, D. C., Glasser, M. F., Dierker, D. L., Harwell, J., and Coalson, T. (2012a). Parcellations and Hemispheric Asymmetries of Human Cerebral Cortex Analyzed on Surface-Based Atlases. *Cerebral Cortex*, 22(10):2241–2262. 3, 41, 51

Van Essen, D. C., Jbabdi, S., Sotiropoulos, S., Chen, C., Dikranian, K., Coalson, T., Harwell, J., Behrens, T., and Glasser, M. F. (2013). Mapping connections in humans and nonhuman primates: aspirations and challenges for diffusion imaging. In *Diffusion*

MRI, 2nd: From Quantitative Measurement to In vivo Neuroanatomy. Academic Press San Diego. 1, 5, 6, 7, 8, 78, 114, 122

Van Essen, D. C. and Ugurbil, K. (2012). The future of the human connectome. *NeuroImage*, 62(2):1299–1310. 3

Van Essen, D. C., Ugurbil, K., Auerbach, E., Barch, D., Behrens, T. E. J., Bucholz, R., Chang, A., Chen, L., Corbetta, M., Curtiss, S. W., Della Penna, S., Feinberg, D., Glasser, M. F., Harel, N., Heath, A. C., Larson-Prior, L., Marcus, D., Michalareas, G., Moeller, S., Oostenveld, R., Petersen, S. E., Prior, F., Schlaggar, B. L., Smith, S. M., Snyder, A. Z., Xu, J., and Yacoub, E. (2012b). The Human Connectome Project: A data acquisition perspective. *NeuroImage*, 62(4):2222–2231. 3

Varela, F., Lachaux, J.-P., Rodriguez, E., and Martinerie, J. (2001). The brainweb: Phase synchronization and large-scale integration. *Nature Reviews Neuroscience*, 2(4):229–239. 2

Veenman, C. L., Reiner, A., and Honig, M. G. (1992). Biotinylated dextran amine as an anterograde tracer for single- and double-labeling studies. *Journal of Neuroscience Methods*, 41(3):239–254. 42

Wang, S. S.-H., Shultz, J. R., Burish, M. J., Harrison, K. H., Hof, P. R., Towns, L. C., Wagers, M. W., and Wyatt, K. D. (2008). Functional Trade-Offs in White Matter Axonal Scaling. *The Journal of Neuroscience*, 28(15):4047–4056. 11, 14

Wedeen, V., Rosene, D., Wang, R., Dai, G., Mortazavi, F., Hagmann, P., Kaas, J., and Tseng, W. (2012). The geometric structure of the brain fiber pathways. *Science*, 335(6076):1628–1634. 3

Wedeen, V., Wang, R., Schmahmann, J., Benner, T., Tseng, W., Dai, G., Pandya, D., Hagmann, P., D'Arceuil, H., and de Crespigny, A. (2008). Diffusion spectrum magnetic resonance imaging (DSI) tractography of crossing fibers. *NeuroImage*, 41(4):1267–1277. 38

Wedeen, V. J., Hagmann, P., Tseng, W.-Y. I., Reese, T. G., and Weisskoff, R. M. (2005). Mapping complex tissue architecture with diffusion spectrum magnetic resonance imaging. *Magnetic Resonance in Medicine*, 54(6):1377–1386. 3

Wolff, S. D. and Balaban, R. S. (1989). Magnetization transfer contrast (MTC) and tissue water proton relaxation in vivo. *Magnetic Resonance in Medicine*, 10(1):135–144. 39

Yang, Q. X., Posse, S., Le Bihan, D., and Smith, M. B. (1996). Double-sampled echo-planar imaging at 3 tesla. *Journal of Magnetic Resonance. Series B*, 113(2):145–150. 38

Zilles, K. and Amunts, K. (2010). Centenary of Brodmann's map conception and fate. *Nature Reviews Neuroscience*, 11(2):139–145. 1